



# MONASH University

***Modelling of lithospheric  
history-dependent stretching***

***From continental rifts to passive margins formation***

*Vittoria Morena Salerno*

*Doctor Of Philosophy*

A thesis submitted for the degree of *Doctor of Philosophy* at  
Monash University in (2015)  
*School of Earth, Atmosphere and Environment*





---

## Copyright notice

© The author (*Vittoria Morena Salerno*). Except as provided in the Copyright Act 1968, this thesis may not be reproduced in any form without the written permission of the author.

© The author (*Vittoria Morena Salerno*). Except as provided in the Copyright Act 1968, this thesis may not be reproduced in any form without the written permission of the author.

I certify that I have made all reasonable efforts to secure copyright permissions for third-party content included in this thesis and have not knowingly added copyright content to my work without the owner's permission.



---

## **Abstract**

Under the effect of divergent forces, continental lithosphere deforms into continental rifts, where stretching is either diffused over large areas or localized in narrow straining zones. Existing models have probed the role of initial lithospheric rheological layering, geothermal gradients and stretching rates on continental rifting evolution. While the boundary conditions imposed by the diverging margins relate to the rifting phase, the initial conditions are inherited features. Many continental rifts underwent several extensional phases, showing a variety of deformation style. Such complexities are not easily explained by a single stretching phase; instead these might find better explanation considering a polyphase rifting history. In this thesis, I address the role of episodic stretching on the long-term evolution of continental rifts. I explore two main types of rifting histories: 1) Rifting-Cooling-Rifting and 2) Rift –Rift. The first type aims to analyse the general aspect of the rifting evolution where rifting phases are intermitted by a cooling stage, which allows for geothermal re-equilibration, and consequently lithosphere can regain its original thickness. In this case, the lithosphere attains a different rheological layering, and this affects subsequent rifting. Alternating stretching velocities between the first and second rifting event generates a series of rifting histories.

In the second case, I propose a possible solution for the evolution of the Sirte Basin, providing an alternative explanation to its structuring. In particular I attempt to understand if the rifting history could have played a primary effect on the shifting in rifting mode over time (from wide to narrow). I use numerical modelling to investigate the development of rifting patterns during polyphase lithospheric extension. The models show that the time-dependent boundary conditions have a fundamental control on the tectonic rifting style and its evolution. The formation of narrow and wide rifts, and their shift in time might be strongly related to the cooling events and changing in boundary conditions during rifting history.

---

## **Declaration**

This thesis contains no material which has been accepted for the award of any other degree or diploma at any university or equivalent institution and that, to the best of my knowledge and belief, this thesis contains no material previously published or written by another person, except where due reference is made in the text of the thesis.



---

## Thesis including published works General Declaration

I hereby declare that this thesis contains no material which has been accepted for the award of any other degree or diploma at any university or equivalent institution and that, to the best of my knowledge and belief, this thesis contains no material previously published or written by another person, except where due reference is made in the text of the thesis.

This thesis 3 unpublished publications. The core theme of the thesis is the modelling of lithospheric

history-dependent stretching, The ideas, development and writing up of all the papers in the thesis were the principal responsibility of myself, the candidate, working within the School of Earth, Atmosphere and Environment under the supervision of Dr. Fabio A. Capitanio (main supervisor), Dr Rebecca J. Farrington and Professor Louis Moresi (supervisors)

(The inclusion of co-authors reflects the fact that the work came from active collaboration between researchers and acknowledges input into team-based research.)

In the case of of four chapters my contribution to the work involved the following:

Thesis chapter	Publication title	Publication status*	Nature and extent (%) of students contribution
2/3	Review on geodynamic modelling of lithospheric stretching and rational lithospheric history-dependent stretching	To be submitted	Comparison of monophasic modelling method with the novel rifting history-dependent modelling approach. Demonstration of the first order role of the deformation history and boundary conditions on the response of the lithosphere deformation modes and basin style. (85%)
4	The role of the strain history on the modes of continental extension	Submitted	General results of the novel approach on numerical modelling and analysis of the lithospheric history-dependent stretching (90%)
5	Strain history controls on the Sirte widest narrow rift basin, Libya	To be submitted	Application of the new approach to the Sirte Basin geological case. (90%)

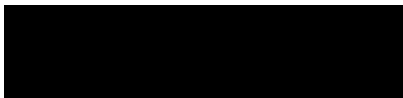
\* e.g. 'published'/'in press'/'accepted'/'returned for revision'

I have / have not renumbered sections of submitted or published papers in order to generate a consistent presentation within the thesis.

**Student signature:** 

**Date:** 1/04/2016

The undersigned hereby certify that the above declaration correctly reflects the nature and extent of the student and co-authors' contributions to this work.

**Main Supervisor signature:**   
1/04/2016

**Date:**



## Acknowledgements

At the end of these four years of my PhD I would like to thank all the people who, for various reasons, have accompanied me on this journey and without them this research thesis wouldn't have been completed.

This PhD wasn't easy, for several reasons: firstly as an international student and secondly for my health problems. However, I was fortunate to have had many people that have helped me and supported me along the way.

Thanking people is not an easy task ..... Even the most beautiful words and sentences are not enough to express my gratitude, but I'll give it a go.

Firstly I want to thank Dr Fabio A. Capitanio, my main supervisor, for having always been willing to offer me his precious theoretical and methodological contribution during many stages of my research work. He always generously did his utmost to teach me the science and the scientific methodology. I want to thank him especially for teaching me new perspectives on how to look at things, which is the essence of being a scientist.

He helped me to contextualize every concept and scientific question in a bigger frame and to how analyse them using computational thinking. Many people are probably questioning if 2-3 hours of Italian espresso coffee, a white board and a Mac can lead to good science. Well, I still have to prove if I am a good scientist, but Fabio's method of "white board, Mac and coffee" definitely was effective for me since I feel very confident and satisfied of what I have understood and learnt thanks to him.

Last but not least, I want to thank him for his friendship and personal support when I was not well, for the many laughs and discussions we had as well as the chats on fine art, philosophy, culinary art, architecture, culture and life! Grazie Fabbie'!

Special thank goes to Dr Rebecca Farrington not only for her theoretical and methodological contribution but also for her help when my "marriage" with the computational part of my PhD was looking very shabby.

I want to thank her for all the help she offered me from the first day I started my PhD. From numerical modelling to psychological (yes really!) support, for her friendship and for the lovely and relaxing times we shared together.

Most importantly, she gave me her support and dedication in the delicate stages of completion of my thesis. I will never forget it Bec! You are truly a good friend and an excellent supervisor! Thank Bec, my "numerical sister"!

I would like to thank Professor Louis Moresi, for the appreciation he showed towards me, the help he gave, and the knowledge he passed on. Also, for giving me all the support I needed through his team of scientists and developers, especially when I was learning how to use the code. Additionally, I want to thank him for giving me the possibility to grow as a scientific communicator putting me in charge of the practical lessons of geodynamics courses. For allowing me to help coordinate the unit as well as letting me present my research to the scientific community at Melbourne University. These experiences were very important steps to understanding what I needed to improve as communicator and person. Thanks Louis for the trust you showed me and for the opportunities you gave me.

A very big thank goes to Dr Giovanni Spampinato and his fiancé' Clara Marri for their support, advise, help, presence even when they were in the other part of the world. I will never forget it. Giovanni deserves special thanks because he came back to Australia at the right time, when I was approaching my deadline and with very limited time, he did his



best to correct my work and put everything in order for me. It was something that very few people would be willing to do and it was a demonstration true friendship. Gio', I am lucky to have a friend like you.

Professor Peter Betts must also be acknowledged for all the help he offered me during all of my candidature. He guided me on the right track when I had difficulties, and he gave me opportunities inside the school and showed me scientific and personal consideration. I want to thank him for the professionalism and respect he showed towards me as a student but also respecting my professional competencies acquired in years of work in Oil&Gas industry. Also, I deeply appreciated the scientific and relaxed discussions we had, which helped me understand the importance of the link between geodynamics and geology. All that you did for me was very important especially towards the end of my PhD adventure. Thanks Pete!!!!

To Dr. John Mansour, Jerico Revote, Dr Mirko Velic, Julian Giordani, Dr Nicolas Riel, Owen Kaluza, Dr Gareth Kennedy, Dr Steve Quinette should also be thanked for their precious help, patience and contribution in building my models and teaching me about computational techniques. John, Julian, Jerico and Mirko you were the best in coping with my constant request of explanations. I really enjoyed learning from you and I can confidently say that we are also good friends.

My "numerical brothers" Ken McLean, Ben Mather and Adam Beall are thanked for always been there for me, for your sincere friendship and the many times they had to put up with my very bad moods. Even though our paths were separated for different reasons, I know we will always be friends.

Professor Christopher Wilson, Dr Sasha Wilson, Dr Vincent Strak, Professor Roberto Weinberg and Professor Sandy Cruden should also be thanked for accepting to be panel members and participating in my millstone talks. They have provided me with excellent comments and suggestions, as well as guiding me on how to improve my research and my communication skills.

I am deeply grateful to Dr Sasha Wilson, Professor Michael Reeder, Robert Oakley and Johanna Laurent for their help in the last month of my candidature. Your assistance was unexpected and much appreciated!

I also wish to express my special thanks to Dr Joao Duarte, Dr Teagan Blaikie, Dr Jozua Van Otterloo, and my "doctor friends" Julie Boyce, Robin Armit, Tom Carmichael, Jim Driscoll as well as Dr Chris Mays for the many chats we had on Geology and on PhD life in general and for their ongoing support throughout my candidature.

To Tien Chin Chen, Silvana Cifaratti, Katie Tran, Christine Jones, Meghan Hough, Petrina Soh, Junnel Alegado, Dr. Massimo Raveggi, Trent Duncan and Doris Seegets-Villiers for the technical support and administrative assistance as well as their professionalism and friendship.

I wish to express my deep gratitude to my beloved mother, Nicoletta Travaglini and father, Giovanni Salerno, for their unlimited love. I wish they could have been here in Australia to share this moment of happiness with me.

Being far from home is not easy for a PhD student and I was the very lucky one to have found a family here in Australia. I would like to thank from the bottom of my heart Mario and Elena Ticli, Mark, Michelle Amelia and Sophia Ticli for their love and support in last 4 years. You have giving me unconditional love and understanding and I will be forever

grateful. This family is very big and a special thanks goes to all the cousins, aunties, uncles, nonni, “comari “ and “comari” I have gained along the way. Thank you all.

Finally, to the one who has been with me all throughout, for understanding me and supporting me with endless love: my partner Rebecca.

Thank you Rebecca firstly for sharing the amazing adventure of life, and for the immense and unequivocal support that led this quest to completion. You are my life□guiding inspiration.

I also thank you for all your support in the very distressing moments, for all those sleepless nights when I was in a science discovering/desperation phase and you patiently waited without ever leaving my side. Thank you Rebecca for all your true love! I dedicate this thesis to you as sign of gratitude.

Last I want to remember my best friend Milena. She left our world a few years ago to chat, sing and play with Jimi Hendrix, Janis Joplin and Sid Vicious. This thesis is dedicated to her as well, the angel that always walks by my side





## Table of Contents

List of Figures.....	
Chapter 2 .....	21
Chapter 3.....	23
Chapter 4.....	24
Chapter 5.....	24
CHAPTER 1: INTRODUCTION.....	
1. Thesis Objective.....	27
2. Outlines.....	28
CHAPTER 2 .....	
1. ABSTRACT .....	33
2. BACKGROUND: LITHOSPHERIC STRETCHING.....	33
3. GEOLOGICAL AND GEOPHYSICAL OBSERVABLE: PART I.....	37
3.1 Styles of rifting basins and passive margins: variability in natural systems.....	37
3.1.1 Intracratonic basins.....	38
3.1.2 Continental Rift.....	42
3.1.3 Failed Rifts (or Aulacogens).....	44
3.1.4 Proto-oceanic troughs.....	46
3.1.5 Passive continental margins.....	47
3.2 Geological and geophysical observations in regions of continental extension (rifts and passive margins).....	50
3.2.1 Seismicity.....	50
3.2.2 Crustal thickness.....	50
3.2.3 Gravity.....	51
3.2.4 Faults.....	52
3.2.5 Heat Flow.....	53
3.2.6 Topography.....	54
3.2.7 Time scale and amount of extension.....	55
4. TYPE OF MODELS.....	55
4.1 Modelling the evolution of geodynamic systems. Background on modelling techniques .....	56
4.2 Models classification based on main processes believed to play the first order influence on rifting evolution.....	56
4.2.1 Rift initiation: causes traditionally taken into account.....	57
4.2.2 Why and how is the lithosphere deformed? Strain localization and delocalization processes.....	60

4.2.3 Kinematic and mechanical (kinematic with rheological constraints and dynamic) models .....	61
4.2.3.1 Kinematic Models.....	64
4.2.3.2 Mechanical models (kinematic models with rheological constraints and dynamic models).....	64
4.2.3.2.1 Non-uniform stretching models: discontinuous and continuous stretching with depth.....	66
4.2.3.2.2 Lithospheric stretching and boundary conditions role at the onset of rifting .....	70
4.2.3.2.3 Buoyancy forces and lower crustal flow.....	75
4.2.3.2.4 Lithospheric flexure.....	75
4.2.3.2.4.1 Flexural models.....	77
4.2.3.2.4.2 Necking models.....	83
4.2.3.2.5 Strain-induced weakening.....	83
4.2.3.2.6 Rheological stratification of the lithosphere.....	94
4.2.3.2.7 Magma-assisted rifting.....	101
5. GEOLOGICAL AND GEOPHYSICAL OBSERVABLE (PART II). COMPLEX RIFTING HISTORIES. RIFTING HISTORIES AND CONCEPTUAL MODELS.....	103
6. POLYPHASE MODELS .....	106
7. ROLE OF BOUNDARY CONDITION VARIATION ON RIFTING HISTORY.....	110
7.1 General approach hypothesis to test the importance of rifting history.....	112
7.2 Approach for the present study.....	113
7.2.1 Methodology .....	114
 CHAPTER 3: CONTINUUM MECHANICS FUNDAMENTALS IN GEODYNAMICS MODELLING AND PROJECT'S RATIONALE.....	
1. INTRODUCTION.....	121
2. PART 1: FUNDAMENTALS OF CONTINUUM MECHANICS.....	122
2.1 Governing, equations.....	122
2.1.1 The equation of mass conservation.....	123
2.1.2 The equation of motion.....	124
2.1.3 The heat equation.....	127
2.1.4 The rheological or constitutive law .....	129
2.1.5 Byerlee law.....	134
2.1.6 Additional equations.....	137
2.1.7 Boussinesq approximation.....	137
2.2 Modelling (numerical/analytical) boundary and initial conditions.....	138
3. PART 2: MODELLING THE LITHOSPHERE .....	141
3.1 Yield Strength Envelope profile constriction .....	141

3.2 Conceptual models and project rationale .....	149
3.2.1 Parameterisation of rifting histories.....	150
3.3 Monophase 1D experiments: parameter choice and validation of reference model for polyphase simulation.....	152
3.3.1 Localization phase diagrams for monophase stretching: R or M history type.....	155
3.3.2 Comparison of localization index phase diagrams present in literature and 1D conceptual monophase model verification.....	157
3.4 Conceptual model for polyphase rifting .....	157
3.4.1 Lithosphere definitions.....	159
3.4.2 Assumptions for the present study.....	159
3.4.2.1 Mechanical lithosphere.....	161
3.4.2.2 Thermal lithosphere and thermal boundary layer.....	161
3.4.3 Schematic model for Monophase versus Polyphase 1D thinning.....	162
3.5 Polyphase 1D experiments: RCR history type.....	165
3.5.1 Localization phase diagrams for polyphase stretching.....	165
3.5.1.1 RCR and RR.....	170
4. DISCUSSION ON 1D MODELLING.....	172
5. PART 3: 2D MODELLING MONOPHASE LITHOSPHERIC STRETCHING.....	174
5.1 Generalities on numerical modelling procedure.....	174
5.2 Underworld, modelling set-up and boundary conditions.....	175
5.2.1 Lithospheric thinning and rifting: the “diagnostic” tool for comparison between different rifting histories.....	178
CHAPTER 4: MODELLING COMPLEX RIFTING EVOLUTION EXEMPLIFIED THROUGH RIFT-COOLING-RIFT (RCR) HISTORY TYPE.....	
The role of the strain history on the modes of continental extension.....	
ABSTRACT.....	187
1. INTRODUCTION.....	188
2. NUMERICAL MODELLING.....	192
2.1 Modelling approach.....	192
2.2 Governing equations.....	194
2.3 Model set up and boundary conditions.....	195
2.4 Lithospheric thinning and rifting .....	197
2.5 Basin Subsidence.....	198
2.6 Melting .....	198
3. RESULTS.....	199
3.1 Lithospheric rifting modes.....	199

3.2 Lithospheric thinning and basin evolutions .....	203
3.3 Subsidence patterns and melting production .....	205
3.3.1 Subsidence Analysis.....	205
3.3.2 Melting production.....	208
3.4 Controls on the modes of lithospheric extension .....	211
4. DISCUSSION.....	214
4.1 Rifting histories and deformation modes .....	214
5. CONCLUSION INFERENCES ON RIFTING EVOLUTION INTERPRETATIONS .....	219
5.1 Basin Style and rifting mode.....	219
5.2 Subsidence .....	220
5.3 Melting production.....	221
5.4 Conclusion.....	222
CHAPTER 5: MODELLING GEOLOGICAL CASE: RIFT-RIFT (RR) HISTORY TYPE	
Strain history controls on the Sirte widest narrow rift basin, Libya.....	
1. INTRODUCTION.....	227
2. GEOLOGICAL SETTING AND LITERATURE REVIEW ON SIRTE BASIN OPENING	234
.....	
2.1 The Sirte Basin System: Geological Setting.....	234
2.2 Basin Stratigraphy and tectonic subsidence.....	235
3. NUMERICAL MODELLING.....	242
3.1. Modelling approach.....	242
3.2. Governing equations.....	242
3.3. Model set up and boundary conditions.....	245
3.4. Lithospheric thinning and rifting and Basin Subsidence.....	246
3.4.1. Basin Subsidence.....	246
3.4.2 Lithospheric thinning.....	247
3.5 Localization index of the lithosphere.....	247
4. RESULTS AND DISCUSSION.....	248
4.1 Subsidence curves and lithospheric thinning.....	248
4.1.1 Monophase tectonic subsidence (M rifting history type).....	249
4.1.2 Two-phase tectonic subsidence (RR rifting history type).....	250
4.1 Crust and mantle lithospheric thinning for Sirte Basin model.....	252
5. Discussion and Conclusion.....	255
CHAPTER 6: CONCLUSIONS.....	
1. Role of the lithospheric rifting history on continental extension.....	263
2. Role of rifting history: assumptions to maintain the generality of the	264
results.....	



3. Significance of the study.....	267
4. Future work.....	269
REFERENCES.....	273



## List of Figures

### Chapter 2

- **Fig. 1** Passive and active end-members idealization.
- **Fig. 2** Basins rift-drift suite in terms of increasing stretching factor and extensional strain rate.
- **Fig. 3** Tectonic subsidence of intracontinental basins.
- **Fig. 4** Hudson Bay Basin, Canada.
- **Fig. 5** Cross-sections of West Siberian Basin.
- **Fig. 6** Diagram illustrating the formation of the Southern Oklahoma Aulacogen
- **Fig. 7** Basin filling pattern resulting from continuous depth-dependent stretching
- **Fig. 8** Volcanic, sediment-nourished, and sediment-starved margins.
- **Fig. 9** Left: Depth to the Moho below sea-level (in km), showing a mantle bulge in the southern Rhine Graben centred on the Kaiserstuhl volcano; Right: Crustal thickness changes in the North Sea area as a result of Mesozoic rifting
- **Fig. 10** Gravity profiles across rift zones
- **Fig. 11a** Heat flows in some continental rifts and surrounding regions, compared to the global heat flow average.
- **Fig. 11b** Rifts, supradetachment basins, and proto-oceanic troughs in terms of their strain rate, total extensional strain, and dip of master faults.
- **Fig. 12** Diagram illustrating the interaction of shear-traction exerted on the base of the lithosphere by asthenospheric flow, deviatoric tension above upwelling mantle convection cells and ridge push forces.
- **Fig. 13** Sketches showing the difference between extension of thick lithosphere without (a) and with (b) magmatic intrusion by diking.
- **Fig. 14** Boundary conditions for dynamic models of lithospheric extension.
- **Fig. 15** Kinematic models of continental extension.
- **Fig. 16** Schematic diagrams to illustrate differences between (a) uniform, (b) discontinuous, and (c) continuous depth-dependent stretching.
- **Fig. 17** Values of the maximum strain achieved in a model lithosphere as a function of duration of straining for two different values of  $O/nRT$ .
- **Fig. 18** Illustrative models showing the different styles of extensional deformation expected with fast and slow rates of extension.
- **Fig. 19** Three-layer lithospheric model, Thermal evolution of the lithosphere and Evolution of lithospheric strength.
- **Fig. 20** Schematic diagram illustrating thermal and crustal buoyancy forces generated during rifting.
- **Fig. 21** Sketches of the lithosphere illustrating three modes of extension emphasizing the regions undergoing the greatest amount of extensional strain
- **Fig. 22** Generalized form of an asymmetric rift basin showing border fault in (a) cross-section and (b) plan view
- **Fig. 23** Modes of extension leading to continental break-up and three-dimensional concept for the temporal and spatial evolution of rifting.

- **Fig. 24** Regional isostatic response to different depths of necking.
- **Fig. 25** Results of model calculations showing that maximum value of  $\sigma$  scales with layer thickness.
- **Fig. 26 (a)** Model geometry showing temperature structure of the crust, mantle lithosphere and sublithospheric mantle. (b,c) Reference model of extension when strain softening is absent. Models of extension involving (d,e) frictional-plastic (brittle) strain softening and (f,g) both frictional-plastic and viscous weakening mechanisms.
- **Fig. 27** Models of extension involving frictional-plastic (brittle) strain softening.
- **Fig. 28** Modelled evolution of mantle core complex during the breakup of non-volcanic continental margins.
- **Fig. 29** Strain fields of four selected models at the final stage of deformation after 13.7 Ma.
- **Fig. 30 (a)** Model setup for numerical simulations of lithospheric stretching. **(b)**, **(c)**, and **(d)**, deformation grid after 1% total strain for a crustal thickness ( $T_c$ ) of 6, 12 and 27 km, respectively. **(e)** Effect of crustal thickness on predicted rift half-width. **(f)** Effect of vertical geothermal gradient on predicted rift half-width.
- **Fig. 31** Model of symmetric rifting. **(a)** Model setup. **(b)** Total strain and **(c)** distribution of upper, middle and lower crust and mantle after 25, 47 and 78 km of extension.
- **Fig. 32 a)** 1D analytical solution giving the lithosphere thickness  $h_L$  and the high strength uppermost mantle thickness as a function of the Moho temperature  $T_M$ . **(b)** Patterns of continental rifting as a function of brittle crust and whole crust thicknesses for dry olivine at  $V=1$  cm/a (top) and 1 mm/a (middle) and for wet olivine at  $V=1$  cm/a (bottom). **(c)** Role of the crustal thickness. Patterns of total strain after 45 km of boundary extensional displacement for  $h_C=30$  km (left) and  $h_C=50$  km (right) for Moho temperatures  $T_M=482$  °C (up) and  $T_M=550$  °C (down), and with  $V=1$  cm/a. **(d)** Role of the applied boundary velocity. Patterns of total strain after 40 km of boundary extensional displacement for  $V=1$  cm/a (left) and  $V=1$  mm/a (right) for Models 1 to 3. **(e)** Role of the initial Moho temperature  $T_M$ . Patterns of total strain in Models 1 to 3 for an initial crustal thickness of 30 km, after 30 km and 60 km of boundary extensional displacement, with  $V=1$  cm/a, and line drawings of corresponding lithosphere scale structures.
- **Fig. 33** Comparison of the predicted average regional isostatic elevation changes for magma-assisted rifting and pure shear necking.
- **Fig. 34** Subsidence of sedimentary basins according to the Uniform Stretching.
- **Fig. 35** Left: Bouguer gravity anomaly map of the onshore parts of the Scandinavian North Atlantic passive margin; Right: Tectonic subsidence curves for four sub-basins and platforms of the Mid-Norwegian margin.
- **Fig. 36** Resolving multiple rift phases by strain-rate inversion in the Petrel Sub-basin, northwest Australia.
- **Fig. 37** (Top) Map showing location of seismic reflection profile. (Bottom) Spatial and temporal variation of strain rate.

- **Fig. 38** Polyphase models
- **Fig. 39** (Top) Geological cross section of the Sirte basin. (Bottom) Strain rates in the Ajdabyia Trough, eastern Sirte Basin of 21 selected wells, spanning the basin north to south.

## Chapter 3

- **Fig. 1** Arbitrary fluid volume,  $V$ , with surface  $S$  and elemental surface normal vector,  $dS$ , within which the fluid properties are to be conserved.
- **Fig. 2 a)** Right: Experimentally established linear dependence between normal stress and shear stress for compressional failure of various rocks. Left: Two principal failure criteria (Mohr-Coulomb). **(b)** Dependence of brittle strength on depth/pressure.
- **Fig. 3** Examples of rheological YSEs (Goetze and Evans, 1979) for continents.
- **Fig. 4** Influence of compositional variation, plate thickness  $a = z$  ( $1330^{\circ}\text{C}$ ) and fluid content on continental YSE computed for typical surface heat flow,  $q_s$ , of  $60 \text{ mW m}^{-2}$  for two different thermal models.
- **Fig. 5** Schematic illustration of a Brace-Goetze lithosphere
- **Fig. 6** Strength profiles for the continental lithosphere as calculated with the model for a Brace-Goetze lithosphere.
- **Fig. 7 (a)** Yield strength envelope profiles and **(b)** localization numbers calculated by the semi-analytical model.
- **Fig. 8** Phase diagrams representing the localization for a) WET, b) MIXED and c) DRY rheology and for the Moho Temperatures and initial strain rate ranges in Tab. 3.2 and 3.3.
- **Fig. 9** Comparison of existing literature models for lithospheric localization.
- **Fig. 10** Schematic representation of the lithospheric system with indication of two possible definitions for Thermal Boundary Layer (TBL).
- **Fig. 11** Schematic evolution of monophasic (a) and polyphase (b) rifting.
- **Fig. 12** 1D polyphase experiments used to test the role of boundary condition at the start of the rifting 1 (red box) and the start of rift 2 (green box).
- **Fig. 13** Phase diagrams representing the localization for a mixed (Tab. 3.3) rheology, Moho Temperatures and initial strain rate ranges in Tab. 3.2.
- **Fig. 14** Grid independency test (Resolution test) performed on a testing domain at 400km depth by 400 km wide numerical domain for increasing resolution mesh of  $n1=25 \times 25$ ,  $n2=250 \times 50$ ,  $n3=100 \times 100$ ,  $n4=400 \times 400$ ,  $n5=500 \times 500$  and  $n6=800 \times 800$  elements.
- **Fig. 15** Numerical model setup.
- **Fig. 16** Crustal ( $\beta$ ) and lithospheric mantle ( $\delta$ ) thinning vs time showing the formation of the wide and narrow rift end members and all the intermediate cases.
- **Tab. 1** Commonly inferred parameters of dislocation creep (power law).
- **Tab. 2** Thermal and mechanical parameters of the lithosphere used in model simulations.
- **Tab. 3** Dislocation creep parameters used in 1D parameters of the lithosphere.

## Chapter 4

- **Fig. 1** Numerical model setup.
- **Fig. 2** Results from numerical models.
- **Fig. 3** Plot of crust and lithospheric mantle thinning factors  $\beta$  and  $\delta$  for the whole domain vs. time.
- **Fig. 4** Subsidence curves for 3 monophasic and 4 polyphasic end-members models.
- **Fig. 5** Strain rate, melting percentage contours and T-P profiles.
- **Fig. 6** Melting production in time.
- **Fig. 7** Phase diagram for the 289 numerical models of two rifting phases intervened by cooling, on a  $\dot{\epsilon}_1$  -  $\dot{\epsilon}_2$  space, i.e. initial strain rate in the first and second rifting phases, respectively.
- **Fig. 8** **a)** schematic representation of changing of plastic thickness,  $thp$ , on the yield envelope profile as function of increasing initial strain rate,  $\dot{\epsilon}_{in}$ . **b)** Crustal thinning factors,  $\beta$  soon after the onset of rifting. **c)** Cartoon showing the Moho height as consequence of the initial strain rate applied to the rifting.
- **Fig. 9** Linear fitting of crustal thinning factor at the onset of the rifting phase and the thickness of the plastic portion of the lithosphere.
- **Fig. 10** Localization indexes for the 289 numerical models and the rifting mode domains, on a  $\dot{\epsilon}_1$  -  $\dot{\epsilon}_2$  space, i.e. initial strain rate in the first and second rifting phases, respectively.

## Chapter 5

- **Fig. 1** Tectonic sketch of the Central Mediterranean–North Africa area with the Sirte basin located in the northern African margin.
- **Fig. 2** Evidence of wide rift.
- **Fig. 3** Evidence of narrow rift.
- **Fig. 4** Tectonic subsidence in Fig. 4b and the inversion of the strain rate in in **Fig. 4c** (after supplementary information in Capitanio et al., 2009; **(d)** Capitanio et al., 2009).
- **Fig. 5** Generalized structural map of the Sirte Basin.
- **Fig. 6** Generalized stratigraphic lithologic correlation chart of the Upper Cretaceous and Tertiary successions of the Sirte Basin
- **Fig. 7** Contour maps of tectonic subsidence (m) of **(a)** Early Cretaceous, 144.0–112.2 Ma; **(b)** Cenomanian, 98.9–93.5 Ma; **(c)** Turonian, 93.5–89 Ma; **(d)** Santonian or Coniacian, 89–83.5 Ma; **(e)** Campanian, 83.5–71.3 Ma; **(f)** Maastrichtian, 71.3–65 Ma; **(g)** Danian–Ypresian, 65–49 Ma; and **(h)** Lutetian–Present, 49–0 Ma.
- **Fig. 8** Model Setup.
- **Fig. 9** Tectonic Subsidence curves calculated from 2D numerical models, simulation monophasic rifting with half stretching velocities between  $\frac{1}{2}v_{xx} = 0.05$  - 3 cm/yr.
- **Fig. 10** Thinning factors for crust,  $\beta$ , and lithospheric mantle,  $\delta$ , plotted at the end of the rifting and as function of time and horizontal size variation.

- **Tab. 1** Commonly inferred parameters of dislocation creep (power law). 1- Mackwell et al. (1998); 2 - Gleason and Tullis (1995) ; 3 - Ranalli and Murphy (1987); 4 - Brace and Kohlstedt (1980); 5 - Kirby and Kronenberg; 6 - Wilks and Carter (1990); 7 - Chopra and Paterson (1984); 8 - Chopra and Paterson (1981);
- **Tab. 2** Thermal and mechanical parameters of the lithosphere used in model simulations
- **Tab. 3** Previous page. Dislocation creep parameters used in 1D parameters of the lithosphere, simulating the deformation of a weak, mixed (average) and strong lithosphere. In bold are the parameters used in the polyphase simulation for 1.





# CHAPTER 1: INTRODUCTION

## 1. Thesis objective

Continental rifts evolve through deformation episodes into a variety of diverse basins with complex structural styles, subsidence and thermal histories, which may include melting. Existing models are based on a monophasic evolution of the rifting process. While they have probed the role of initial lithospheric rheological layering, geothermal gradients and stretching rates on continental rifting, they are not able to fully explain many complexities found in continental rifts and passive margins. In particular, rifting evolves through several extensional phases, which are not explained by a single rifting approach. In fact, the evolution of most basins on Earth includes more complex rifting histories with tectonics activity alternated to quiescence, time-dependent subsidence, stretching velocities and possible rifting migration and melting episodes. Hence, no single rifting event occurs on a pristine lithosphere, so that the initial conditions are hardly determined with precision. Therefore, their large variability over time and space limits the applicability of single-phase rifting model (Mckenzie, 1978). As an example, I will consider the Norway Margin geological case (Chapter 2) (Gabrielsen et al., 1999; Reemst & Cloetingh, 2000), where a long-lasting rifting history includes several rifting episodes (290-235 Ma, 170-95 Ma, 75-57 Ma), between the initial rifting and break-up, with oceanisation by ~ 55 Ma. Similar episodic rifting histories can be observed in the Iberian Basin (Van Wees et al., 1998), West Antarctic Rift System (Huerta and Larry, 2007; Corti et al., 2013), Michigan Basin (Bond and Kominz, 1984), Parana Basin (Zalan et al., 1990) Southwest Ordos Basin (Xie, 2007), Illinois Basin, Farley Well (Bond and Kominz, 1984), Moroccan Basin (Ellouz et al., 2003), Gippsland Basin (Falvey and Mutter, 1981; P. Yin, 1985), Jeanne D'Arc Basin (Stampfli et al., 2002), Baikal Basin (Moore et al., 1997), Williston Basin, North Dakota (Bond and Kominz, 1984), Williston Basin, Saskatchewan (Fowler and Nisbet, 1985), Cantabrian Basin (Stampfli et al., 2002), Lusitanian Basin (Stampfli et al., 2002). Other basins, instead show abrupt changes in strain rate and subsidence rate during long-term rifting, such as the Petrel Sub-basin, Australia (Baldwin et al., 2006), the Red Sea (e.g. Reilinger and McClusky, 2011, Almalki et al., 2014), Libya's Sirte Basin (Capitanio et al. 2009), South China Sea (Chen, 2014), and many others (see Sengor, 2001).

In this thesis, I address the role of episodic stretching on the long-term evolution of continental rifts. By means of numerical modelling, I investigate the development of rifting patterns as a consequence of distinct phases of lithospheric extension under different stretching rates, modifying the lithosphere's rheological layering, and intervening cooling, when the lithosphere regains its original thickness, and their effect on subsequent rifting. The models show that early rifting stages have a fundamental control on lithospheric-scale strain localization/delocalization and, consequently, on the tectonic rifting style and its evolution.

In particular this thesis addresses the questions outlined within the context that changes in boundary condition magnitude can be the first order factor generating the switch in deformation mode from one rifting phase to another. Specifically, with this thesis I aimed to determine if a variation in boundary condition can create different rifting histories and how these variations lead to the diversity of deformation found in the rift-drift suite of basins. The validity of this general approach has not been explored before in literature for lithospheric extension. Similar work was conducted by [Nalibof & Buiter \(2015\)](#) for extension settings. A similar approach has been previously used in the context of tectonic accretion (Ellis et al., 1999).

## 2. Outlines

Due to the fact that this approach has been used very limitedly, I need to follow a simple structure governed by the scientific methodology tailored for geodynamics modelling.

Therefore, each chapter represents the following steps:

- 1) Identification of the scientific questions after consideration of the geological observables and work hypothesis.
- 2) Rationale of the research and conceptual model; Physical parameters testing; Validation of the conceptual model.
- 3) Design and computation of the reference numerical model and validation.
- 4) Realization of the polyphase models to test the role of variation of boundary conditions and rifting history. Validation of the new approach.
- 5) Application of the new approach to a geological case.

An outline of the thesis chapters is presented below. Since chapters 4 and 5 are two stand-alone papers in preparation, the reader will find repetitions on the following topic from chapters 2 and 3:

- Posing of the scientific problem
- Numerical methodology (e.g. model set-up, code, boundary and initial conditions)
- Use of the same analytical means (crust and mantle lithosphere thinning vs. time, tectonic subsidence curves, lithosphere strain localization index);

**Chapter 2** firstly provides the classification of the geological structures derived from lithospheric extension and then offers a review of the existing models and the state of the art of the research related lithospheric stretching. Then, the chapter highlights supplementary geological observables, which leads to the scientific question setting the stage for the rationale of the project. The geological cases and models review presented in this study are taken from Kearey et al. (2010), Allen and Allen (2005) and Fernandez and Ranalli (1997).

In **Chapter 3**, I firstly present the continuous mechanics laws needed to perform geodynamic modelling. The second part of the chapter describes the rationale of the project, developed through 1D conceptual models of polyphase history-dependent stretching. Here, I test the rheological parameters and physical parameters. The final part of the chapter shows the monophasic computational model, needed as a base for the 2D polyphase model, given the absent in literature of a benchmark for numerical polyphasic modelling. Tests on numerical models are presented along with the results on crust and lithospheric thinning and basin style of variation of horizontal velocities. The results are compared with literature models in order to validate the 2D model.

In **Chapter 4**, the 1D polyphase history-dependent conceptual model is translated in into numerical simulations. The base for the numerical model is the monophasic 2D model developed in part 3 and in the previous chapter. 2D results test how rift history influences the final basin deformation, subsidence patterns and magma production. In this chapter, I analyse the general aspects of the polyphase rifting, aiming to demonstrate the general validity of the approach.

The second phase of the modelling methodology imposes a validation of the approach by testing it with a specific geological case.

In **Chapter 5**, I have modelled the evolution of the Sirte Basin, validating the polyphase history-dependent stretching with independent geological observations. This is presented in Chapter 5.

## Declaration for Thesis Chapter 2

**Monash University**

### Declaration for Thesis Chapter 2

#### Declaration by candidate

In the case of Chapter 2, the nature and extent of my contribution to the work was the following:

Nature of contribution	Extent of contribution (%)
Analysis of the literature geological/geophysical data and models plus interpretation of existing data used to formulate the scientific questions and the foundation (hypothesis) of research's rationale. The chapter structure, synthesis of the part 1 and 2 of the literature data and models as well as part 3 of scientific questions, are going to be the basis for a review paper in conjunction with revisited 2 and 3 parts of Chapter. 3.	85

The following co-authors contributed to the work. If co-authors are students at Monash University, the extent of their contribution in percentage terms must be stated:

Name	Nature of contribution	Extent of contribution (%) for student co-authors only
Dr. Rebecca J. Farrington	Supervisory role.	5
Dr. Fabio A. Capitanio	Supervisory role.	5
Dr. Giovanni Spampinato	Proof reading. Editing.	5

The undersigned hereby certify that the above declaration correctly reflects the nature and extent of the candidate's and co-authors' contributions to this work\*.

**Candidate's  
Signature**

	<b>Date</b> 30/11/2015
---	---------------------------

**Main  
Supervisor's  
Signature**

	<b>Date</b> 30/11/2015
---	---------------------------



## CHAPTER 2

### 1. ABSTRACT

Academic and industrial geophysical research programs have provided information on the crustal and lithospheric configuration of tectonically active rifts, paleo-rifts and passive margins. Petrologic and geochemical studies have advanced the understanding of rift-related magmatic processes. Numerical models, based on geophysical and geological data, have contributed at lithospheric and crustal scales towards the understanding of dynamic processes that govern the evolution of rifted basins. Yet geological evidence leads toward a need to change the modelling approach, as there is still no methodology able to highlight the common denominator at the foundation of all the differences we find in rifting areas. This chapter summarizes the state of knowledge on models realised in the last decades in order to (i) understand the dynamic processes controlling the evolution of extensional basins, (ii) constrain the geological interpretation and (iii) set the stage for the following chapters.

### 2. BACKGROUND: LITHOSPHERIC STRETCHING

During the last 50 years, regions of continental extensions have drawn great interest from scientific and technical community for several reasons.

Firstly, rifts zones (extensional basins and passive margins) host energetic resources such as petroleum reservoirs and minerals fields (e.g. rift basins: North Sea, Sirte and West Siberian basins, Dnieper-Donets Basin and Gulf of Suez, grabens; passive margins: Campos Basin, Gabon and Angola shelves, Niger and Mississippi deltas ([Ziegler, 1996a](#))). These regions are targeted for prospectivity studies and have the potential to provide sustainable energy, for example geothermal energy (e.g. Ethiopian rift valley, Campi Flegrei – Italy, Victoria Region - Australia). Therefore understanding the evolution of any rifted area is paramount for evaluating economic factors such as, for example, the risks associated with exploration and exploitation of hydrocarbons in extensional basins. In order to assess if the hydrocarbons in place are qualitatively and quantitatively economic, it is standard to adopt a multidisciplinary approach and make use of integrated analysis of different geological and geophysical methods based on the geological/geophysical data to reconstruct the basin history in terms of temperature (maturation) and architecture (source rock, traps, seals etc).

However, there are several natural hazards associated with rifting areas such as for example seismic and volcanic risks. A simple distinction would help in understanding the risks related with the rifting process between tectonically both active and inactive rifts and those that evolved in continental and oceanic lithosphere.

Tectonically active intercontinental (intraplate) rifts, such as the Rhine Graben, the East African Rift, the Baikal Rift and the Shanxi Rift of China, correspond to important earthquake and volcanic hazard zones. The globe encircling mid-ocean ridge system forms an immense intra-oceanic active rift system that encroaches in the Red Sea and the Gulf of California onto continents.

Rifts that are tectonically no longer active are referred to as paleo-rifts, aulacogens, inactive or aborted rifts and failed arms, in the sense that they did not proceed to crustal separation. Conversely, the evolution of successful rifts culminated in continental break-up, formation new oceanic basins and development of conjugate pairs of passive margins. The last, but by no means least, understanding the dynamic evolution of rifts has implications for a better understanding of the physics of the Earth. In fact, extensional basins and passive margins are expressions of a particular interaction between the deep interior and surface of the Earth.

In the past, a generic distinction was made to explain the leading causes of rifting. Lithospheric stretching initiation was usually ascribed to 2 main processes: **passive** and **active** rifting (Sengor and Burke, 1978; Wilson, 1989; Olsen and Morgan, 1995) (Fig. 2-1).

In the case of passive rifting, unspecified tensional stresses (generally indicated as far-field forces) cause the lithosphere to fail, allowing hot mantle rocks to penetrate the lithosphere (McKenzie, 1978; McKenzie and Bickle, 1988; Khain, 1992). Crustal doming and mantle activity are considered as secondary processes. McKenzie's (1978) widely cited model of the origin of sedimentary basins belongs to this class of passive rifting. For passive rifting to occur, rifting occurs first and doming may follow but not precede it. Rifting is therefore a passive response to a regional stress field (Fig. 2-1a).

In the case of active rifting, it has been suggested that continental stretching is in some cases associated with mantle plume activity (Spohn and Schubert 1983; Houseman and England 1986; Dewey and Burke, 1975; Bott and Kusznir, 1979; Spohn and Schubert, 1982) and that tensional stresses generated by the uplift may then promote rifting (Fig. 2-1b). Mantle plumes are commonly associated with very high volume basaltic igneous provinces such as the Karoo, Deccan, and Parana examples. Plume activity has been



invoked as a particularly effective mechanism of generating new ocean basins, such as in the Atlantic region. The opening of the northern Atlantic Ocean in the Paleocene has been related to the impingement of the Icelandic plume on the base of the lithosphere (White and McKenzie 1989). Mantle plume effects may have played a major role during the super-continental break-up of Rodinia (c. 750Ma), Gondwana (c. 550Ma), and Pangea (c. 250Ma).

It is, however, questionable whether a rift that occurred in a given area was either active or passive. Phanerozoic rifts shown that rift-related volcanic activity and doming of rift zones is basically a consequence of lithospheric extension and is not the main driving force of rifting. The fact that rifts can become tectonically inactive at all stages of their evolution, even if they have progressed to the Red Sea stage of sea-floor spreading, supports this concept. However, as extrusion of large volumes of rift-related subalkaline tholeiites must be related to a thermal anomaly within the upper mantle, a distinction between “active” and “passive” rifting is to a certain degree valid. Natural examples that could be explained partially by active and passive rifting models are respectively the East African-Ethiopian rifts and the wide Basin and Range provinces of SW USA. Many other cases may exhibit aspects of both (Khain, 1992) and the two processes could alternate and interact in time as showed by numerical experiments (Huismans et al., 2001).

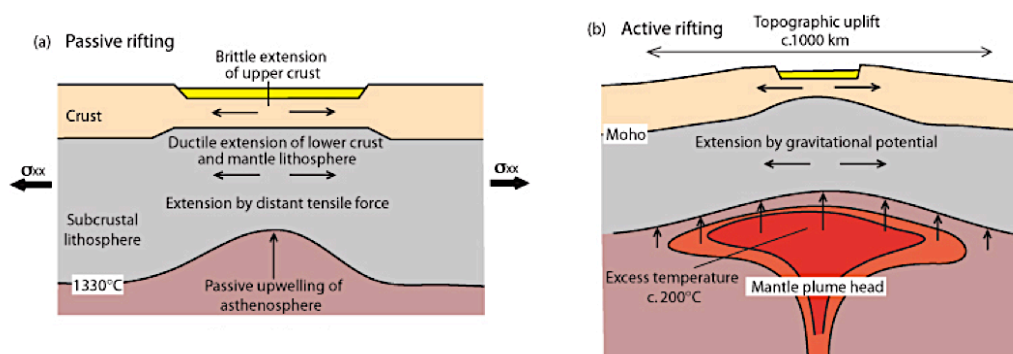


Figure 2.1. Passive and active end-members idealisation. (a) Passive rifting driven by a distant tensile deviatoric stress  $\sigma_{xx}$  causing thinning of the lithosphere and passive upwelling of hot asthenosphere. (b) Impingement on the base of the lithosphere of a mantle plume causes long-wavelength topographic (or dynamic topography driven) doming and gravitationally driven extension of the lithosphere.

In general it is possible to recognise that, whichever is the trigger (e.g. passive or active rifting), lithospheric extension is undoubtedly one physical process (the stretching of a piece of lithosphere with mechanical thinning and thermal attenuation) able to create an exceptional and complex rift-drift suite of basins/passive margins synthetically represented in (Figs. 2-1 and 2-2) (Allen & Allen, 2005, 2013). They are very different in terms of symmetry, timing and type (crust vs lithospheric) of breakup (if it is to occur), number of rifting phases and quiescence periods, occurrence of magmatism (e.g. high velocity under plated bodies and/or volcanic deposits in surface) and so forth.

Hence the question is: “How is the same geodynamic/physical process able to create so many different geological features? ”

This fundamental question and all the reasons mentioned above, have led to numerous studies focused on the evolution of continental lithospheric stretching. The researches have attempted to unravel the origin of many differences in basins and passive margin architectures, heat flow, seismicity, etc simulating the process with analogue and numerical modelling techniques i.e. McKenzie, 1978; Royden and Keen, 1980; England, 1983; Braun and Beaumont, 1987, 1989; Christensen, 1992; Regenauer-Lieb et al., 2008; Withjack and Jamison, 1986; Tron and Brun, 1991; Gartrell, 1997; Clifton et al., 2000; Brun, 2002; Michon and Marle, 2003; Corti et al., 2003, 2007; Bassi, 1993; Buck et al., 2003; Burov and Poliakov, 2001; Pascal et al., 2002; van Wijk et al., 2001, 2008; van Wijk and Cloetingh, 2002; van Wijk, 2005; Buiter et al., 2006; Huismans and Beaumont, 2002, 2003, 2008, 2011; Huismans et al., 2005; Ellis et al., 2011; Allken et al., 2011, 2012, 2013; Brune et al., 2012, 2013, 2014) These models provided insights into the possible causes of a rift and passive margin styles, subsidence patterns and the occurrence of magmatism in specific geological areas. However an explanation of which is the first order element of the system that leads to this variety of deformations is lacking. Therefore a *general approach* is needed, one that is able to consider the deformation at larger scales (e.g. from surface to 660 km) and evaluate its feedback in the basin style, subsidence pattern and magmatism occurrence.

Here, I present first a classification on the type of basins and passive margins based on geological observations (Section 2), followed by a description of the main differences in geophysical data (Section 3). Subsequently, I show a classification of models present in the literature integrating and updating that realized by Fernzadez and Ranalli (1997), Allen and Allen (2005, 2013) and Kearey et al., (2009) with more recent contributions

pointing out that the majority of them are developed considering a single rifting phase (Section 4). I then highlight that the rifting process is a discontinuous process made up of several rifting phases with possible intermittent tectonic quiescence phases. Geological examples are then shown (Section 5). Finally I present the few models that were performed taking into account the polyphase nature of the rifting (Section 6).

### **3. GEOLOGICAL AND GEOPHYSICAL OBSERVABLE: PART I**

#### **3.1 Styles of rifting basins and passive margins: variability in natural systems**

Lithospheric extension is the geodynamic process leading to the rifting of the continental crust that may culminate in plate rupture and the formation of a new ocean basin. While it is not possible to detect in time how this process affects the uppermost mantle and understand its role on the interaction between the lithosphere and the asthenosphere, its effects and different expressions on surface can be recognized thanks to a variety of basins and passive margins.

In a first attempt to unravel how this process evolves in time and space it is possible to classify basins and passive margins as follow ([Allen and Allen, 2013](#)):

- the first evolutionary stage includes the formation of continental basins as Intra-cratonic basins (generated by a long protracted lithospheric extension), rift and failed rift basins (divided usually in narrow and wide rifts), Proto-oceanic troughs (when the rate of deformation is very high, [Fig. 2-2](#))
- the second evolutionary stage includes the variety of passive conjugate margins around the world and is divided as volcanic (the majority of them) and non-volcanic. Also they occur with different degrees of symmetry/asymmetry ([Fig. 2-2](#)).

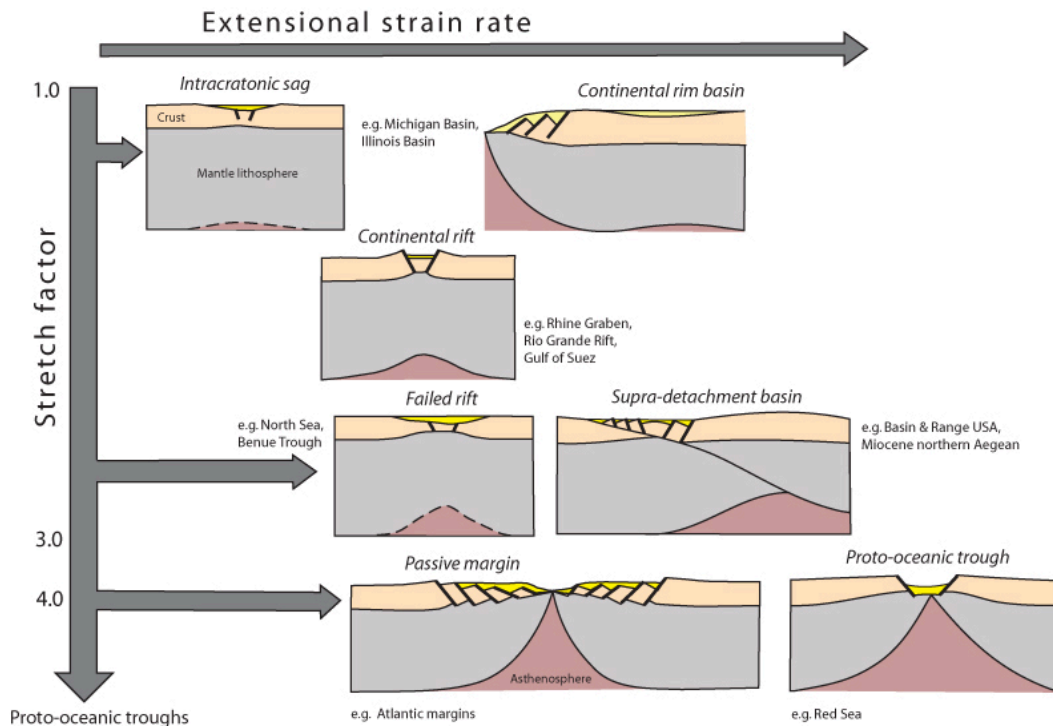


Figure 2.2 Basins rift-drift suite in terms of increasing stretching factor and extensional strain rate.

All the above geological regions are different in terms of geometry (size and shape, width, length, asymmetry/symmetry), subsidence patterns, magmatism and sediment infill. In the following paragraphs of Section 3, I describe the main geological characteristics and differences of basins and passive margins formed due to lithospheric extension. These regions are also different in terms of seismicity (earthquakes occurrence, hypocenter depth etc.), heat flow, topography etc.. I describe the main differences in the second part of Section 3 in terms of geophysical observables.

### 3.1.1 Intracratonic basins (Fig. 2-2)

These basins have no apparent connection with plate tectonics. They are thought to reflect very slow thermal subsidence (for times of the order of a hundred million years) after a heating event located under the continental lithosphere. But the reasons for depression below the original crustal level are not well understood. Erosion during the thermal uplift seems untenable, as does lithospheric stretching. Was the lithosphere denser in the area under the basin? Was the lithosphere thinned by “erosion” from beneath? Whatever the reason, the subsequent subsidence can be modeled very well by cooling and isostatic adjustment. Allen and Armitage (2010 and 2012) modeled the development of these

basins as protracted rifting finding a better fit between the backstripping curves and the modeled subsidence curves.

These exhibit a prolonged subsidence history, occasionally marked by an initial stage of relatively fast subsidence followed by a period of decreasing subsidence rate (Nunn & Allen 1984; Stel et al., 1993; Xie & Heller, 2009; Armitage & Allen, 2010), somewhat similar to that of oceanic basins (Sleep 1977). In Fig. 2.3, there are some examples of intracontinental rifts around the globe. In particular Illinois Basin, Farley well (Bond and Kominz, 1984), Michigan Basin (Bond and Kominz, 1984), Williston Basin, North Dakota (Bond and Kominz, 1984), Williston Basin, Saskatchewan (Fowler and Nisbet, 1985), Northeast German Basin (Scheck and Bayer, 1999), Southwest Ordos Basin (Xie, 2007), Paris Basin (Prijac et al., 2000) and Parana Basin (Zalan et al., 1990), all taken from the work of Xie & Heller (2009). The backstripping curves are compared with curves calculated from the McKenzie (1978) stretching model.

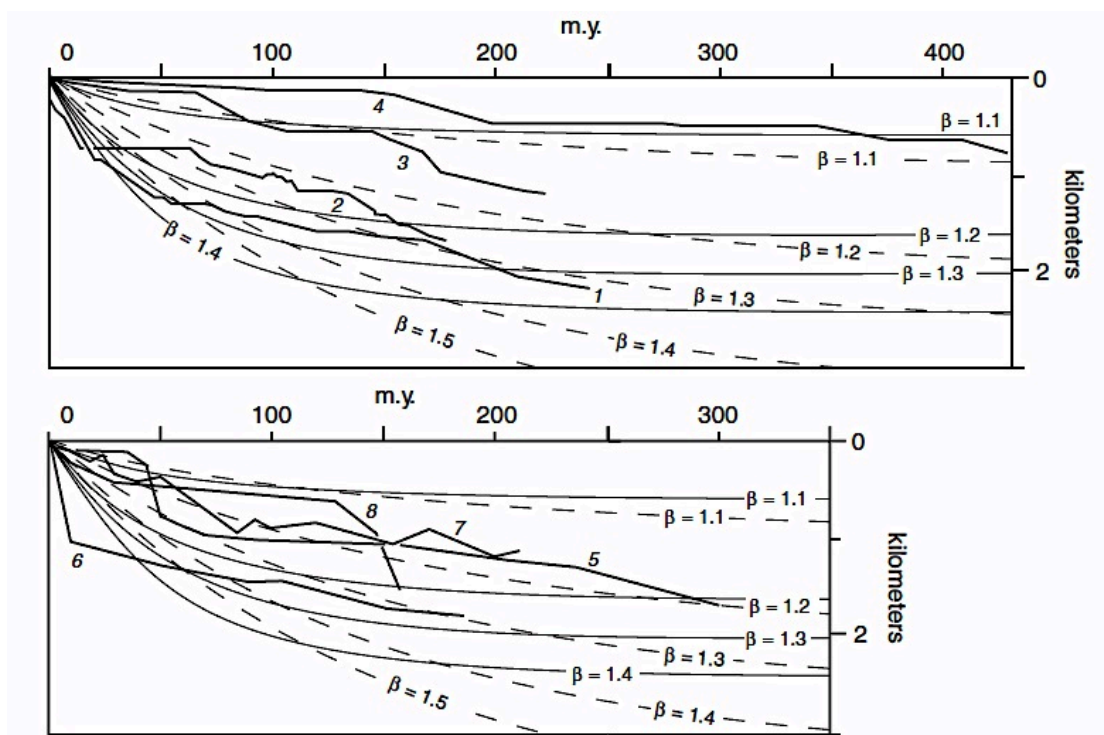


Figure 2.3 Tectonic subsidence of intracontinental basins. 1—Illinois Basin, Farley well (Bond and Kominz, 1984); 2—Michigan Basin (Bond and Kominz, 1984); 3—Williston Basin, North Dakota (Bond and Kominz, 1984); 4—Williston Basin, Saskatchewan (Fowler and Nisbet, 1985); 5—Northeast German Basin (Scheck and Bayer, 1999); 6—Southwest Ordos Basin (Xie, 2007); 7—Paris Basin (Prijac et al., 2000); 8—Parana Basin (Zalan et al., 1990). Comparison of intracontinental basin subsidence curves (numbered heavy lines) with post-rift thermal subsidence curves calculated from the McKenzie (1978) stretching model. Time (m.y.) is shown since basin formation. Thin solid lines assume lithosphere thickness of 125 km; dashed lines assume lithosphere thickness of 200 km. Stretching factors ( $\beta$ ) from 1.1 to 1.5 are shown. (modified from Xie & Heller (2009)).

Many intracratonic basins are located in non-orogenic areas on cratons (Allen & Allen, 2005). In some cases, cratonic basins are connected by a rift or failed rift zone to the ocean, as in Neoproterozoic Centralian Superbasin of Australia (Walter et al. 1995; Lindsay 2002), the Lower Paleozoic Illinois and Oklahoma basins of USA (Braile et al., 1986; Kolata & Nelson 1990; Leighton et al., 1990) and the Mesozoic phase of Chad Basin of north-central Africa (Bruke 1976). This geometry suggests that many cratonic basins lie at the tips of failed rifts extending into the continental plate at high angle from the extensional plate margin, which may be the site of former triple junctions (Bruke & Dewey 1973). The association of cratonic basins with continental stretching is supported by local occurrence of rifts below the sag-type basin-fill. Stretch factors are, however, very low beneath the cratonic basin, for example 1.05 to 1.2 in the Hudson Bay (Hanne et al., 2004) (Fig. 2.4) and  $< 1.6$  in the West Siberian Basin (Saunders et al. 2005).

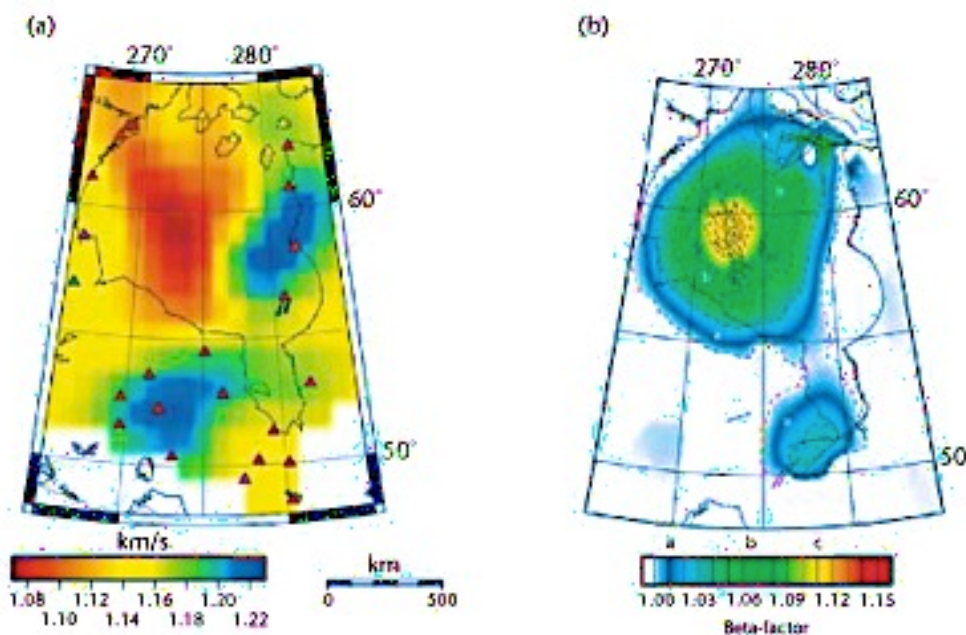


Figure 2.4 Hudson Bay Basin, Canada (a) Seismic velocity anomalies based on tomographic reconstructions (Pawlak et al. 2011), representative of the mid-crust, showing a slowing in the region beneath the main sedimentary depocentre; and (b) calculated stretch factors based on modelling of sediment thickness. (modified from Allen and Allen, 2013).

They are often rounded, equidimensional, extending for hundreds of kilometers. Some cratonic basins are large, with surface areas ranging from the relatively small Anglo-Paris Basin ( $10^5 \text{ km}^2$ ), through to the large Hudson Bay ( $1.2 \times 10^6 \text{ km}^2$ ), Congo ( $1.4 \times 10^6 \text{ km}^2$ )



and Parana' basins ( $1.4 \times 10^6 \text{ km}^2$ ) to the giant Centralian Superbasin ( $2 \times 10^6 \text{ km}^2$ ) and West Siberia Basin ( $3.5 \times 10^6 \text{ km}^2$ ) (Sanford 1987; Leighton & kolata 1990; Walter et al. 1995; Vyssotski et al, 2006; Crosby et al. 2010). As a general feature, their sediment fill represent a shallow-water carbonatic sediments (carbonates, shales, sandstones), thicker and more complete than in adjacent areas of the craton but still relatively thin, hundreds of meters.

In cross section, they are commonly simple saucers (basins), with sedimentary thickness typically less than 5 km, and rarely  $< 6\text{-}7 \text{ km}$  (as in the West Siberian (Fig. 2.5), Illinois and Parana' basins). However, in some cases, the circular planform shape is a results of later compartmentalization of a previously more extensive platform or ramp, as in the cratonic basins of North Africa, such as Al Khufra, Murzuk and Ghadmes (Selley,1972,1997; Boote et al., 1998) and the latest Proterozoic-Early Ordovician 'Sauk' sequence of east-central North America (Sloss 1963, 1988). They experience a long-lived of subsidence, measured in hundreds of millions of years, implying slow sediment accumulation rates. The cratonic basins of North America, for instance, accumulated sediments at rate of  $20 \text{ to } 30 \text{ m Myr}^{-1}$  (Sloss 1988), which is extremely slow compared to rifts, failed rifts, young passive margins, foreland basins and strike-slip basins (Allen & Allen 2005), but relatively fast compared to the adjacent platforms. Laterally equivalents platforms areas, such as the Transcontinental Arch od USA, accumulated ca. 1 km of sediments between Cambrian and Permian, at a rate of  $3\text{-}4 \text{ m Myr}^{-1}$  (Sloss 1998).

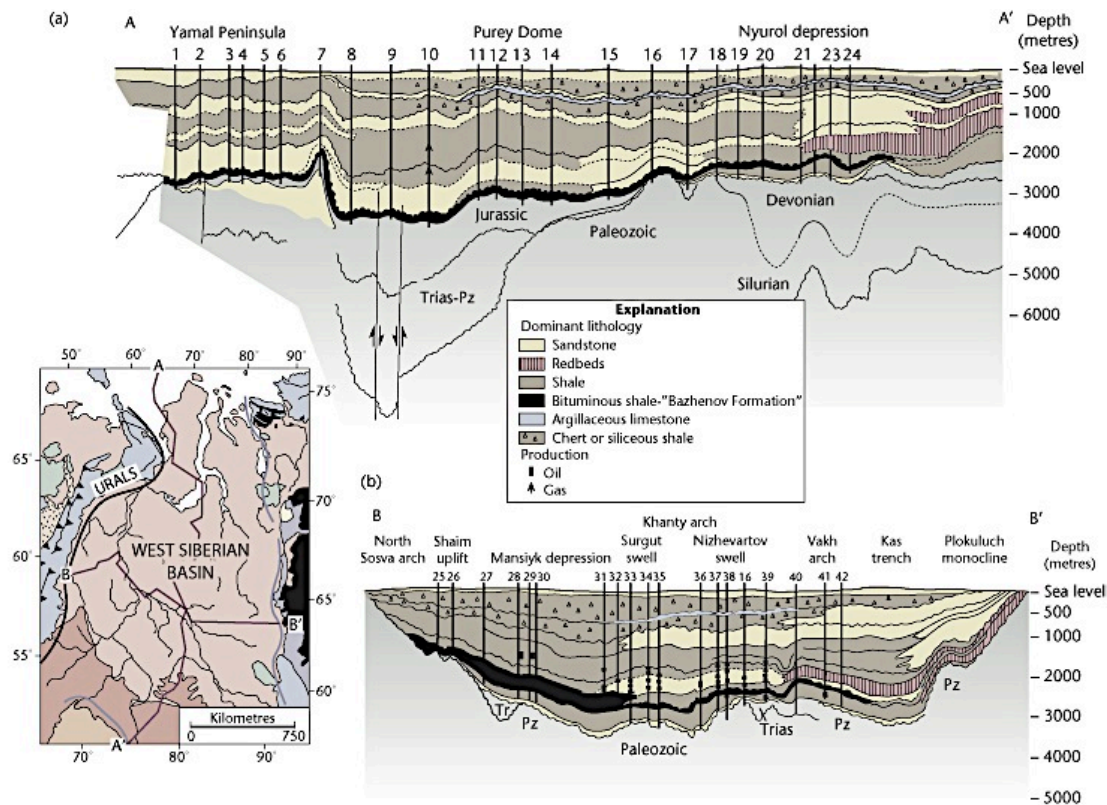


Figure 2.5 Cross-sections of West Siberian Basin A-A' and B-B', along transects shown in the geological pam. From Vyssotki et al. (2006) and Saunders et al. (2005) (modified from Allen and Allen, 2013).

Although cratonic basins are very long-lived structures, it is important to recognize that basin-fill is commonly composed of a number of different mega-sequences (or sequences of Sloss 1963), some of which may be associated with entirely different mechanisms of formation, such as strike-slip deformation, flexure and unequivocal stretching. Consequently, it is important wherever possible, to extract the craton basin mega-sequence from the poly-history basin-fill (Kingston et al., 1983a) for analysis. In other cases, basins have remained as cratonic basins throughout their history but have existed long enough to have been strongly affected by tectonic mechanisms of subsidence and uplift. Consequently, there may be primary mechanisms for the basin formation, and different mechanisms for later modification (Allen & Armitage 2012).

### 3.1.2 Continental Rift (Fig. 2-2)

Continental rifts are areas of crustal extension that overlie thinned crust generally located within continental lithosphere on cratons.

Regions of rifting at the present day are characterized by low intensity Bouguer gravity anomalies, high heat flow, and volcanic activity, all of which suggest that in addition to crustal extension, a thermal anomaly exists at depth.



Some rifts continue to open and eventually become ocean basins floored by oceanic crust rather than continental crust; the basin description here then applies to this earliest stage of the rifting. In other cases, the rifts fail to open fully into ocean basins (perhaps some adjacent and parallel rift becomes the master rift), so they remain floored by thinned continental crust rather than new oceanic crust. A modern example: the East African rift valleys. An ancient example: the Triassic–Jurassic Connecticut and Newark basins in eastern North America.

They are usually classified based on their width (and possibly on mode of deformation that have caused this width) in Narrow or Wide rifts.

Examples of Narrow rifts are:

- East African Rift System (e.g. [Buck, 1991](#); [Corti et al., 2012](#));
- Rio Grande rift (e.g. [Allen et al., 2015](#));
- Baikal rift (e.g. [Thybo & Nielsen, 2009](#))
- Northern Red Sea or Gulf of Suez (e.g. [Almalki et al., 2014](#))
- West Antarctic rift (e.g. [Corti et al., 2013](#); [Huerta & Harry, 2007](#))
- European Cenozoic Rift System (Rhine Graben, North Sea (e.g. [Cloetingh & Ziegler](#))
- Yemen Somalia ([Şengör & Natal'in , 2001](#))
- Yinchuan Graben ([He et al., 2003](#))

Examples of Wide rifts are:

- Basin and Range basin (e.g. [Buck, 1991](#); [Brun, 1999](#))
- Aegean sea (e.g. [Buck, 1991](#); [Brun, 1999](#))
- Tibet plateau (e.g. [Allen & Allen, 2013](#) and references therein)

It is possible that pre-breakup inherited architecture determined the geometry of passive margins

- Wide (Non)- Volcanic Rifting: Brazilian Esposito Santo Margin – West African north Angolian Margin (e.g. [Brune et al., 2014](#); [Unternehr, et al., 2010](#))
- Wide Volcanic Rifting: Greenland-Norway conjugate margin. ([Artemjev and Artyushkov, 1971](#); [Illies and Greiner, 1978](#); [Bonatti, 1985](#); [Morgan et al., 1986](#); [Rosendahl, 1987](#); [Steckler et al., 1988](#); [Behrendt et al., 1991](#); [Ziegler, 1995](#); [Prodehl et al., 1997](#))

Also, there are core-complexes. Sometimes they are considered as by themselves in some classification and sometimes they are considered variation of Wide rifts. ([Corti et al., 2003](#) and references therein)

Sediment supply from the adjacent highlands of the uplifted fault blocks is usually abundant, although in the East African rifts the land slope is away from the rim of the highlands, and surprisingly little sediment reaches the rift basins.

The sediment fill is generally coarse to fine siliciclastics, usually non-marine with often lacustrine sediments and interbedded basalts.

### 3.1.3 Failed Rifts (or Aulacogens) (Fig. 2-2)

Failed rift are generally extending from the margins toward the interiors of cratons and are generally long, narrow and linear (Allen & Allen, 2013). These are generally tens of kilometers wide and hundreds of kilometers long.

Aulacogens are thought to represent the third, failed arm of a three-armed rift while the other two arms continued to open to form an ocean basin. In modern settings, aulacogens end at the passive continental margin. Example can be found in the Southern Oklahoma Aulacogen (Fig. 2-6) and the Benue Trough, underlying the Congo River Basin in West Africa. The ocean eventually closes to form an orogenic belt, so in ancient tectonic settings aulacogens end at an orogenic belt.

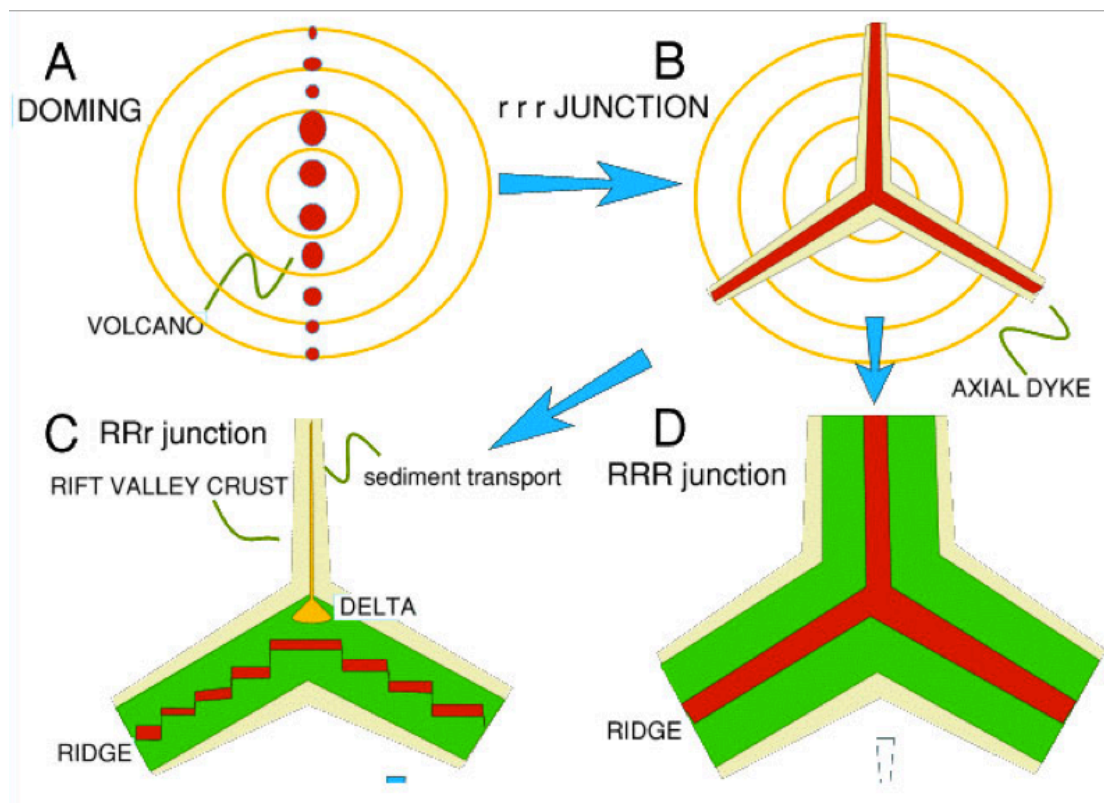


Figure 2.6 Diagram illustrating the formation of an aulacogen, including its initial formation as a triple junction and the change into an aulacogen and spreading centers (from <http://www.geosci.usyd.edu.au/users/prey/Teaching/ACSGT/EReports/eR.2003/GroupB/Report1/styles.html> (see also Burke & Whiteman, 1973 for examples of aulacogen formation). (B) rrr is a rift-rift-rift triple junction, (C) RRr is a Ridge-Ridge-rift and (D) RRR is a Ridge-Ridge-Ridge

junction. See, e.g., [Kearey et al., \(2010\)](#) and [Sengtir et al. \(1978\)](#) for an extensive explanation on stability of triple junctions, since this is outside of the aim of this work. This is just a schematic example to show how a failed rift can be formed. Generally the study of triple junction stability should be gained at the first year of geology everywhere in the world and the reader should already have the knowledge of what RRR, RRR and rrr are.

The cessation of rifting happened before the onset of seafloor spreading and passive margin formation. The rift phase is identical to that outlined in the previous paragraphs. During cooling, failed rifts widen and post-rift sedimentary rocks onlap the previous rift shoulders, producing a steer's head geometry ([Fig. 2.6](#)).

A sedimentary evolution from non-marine to shallow-marine in the syn-rift phase and deeper-marine in the post-rift phase is typical.

The Benue Trough is 1000 km long and 100 km wide, and is filled with < 5 km of fluvial, deltaic and marine Cretaceous sedimentary rocks. At the southwestern end of the failed rift, the Tertiary Niger Delta has built a deltaic wedge and submarine fan deposits 13 km thick. A similar focusing of river drainage and delta growth along failed arms is found in the Lena Delta of the giant West Siberian Basin ([Vyssotsky et al. 2006](#)) and the Brent Delta of the Viking Graben in the North Sea Basin ([Morton et al. 1992](#)).

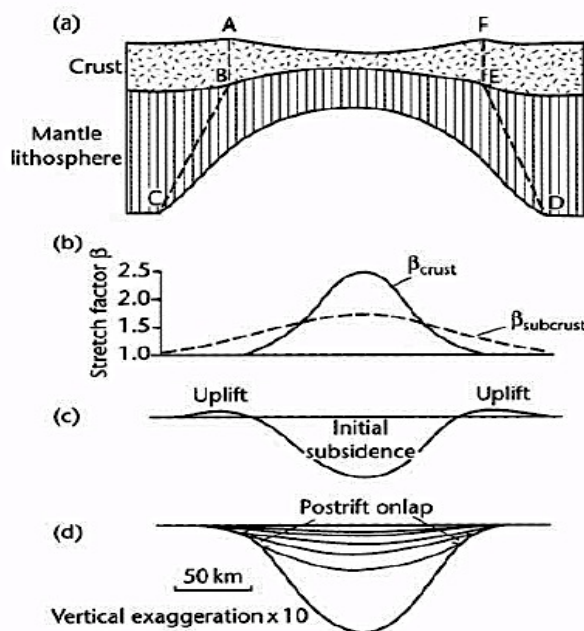


*Figure 2.7 Basin filling pattern resulting from continuous depth-dependent stretching (Rowley and Sahagian 1986; White and McKenzie 1988). (a) Geometry of a tapering region of extension in the subcrustal lithosphere; (b) Stretch factors in the crust and subcrustal lithosphere as a function of horizontal distance; (c) Initial subsidence and uplift immediately after stretching, showing prominent rift flank uplift; (d) Total subsidence 150 Myr after rifting, showing progressive onlap of the basin margin during the thermal subsidence phase, giving a "steer's head" geometry.*

Apart from the Southern Oklahoma Aulacogen and the Benue Trough of central-western Africa another excellent example of aborted rifts is the North Sea. In the northern North

Sea, a major period of rifting took place in the middle Jurassic. At this time, sedimentation was controlled by NNW-trending major structures that define the graben. In the N-S oriented Viking Graben, fluvial deposits pass northwards into deltaic and shallow marine deposits of the Brent Group (Morton et al. 1992). The Mid-Cretaceous saw the end of the rift phase and sediment overlapped the graben shoulders onto the East Shetland Platform in the west and the Norwegian Platform in the east. Thick deposits of Cretaceous chinks, Paleogene submarine fan sandstone and basinal shales, and Neogene mudstone typify this post-rift phase. In the southern part of North Sea, the basin was filled by major sediments supplied from rivers draining the European mainland, producing mega-clinoforms due to westward delta progradation. The southern-central North Sea therefore shows the tendency for shallowing due to basin filling during the later stage of thermal subsidence of failed rifts.

#### 3.1.4 Proto-oceanic troughs (Fig. 2-2)

For greater stretching, continental rifts or back-arc basins may evolve into new oceanic basins through a stage known as a proto-oceanic trough. Proto-oceanic troughs are characterized by young oceanic crust and very high surface heat flows. The southern Red Sea contains young (< 5Myr) oceanic crust along its 50 km-wide axial zone, with flanking shelves interlined by stretched continental lithosphere. To the south, the Red Sea undergoes a transition to the continental Afar Rift, and to the north into the continental Gulf of Suez Rift. The sedimentary evolution of the Red Sea area comprises Oligo-Miocene syn-rift deposition of continental and shallow-marine sediments. As stretching continued through the Miocene, thick evaporites formed in the periodically isolated, proto-oceanic trough. During the Pliocene to Holocene, the Red Sea accumulated pelagic foraminiferal-pteropod oozes in deep water.

At the transition from rift basin to a youthful ocean basin, subsidence commonly outpaces sediments supply, leading to the deposition of distinctive facies associations indicative of sediment starvation:

- Evaporites: the intermittent connection of developing rifts with the sea during the incipient stages provides ideal conditions for the formation of thick evaporites s. s. Such evaporites occur along the margins of Atlantic Ocean (Emery 1977; Rona 1982) and Red Sea (Lowell & Genik 1972).
- Black organic-rich shales. High organic productivity and restricted marine circulation may allow the preservation of organic-rich shales.

- Pelagic carbonates. In the new ocean basins with little particulate sediments supply, deep-water pelagic carbonates may directly overlie the foundered pre-rift 'basement' or newly created seafloor. The faulted basement topography controls the type of deposit, with uplifted fault block edges and seamounts accumulating shallow-water carbonates, and intervening troughs being the site of fine-grained oozes. This pattern of sedimentation is related to fault block shoulder and troughs and has been interpreted to form the Triassic-Jurassic evolution phase of the Tethyan realm of southern Europe ([Bernoulli & Jenkyns 1974](#)).

In many basins it is evident a marked increase in subsidence between the initial rifting (when the sedimentation keeps pace with subsidence) and rifting climax (when subsidence is faster than sedimentation). [Gupta et al., \(1998\)](#) proposed a mechanism to explain this transition from slow to rapid subsidence. They have found that the influence of segment linkage on fault-displacement-rate patterns along an evolving normal fault array could be the cause of the abrupt change in subsidence. In particular they suggest that the linkage process is controlled by a stress feedback mechanism, which leads to enhanced growth of optimally positioned faults.

### 3.1.5 Passive continental margins (Fig. 2-2)

Passive continental margins involve strongly attenuated continental crust stretched over a region of 50-150 km wide, and exceptionally as much as 400-500 km ([Keen et al. 1987](#)), overlain by thin or thick sediment prisms. They are seismically active (e.g, [Wolin et al., 2012](#) and references therein), and in mature examples heat flows are near-normal (the average surface heat flow is  $65 \pm 1.6 \text{ mW m}^{-2}$ ; see [Allen & Allen, 2005](#); [Turcotte & Schubert, 2015](#). These authors use "near-normal" as the values are similar to "the norm"). Passive continental margins (also known as Atlantic-type margins) are characterized by seaward thickening prisms of marine sediments overlying a faulted basement with syn-rift sedimentary sequences, often of continental origin. The post-rift seaward-thickening sediment prisms consist predominantly of shallow marine deposits. Seismic reflection sections show that some passive margins are underlain by listric extensional faults that connect into a major, low angle detachment surface. The post-rift or drift phase (drifting of the continent: see, e.g., [Kearey et al., 2010](#)) in contrast is typically dominated by gravity-controlled deformation (salt tectonics, mud diapirism, slumps, slides, listric growth faults in soft sediments).

Passive margins overlie earlier rift systems that are generally subparallel to the ocean margins, or less commonly at high angles to the ocean margin (as in the case of failed arms of triple junctions such as the Benue Trough, Nigeria), or along transform fault zones (e.g., Grand Banks and Gulf of Guinea). The early syn-rift phase of sedimentation is commonly separated from a later drifting phase by an unconformity (the “break-up” unconformity of [Falvey 1974](#)). Some passive margins may exhibit considerable subaerial relief at the end of rifting (leading to major unconformities), as in the case of the Rockall Bank, northeastern Atlantic, whereas in others the end of rifting may have occurred when the sediment surface was in deep water, as in the Bay of Biscay and Galicia margin of Iberia ([Montadert et al. 1979](#)).

Two end-members of passive margin can be identified based on the thickness of sediments: (i) starved margins (2-4km thick), and (ii) nourished margins (generally 5-12 km thick). In the central Atlantic, the American margin is nourished whilst the European margin is starved. In addition, some passive margins are associated with strong volcanic activity, generally tholeiitic, at the time of break-up ([White and McKenzie 1989](#)).

This volcanicity is commonly associated with subaerial emergence, as in the northern North Atlantic in the Early Tertiary (e.g., [Skogseid et al. 2000](#)). Since passive margins represent the rifted edges of a piece of continental lithosphere, now separated by an ocean basin, it is possible to identify the original matching margins on either side of the ocean. These are known as conjugate margins. They are particularly well developed on either side of the northern Atlantic (e.g. Southern Grand Bank-Iberia/Galicia; Flemish Cap-Coban Spur; Labrador SW Greenland). Comparison of conjugate margins is informative regarding the geometry of extension prior to ocean basin development. For example, deep seismic reflection profiles show some conjugate pairs of passive margin to be symmetric, with seaward dipping, rotated fault blocks, whereas other deep profiles suggest the presence of a flat-lying or landward-dipping detachment or shear zone, producing a markedly asymmetrical pattern. The profiles across the Labrador and SW Greenland margins show that although the brittle upper crust has been extended symmetrically, the lower crustal extension is particularly asymmetrical. Some margins show thin sediment covering wide regions of highly faulted, upper crust, commonly separated from underlying serpentinized upper mantle by a horizontal detachment (e.g., Iberia, Galicia, and SW Greenland margins). Other margins with thick sediment prisms consist of one or two major tilted crustal blocks and lack a horizontal detachment (e.g., Labrador margin). In summary, these observations collectively suggest that there are a number of different



archetypes of passive margin: volcanic-active margins are characterized by extrusive basalts, lower crustal igneous accretions, and significant uplift at the time of break-up. Continental extension and ocean spreading are thought to be intimately related to mantle plume activity; non-volcanic margins lack evidence of high thermal activity at the time of break-up.

Margins may be: (i) sediment-starved, with thin sediment veneers of 2-4km draping large arrays of rotated syn-rift fault blocks above a sub-horizontal detachment, as in the Bay of Biscay, or (ii) sediment-nourished, with very thick (< 15 km) post-rift sedimentary prisms overlying a small number of tilted upper crustal fault blocks and a wide region of mid-lower crustal extension, as in the Baltimore Canyon region of the Eastern Seaboard of North America and the Labrador margin (Fig. 2.8).

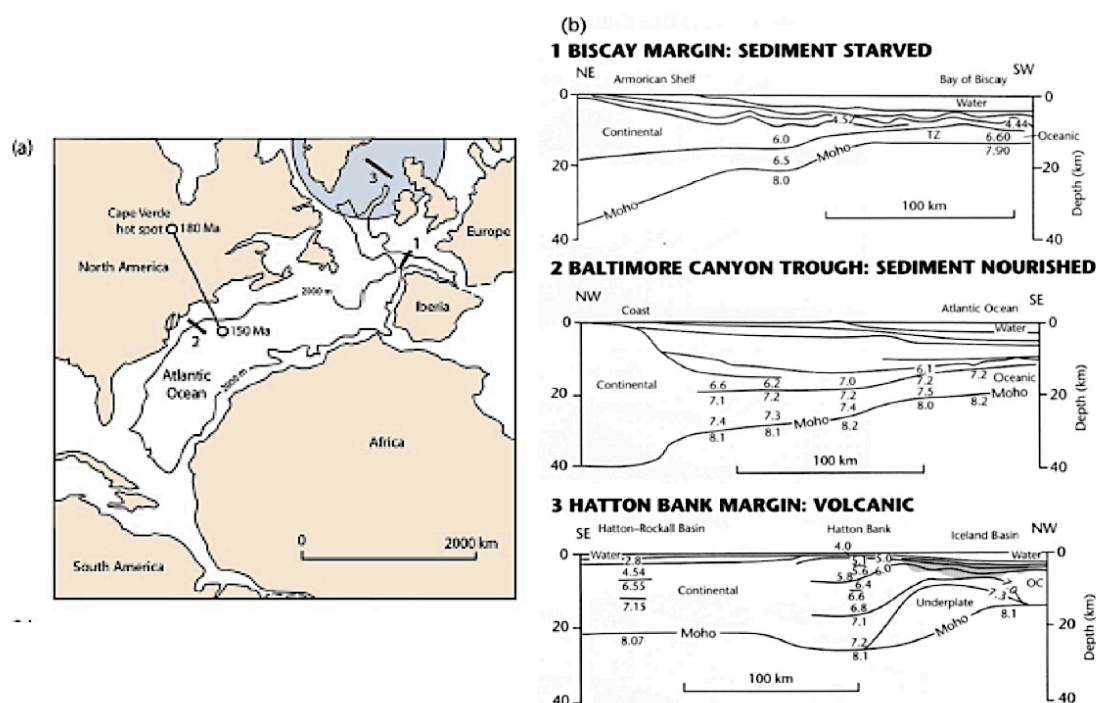


Figure 2.8 Volcanic, sediment-nourished, and sediment-starved margins. (a) Location of margins in the central-north Atlantic region on a Middle Jurassic reconstruction (170 Ma), shortly after the onset of seafloor spreading; (b) Biscay margin, which is sediment starved; (c) Baltimore Canyon Trough margin, which is thickly sedimented; (d) Hatton Bank margin, which is characterized by important magmatic activity. Shaded area shows extent of extrusive basalts. Moho is overdeepened due to presence of igneous underplate. TZ, ocean-continent transition zone; OC, ocean crust. (modified from White and McKenzie 1989).

## 3.2 Geological and geophysical observations in regions of continental extension (rifts and passive margins)

Here I present the physically relevant observables commonly found in rift-drift suite basins ([Allen & Allen, 2005](#)). See Fig. 2.2 for a reminder of the classification and for definitions of every type of basin considered under the “rift-drift suite” .

### 3.2.1 Seismicity

Rift zones are characterized by high levels of earthquake activity. On the continental lithosphere, earthquake epicenters commonly delineate active rift zones or reactivated orogenic belts, as in southern Africa. Focal mechanism solutions in general indicate normal dip-slip faulting with orientations roughly parallel to the long-axis orientation of the rift. In some continental rifts, such as the Rhine Graben, strike-slip focal mechanisms dominate dip-slip solutions by 3 : 1. Although earthquakes are common in regions of continental rifting, they typically have moment magnitudes of up to 5.0 (Rhine Graben) or 6.0 (East African Rift), with shallow focal depths of < 30km, indicating that the earthquakes are located in the brittle mid-upper crust.

### 3.2.2 Crustal thickness

Seismic studies show that the Moho is shallow beneath rift zones. The southern Rhine Graben is an example. The Moho reaches a depth of 24km near the Kaiserstuhl volcano due west of Freiburg, Germany directly beneath the centre of the graben. The Moho is dome-shaped, deepening to the north, NW and NE to about 30km. Approximately 3km of syn-rift sedimentary rocks are found in the graben, so the continental crust has been thinned from 30km to 21 km, that is, by a factor of c. 1.4 ([Fig. 2.9](#)). In the North Sea failed rift, the crust (pre-Triassic) is > 31 km thick beneath the Shetland Platform and Scandinavian Shield, but is ca. 16km thick beneath the Viking Graben ([Klemperer 1988](#)). The continental crust has therefore been thinned by a factor of approximately 2 immediately beneath the deepest part of the Viking Graben ([Fig. 2.9](#)).

An important observation, however, is that some regions of extensive, diffuse extension such as the Basin and Range, SW USA, are located on previously thickened crust. The Moho was therefore anomalously deep at the onset of extension, and extension of thinning has brought the Moho back to “normal” depth. This is also the case for the Tibetan Plateau, which is undergoing active extension and overlies crust as much as 70km thick.



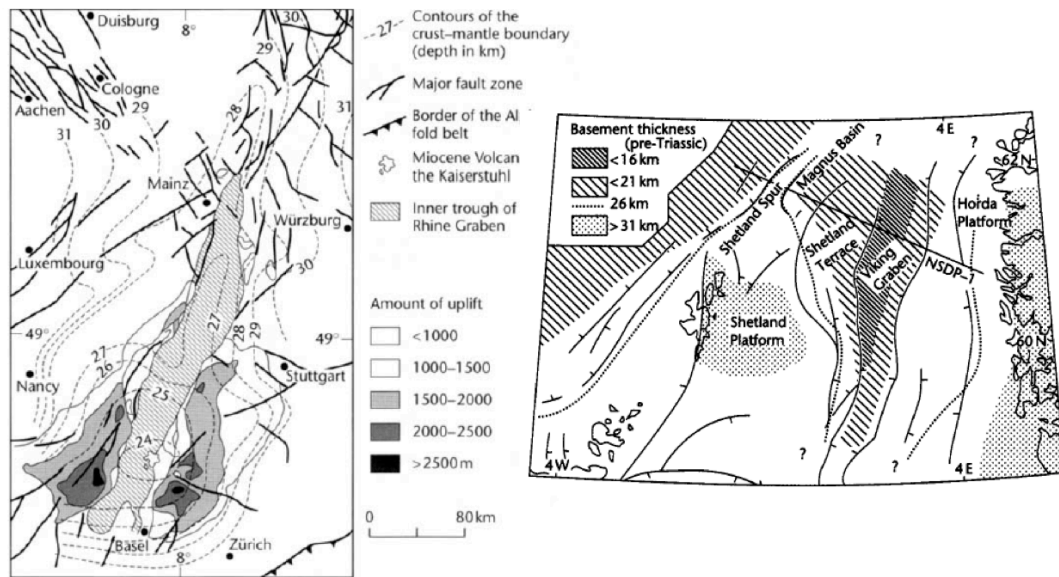


Figure 2.9 Left: Depth to the Moho below sea-level (in km), showing a mantle bulge in the southern Rhine Graben centred on the Kaiserstuhl volcano (Illies 1977). The largest amounts of denudation are found on the rift flanks above the shallow mantle. Right: Crustal thickness changes in the North Sea area as a result of Mesozoic rifting (after Klemperer 1988). Contour map of the interpreted thickness of the prerifting basement (pre-Triassic) showing that the Viking Graben has been stretched by a factor of 2 compared to the Shetland Platform (after Allen and Allen, 2005).

### 3.2.3 Gravity

Long wavelength, negative Bouguer gravity signature characterize many rift zones (Allen & Allen, 2005). Short wavelength, relatively high intensity Bouguer gravity anomalies can be observed in the centre of the rift zone (Fig. 2-10). The conventional explanation is that rift zones have anomalously hot material in the mantle beneath the rift, producing a mass deficit and therefore a negative gravity anomaly. The subsidiary gravity high is thought to be due to the intrusion of dense magma bodies within the continental crust. Regions of widespread, diffuse extension such as the Basin and Range province of SW USA show a series of gravity highs which are located in correspondence of basement blocks, and c. 20km wide gravity lows corresponding to sedimentary infill. The gravity lows most likely reflect the mass deficit of low-density basin sediments.

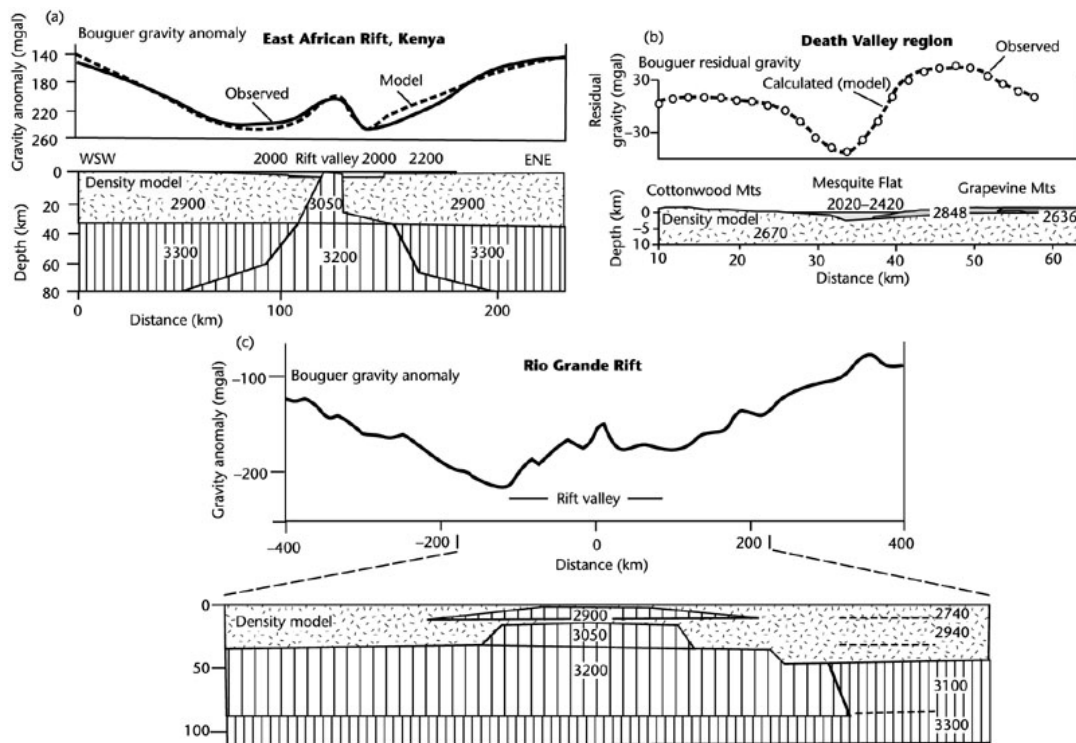


Figure 2.10 Gravity profiles across rift zones. (a) Gravity profile and density model across the Gregory Rift, Kenya. The secondary gravity high is modeled as due to the intrusion of dense magma bodies beneath the rift valley (after Baker and Wohlenberg 1971); (b) Gravity profile and density model for a profile across Mesquite Flat, northern Death Valley, California (after Blakeley et al. 1999); (c) Gravity profile (c. 33° N) and density model for the Rio Grande Rift of New Mexico (after Ramberg 1978). The secondary gravity high is thought to be due to the presence of dense igneous bodies beneath the rift. Densities are in  $\text{kg m}^{-3}$ .

### 3.2.4 Faults

Rift zones are defined by normal dip-slip faults with a variable number of strike-slip faults depending on the orientation of the rift axis in relation to the bulk extension direction. Consequently, the central Death Valley Basin is close to orthogonal to the extension direction and is characterized by dip-slip normal faults, whereas the northern Death Valley Basin is more oblique and has faults with important strike-slip motion (Burchfiel and Stewart 1966). Faults in rifts are not infinite in extent: instead there is a displacement-length relationship, with most of the slip being taken up on a small number of interacting major fault segments. Fault displacement dies out towards the tips of fault segments. The Jurassic Brent-Strathspey- Statfjord fault array system in the North Sea Basin (McLeod et al. 2000), the Neogene fault array of the Gulf of Suez in eastern Sinai (Sharp et al. 2000) and the modern fault array of the Lake Tanganyika Basin (Rosendahl et al. 1986) are all excellent examples. Most major border faults dip steeply towards the basin centre.

However, some rift bounding faults are low-angle and listric, taking up very large

amounts of horizontal extension, as in the supradetachment basins of SW USA. Metamorphic rocks may be unroofed from <25 km depth in these “core complexes” (Wernicke 1985).

### 3.2.5 Heat Flow

The presence of active volcanoes and elevated heat flows in rift zones demonstrates active thermal processes. However, the measured values of heat flow are often difficult to interpret, because of complications due to convective heat transport, shallow magmatic intrusions, groundwater convection, and variability of conductive sediments and rocks. In general, rift zones have heat flows of 90-110 mW m<sup>-2</sup>. This is up to a factor of 2 higher than in surrounding unstretched terranes (Fig. 2.11a). Values are higher in volcanic rifts such as the Eastern Rift, Kenya, and lower in non-volcanic rifts such as those of Malawi, Tanganyika, and the Jordan-Dead Sea Rift zone of the Middle East. In areas devoid of active tectonics and volcanicity, continental heat flow values appear to be strongly correlated with the type of underlying crust.

In NE North America, for example, the higher heat flows over the Appalachians (average 58mWm<sup>-2</sup>) than over the North American Shield (average 29 mW m<sup>-2</sup>) may be explained by the different thicknesses of underlying tonalitic crust (Pinet et al. 1991) containing the radiogenic heat producing elements such as uranium, thorium, and potassium. In general, granitic terranes have high surface heat flows, whereas mafic and ultramafic igneous rocks and many sedimentary rocks are associated with low surface heat flows. The large variation caused by this internal radiogenic heat production makes the interpretation of surface heat flows - in terms of continental stretching – problematical (Allen & Allen, 2005).

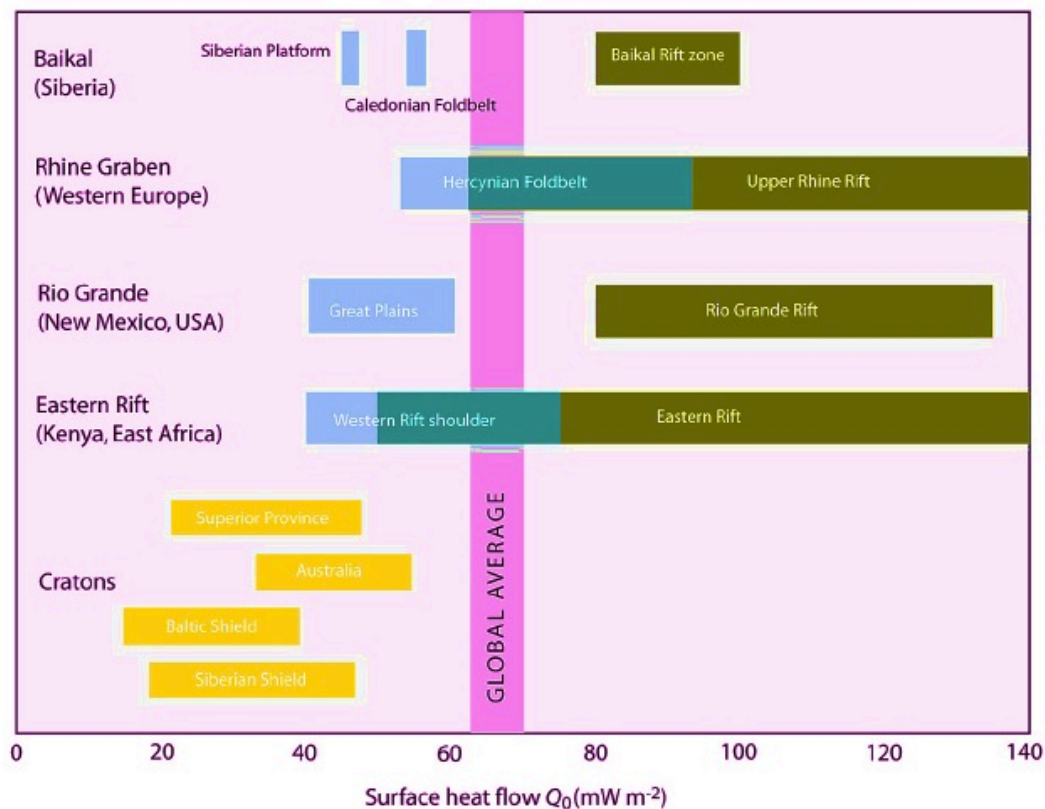


Figure 2.11a Heat flows in some continental rifts and surrounding regions, compared to the global heat flow average. Dark boxes are rift zones; light boxes are rift flanks or adjacent unstretched regions. (modified after Allen & Allen 2013).

### 3.2.6 Topography

Currently or recently active rift zones typically have elevated rift flank topography bordering a depositional basin. There may be two length scales of surface uplift. The best examples of the large length scale (several hundred km) are the >3 km-high topographic swells of Ethiopia and East Africa (Baker et al. 1972; King and Williams 1976). Other domal uplifts are found in northern Africa such as those in the Tibesti and Hoggar regions. These swells are commonly associated with widespread volcanic activity. Whereas the large domes of eastern and northeastern Africa are currently undergoing rifting, the smaller domes of north-central Africa are not. At a smaller length scale (<100 km) are the linear rift flank uplifts associated with border fault arrays. The < 1 km-high highlands bordering the Gulf of Suez are a good example. Border fault footwalls involve upward tectonic fluxes, leading to enhanced denudation.

In the southern Rhine Graben, tectonically driven exhumation of the rift flank has resulted in 2-3km of erosion, exposing Hercynian crystalline basement in the Vosges of Alsace (France) and the Black Forest of Germany. Regions of extensive, diffuse extension are associated with plateau-type topography, such as the Basin and Range, USA and

especially Tibet. In the first case, shallow subduction of relatively buoyant oceanic lithosphere beneath the North American Plate, and in the second case, thickening of continental lithosphere during India-Asia collision, are the driving forces for extensive topographic uplift and extension.

### 3.2.7 Time scale and amount of extension

Extensional basins vary greatly in their duration of subsidence, total extensional strain, and therefore in their strain rate. [Friedmann & Burbank \(1995\)](#) believed there were two distinct families of basins, which could be recognized according to their strain rate, total extensional strain (or stretch factor  $\beta$ ), and the dip of master faults ([Fig. 2.11b](#)): Discrete continental rifts located on normal thickness crust (such as the Rhine Graben, Baikal Rift, Rio Grande Rift) extend slowly ( $<1 \text{ mm yr}^{-1}$ ) over long periods of time (10-30 Myr), with low total extensional strain (generally  $<10 \text{ km}$ ). Master fault angles are steep (45-70°). Seismicity suggests that crustal extension takes place down to mid-crustal levels. At higher strain rates, narrow rifts may evolve through increased stretching into passive margins; supra-detachment basins occur within wide extended domains with thickened crust. They typically extend quickly ( $<20 \text{ mm yr}^{-1}$ ) over short periods of time (5 - 12 Myr) with a high amount of total extensional strain (10-80 km). Master faults (detachments) are shallow in dip (10-30°), but may have originated at higher angles. Local anomalies in the ductile lower crust are amplified to produce core complexes ([Wernicke, 1985](#)).

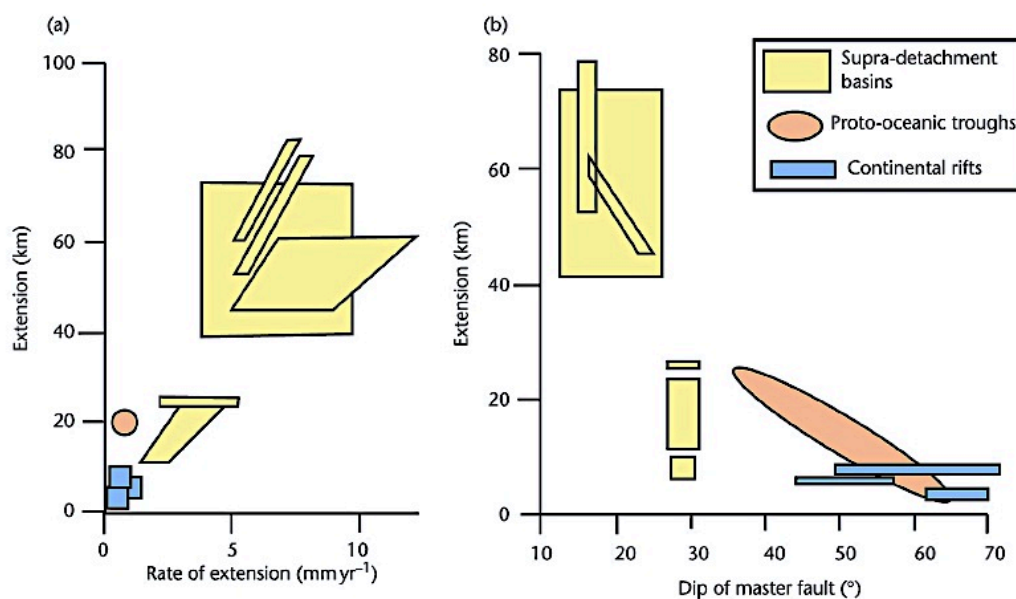


Figure 2.11b Rifts, supradetachment basins, and proto-oceanic troughs in terms of their strain rate, total extensional strain, and dip of master faults, based on [Friedmann and Burbank \(1995\)](#). (After [Allen and Allen, 2005](#)).

## 4. TYPE OF MODELS

### 4.1 Modelling the evolution of geodynamic systems. Background on modelling techniques

The geodynamics models are usually built to simulate geodynamic processes at crustal, lithospheric or mantle scale using kinematic or dynamic boundary conditions in 1, 2 and 3 dimensions. They can be used to investigate the role played by a particular sub-process and/or specific initial conditions during lithospheric extension (e.g. buoyancy forces, lower crustal flow, lithospheric flexure, thermal and/or strain-induced hardening/weakening, rheological stratification of the lithosphere, plume impingements, magma-assisted rifting etc.).

In particular, numerical and analogue modelling techniques share the advantages and disadvantages of trying to capture aspects of a geodynamic process in a model. For example, both methods allow the evolution of structures to be observed, which can be helpful in generating ideas on the origin and development of structures observed in the field and from geophysical data. With numerical and analogue models it is possible to vary model parameters and determine their relevance for the process under consideration. Advantages of the *numerical method* are the easy quantification of model results, including the possibility of tracking stresses, strain and strain-rates during the evolution of the model, and the relatively large freedom in choice of material properties (including a relatively easy implementation of temperature dependent rheologies), boundary conditions and geometries. Some models lose accuracy when dealing with large deformation situations (due to remeshing, for example) or large viscosity contrasts or have problems of other nature, particularly for lithospheric extension, when dealing with 3D deformation. The resolution of 3D models is in general still quite low and consequently to have a resolution useful to pictures narrow shear zone, the modeler needs to compromise on size or computational domain (see e.g. [Gerya, 2013](#); [Allken et al., 2011, 2012, 2013](#); [Brune, & Autin, 2013](#); [Brune et al., 2012](#)). The continuum approach limits also the detailed modelling of brittle tectonics and differential movements along evolving faults.

*Analogue models* on the other hand are very suitable for studying the 3D evolution of structures with time. This makes it possible to evaluate the effects of, for example, lateral changes in material properties or oblique extension. They have the ability to reproduce detailed modelling of brittle tectonics and differential movements along evolving faults.



They provide detailed information on the distribution and growth of discrete faults. The technique is limited in the application of temperature dependent rheologies, phase changes and variations in geometries.

Numerical and analogue techniques are partly complementary and the combination of both methods may help establish the robustness of model results (see also [Smart & Couzens-Schultz 2001](#); [Koyi 1997](#)).

Classifications of lithospheric extension models predicting basin formation can be done considering:

- the physical assumption used to build the model and perform the simulations ( e.g. see classification of [Fernandez and Ranalli 1997](#).) or;
- the kind of processes believed to play a first order role (or to be dominant) in determining the mode of extension through time and that dictates therefore the final deformation status (e.g. see classification of [Kearey et al., 2010](#)).

Here I have chosen to classify the models taking into account the inferred dominant processes. This will allow introducing the approach used in the preset study, which differs from other authors' methodologies. Also, I have chosen to focus the review on numerical models since this is the technique I have used to perform my research. So from now on, I present only computational models.

## **4.2 Models classification based on main processes believed to play the first order influence on rifting evolution**

### **4.2.1 Rift initiation: causes traditionally taken into account**

Continental rifting requires the existence of a horizontal deviatoric tensional stress that is sufficient to break the lithosphere. The deviatoric tension may be caused by stresses arising from a combination of sources, including:

- (i) plate motions;
- (ii) thermal buoyancy forces due to asthenospheric upwellings;
- (iii) tractions at the base of the lithosphere produced by convecting asthenosphere; and/or
- (iv) buoyancy (gravitational) forces created by variations in crustal thickness ([Huisman et al., 2001](#)). These stresses may be inherited from a previous tectonic regime or they may develop during extension.

[Fig. 2.12](#) (after [Ziegler et al., 2001](#)), in conjunction with [Fig. 2.1](#), gives a schematic

representation of the forces involved in rifting initiation.

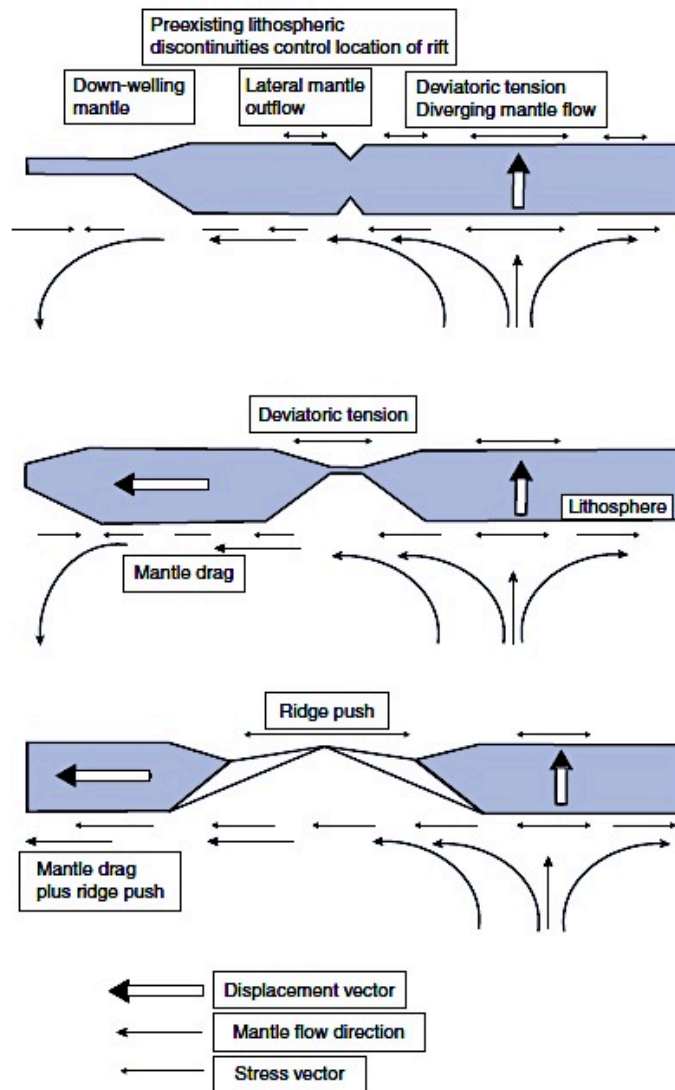


Figure 2.12 Diagram illustrating the interaction of shear-traction exerted on the base of the lithosphere by asthenospheric flow, deviatoric tension above upwelling mantle convection cells and ridge push forces. Modified from Ziegler PA, Cloetingh S, Guiraud R, and Stampfli GM (2001).

Full lithosphere breakup (Kearey et al., 2010) leading to the formation of a new ocean basin only occurs if the available stresses exceed the strength of the entire lithosphere. For this reason lithospheric strength is one of the most important parameters that governs the formation and evolution of continental rifts and rifted margins.

The horizontal force required to rupture the entire lithosphere can be estimated by integrating yield stress with respect to depth. The integrated yield stress, or lithospheric strength, is highly sensitive to the geothermal gradient as well as to crustal composition and crustal thickness. A consideration of these factors suggests that a force of  $3 \times 10^{13} \text{ N m}^{-1}$  may be required to rupture lithosphere with a typical heat flow value of  $50 \text{ mW m}^{-2}$  (Buck et al., 1999). In areas where lithosphere exhibits twice the heat flow, such as in the



Basin and Range Province, it may take less than  $10^{12} \text{ N m}^{-1}$  (Kusznir & Park, 1987; Buck et al., 1999). Several authors have estimated that the tectonic forces available for rifting are in the range  $3\text{--}5 \times 10^{12} \text{ N m}^{-1}$  (Forsyth & Uyeda, 1975; Solomon et al., 1975). If correct, then only initially thin lithosphere or lithosphere with heat flow values greater than  $65\text{--}70 \text{ mW m}^{-2}$  is expected to undergo significant extension in the absence of any other weakening mechanism (Kusznir & Park, 1987). Elsewhere, magmatic intrusion or the addition of water may be required to sufficiently weaken the lithosphere to allow rifting to occur.

Another important factor that controls whether rifting occurs is the mechanism that is available to accommodate the extension. At any depth, deviatoric tension can cause yielding by faulting, ductile flow, or dike intrusion, depending on which of these processes requires the least amount of stress. For example, if a magma source is available, then the intrusion of basalt in the form of vertical dikes could permit the lithosphere to separate at much lower stress levels than is possible without the diking. This effect occurs because the yield stress that is required to allow basaltic dikes to accommodate extension mostly depends on the density difference between the lithosphere and the magma (Buck, 2004). By contrast, the yield stresses required to cause faulting or ductile flow depend upon many other factors (e.g. strain rates, temperature, viscosity) that result in yield strengths that can be up to an order of magnitude greater than those required for lithospheric separation by diking (Kearey et al., 2010) (Fig. 2.13). High temperatures ( $>700^\circ\text{C}$ ) at the Moho, such as those that can result from the thermal relaxation of previously thickened continental crust, also may contribute to the tectonic forces required for rift initiation. For high Moho temperatures gravitational forces become increasingly important contributors to the stresses driving rifting.

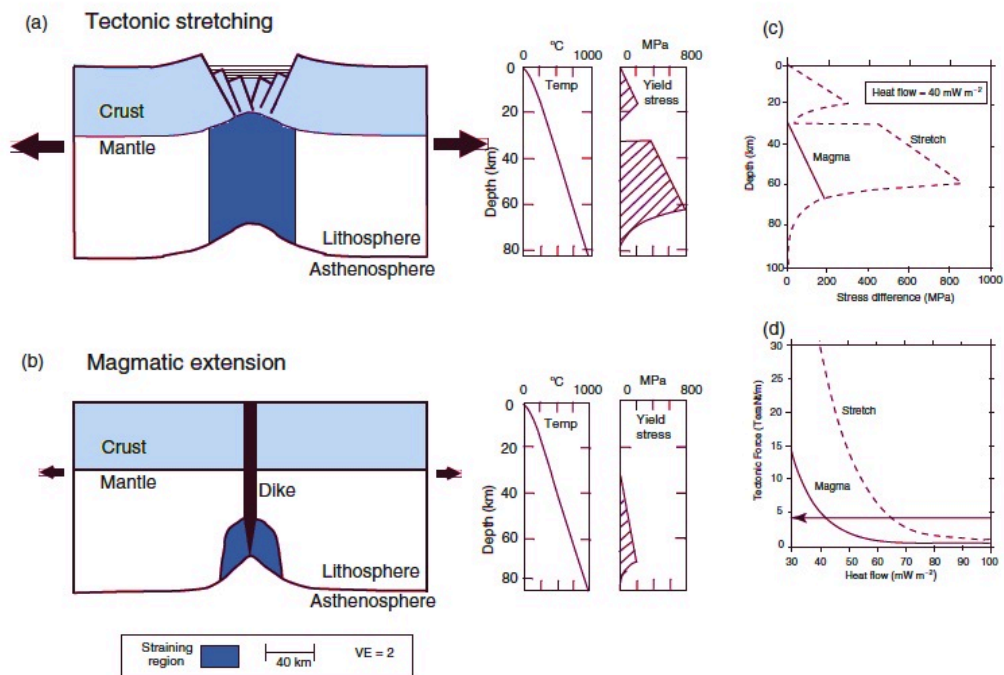


Figure 2.13 Sketches showing the difference between extension of thick lithosphere without (a) and with (b) magmatic intrusion by diking. Temperature and yield stress curves for each case are shown to the right of the sketches. VE, vertical exaggeration. (c) Example of yield stresses for strain rate  $10^{-14} \text{ s}^{-1}$  for 30-km-thick crust. Solid line, stress difference for magmatic rifting; dashed line, stress difference for lithospheric stretching. (d) Tectonic force for rifting with and without magma as a function of heat flow. The bold black line in (d) shows the estimated value of driving forces (modified after Buck, 2004).

Finally, the location and distribution of strain at the start of rifting may be influenced by the presence of pre-existing weaknesses in the lithosphere. Contrasts in lithospheric thickness or in the strength and temperature of the lithosphere may localize strain or control the orientations of rifts. This latter effect is illustrated by the change in orientation of the Eastern branch of the East African Rift system where the rift axis meets the cool, thick lithospheric root of the Archean Tanzanian craton. The Tanzanian example suggests that lateral heterogeneities at the lithosphere–asthenosphere boundary rather than shallow level structures in the crust are required to significantly alter rift geometry (Foster et al., 1997). This option for the East African Rift was recently investigated with the work of Koptev et al. (2015).

#### 4.2.2 Why and how is the lithosphere deformed? Strain localization and delocalization processes

The localization of strain into narrow zones during extension is achieved by processes that lead to a mechanical and thermal weakening of the lithosphere. Lithospheric

weakening may be accomplished by the elevation of geotherms during lithospheric stretching, heating by intrusions, interactions between the lithosphere and the asthenosphere, and/or by mechanisms that control the behavior of faults and shear zones during deformation (Kearey et al., 2010).

Working against these strain softening mechanisms are processes that promote the mechanical strengthening of the lithosphere. Lithospheric strengthening may be accomplished by the replacement of weak crust by strong (cold and/or dry) upper mantle during crustal thinning (in case of low rate of stretching) and by the crustal thickness variations that result from cooling.

These and other strain hardening mechanisms are believed to promote the delocalization of strain during rifting. Competition among these mechanisms, and whether they result in a net weakening or a net strengthening of the lithosphere, controls the evolution of deformation patterns within rifts.

#### **4.2.3 Kinematic and mechanical (kinematic with rheological constraints and dynamic) models.**

To determine how the lithospheric stretching can lead to many structural styles, subsidence patterns and occurrence of episodic magmatism (Section 3 and paragraphs therein) and also how the different combinations of lithospheric weakening and strengthening mechanisms control the response of the lithosphere to extension, geoscientists have developed *physical models* of rifting using different approaches.

One approach, called *kinematic modelling*, involves using information on the geometry, displacements, and type of strain to make predictions about the evolution of rifts and rifted margins. A common characteristic of kinematic models of lithospheric extension is that prescribing a velocity field, which is linked as an advective term to the heat transport equation, imposes deformation. No rheological laws (describing the deformational behaviors, e.g. brittle, viscous, elastic, visco-elastic, visco-plastic, visco-elasto-plastic ) nor governing equations (describing the dynamic of the deformation) are incorporated and only vertical forces are considered, related to loading/unloading associated with infilling of basins, erosion of shoulders, and mass redistribution due to lithospheric stretching. Seismicity with focal mechanisms and GPS velocities of sites are the data types that frequently are used to generate these types of models. Among the most common kinematic examples are the pure shear (McKenzie, 1978), the simple shear (Wernicke, 1985), and the crustal delamination (Lister et al., 1986) models of extension

(Fig. 2-15. The specific description of these models is in the following paragraph). The predictions from these models are tested with observations of subsidence and uplift histories within rifts and rifted margins, and with information on the displacement patterns recorded by faults and shear zones.

This approach has been used successfully to explain differences in the main features of extensional sedimentary basins and their evolution through time. This capability is due to the high variety of deformation modes that can be imposed by predefining the velocity field. However, one *major limitation* of kinematic modelling is that it does not address the underlying causes of these differences since in kinematic models there is no control over the compatibility between the imposed mode of deformation and the actual mechanical behaviour of rocks.

By contrast, *mechanical models* employ information about the net strength of the lithosphere and how it changes during rifting to test how different physical processes affecting rift evolution. The mechanical models are often divided in *kinematic models with rheological constraints* and *Dynamic models* (Fernandez and Ranalli, 1997).

In order to compute the lithospheric strength the *kinematic models with rheological constraints* approach uses 1D yielding strength envelope profiles, YSE, as analytic tool (see Chapter 3 for explanation on the use and the concepts behind the YSE profiles) even if the sometimes the models are 2D (e.g. England 1983). These one-dimensional approaches do not provide the actual deformation of the lithosphere, but they introduce rheological controls on the mode of deformation. Specifically, the rheological behaviours of lithospheric layers (described by rheological laws of brittle, elastic and viscous behaviours) under stretching and their variation with depth, temperature distribution and initial composition are taken into account.

*Kinematic models with rheological constraints* predict that two competing effects arise during finite continental extension: weakening produced by lithospheric thinning (mechanical and thermal thinning) and strengthening produced by thermal relaxation (thermal thickening) (see England, 1983 for and exhaustive explanation. These concepts are used as main assumption in my model – Chapter 3 – and as interpretation tools for my general results – Chapter 5). According to the interplay of these effects, the locus of extension may migrate or localize and so it is possible to correlate the distribution and net strength of the lithosphere with formation of narrow and wide rifts. In this way the predefined velocity field will no longer be valid. An application of this methodology is the analysis of the correlation of necking level, with strength envelopes (Cloetingh et al.,

1995a; Kooi et al., 1992). The necking level usually corresponds to a strong layer in the lithosphere (upper-middle crust or uppermost mantle, according to geothermal gradient). When two well-defined strong layers are present, however, the necking level loses its geometric meaning.

A simple procedure to evaluate the progress of extension is to compare the total strength of a stretched lithospheric column with that corresponding to an undeformed lithosphere on the basis of a reference 1D rheological model. Models that can be classified as *Kinematic models with rheological constraints* are Sawyer (1985), Kuszniir and Park (1987) and Buck (1991).

The use of rheological constraints in kinematic models improved greatly the understanding of the lithospheric stretching process. In fact, it yields some relations between the mode of deformation (narrow or localized /wide or diffuse rifts) and strain rate, initial geotherm, and crust/mantle thickness ratio. However, a complete account of lithospheric deformation requires the use of *two- or three-dimensional dynamic models*. In order to do so there is needed to use equations, which relate dynamic quantities (stress) to kinematic quantities (strain or strain rate) through material parameters (rheological parameters and laws) (Ranalli, 1995). This means that together with rheological laws, additional equations are necessary to describe the behaviour of mantle and lithospheric rocks, namely, governing equations which are the equations of continuity, motion and heat balance (see Chapter 4 for explanation).

Another important role is also played by the *boundary conditions* chosen to drive the extension. They can be either *kinematic* (constant strain rate or constant velocity) or *dynamic* (constant tectonic force) and/or *thermal* (fixed heat flow or a fixed temperature at the base of the lithosphere). They are shown in Fig. 2.14.

In this way the mantle and lithosphere dynamics are fully described in 2 and 3 dimensions and in particular this latter approach permits inhomogeneous strains and a quantitative evaluation of how changes to lithospheric strength and rheology influence rift behaviour. Examples of this kind of models are England (1983), Jarvis and McKenzie (1980), Bassi, 1995, Kuszniir, (1982), Parsons and Sclater (1977), Buck, 1986, Keen and Boutilier, 1995). And most recently Huismans and Beaumont (2002, 2003, 2007, 2014).

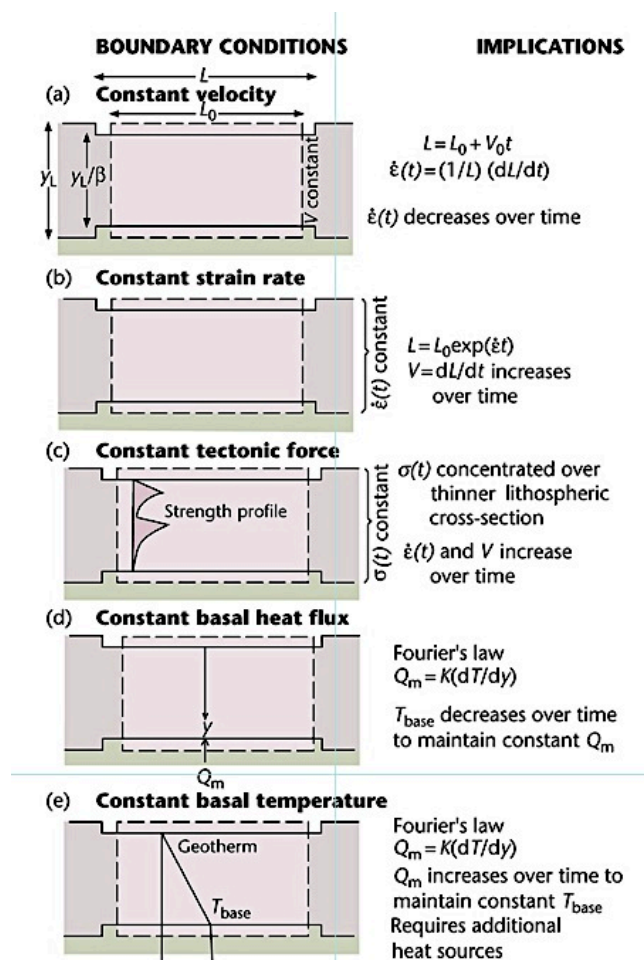


Figure 2.14 Boundary conditions for dynamic models of lithospheric extension. (a) Constant velocity of extension over time, which implies that the strain rate must decrease over time; (b) Strain rate constant over time, which implies that the extension velocity must increase over time; (c) Constant tectonic force (deviatoric stress) over time, which causes the same force to be concentrated over a thinner lithospheric cross-section over time. This force becomes concentrated in the strong layers in the lithosphere, which undergo large scale necking. The strain rate therefore increases over time; (d) Constant basal heat flux over time, which implies, via Fourier's law, that the temperature at the base of the lithosphere must decrease over time; (e) Constant basal temperature over time, which implies that the basal heat flux must increase with time, as in the uniform stretching model of McKenzie (1978a). This requires additional heat sources to increase the basal heat flux. (after Allen & Allen, 2013)

I will start the next section describing the kinematic models briefly and then I will continue with the description of the other two categories together. This is because the main reason for which the models are made is to study a particular sub-process involved in the rifting of the lithosphere. Consequently, I am going to classify and describe the models present in literature taking into account the main physical processes believed to be predominant during the deformation.

#### 4.2.3.1 Kinematic Models

A very simple one-dimensional approach to explain the subsidence observed in passive margins and sedimentary basins was proposed by McKenzie (1978). The model assumes

1. Stretching is uniform with depth;
2. Stretching is instantaneous;
3. Stretching is by pure shear;
4. The necking depth is zero;

5. Airy isostasy is assumed to operate throughout;
6. There is no radiogenic heat production;
7. Heat flow is in one dimension (vertically) by conduction;
8. The stretching phase is followed by thermal relaxation.

It is clear that there are a number of observations in regions of continental extension that suggest that the assumptions in the uniform stretching model should be re-examined.

In particular the pure-shear models do not account for the asymmetry and/or high uplift of the flanks observed in many basins. An alternative kinematic model of basin formation was proposed by [Wernicke \(1985\)](#), who assumed a detachment across the entire lithosphere to explain the uplift of the Colorado Plateau adjacent to the Basin and Range by local isostasy. Simple-shear deformation produces a lateral offset between mantle and crustal thinning and asymmetry in the resulting basin (see e.g., [Buck et al., 1988](#), and [Kusznir and Egan, 1989](#), for a quantitative analysis). Depending on the depth, dip, and number of detachments, different styles of deformation can be reproduced, such as simple shear ([Buck et al., 1988](#)), combined simple shear and pure shear ([Kusznir et al., 1987](#)), cantilever ([Kusznir and Ziegler, 1992](#)) and delamination model ([Lister et al., 1986](#)). Including detachments and faults in kinematic models implies that some lithospheric levels can act as decoupling horizons. However, faults and detachments merely play a role of slip surfaces and no considerations on the stress necessary to produce this slip are taken into account. See [Fig. 2.15](#) for a synthetic representation of these three main kinematic models.



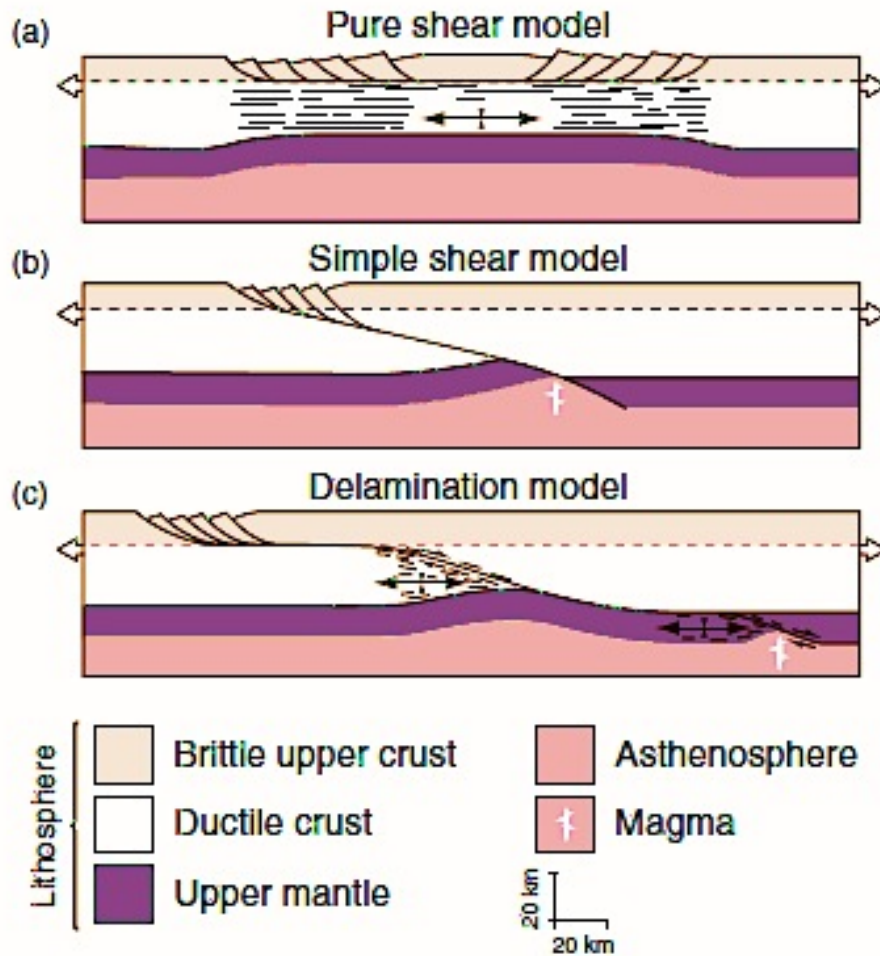


Figure 2.15 Kinematic models of continental extension (after Lister et al., 1986, with permission from the Geological Society of America).

#### 4.2.3.2 Mechanical models (kinematic models with rheological constraints and dynamic models)

##### 4.2.3.2.1 Non-uniform stretching models: discontinuous and continuous stretching with depth.

The simple geometrical uniform, depth-independent stretching model does not take into account the layered rheological stratification of the lithosphere. Since rheological properties vary with temperature and pressure, the lithosphere is expected to extend more realistically in a non-uniformly manner with depth. The distribution of lithospheric extension with depth may be *discontinuous* or *continuous* as represented in Fig. 2.16. In the first case the upper and lower portion of the lithosphere are decoupled at a certain depth that may or may not correspond to the crust-mantle boundary. The portion of the lithosphere above this horizon extends by a certain factor  $\delta$ , with regard to the underlying lower lithosphere, which extends by a factor  $\beta$ . The upper and lower



lithospheric extensions are considered independent but uniform throughout their respective layer thickness. Clearly, when  $\delta=\beta$  uniform extension occurs. The main differences with respect to the uniform stretching may be summarized in the following points:

- The thermal gradient after extension is no longer linear with depth, but ‘two-legged’.
- Discontinuous stretching raises the lithosphere-asthenosphere boundary to a more shallow level than in the uniform case thus solving the ‘heating problem’. Thinning the sub-crustal lithosphere more than the upper crust may lead to an increased heat input during extension.
- A minor amount of crustal thinning for the same total subsidence is required.

As in the uniform case, the total subsidence is made up by two contributions: an initial, fault- controlled, subsidence and a subsequent thermal subsidence. The initial subsidence depends on the amount of the initial crustal thickness ( $y_c$ ), the decoupling depth and the relative magnitudes of  $\delta$  and  $\beta$  whereas the thermal subsidence is hardly affected. Considering the situation of instantaneous stretching, i.e. no heat loss during the rifting process, the thermal subsidence reflects the amount of sub-crustal thinning. This provides a simple way to estimate the stretching factors of the crust and mantle-lithosphere directly from the amount of syn- and post-rift subsidence. [Royden & Keen \(1980\)](#) applied this model to the Nova Scotia and Labrador continental margins. In their formulation the decoupling horizon was located at the base of the crust and instantaneous extension was assumed.

A general agreement was found between the theoretical subsidence predicted by their model and the subsidence calculated from deep well data. Moreover, the results explained the uplift typically experienced by many basin margins during early rifting phases and showed that the thermal subsidence can account for the long-term tectonic subsidence observed. A more refined model approach was adopted by [Van Wees et al. \(2000\)](#) to explain the Late Permian-Early Jurassic evolution of the Southern Permian Basin, the southern part of the CEBS. Detailed thickness and facies analyses based on wells and reflection-seismic data indicating only minor faults contradict the simple pure shear model used previously (e.g [Dadl  z et al., 1995](#)). In order to establish a quantitative framework for the evolution of the Southern Permian Basin, [Van Wees et al. \(2000\)](#)

proposed a model allowing for multiple rifting phases as well as differential extension of the crust and the mantle-lithosphere.

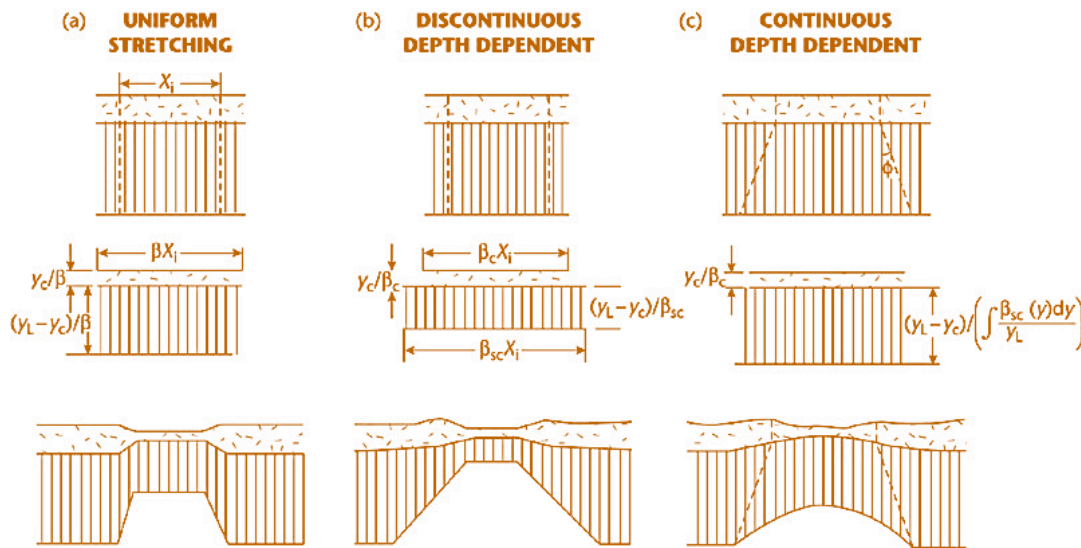


Figure 2.16 Schematic diagrams to illustrate differences between (a) uniform, (b) discontinuous, and (c) continuous depth-dependent stretching. (a) Uniform extension in which the crust and subcrustal lithosphere extend by identical amounts; (b) Discontinuous depth-dependent extension in which the crust extends by a different amount to the subcrustal lithosphere, necessitating a decoupling between the two layers. The crustal and subcrustal extensions are independent but are uniform throughout the crust and subcrustal lithosphere (Royden and Keen 1980; Beaumont et al. 1982; Hellinger and Sclater 1983); (c) Continuous depth-dependent extension in which the stretching is a continuous function of depth in the subcrustal lithosphere and the crustal stretching is the same as in (a) and (b) (Rowley and Sahagian 1986).

The obtained results indicated that the basin wide Late Permian- Triassic subsidence required an active mechanism, although there is almost no evidence of synchronous active faulting. In this regard, a relative important component of Late Permian and Triassic tectonic subsidence can be explained by thermal relaxation of a major lithospheric thermo-mechanical attenuation during Early Permian and by consequent delayed infilling of the topographic depressions developed during Late Permian. The results of [Van Wees et al. \(2000\)](#) suggested a thermal-induced thinning of the mantle rather than a mechanical driven crustal extension as responsible mechanism for the Early Permian stretching event. Following their hypothesis, thinning of the crust below the Southern Permian Basin may be partly attribute to its mechanical extension and partly to magmatic destabilization of the crust-mantle boundary followed by reactivation of the lower crust.

Although discontinuous non-uniform stretching models have been successful in explaining some first order features in long-term subsidence patterns of basins, they rely on a number of requirements:

- The focal depths of earthquakes in old cratons suggest that the upper part of the lithosphere has relatively high strength and shows active seismic activity. In contrast, the underlying lower part is almost completely a-seismic. This difference may contribute to the ductile deformation mechanisms within the lower layers of the lithosphere which may lead to a rheological de-coupling at mid-crustal level. This feature may induce different amounts of extension within the two layers (e.g. [Sibson, 1983](#); [Ranalli, 1995](#)). However, the existence of an intra-lithospheric discontinuity is not universally proven.
- The mechanism by which the lithospheric mantle may stretch differently is an 'ad-hoc' requirement which creates another space problem within the mantle. To overcome this limitation, a combination of extension and magmatic intrusion during rifting has been proposed (e.g. [Royden & Keen, 1980](#)). However, it leads to a complex formulation hiding the natural simplicity of the model.

All the above requirements may be removed by considering a non-uniform but *continuous stretching* with depth. This formulation requires the stretching to be a continuous function of depth in the mantle-lithosphere with a decreasing rate with depth as the extension is diffused over a wider area. The amount of stretching depends on the depth beneath the crust and on the angle  $\theta$  between the vertical and the boundary of the stretched region ([Fig. 2.16](#)). Greater values of  $\theta$  increase the amount of the initial subsidence, while at the same time reducing the amount of the post-rift thermal subsidence. There are mainly two important implications of stretching the mantle over a wider area than the crust:

1. A point located at the rift shoulder experiences an initial uplift followed by a subsequent phase of subsidence. [Sleep \(1971\)](#) has demonstrated that in absence of erosion it will approximately return to its initial elevation, while if erosion occurs it will sink to a deeper level than the initial one.
2. Predicted stratigraphic onlap at basin margins causes the so-called '*steer's head*' geometry during the following post-rift subsidence phase (e.g. [White & McKenzie, 1988](#)) ([Fig 2.6](#)).

#### **4.2.3.2.2 Lithospheric stretching and boundary conditions role at the onset of rifting**

During horizontal extension, lithospheric stretching results in a vertical thinning of the crust and an increase in the geothermal gradient within the zone of thinning (McKenzie, 1978). These two changes in the physical properties of the extending zone affect lithospheric strength in contrasting ways. Crustal thinning or necking tends to strengthen the lithosphere because weak crustal material is replaced by strong mantle lithosphere as the latter moves upward in order to conserve mass. The upward movement of the mantle also may result in increased heat flow within the rift. This process, called heat advection, results in higher heat flow in the rift because the geotherms become compressed rather than through any addition of heat. The compressed geotherms tend to result in a net weakening of the lithosphere, whose integrated strength is highly sensitive to temperature (Section 2.10). However, the weakening effect of advection is opposed by the diffusion of heat away from the zone of thinning as hot material comes into contact with cooler material. If the rate of heat advection is faster than the rate of thermal diffusion and cooling then isotherms at the base of the crust are compressed, the geotherm beneath the rift valley increases, and the integrated strength of the lithosphere decreases. If thermal diffusion is faster, isotherms and crustal temperatures move toward their pre-rift configuration and lithospheric weakening is inhibited. England (1983) (Fig. 2-17) and Kuszniir & Park (1987) (Fig. 2-18) showed that the integrated strength of the lithosphere in rifts, and competition between cooling and heat advection mechanisms, is strongly influenced by the rate of extension.

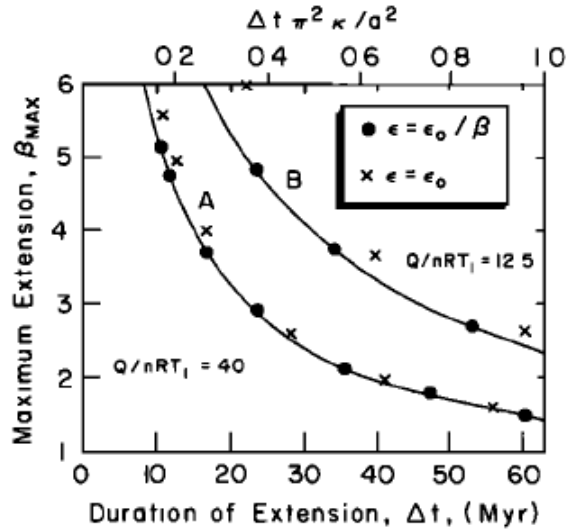


Figure 2.17 Values of the maximum strain achieved in a model lithosphere as a function of duration of straining for two different values of  $Q/nRT$  (see Tab.3.1, 3.2 and 3.3 for definition of variables and quantities). The circles refer to the decaying strain rate case (and the crosses refer to the constant strain rate). The smooth lines have been drawn through the former symbols; for the reasons given in the text, the crosses always lie above their respective lines. The dimensional times are those for the parameter values given in the notation list.

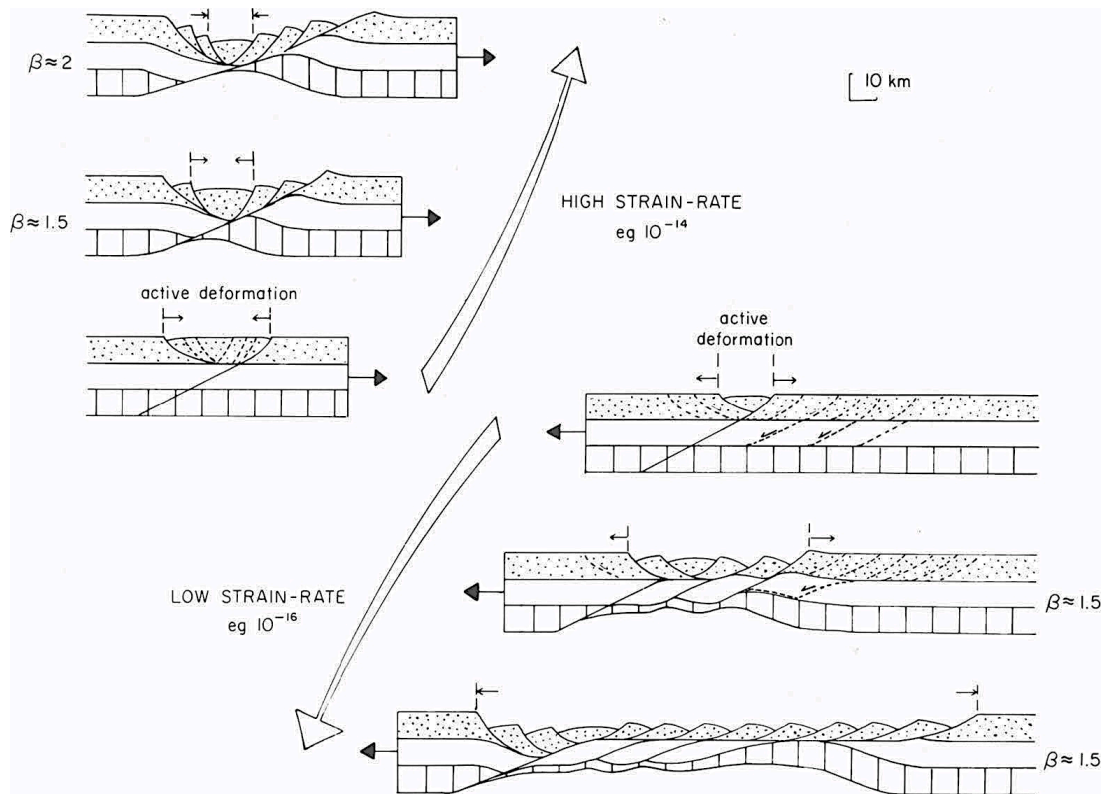


Figure 2.18 Illustrative models showing the different styles of extensional deformation expected with fast and slow rates of extension. At fast strain rates (e.g.  $10^{-14} \text{ s}^{-1}$ ) strain softening might be expected to localize the deformation near the original site of complete lithosphere failure causing progressive narrowing and intensification of the active deformation and leading potentially to high  $\beta$  values and complete crustal separation. At slow strain rates (e.g.  $10^{-16} \text{ s}^{-1}$ ) local strain hardening might be expected to transfer deformation laterally to previously undeformed areas thus progressively widening the zone of active deformation but with a limiting value of around 1.5. Note in the slow strain-rate model the use of detachment horizons between the crustal layers to transfer the deformation.

Fast strain rates ( $10^{-13} \text{ s}^{-1}$  or  $10^{-14} \text{ s}^{-1}$ ) result in larger increases in geothermal gradients than slow rates ( $10^{-16} \text{ s}^{-1}$ ) for the same amount of stretching.

This effect suggests that high strain rates tend to localize strain because inefficient cooling keeps the thinning zone weak, allowing deformation to focus into a narrow zone. By contrast, low strain rates tend to delocalize strain because efficient cooling strengthens the lithosphere and causes the deformation to migrate away from the center of the rift into areas that are more easily deformable. The amount of net lithospheric weakening or strengthening that results from any given amount of stretching also depends on the initial strength of the lithosphere and on the total amount of extension. The total amount of thinning during extension usually is described by the stretching factor ( $\beta$ ), which is the ratio of the initial and final thickness of the crust ([McKenzie, 1978](#)).

The thermal and mechanical effects of lithospheric stretching at different strain rates are illustrated in [Fig. 2.19-19](#), which shows the results of two numerical experiments conducted by [van Wijk & Cloetingh \(2002\)](#). In these models, the lithosphere is divided into an upper crust, a lower crust, and a mantle lithosphere that have been assigned different rheological properties. [Figures 2-19a](#) shows the thermal evolution of the lithosphere for uniform extension at a rate of  $16 \text{ mm a}^{-1}$ . At this relatively fast rate, heating by thermal advection outpaces thermal diffusion, resulting in increased temperatures below the rift and strain localization in the zone of thinning. As the crust thins, narrow rift basins form and deepen. Changes in stretching factors for the crust ( $\beta$ ) and mantle ( $\delta$ ) are shown in [Fig. 2.19 b](#). The total strength of the lithosphere ([Fig. 2.19 c](#)), obtained by integrating the stress field over the thickness of the lithosphere, gradually decreases with time due to stretching and the strong temperature dependence of the chosen rheologies. Eventually, at very large strains, the thermal anomaly associated with rifting is expected to dissipate. These and many other models of rift evolution that are based on the principles of lithospheric stretching approximate the subsidence patterns measured in some rifts and at some rifted continental margins ([van Wijk & Cloetingh, 2002](#); [Kusznir et al., 2004](#)).

The experiment shown in [Fig. 2.19 d-e](#) shows the evolution of rift parameters during lithospheric stretching at the relatively slow rate of  $6 \text{ mm a}^{-1}$ . During the first 30 Ma, deformation localizes in the center of the rift where the lithosphere is initially weakened as isotherms and mantle material move upward. However, in contrast with the model shown in [Fig. 2.19 a-c](#), temperatures begin to decrease with time due to the efficiency of conductive cooling at slow strain rates. Mantle upwelling in the zone of initial thinning ceases and the lithosphere cools as temperatures on both sides of the central rift increase

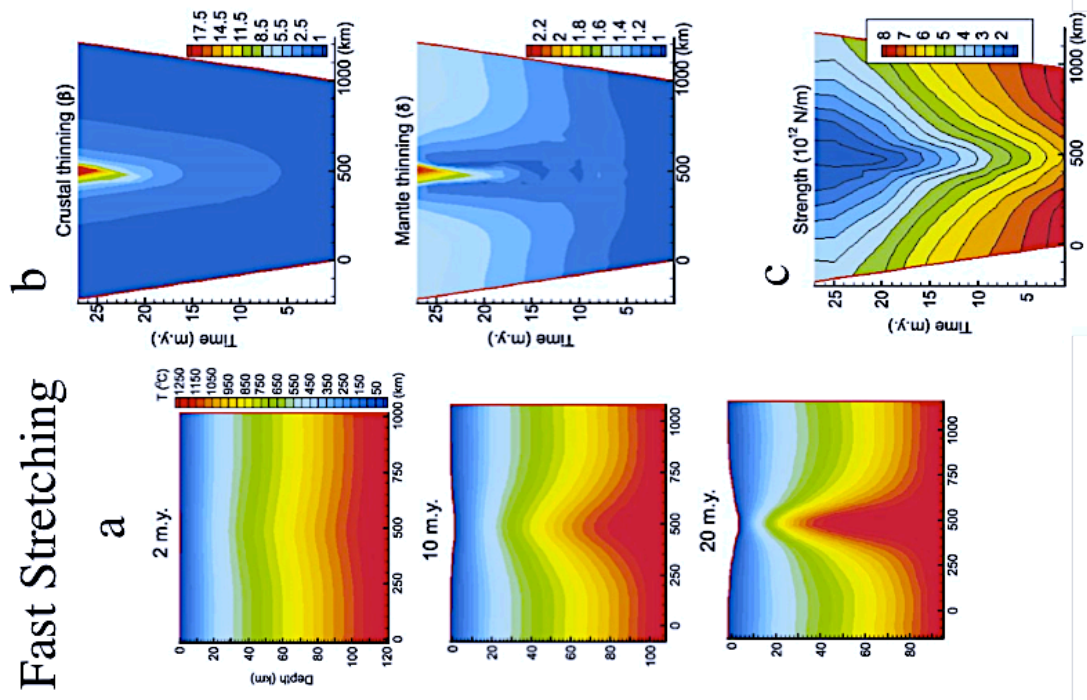
(Fig. 2.19 d). At the same time, the locus of thinning shifts to both sides of the first rift basin, which does not thin further as stretching continues. The mantle thinning factor (Fig. 2.19 e) illustrates this behaviour. During the first 45 Ma, upwelling mantle causes  $\delta$  to be larger in the central rift than its surroundings. After this time,  $\delta$  decreases in the central rift as new upwelling zones develop on its sides. The total strength of the lithosphere (Fig. 2.19 f) for this low strain rate model shows that the central rift is weakest until about 55 Ma. After this time the weakest areas are found on both sides of the central rift basin.

In the view of these authors this model shows how the strong dependence of lithospheric strength on temperature causes strain delocalization and the formation of wide rifts composed of multiple rift basins at slow strain rates.

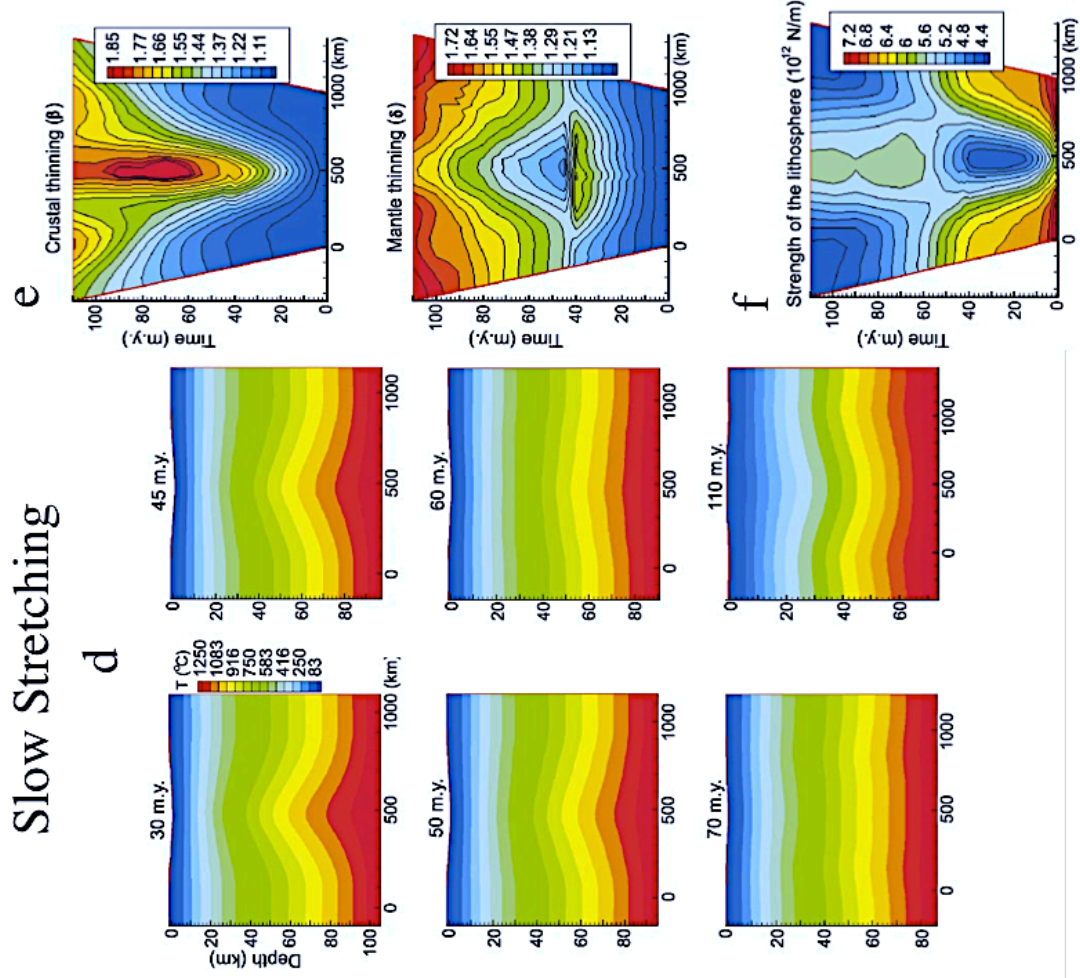
*Figure 2.19 (a) Three-layer lithospheric model where the base of the lithosphere is defined by the 1300°C isotherm at 120 km. Differential stress curves show a strong upper crust and upper mantle and a lower crust that weakens with depth. Thermal evolution of the lithosphere (b–d) during stretching for a horizontal extensional velocity of 16 mm yr<sup>-1</sup>. Evolution of lithospheric strength (g) and of thinning factors for the crust (e) and mantle (f) for a velocity of 16 mm yr<sup>-1</sup>. Thermal evolution of the lithosphere (h–j) during stretching for a velocity of 6 mm yr<sup>-1</sup>. Evolution of lithospheric strength (m) and of thinning factors for the crust (k) and mantle (l) for a velocity of 6 mm yr<sup>-1</sup> (image provided by J. van Wijk and modified from van Wijk & Cloetingh, 2002, with permission from Elsevier).*



## Fast Stretching



## Slow Stretching





The model predicts that continental break-up will not occur for sufficiently slow rift velocities. It shows the effect of a low stretching velocity on the temperature field which in turn influences the delocalization of the strain.

The main limitation of this model is that the authors have used a the thermal field to define the thinning and thickening of the crust (the thickness of the crust changes in time accordingly with the variation of the temperature field), which is conceptually wrong since the Moho as a compositional definition and it is not an isotherm. The only part of the lithosphere that can behave thermally (as a thermal boundary layer, so able to change the thickness as function of the temperature distribution) is the lithospheric mantle. If we consider as bottom limit of lithosphere the lithospheric-asthenosphere boundary (TBL ), which is an isotherm, this able to move upward and downward respectively with the decrease and increase of geothermal gradient. This point is discussed in the rationale of my project in Chapter 3.

Another important piece of work done by [van Wijk et al. \(2001\)](#) shows the direct consequence of the stretching velocity used and the production of magma.

In this study the lithosphere was stretched to realistic thinning factors. Lithospheric stretching resulted in a lithosphere almost unaffected by extension further away from the rift centre, a zone characterized by larger thinning factors closer to the rift centre and a very small zone with very high thinning factors where possible breakup occurs. The degree of thinning depends on stretching velocity, which in conjunction with the rising of the geothermal gradient affects the amounts of melt generated. They have tested this for the mid-Norwegian margin, constraining with observations the timing of melt production (late syn-rift) and the amounts of melt. This work pointed out that a mantle plume is not always a prerequisite to generate a volcanic margin. Instead dynamical processes related to lithospheric rifting may enhance the produced melt volumes sufficiently to explain the sometimes enigmatic amounts of melt observed at volcanic margins

#### **4.2.3.2.3 Buoyancy forces and lower crustal flow**

In addition to crustal thinning and the compression of geotherms, lithospheric stretching results in two types of buoyancy forces that influence strain localization during rifting. First, lateral variations in temperature, and therefore density, between areas inside and outside the rift create a thermal buoyancy force that adds to those promoting horizontal extension ([Fig. 2.20](#)). This positive reinforcement tends to enhance those aspects of lithospheric stretching that promote the localization of strain. Second, a crustal buoyancy

force is generated by local (Airy) isostatic effects as the crust thins and high-density material is brought to shallow levels beneath the rift (Fleitout & Froidevaux, 1982). Because the crust is less dense than the underlying mantle, crustal thinning lowers surface elevations in the center of the rift (Fig. 2.20). This subsidence places the rift into compression, which opposes the forces driving extension. The opposing force makes it more difficult to continue deforming in the same locality, resulting in a delocalization of strain as the deformation migrates into areas that are more easily deformable (Buck, 1991).

*Figure 2.20 Schematic diagram illustrating thermal and crustal buoyancy forces generated during rifting. A and B represent vertical profiles outside and inside the rift valley, respectively. Pressure and temperature as a function of depth for each profile are shown to the right of sketch (modified from Buck, 1991). Differences in profiles generate lateral buoyancy forces.*

influence the style of extension.

Models of continental extension that emphasize crustal buoyancy forces incorporate the effects of ductile flow in the lower crust. [Buck \(1991\)](#) and [Hopper & Buck \(1996\)](#) showed that the pressure difference between areas inside and outside a rift could cause the lower crust to flow into the zone of thinning if the crust is thick and hot. Efficient lateral flow in a thick, hot, and weak lower crust works against crustal buoyancy forces by relieving the stresses that arise from variations in crustal thickness.

This effect may explain why the present depth of the Moho in some parts of the Basin and Range Province, and therefore crustal thickness, remains fairly uniform despite the variable amounts of extension observed in the upper crust. In cases where low yield strengths and flow in the lower crust alleviate the effects of crustal buoyancy, the zone of crustal thinning can remain fixed as high strains build up near the surface. [Buck \(1991\)](#) and [Hopper & Buck \(1996\)](#) defined this latter style of deformation as core complex-mode extension ([Fig. 2.21](#)). Studies of flow patterns in ancient lower crust exposed in metamorphic core complexes (e.g. [Klepeis et al., 2007](#)) support this view.

The relative magnitudes of the thermal and crustal buoyancy forces may be affected by two other parameters: strain rate and strain magnitude. [Davis & Kusznir \(2002\)](#) showed that the strain delocalizing effects of the crustal buoyancy force are important at low strain rates, when thermal diffusion is relatively efficient and after long (>30 Myr) periods of time. In addition, thermal buoyancy forces may dominate over crustal buoyancy forces immediately after rifting when strain magnitudes are relatively low. This latter effect occurs because variations in crustal thicknesses are relatively small at low stretching ( $\beta$ ) factors. This study, and the work of [Buck \(1991\)](#) and [Hopper & Buck \(1996\)](#), suggests that shifts in the mode of extension are expected as continental rifts evolve through time and the balance of thermal and crustal forces within the lithosphere changes.

#### **4.2.3.2.4 Lithospheric flexure**

##### **4.2.3.2.4.1 Flexural models**

Border faults that bound asymmetric rift basins with uplifted flanks are among the most common features in continental rifts ([Fig. 2.22](#)). Some aspects of this characteristic morphology can be explained by the elastic response of the lithosphere to regional loads caused by normal faulting. Plate flexure describes how the lithosphere responds to long-term (>10<sup>5</sup> years) geologic loads. By comparing the flexure in the vicinity of different

types of load it has been possible to estimate the effective long-term elastic thickness ( $T_e$ ) of continental lithosphere using forward models of topography and gravity anomaly profiles (Weissel & Karner, 1989; Petit & Ebinger, 2000). The value of  $T_e$  in many rifts, such as the Basin and Range, is low (4 km) due to the weakening effects of high geothermal gradients.

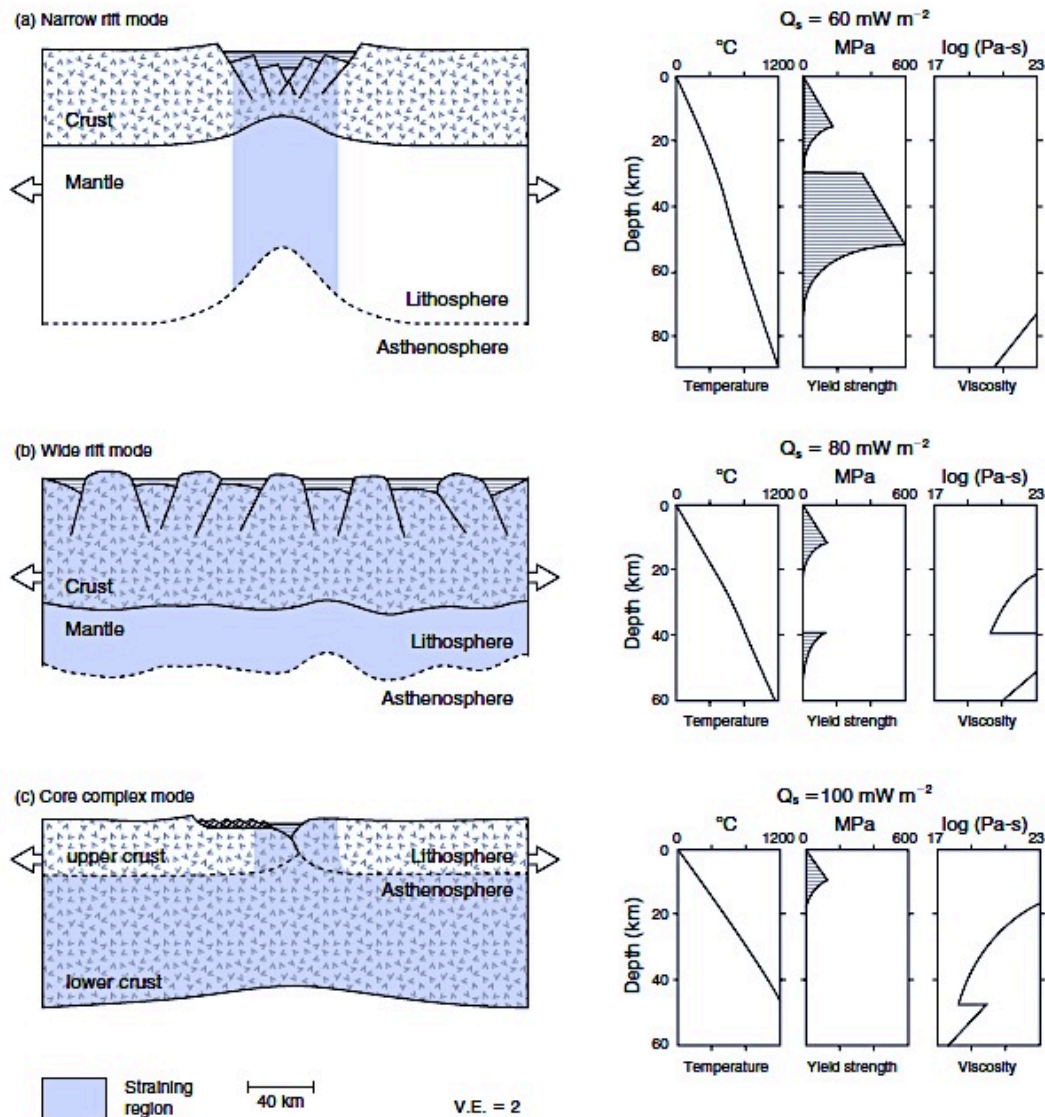


Figure 2.21 Sketches of the lithosphere illustrating three modes of extension emphasizing the regions undergoing the greatest amount of extensional strain (modified from Buck, 1991). (a) Narrow mode, (b) wide mode, (c) core complex mode. Lithosphere is defined as areas with effective viscosities of  $>10^{21} \text{ Pa s}^{-1}$ . The plots to the right of each sketch show initial model geotherms, yield strengths (for a strain rate of  $10^{-15} \text{ s}^{-1}$ ) and effective viscosities for a dry quartz crust overlying a dry olivine mantle. From top to bottom the crustal thicknesses are 30 km, 40 km, and 50 km.  $Q_s$ , initial surface heat flow. (c) Shows layers labelled at two scales: the upper crust and lower crust labels on the left side of diagram show a weak, deforming lower crust (shaded); the lithosphere and asthenosphere labels on the right side of diagram show a scale emphasizing

*that the zone of crustal thinning (shaded column) is localized into a relatively narrow zone of weak lithosphere.*

However, in other rifts, including those in East Africa and in the Baikal Rift, the value of  $T_e$  exceeds 30 km in lithosphere that is relatively strong (Ebinger et al., 1999). The physical meaning of  $T_e$ , and its relationship to the thickness ( $T_s$ ) of the seismogenic layer, is the subject of much discussion. Rheological considerations based on data from experimental rock mechanics suggest that  $T_e$  reflects the integrated brittle, elastic, and ductile strength of the lithosphere. It, therefore, is expected to differ from the seismogenic layer thickness, which is indicative of the depth to which short term (periods of years) anelastic deformation occurs as unstable frictional sliding (Watts & Burov, 2003). For these reasons,  $T_e$  typically is larger than  $T_s$  in stable continental cratons and in many continental rifts.

The deflection of the crust by slip on normal faults generates several types of vertical loads. A mechanical unloading of the footwall occurs as crustal material in the overlying hanging wall is displaced downward and the crust is thinned. This process creates a buoyancy force that promotes surface uplift. Loading of the hanging wall may occur as sediment and volcanic material are deposited into the rift basin. These loads combine with those that are generated during lithospheric stretching. Loads promoting surface uplift are generated by increases in the geothermal gradient beneath a rift, which leads to density contrasts. Loads promoting subsidence may be generated by the replacement of thinned crust by dense upper mantle and by conductive cooling of the lithosphere if thermal diffusion outpaces heating. Weissel & Karner (1989) showed that flexural isostatic compensation following the mechanical unloading of the lithosphere by normal faulting and crustal thinning leads to uplift of the rift flanks. The width and height of the uplift depend upon the strength of the elastic lithosphere and, to a lesser extent, on the stretching factor ( $\beta$ ) and the density of the basin infill. Other factors may moderate the degree and pattern of the uplift, including the effects of erosion, variations in depth of lithospheric necking (van der Beek & Cloetingh, 1992; van der Beek, 1997) and, possibly, small-scale convection in the underlying mantle (Steckler, 1985). Ebinger et al. (1999) showed that increases in the both  $T_e$  and  $T_s$  in several rift basins in East Africa and elsewhere systematically correspond to increases in the length of border faults and rift basin width. As the border faults grow in size, small faults form to accommodate the monoclinial bending of the plate into the depression created by slip on the border fault (Fig. 2-22). The radius of curvature of this bend is a measure of flexural rigidity. Strong

plates result in a narrow deformation zone with long, wide basins and long border faults that penetrate deeper into the crust.

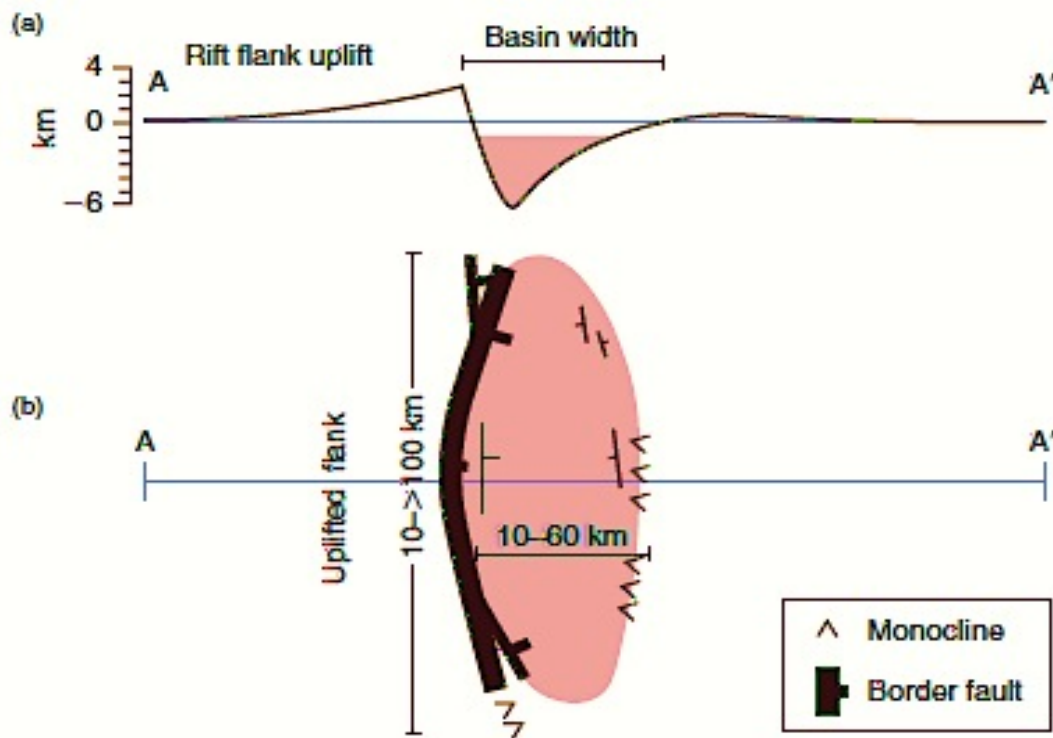


Figure 2.22 Generalized form of an asymmetric rift basin showing border fault in (a) cross-section and (b) plan view (after Ebinger et al., 1999, with permission from the Royal Society of London). Line of section (A–A') shown in (b). Shading in (b) shows areas of depression.

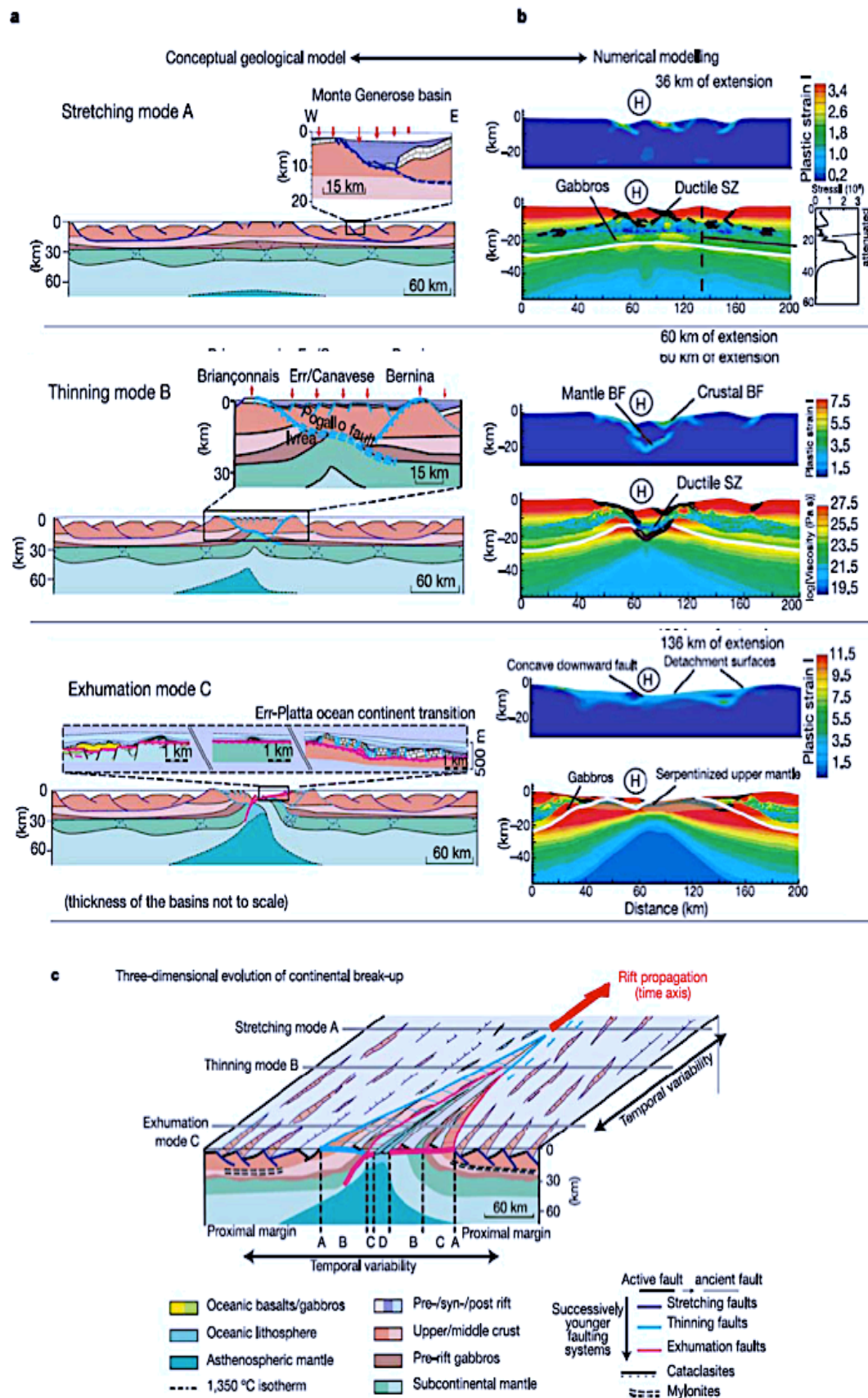
Weak plates result in a very broad zone of deformation with many short, narrow basins and border faults that do not penetrate very deeply. These studies suggest that the rheology and flexural rigidity of the upper part of the lithosphere control several primary features of rift structure and morphology, especially during the first few million years of rifting. They also suggest that the crust and upper mantle may retain considerable strength in extension (Petit & Ebinger, 2000).

Lithospheric flexure also plays an important role during the formation of large-magnitude normal faults. Large displacements on both high- and low-angle fault surfaces cause isostatic uplift of the footwall as extension proceeds, resulting in dome-shaped fault surfaces (Buck et al., 1988; Axen & Bartley, 1997; Lavier et al., 1999; Lavier & Manatschal, 2006). Lavier & Manatschal (2006) showed that listric fault surfaces whose



dip angle decreases with depth (i.e. concave upward faults) are unable to accommodate displacements large enough (>10 km) to unroof the deep crust. By contrast, low-angle normal faults whose dips increase with depth (i.e. concave downward faults) may unroof the deep crust efficiently and over short periods of time if faulting is accompanied by a thinning of the middle crust and by the formation of serpentinite in the lower crust and upper mantle (Kearey et al., 2010). The thinning and serpentinization weaken the crust and minimize the force required to bend the lithosphere upward during faulting, allowing large magnitudes of slip (Kearey et al., 2010)..

*Figure 2.23 Modes of extension leading to continental break-up and three-dimensional concept for the temporal and spatial evolution of rifting. a, Conceptual models for the different phases of extension based on observations from the Alpine and Iberia/Newfoundland margins. They are set apart by different styles of deformation. The stretching mode (A) is characterized by listric faulting and a differential subsidence of half-grabens exemplified by the Monte Generoso basin<sup>12</sup>. The thinning mode (B) is the least documented of the modes but it can be characterized by maximum thinning of the lithosphere and the presence of a major ductile shear zone (Pogallo shear zone<sup>21</sup>) accommodating differential motion (up to 10 km upward) between the upper crust and the lower crust/upper mantle. It is accompanied by not much uplift of the rift flanks and subsidence in the hanging wall. The exhumation mode (C) is well documented and distinguished by the exhumation of serpentinitized upper mantle from less than 10km depth along a downward-concave fault. b, Modelled evolution during lithospheric extension. The plastic strain (brittle deformation) and viscosity field are plotted for the different phases of the modelled evolution of the lithosphere. Note the similarity between the observed and modelled structures. The stress envelope is plotted for a given depth profile (dashed lines for 36 km of extension). For each viscosity field the Mohorovic boundary is shown by a white line. Schematic representation of the temporal and spatial evolution of the three consecutive phases of rifting leading to breakup and seafloor spreading. Lavier & Manatschal (2006) (next page).*





#### 4.2.3.2.4.2 Necking models

An important concept in the study of the kinematics of lithosphere extension is the level of necking, defined as the level which, in the absence of buoyancy forces, would not move vertically during extension. The depth of necking is defined as the depth in the lithosphere that remains horizontal during thinning if the effects of sediment and water loading are removed (Braun and Beaumont, 1989a; Weissel and Karner, 1989; Kooi et al., 1992). For the McKenzie uniform stretching model, the necking depth is implicitly 0 km. That is, all depths below the surface experience an upward advection during thinning (when sediment/water loading is removed).

Because of the changes in mass distribution related to extension, different necking levels result in different flexural responses (Fig. 224).

If the necking depth is in the strong mantle lithosphere, there is a regional flexural uplift, causing a pronounced rift shoulder. We would expect a deep necking depth where the lithosphere is cold and strong, with a strong subcrustal mantle, such as in the Transantarctic Mountains and Red Sea region (Cloetingh et al. 1995). However, if the necking depth is within the upper-midcrust, there is a downward regional flexure, promoting subsidence of the rift margins. This should occur where the lithosphere is weak, or where the crust is thickened, as in the Pannonian Basin of eastern Europe (Horvath and Cloetingh 1996). The level of necking therefore controls the amount of rift shoulder denudation, and consequently, the sediment delivery to the basin during the syn-rift phase (van Balen et al. 1995; Ter Voorde and Cloetingh 1996). There is theoretically an equilibrium depth of necking where there is no net flexural response. For a sediment-filled basin and initial crustal thickness of 33km within a 100km-thick lithosphere, this equilibrium depth is c. 10km. Odinsen et al. (2000) used a necking depth of 18km for their analysis of the northern North Sea, which therefore can be viewed as a relatively deep necking depth, promoting regional flexural uplift.

#### 4.2.3.2.5 Strain-induced weakening

Although differences in the effective elastic thickness and flexural strength of the lithosphere may explain variations in the length of border faults and the width of rift basins, they have been much less successful at explaining another major source of variability in rifts: *the degree of strain localization in faults and shear zones*. In some settings normal faulting is widely distributed across large areas where many faults accommodate a relatively small percentage of the total extension.

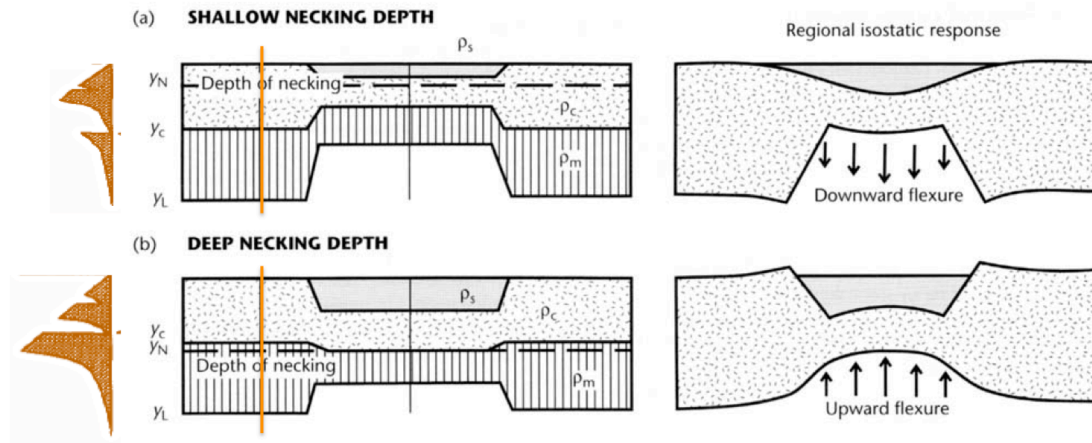


Figure 2.24 Regional isostatic response to different depths of necking, based on Braun and Beaumont (1989), Kooi et al. (1992), Cloetingh et al. (1997).  $y_c$ ,  $y_L$  and  $y_N$  are the initial thicknesses of the crust and lithosphere and the necking depth respectively;  $\rho_c$ ,  $\rho_m$ , and  $\rho_s$  are the densities of the crust, mantle, and sediments respectively. In (a) a shallow depth of necking results in a net downward acting force on the lithosphere, causing a regional downward flexure. In (b) the necking depth is deep, resulting in an upward acting force on the lithosphere that causes flexural uplift of the rift flanks. (modified after Allen and Allen, 2005).

However, in other areas or at different times, extension may be highly localized on relatively few faults that accommodate a large percentage of the total extension. Two approaches have been used to explain the causes of this variability. The first incorporates the effects of a strain-induced weakening of rocks that occurs during the formation of faults and shear zones. A second approach, which takes into account the *Rheological stratification of the lithosphere*, shows how vertical contrasts in the rheology of crustal layers affect the localization and delocalization of strain during extension.

In order for a normal fault to continue to slip as the crust is extended it must remain weaker than the surrounding rock. The deflection of the crust by faulting changes the stress field surrounding the fault. Assuming elastic behaviour, Forsyth (1992) showed that these changes depend on the dip of the fault, the amount of offset on the fault, and the inherent shear strength or cohesion of the faulted material. This author argued that the changes in stresses by normal faulting increase the yield strength of the layer and inhibit continued slip on the fault. For example, slip on high-angle faults create surface topography more efficiently than low-angle faults, so more work is required for large amounts of slip on the former than on the latter. These processes cause an old fault to be replaced with a new one, leading to a delocalization of strain. Buck (1993) showed that if the crust is not elastic but can be described with a finite yield stress (elasto-plastic), then the amount of slip on an individual fault for a given cohesion depends on the thickness of the elastic-plastic layer (Fig. 2.25). In this model the viscosity of the elastic-plastic layer

is adjusted so that it adheres to the Mohr–Coulomb criterion for brittle deformation. For a brittle layer thickness of  $>10$  km and a reasonably low value of cohesion a fault may slip only a short distance (a maximum of several kilometers) before a new one replaces it. If the brittle layer is very thin, then the offset magnitude can increase because the increase in yield strength resulting from changes in the stress field due to slip is small. Although layer thickness and its inherent shear strength play an important role in controlling fault patterns, a key process that causes strain localization and may lead to the formation of very large offset (tens of kilometers) faults is a reduction in the cohesion of the faulted material.

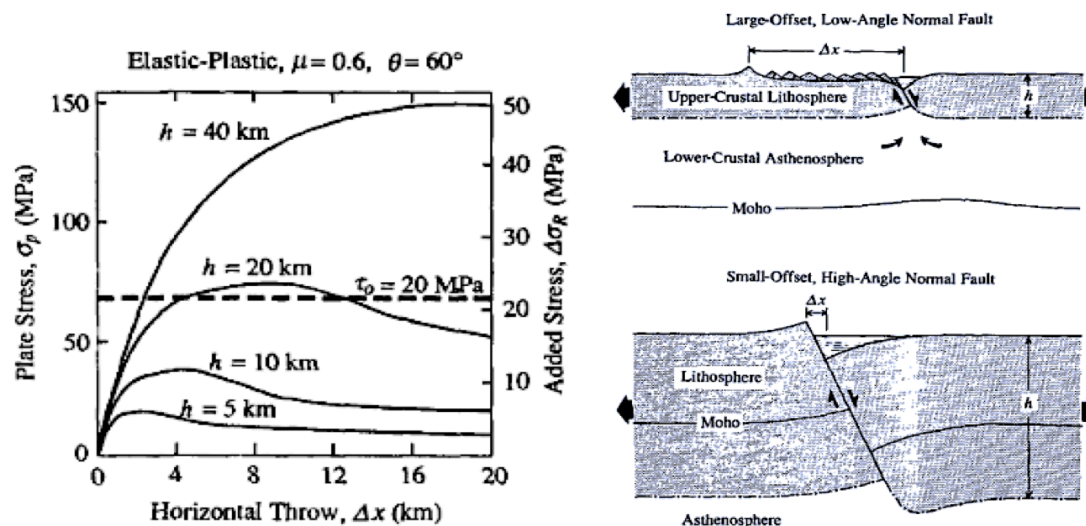


Figure 2.25 Results of model calculations showing that maximum value of  $\sigma_p$  scales with layer thickness. On right side is added regional stress needed to continue slip on fault ( $\sigma_p/k_\mu$ ) for  $\mu = 0.6$ . Dashed line shows added stress needed to break new fault in layer with  $\tau_0 = 20$  MPa. It illustrates the model result where lithospheric thickness,  $h$ , may control horizontal throw on a normal fault,  $\Delta x$ . Offset on a normal fault cutting a thin layer can be large enough to cause rotation of part of fault to a flat position, whereas for a fault cutting thick lithosphere,  $\Delta x$  is strictly limited. Top drawing is based on results in Buck (1988) in which sediment (indicated by parallel lines) fills in fault-bounded basin (modified after Buck, 1993).

During extension, cohesion can be reduced by a number of factors, including increased fluid pressure (Sibson, 1990), the formation of fault gouge, frictional heating (Montési & Zuber, 2002), mineral transformations (Bos & Spiers, 2002). Lavier et al. (2000) used simple two-layer models to show that the formation of a large-offset normal fault depends on two parameters:

- the thickness of the brittle layer and
- the rate at which the cohesion of the layer is reduced during faulting.

The models include an upper layer of uniform thickness overlying a ductile layer having very little viscosity. In the ductile layer the yield stress is strain-rate- and temperature-dependent following dislocation creep flow laws. In the upper layer brittle deformation is modeled using an elastic-plastic rheology. The results show that where the brittle layer is especially thick ( $>22$  km) extension always leads to multiple normal faults. In this case the width of the zone of faulting is equivalent to the thickness of the brittle layer. However, for small brittle layer thicknesses ( $<22$  km), the fault pattern depends on how fast cohesion is reduced during deformation. To obtain a single large offset fault, the rate of weakening must be high enough to overcome the resistance to continued slip on the fault that results from flexural bending. These studies provide some insight into how layer thickness and the loss of cohesion during faulting control the distribution of strain, its symmetry, and the formation of large-offset faults. However, at the scale of rifts, other processes also impact fault patterns. In ductile shear zones changes in mineral grain size may promote a switch from dislocation creep to grain-size-sensitive diffusion creep, which can reduce the yield strengths of layers in the crust and mantle. In addition, the rate at which a viscous material flows has an important effect on the overall strength of the material.

The faster it flows, the larger the stresses that are generated by the flow and the stronger the material becomes.

This latter process may counter the effects of cohesion loss during faulting and could result in a net strengthening of the lithosphere by increasing the depth of the brittle–ductile transition. At the scale of the lithosphere, it therefore becomes necessary to examine the interplay among the various weakening mechanisms in both brittle and ductile layers in order to reproduce deformation patterns in rifts. [Huisman & Beaumont \(2003, 2007\)](#) extended the work of [Lavie et al. \(2000\)](#) by investigating the effects of strain-induced weakening in both brittle (frictional plastic) and ductile (viscous) regimes on deformation patterns in rifts at the scale of the lithosphere and over time periods of millions of years. This study showed that strain softening in the crust and mantle can produce large-offset shear zones and controls the overall symmetry of the deformation. [Figure 2-26a](#) shows a simple three-layer lithosphere where brittle deformation is modeled by using a frictional-plastic rheology that, as in most physical experiments, is adjusted so that it adheres to the Mohr–Coulomb failure criterion. Ductile deformation is modeled using a thermally activated power law rheology. During each experiment, ambient conditions control whether the deformation is frictional- plastic (brittle) or viscous

(ductile). Viscous flow occurs when the state of stress falls below the frictional plastic yield point. Variations in the choice of crustal rheology also allow an investigation of cases where the crust is either coupled or decoupled to the mantle lithosphere.

Coupled models involve deformation that is totally within the frictional-plastic regime. Decoupled models involve a moderately weak viscous lower crust.

Strain-induced weakening is specified by linear changes in the effective angle of internal friction for frictional-plastic deformation and in the effective viscosity for viscous deformation. The deformation is seeded using a small plastic weak region.

A reference model (Fig. 2.26b,c) shows how a symmetric style of extensional deformation results when strain softening is absent. An early phase of deformation is controlled by two conjugate frictional-plastic shear zones (S1A/B) that are analogous to faults and two forced shear zones in the mantle (T1A/B). During a subsequent phase of deformation, second generation shear zones develop and strain in the mantle occurs as focused pure shear necking beneath the rift axis. Figures 2.26d,e show the results of another model where frictional-plastic (brittle) strain softening occurs and the resulting deformation is asymmetric. An initial stage is very similar to the early stages of the reference model, but at later times strain softening focuses deformation into one of the conjugate faults (S1B). The asymmetry is caused by a positive feedback between increasing strain and the strength reduction that results from a decreased angle of internal friction. Large displacements on the S2A and T1B shear zones cut out a portion of the lower crust (LC) at point C (Fig. 2.26, insert) and begin to exhume the lower plate. By 40 Ma, a symmetric necking of the lower lithosphere and continued motion on the asymmetric shear zones results in the vertical transport of point P until mantle lithosphere is exposed. The model shown in Fig.2.26f,g combines both frictional-plastic and viscous weakening mechanisms. The early evolution is similar to that shown in Fig. 2.26d, except that S1B continues into the ductile mantle. The two softening mechanisms combine to make deformation asymmetric at all levels of the lithosphere where displacements are mostly focused onto one shear zone. These models show how a softening of the dominant rheology in either frictional-plastic or viscous layers influences deformation patterns in rifts through a positive feedback between weakening and increased strain.

The effect of strain-dependent weakening on fault asymmetry is also highly sensitive to rift velocity. This sensitivity is illustrated in the models shown in Fig. 2.27.

The first model (Fig. 2.27a) is identical to that shown in Fig. 2.26d and e except that the velocity is decreased by a factor of five to  $0.6 \text{ mm a}^{-1}$ . Reducing the velocity has the

effect of maintaining the thickness of the frictional-plastic layer, which results in deformation that is more strongly controlled by the frictional regime than that shown in [Fig. 2.26e](#). The overall geometry matches a lithospheric-scale simple shear model (cf. [Fig. 2.15b](#)) in which the lower plate has been progressively uplifted and exhumed beneath a through-going ductile shear zone that remains the single major weakness during rifting. By contrast, a velocity that is increased to  $100 \text{ mm a}^{-1}$  ([Fig. 2.27b](#)) results in deformation that is more strongly controlled by viscous flow at the base of the frictional layer than that in the model involving slow velocities. However, at high velocities the strain softening does not develop in part because of the high viscous stresses that result from high strain rates. The model shows no strong preference for strain localization on one of the frictional fault zones. The deformation remains symmetrical as the ductile mantle undergoes narrow pure shear necking. These results suggest that increasing or decreasing rift velocities can either promote or inhibit the formation of large asymmetric structures because varying the rate changes the dominant rheology of the deforming layers.

These experiments illustrate the sensitivity of deformation patterns to strain-induced weakening mechanisms during faulting and ductile flow. The results suggest that extension is most likely to be asymmetric in models that include frictional-plastic fault zone weakening mechanisms, a relatively strong lower crust, and slow rifting velocities. However, before attempting to apply these results to specific natural settings, it is important to realize that the effects of strain-induced weakening can be suppressed by other mechanisms that affect the rheology of the lithosphere. For example, a comparison of two models, one incorporating a weak lower crust ([Fig. 2.27c](#)) and the other a strong lower crust ([Fig. 2.27d](#)), illustrates how a weak crust can diminish crustal asymmetry.



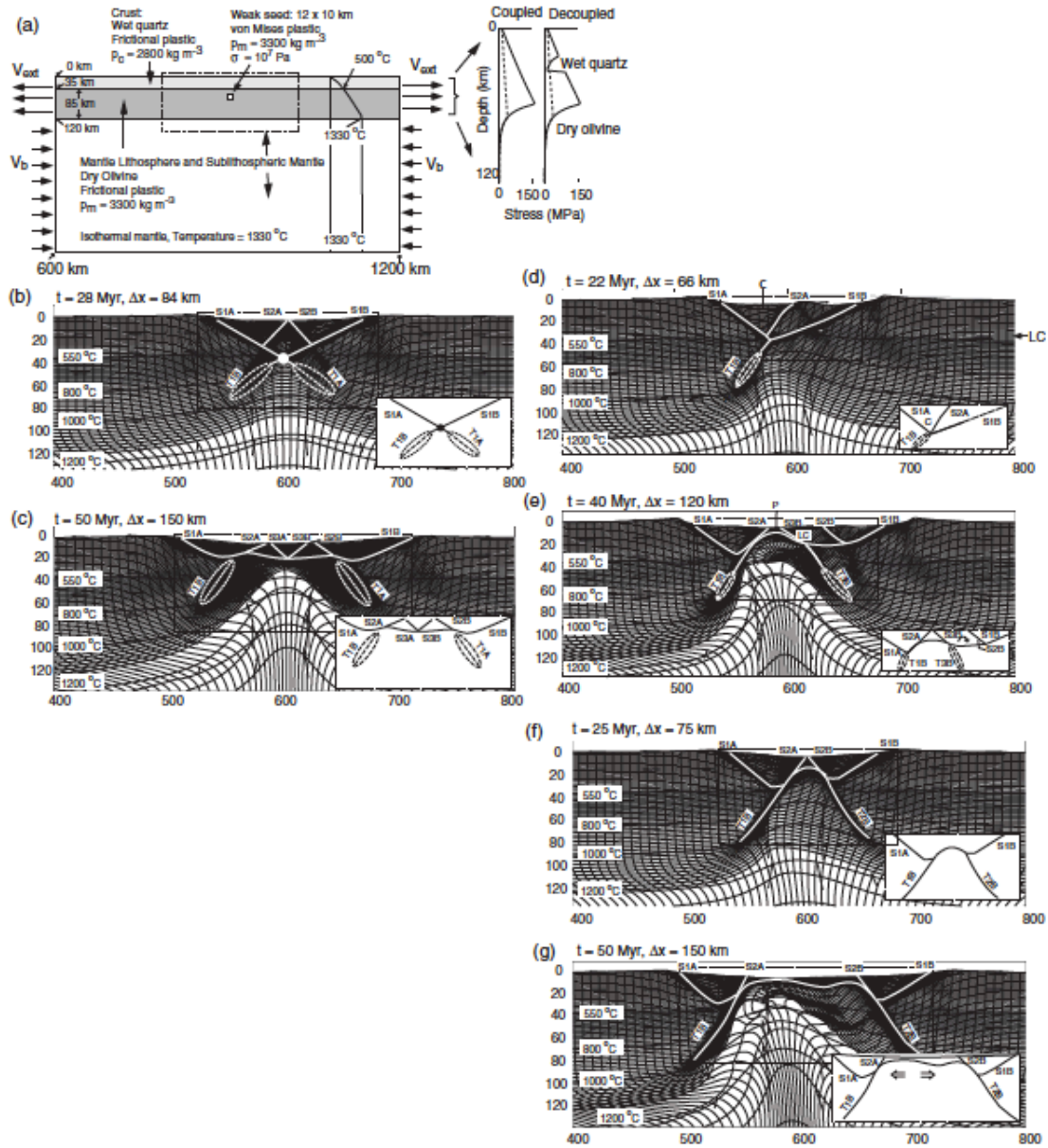


Figure 2.26 (a) Model geometry showing temperature structure of the crust, mantle lithosphere and sublithospheric mantle (modified from Huisman & Beaumont, 2003). Initial (solid lines) and strain softened (dashed lines) strength envelopes are shown for an imposed horizontal extensional velocity of  $V_{ext} = 3 \text{ mm yr}^{-1}$ , with  $V_b$  chosen to achieve mass balance. Decoupling between crust and mantle is modeled using a wet quartzite rheology for the lower crust. (b,c) Reference model of extension when strain softening is absent. Models of extension involving (d,e) frictional-plastic (brittle) strain softening and (f,g) both frictional-plastic and viscous weakening mechanisms. Models in (b–g) show a subdivision of the crust and mantle into an upper and lower crust, strong frictional upper mantle lithosphere, ductile lower lithosphere, and ductile sublithospheric mantle. Scaling of quartz viscosity makes the three upper layers frictional-plastic in all models shown.  $t$ , time elapsed in millions of years;  $\Delta x$ , amount of horizontal extension. Vertical and horizontal scales are in kilometers.  $V_{ext} = 3 \text{ mm yr}^{-1}$  for every model.

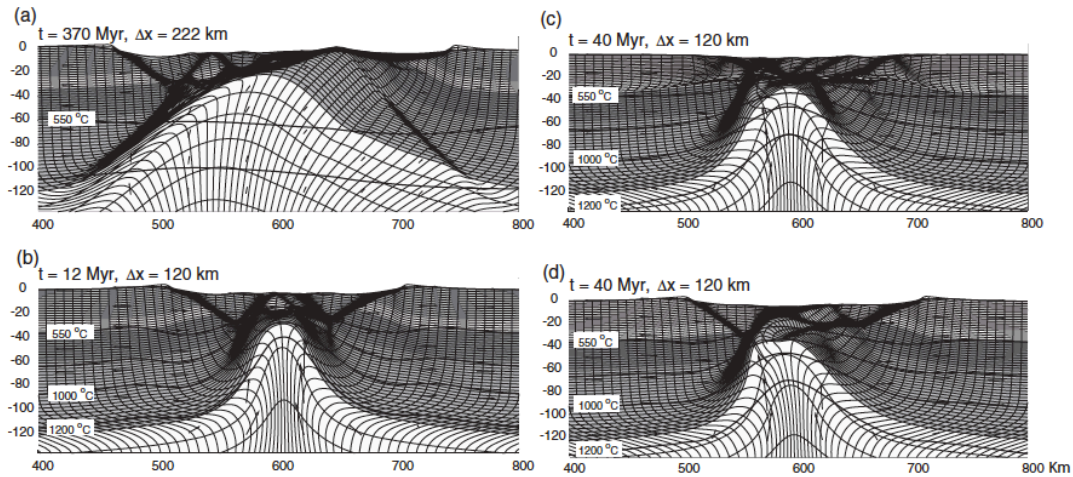


Figure 2.27 Models of extension involving frictional-plastic (brittle) strain softening at (a) low extensional velocities ( $V_{ext} = 0.6 \text{ mm a}^{-1}$ ) and (b) high extensional velocities ( $V_{ext} = 100 \text{ mm a}^{-1}$ ). Models also show rift sensitivity to (c) a weak and (d) a strong middle and lower crust at  $V_{ext} = 3 \text{ mm a}^{-1}$  (images provided by R. Huismans and modified from Huismans & Beaumont, 2007, with permission from the Geological Society of London).  $t$ , time elapsed in millions of years;  $\Delta x$  amount of horizontal extension. Vertical and horizontal scales are in kilometers.

This suppression occurs because conjugate frictional shears that develop during rifting sole out in the weak ductile lower crust where they propagate laterally beneath the rift flanks. As rifting progresses, viscous flow in a weak lower crust results in a nearly symmetric ductile necking of the lower lithosphere. These examples show that the degree of rift asymmetry depends not only on strain softening mechanisms and rifting velocities, but also on the strength of the lower crust.

An important contribution to the understanding of the extension deformation comes from the works of Weinberg et al. (2007), Rosenbaum et al., (2010), Regenauer-Lieb et al (2008), Regenauer-Lieb & Yuen (2006), and Karrech et al., (2011). They investigate the role of the elastic rheology during the extension of the lithosphere and in particular the effect of energy feedbacks on continental strength. They have found that regions defined initially with elastic cores, which become areas of the highest energy dissipation where feedback effects between brittle and ductile materials can operate most efficiently, leading to self-induced weakening (Fig. 2.28 and Fig. 2.29)

A recent piece of work in 2D was done by Brune et al. (2014). These authors were able to explain the genesis of hyper-extended margins as function of migration, which is promoted by crustal flow in combination with low stretching velocity. More recent studies on the influence of rheology and heterogeneities have been done by Sharples et al. (2015). In this work they have tested the role of the factors controlling the extensional



deformation. Symmetry, and fault spacing depend on rheology such as the yielding mechanism and strain softening, and physical aspects such as initial heterogeneities and the strength of the lower crust compared to the upper crust. With time-dependent numerical models they have investigated the influence of the yielding mechanism, lower crust strength, strain weakening, and initial heterogeneity. The results allow to infer that these elements have a major role on: the style of rifting, fault spacing, and integrated strength in the upper crust.

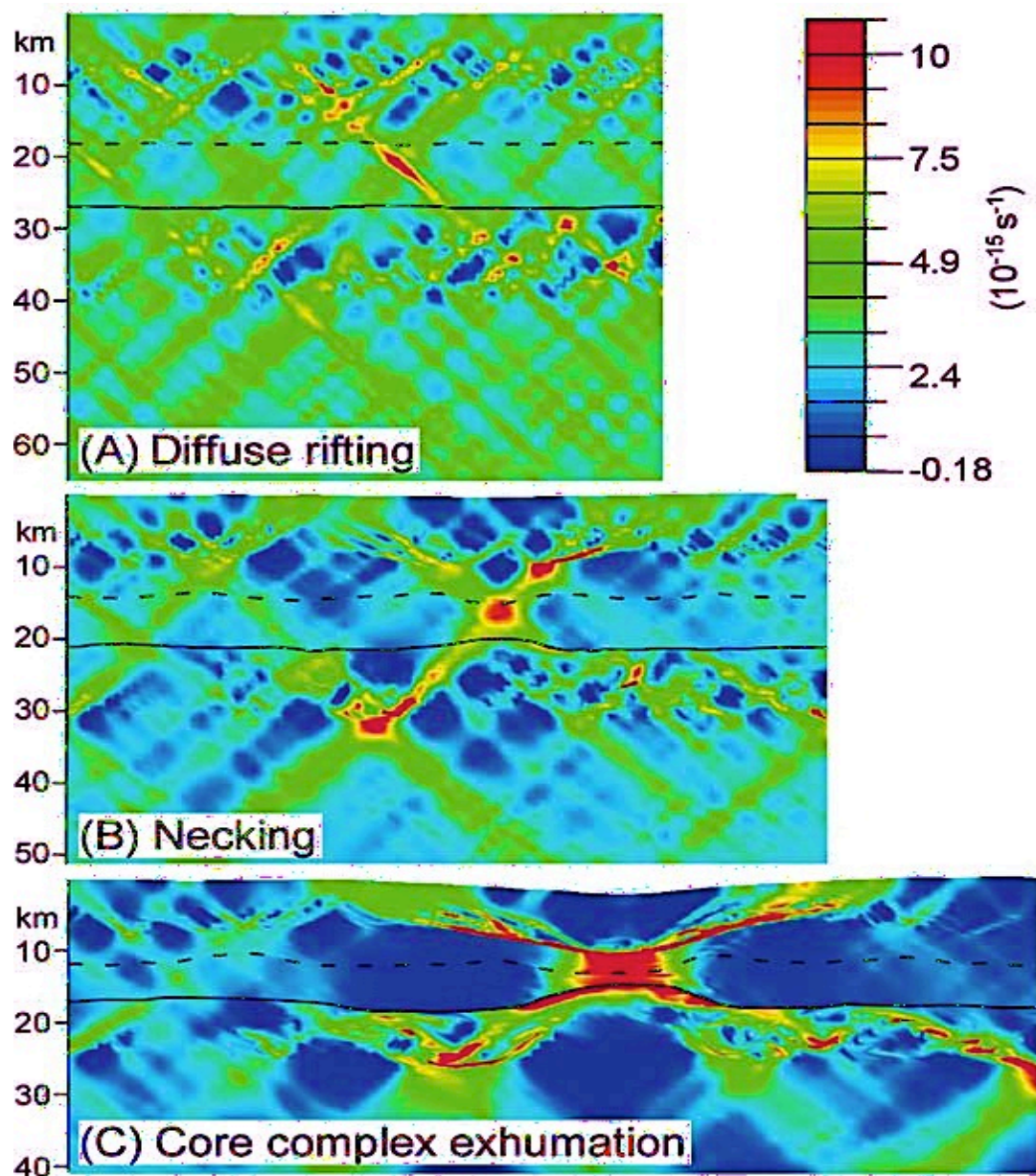
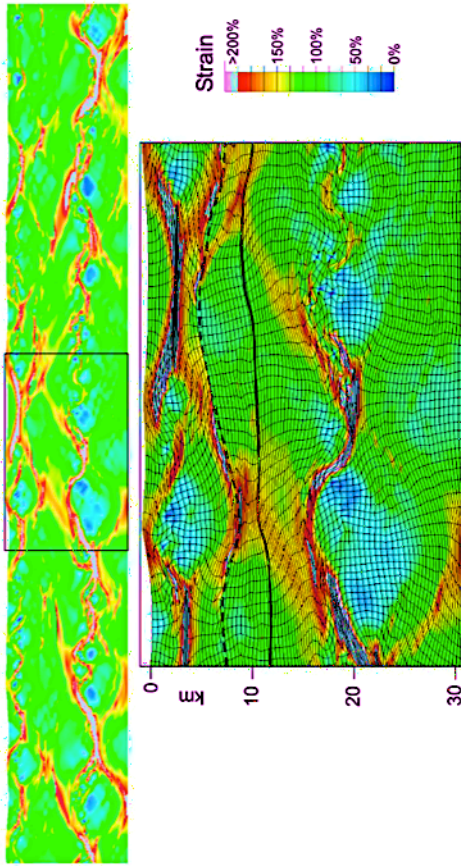


Figure 2.28 Modelled evolution of mantle core complex during the breakup of nonvolcanic continental margins. Crust-mantle boundary (Moho) is indicated by continuous black line. Dashed line separates

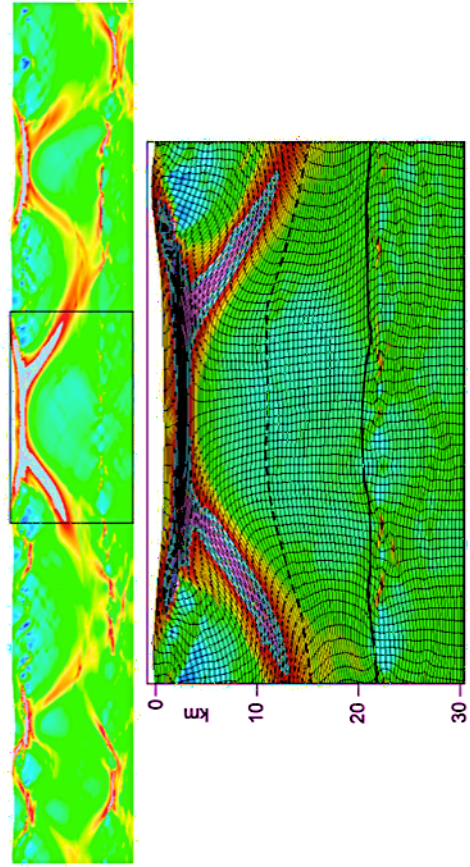
quartz-dominated upper-middle crust and feldspar-dominated lower crust. Initial crustal thickness is 30 km and surface heat flow is 50 mW/m<sup>2</sup>. Diagrams show strain rate for (A) diffuse rifting ( $\beta = 1.1$ ), (B) crustal necking ( $\beta = 1.4$ ), and (C) core complex exhumation ( $\beta = 1.8$ ) stages. Low-angle shear zones are initiated during necking stage both in crust and upper mantle. No vertical exaggeration (after Weinberg et al. 2007).

Figure 2.29 (Next Page) Strain fields of four selected models at the final stage of deformation after 13.7 Ma. Each panel shows whole model and enlarged section. Dashed lines indicate boundary between the quartz and feldspar layers, and continuous lines indicate Moho. (a) Model 1 (crustal thickness 30 km; surface heat flow 50 mW m<sup>-2</sup> ; initial Moho temperature 321°C) showing relatively well connected shear zones from different lithospheric levels forming crosscutting translithospheric master shear zone dipping  $\sim 30^\circ$  (from upper right to lower left in the inset). (b) Model 4 (crustal thickness 60 km; surface heat flow 50 mW m<sup>-2</sup> ; initial Moho temperature 540°C) showing doming of the middle lower crust. Here, Moho strain localization is inhibited, and upper crustal shear zones detach in the contact between the quartz and feldspar layers. The half wavelength of the crustal dome is  $\sim 50$  km, and amplitude is  $\sim 5$  km (as measured at the boundary between the quartz and the feldspar layers). In contrast, Moho topography is subdued. (c) Model 6 (crustal thickness 40 km; surface heat flow 60 mW m<sup>-2</sup> ; initial Moho temperature 431°C) showing a well- developed mantle dome and minor short-wavelength domes in the crust. The half wavelength of the mantle dome is  $\sim 45$  km, and its amplitude is  $\sim 8$  km. (d) Model 15 (crustal thickness 50 km; surface heat flow 80 mW m<sup>-2</sup> ; initial Moho temperature 575°C) showing strong crustal deformation and crosscutting shear zones linking crustal and Moho detachments through a weakly localized shear band in feldspar layer. (modified after Rosenbaum et al. 2010).

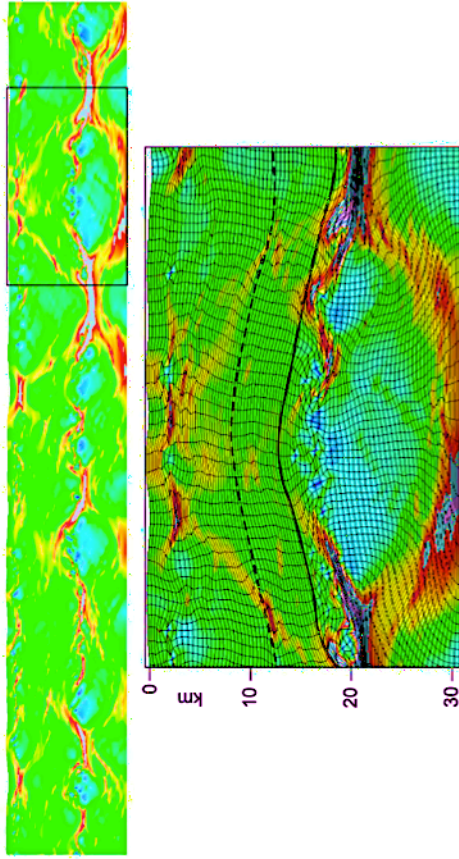
(a) Model 1



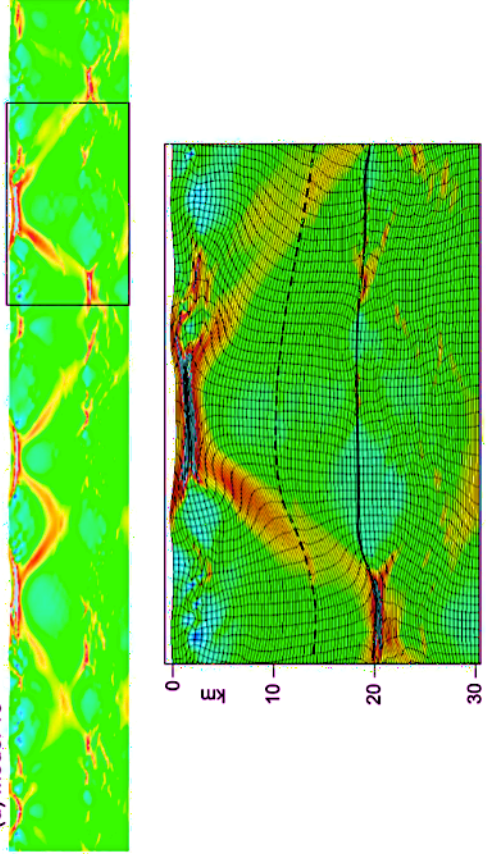
(b) Model 4



(c) Model 6



(d) Model 15





Models with an anisotropic yielding mechanism result in more realistic lithospheric strength profiles, slip plane angle distributions, and fault interaction than models with an isotropic yielding mechanism. Thanks to numerical models they have been able to understand that the heterogeneity type and yielding mechanisms have the largest effect on the resulting symmetry of deformation, whereas the amount of strain weakening has the greatest influence on asymmetry.

#### 4.2.3.2.6 Rheological stratification of the lithosphere

In most quantitative models of continental rifting, the lithosphere is assumed to consist of multiple layers that are characterized by different rheologies. This vertical stratification agrees well with the results from both geophysical investigations of continental lithosphere and with the results of laboratory experiments that reveal the different behaviours of crust and mantle rocks over a range of physical conditions.

In the upper part of the lithosphere strain is accommodated by faulting when stress exceeds the frictional resistance to motion on fault planes. In the ductile layers, strain is described using temperature-dependent power law rheologies that relate stress and strain-rate during flow. Using these relationships, experimentally derived friction and flow laws for crustal and mantle rocks can be incorporated into models of rifting. This approach has allowed investigators to study the effects of a rheological stratification of the lithosphere on strain localization and delocalization processes during extension, including the development of large-offset normal faults. The sensitivity of strain patterns to the choice of crustal rheology for different initial conditions are illustrated below using three different physical models of continental rifting. [Behn et al., \(2002\)](#) explored how the choice of crustal rheology affects the distribution of strain within the lithosphere during extension using a simple two-layer model composed of an upper crustal layer and a lower mantle layer ([Fig. 2.30a](#)). These authors incorporated a strain-rate softening rheology to model brittle behaviour and the development of fault-like shear zones. Ductile deformation was modeled using temperature dependent flow laws that describe dislocation creep in the crust and mantle. Variations in the strength (effective viscosity) of the crust at any given temperature and strain rate are defined by material parameters that are derived from rock physics experiments. The use of several flow laws for rocks with different mineralogies and water contents allowed the authors to classify the rheologies as either weak, intermediate, or strong. Variations in crustal thickness and thermal structure were added to a series of models to examine the interplay among these

parameters and the different rheologies.

The results show that when crustal thickness is small, so that no ductile layer develops in the lower crust, deformation occurs mostly in the mantle and the width of the rift is controlled primarily by the vertical geothermal gradient (Fig. 2.30b,f). By contrast, when the crustal thickness is large the stress accumulation in the upper crust becomes much greater than the stress accumulation in the upper mantle (Fig. 2.30c,d). In these cases the deformation becomes crust-dominated and the width of the rift is a function of both crustal rheology and the vertical geothermal gradient (Fig. 2.30e,f).

Figure 2.30e illustrates the effects of the strong, intermediate and weak crustal rheologies on rift morphology (half-width). The models predict the same rift half-width for mantle-dominated deformation. However, the transition between mantle- and crust-dominated deformation begins at a slightly larger crustal thickness for the strong rheology than for the intermediate or weak rheologies.

In addition, the strong crustal rheology results in a rift half-width for the crust-dominated regime that is  $\sim 1.5$  times greater than the value predicted by the intermediate rheology and  $\sim 4$  times greater than that predicted by the weak rheology. Figure 2.30f summarizes the combined effects of crustal thickness, crustal rheology, and a vertical geothermal gradient on rift half-width. These results illustrate that the evolution of strain patterns during lithospheric stretching is highly sensitive to the choice of crustal rheology, especially in situations where the crust is relatively thick.

A similar sensitivity to crustal rheology was observed by Wijns et al. (2005). These authors used a simple two layer crustal model where a plastic yield law controlled brittle behaviour below a certain temperature and the choice of temperature gradient controlled the transition from a brittle upper crust into a ductile lower crust. This formulation and a 20-km-thick upper crust lying above a 40-km-thick lower crust allowed them to investigate how a mechanically stratified crust influenced fault spacing and the distribution of strain during extension. They found that the ratio of the integrated strength of the upper and lower crust governs the degree of strain localization on fault zones. When this ratio is small, such that the lower crust is relatively strong, extension results in widely distributed, densely spaced faults with a limited amount of slip on each fault. By contrast, a large strength ratio between the upper and lower crust, such that the lower crust is very weak, causes extension to localize onto relatively few faults that accommodate large displacements. In this latter case, the large-offset faults dissect the upper crust and exhume the lower crust, leading to the formation of metamorphic core

complexes. [Wijns et al. \(2005\)](#) also concluded that secondary factors, such as fault zone weakening and the relative thicknesses of the upper and lower crust, determine the exact value of the critical ratio that controls the transition between localized and delocalized extension.

The results of [Wijns et al. \(2005\)](#), like those obtained by [Behn et al. \(2002\)](#), suggest that a weak lower crust promotes the localization of strain into narrow zones composed of relatively few faults. This localizing behaviour reflects the ability of a weak lower crust to flow and transfer stress into the upper crust, which may control the number of fault zones that are allowed to develop.

This interpretation is consistent with field studies of deformation and rheology contrasts in ancient lower crust exposed in metamorphic core complexes (e.g. [Klepeis et al. 2007](#)). It is also consistent with the results of [Montési & Zuber \(2003\)](#), who showed that for a brittle layer with strain localizing properties overlying a viscous layer, the viscosity of the ductile layer controls fault spacing. In addition, a weak lower crust allows fault blocks in the upper crust to rotate, which can facilitate the dissection and dismemberment of the upper crust by faulting.

A third numerical model of rifting illustrates how the interplay among strain-induced weakening, layer thickness, and rheological contrasts can influence deformation patterns in a four-layer model of the lithosphere. [Nagel & Buck \(2004\)](#) constructed a model that consisted of a 12-km-thick brittle upper crust, a relatively strong 10-km-thick lower crust, a thin (3 km) weak mid-crustal layer, and a 45-km-thick upper mantle ([Fig. 2.31a](#)). The model incorporates temperature-dependent power law rheologies that determine viscous behaviour in the crust and mantle. The mantle and upper and lower crust also follow the Mohr–Coulomb failure criterion and cohesion loss during faulting is included.

The model also incorporates a predefined bell-shaped thermal perturbation at its center that serves to localize deformation at the beginning of extension. The horizontal thermal gradient created by this perturbation, and the predetermined vertical stratification, control the mechanical behaviour of the lithosphere during rifting.

As extension begins, the upper mantle and lower crust undergo localized necking in the hot, weak center of the rift. Deformation in the upper crust begins as a single graben forms above the area of necking in the lower crust and mantle and subsequently evolves into an array of parallel inward dipping normal faults.

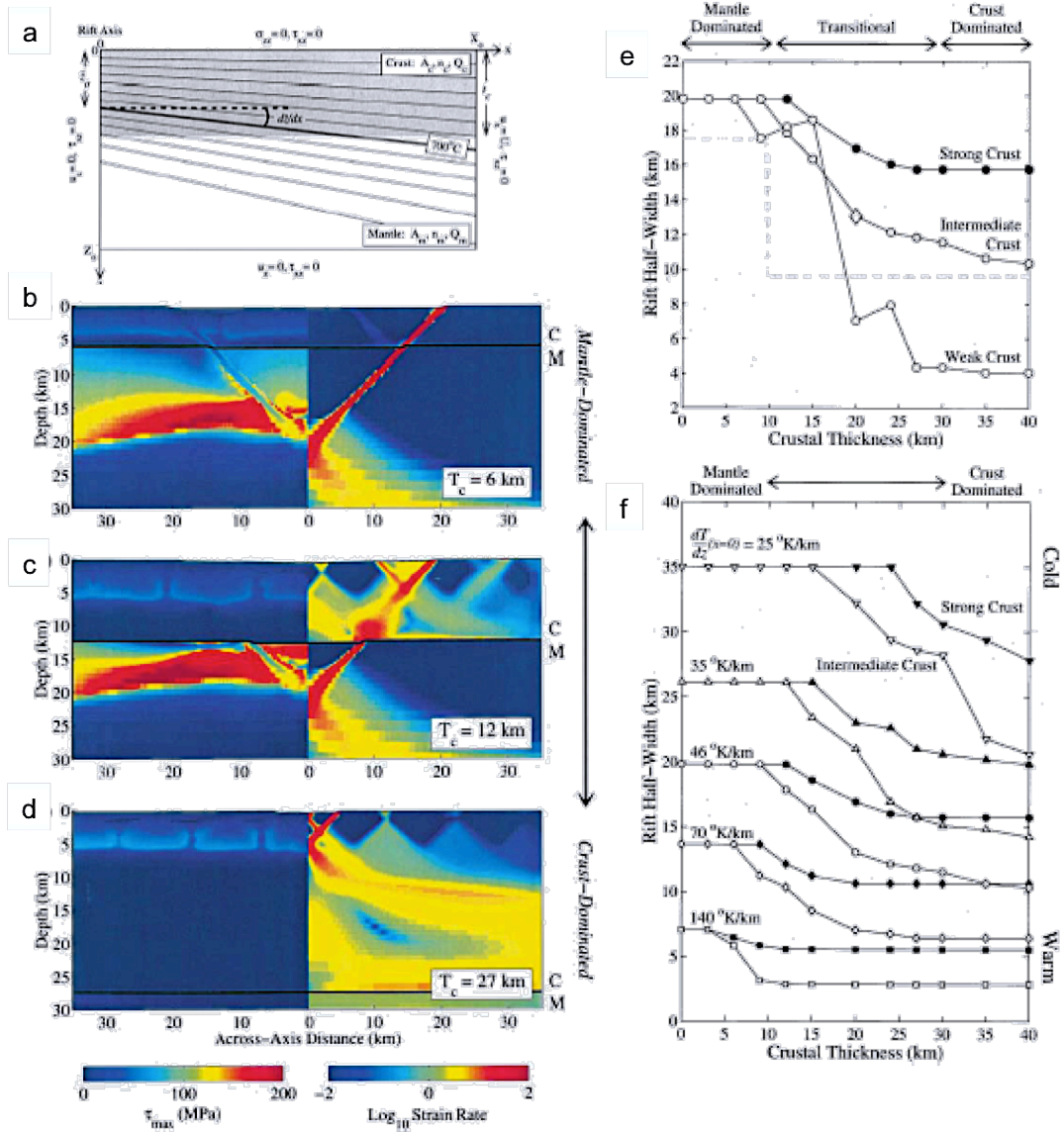


Figure 2.30 (a) Model setup for numerical simulations of lithospheric stretching. The transition from mantle- to crust dominate deformation is illustrated by (b), (c), and (d), which show the deformation grid after 1% total strain for a crustal thickness ( $T_c$ ) of 6, 12 and 27 km, respectively. Colour scale indicates the magnitude of shear stress on left and normalized strain-rate on right. C and M mark the base of the crust and top of the mantle, respectively. (e) Effect of crustal thickness on predicted rift half-width. (f) Effect of vertical geothermal gradient on predicted rift half-width (modified from Behn et al., 2002). Each point in (e) and (f) represents an experiment. Black, strong; gray, intermediate; and white, weak rheology (modified after Behn et al., 2002).

The faults root down into the weak mid-crustal layer where distributed strain in the upper crust is transferred into the necking area in the strong lower parts of the model (Fig 2.31b,c). An evolution of this work was performed by Gueydan et al. (2008) (Fig. 2-32). In this work the authors have investigated the role of the uppermost mantle strength in the pattern of lithosphere rifting by means of thermo-mechanical finite-

element models. In the lithosphere, the mantle/crust strength ratio ( $SM/SC$ ) that

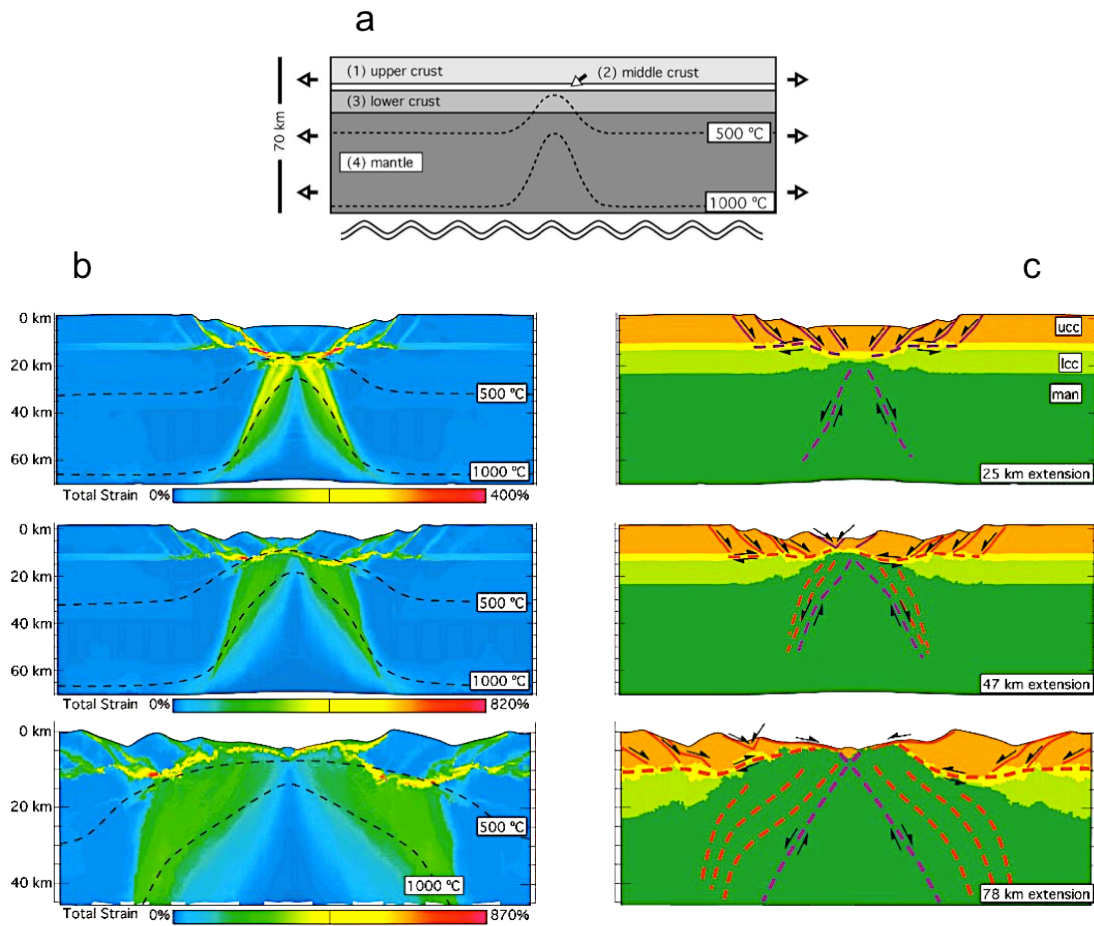


Figure 2.31 Model of symmetric rifting. (a) Model setup. (b) Total strain and (c) distribution of upper, middle and lower crust and mantle after 25, 47 and 78 km of extension. Solid black lines, active zones of deformation; red dashed lines, inactive zones; thin black lines, brittle faults; dashed black lines, ductile shear zones. (modified after Nagel & Buck, 2004).

decreases with increasing Moho temperature  $T_M$  allows two strength regimes to be defined: mantle dominated ( $SMNSC$ ) and crust dominated ( $SMbSC$ ). The transition between the two regimes corresponds to the disappearance of a high strength uppermost mantle for  $T_M$  700 °C. 2D numerical simulations for different values of  $SM/SC$  show how the uppermost mantle strength controls the style of continental rifting (Fig. 2.32). A high strength mantle leads to strain localisation at lithosphere scale, with two main patterns of narrow rifting: “coupled crust–mantle” at the lowest  $T_M$  values and “deep crustal décollement” for increasing  $T_M$  values, typical of some continental rifts and non-volcanic passive margins. The absence of a high strength mantle leads to distributed deformations and wide rifting in the upper crust (Fig. 2.32).



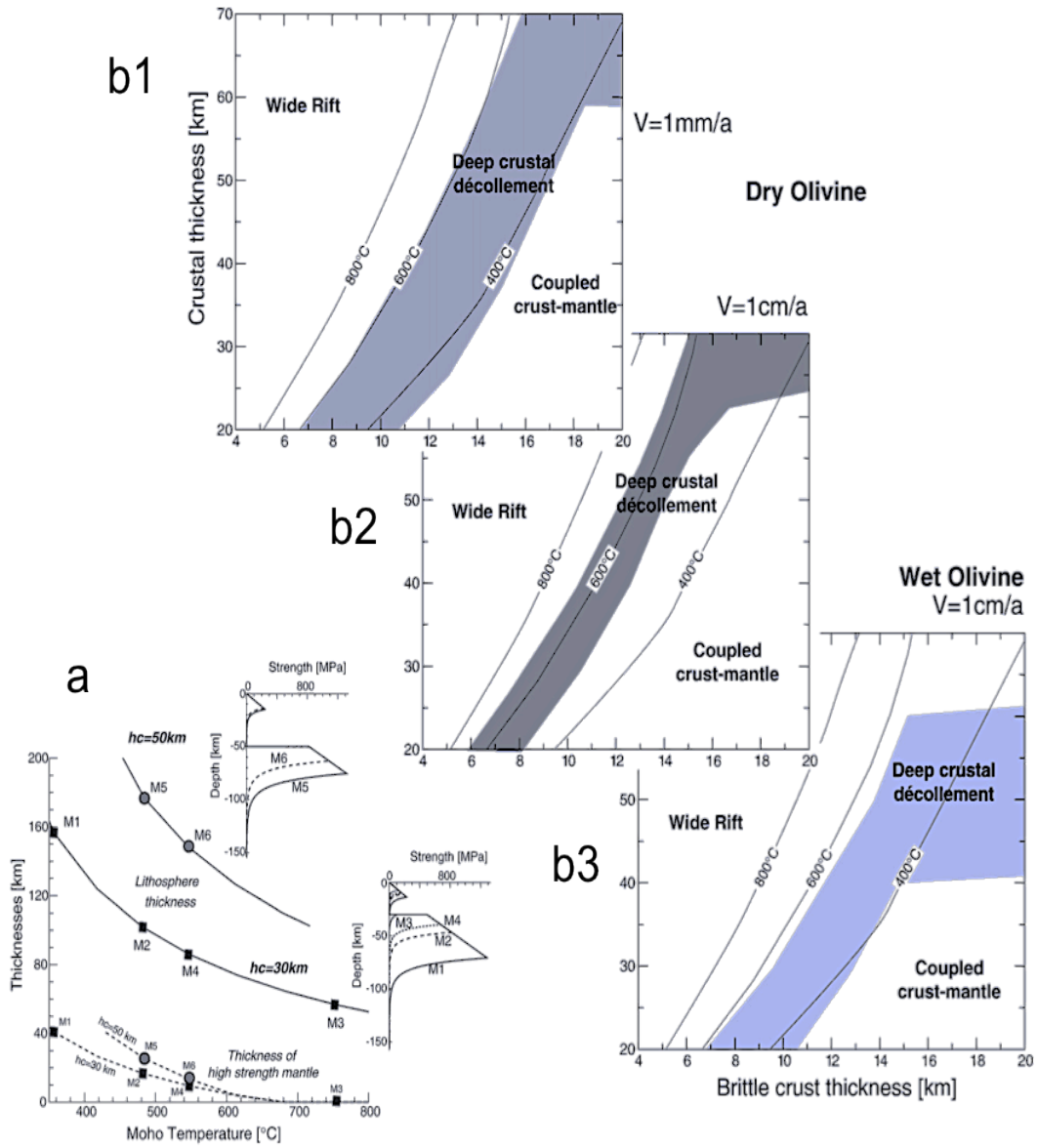


Figure 2.32 (a) 1D analytical solution giving the lithosphere thickness  $h_L$  and the high strength uppermost mantle thickness as a function of the Moho temperature  $T_M$ . Four strength profiles (Models 1 to 4) are used for a crustal thickness  $h_C = 30$  km. Two strength profiles (Models 5 and 6) are used for a crustal thickness  $h_C = 50$  km. (b) Patterns of continental rifting as a function of brittle crust and whole crust thicknesses for dry olivine at  $V = 1$  cm/a (top) and 1 mm/a (middle) and for wet olivine at  $V = 1$  cm/a (bottom). The patterns boundaries are plotted using the strength ratio value  $SM/SC$ . (after Gueydan et al., 2008)

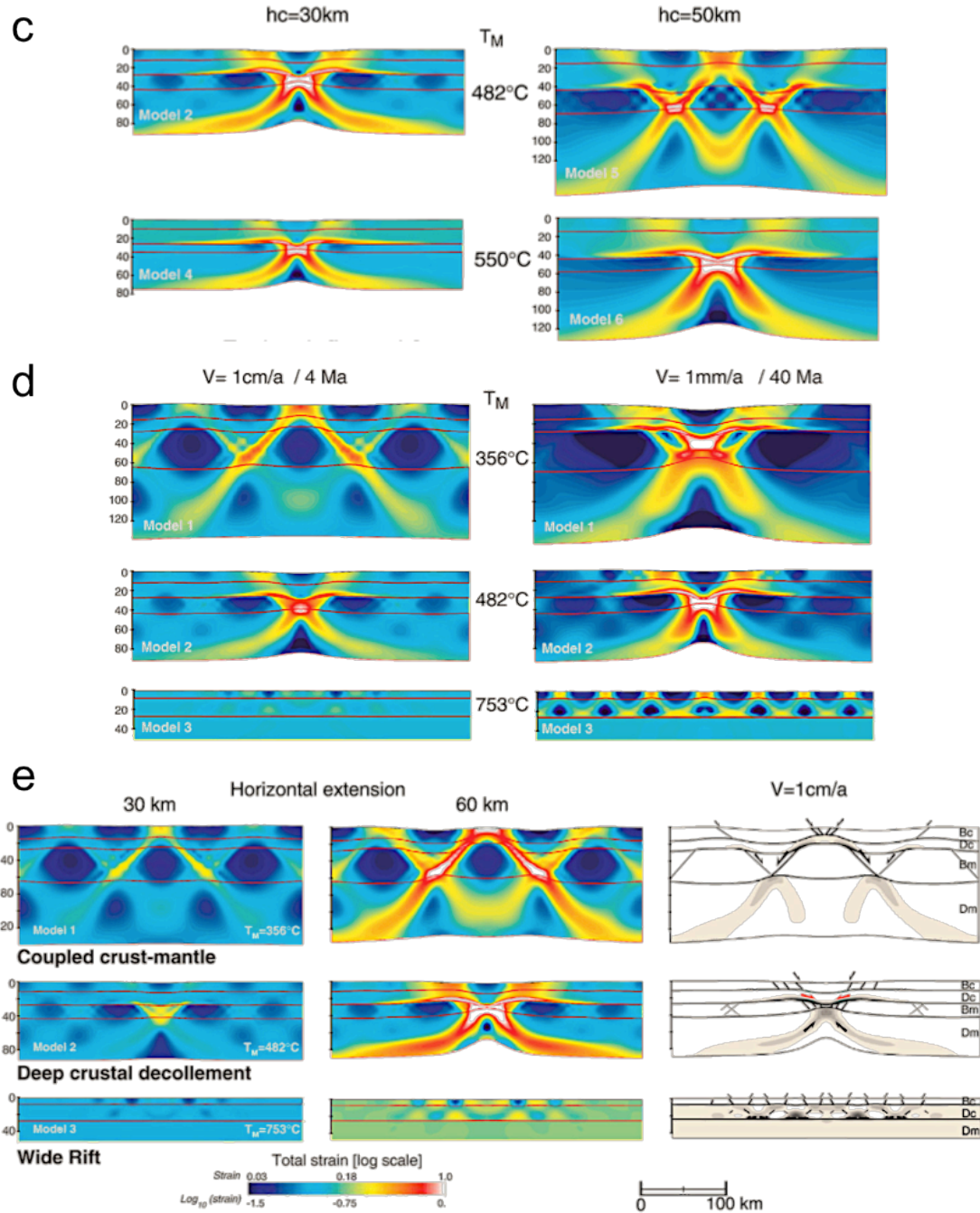


Figure 2.32 Continued. (c) Role of the crustal thickness. Patterns of total strain after 45 km of boundary extensional displacement for  $h_c = 30 \text{ km}$  (left) and  $h_c = 50 \text{ km}$  (right) for Moho temperatures  $T_M = 482^\circ\text{C}$  (top) and  $T_M = 550^\circ\text{C}$  (bottom), and with  $V = 1 \text{ cm/a}$ . Model as in Figs.1-29a. (d) Role of the applied boundary velocity. Patterns of total strain after 40 km of boundary extensional displacement for  $V = 1 \text{ cm yr}^{-1}$  (left) and  $V = 1 \text{ mm yr}^{-1}$  (right) for Models 1 to 3. Model as in Figs.2-29 a. (e) Role of the initial Moho temperature  $T_M$ . Patterns of total strain in Models 1 to 3 for an initial crustal thickness of 30 km, after 30 km and 60 km of boundary extensional displacement, with  $V = 1 \text{ cm yr}^{-1}$ , and line drawings of corresponding lithosphere scale structures. Model as in Figs.2-29a. (after Gueydan et al., 2008)

#### 4.2.3.2.7 Magma-assisted rifting

Most quantitative treatments of continental rifting focus on the effects of variations in lithospheric conditions. This emphasis reflects both the success of these models at explaining many aspects of rifting and the relative ease at which geoscientists can constrain the physical properties of the lithosphere compared to those of the asthenosphere. Nevertheless, it is evident that interactions between the asthenosphere and the lithosphere form crucial components of rift systems (Ebinger, 2005). One of the most important aspects of these interactions involves magmatism, which weakens the lithosphere and causes strain localization.

Among its possible effects, mafic magmatism may allow rifting to initiate in regions of relatively cold or thick continental lithosphere. In addition to its weakening effects, the availability of a significant source of basaltic magma influences the thickness, temperature, density, and composition of the lithosphere.

The presence of hot, partially molten material beneath a rift valley produces density contrasts that result in thermal buoyancy forces. As the two sides of the rift separate, magma also may accrete to the base of the crust where it increases in density as it cools and may lead to local crustal thickening. These processes can create bending forces within the lithosphere as the plate responds to the changing load, and affect the manner in which strain is accommodated during rifting. The changes may be recorded in patterns of uplift and subsidence across rifts and rifted margins. Buck (2004) developed a simple two-dimensional thermal model to illustrate how rifting and magma intrusion can weaken the lithosphere and influence subsidence and uplift patterns. The emplacement of large quantities of basalt in a rift can accommodate extension without crustal thinning. This process has been observed in the mature rift segments of northern Ethiopia where strain accommodation by faulting has been greatly reduced as magmatism increased (Wolfenden et al., 2005). If enough material intrudes, the crustal thickening that can result from magmatism can lessen the amount of subsidence in the rift and may even lead to regional uplift. This effect is illustrated in Fig. 2.33, which shows the average isostatic elevation through time for magma-assisted rifting compared to a typical subsidence curve for lithospheric stretching due to thermal relaxation (McKenzie, 1978). The uplift or subsidence result from changes in density related to the combined effects of crustal thinning, basalt intrusion and temperature differences integrated over a 100 km wide rift to a depth of 150 km. Buck (2004) suggested that this process might explain why some continental margins, such as those off the east coast of Canada (Royden & Keen, 1980),

show less initial tectonic subsidence related to crustal thinning compared to the long-term (tens of millions of years) subsidence induced by cooling. Two other problems of rift evolution that also might be resolved by incorporating the effects of magmatism and/or flow of the asthenosphere include the extra subsidence observed at some rifted margins and the lack of magma that characterize nonvolcanic margins (Buck, 2004).

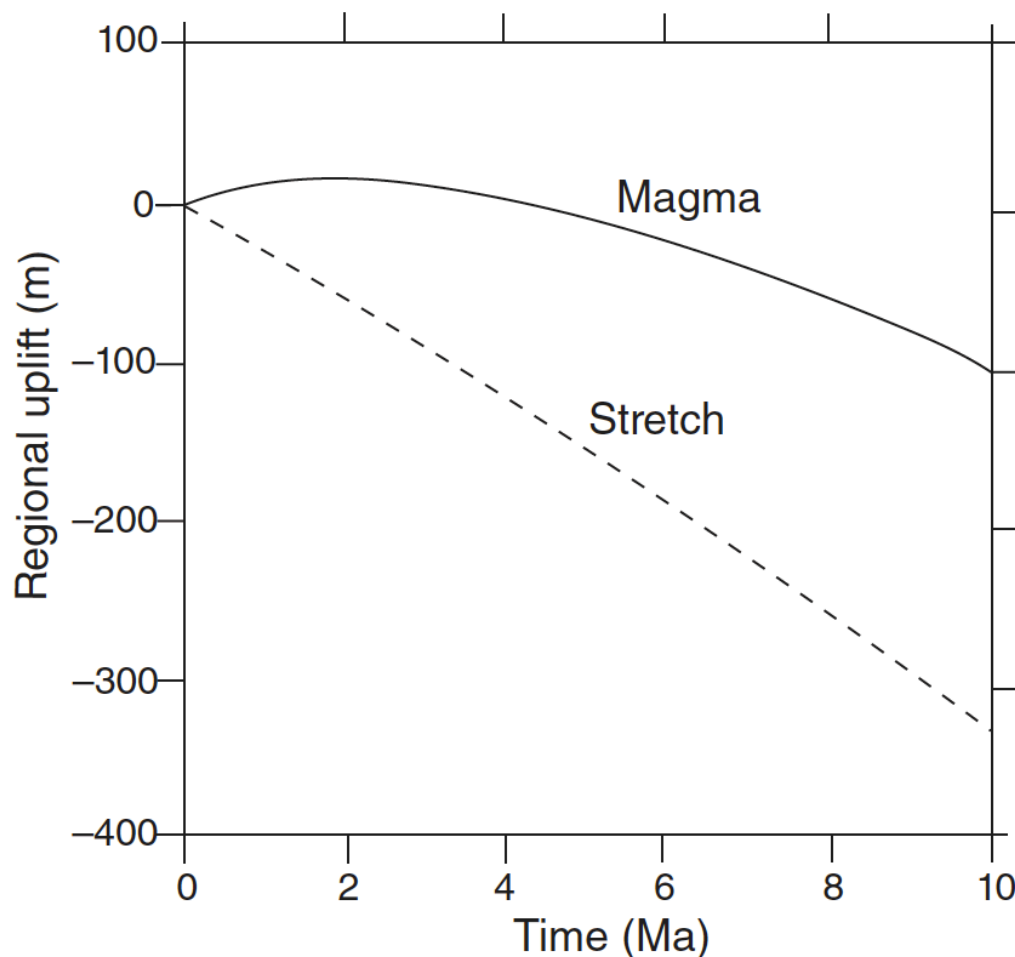


Figure 2.33 Comparison of the predicted average regional isostatic elevation changes for magma-assisted rifting (solid line) and pure shear necking (dashed line) (from Buck, 2004).

## 5. GEOLOGICAL AND GEOPHYSICAL OBSERVABLE (PART II). COMPLEX RIFTING HISTORIES. RIFTING HISTORIES AND CONCEPTUAL MODELS.

The models examined previously have given a great boost in the comprehension of the dynamics of the rifting process, connecting the initial conditions - such as variation of initial rheological properties, lithosphere layering and geothermal gradient (e.g. [Gueydan et al. 2008](#); [Buck 1991](#); [Buck, 2004](#); [Rosenbaum et al. 2010](#)) - and the boundary conditions at the onset of rifting - such as the stretching velocity, strain rate or initial force (e.g. [England, 1983](#); [van wijk and Cloetingh, 2002](#); [Buck, 1991](#); [van Wjik et al. 2001](#)) - with *the final deformation phase of rift basins and margins, subsidence patterns and magma occurrence*.

All these models are based on the idea first proposed by [McKenzie \(1978\)](#), that rifting and lithospheric stretching should be modelled using a *single rifting phase* followed by the thermal subsidence period ([Fig. 2.34](#)).

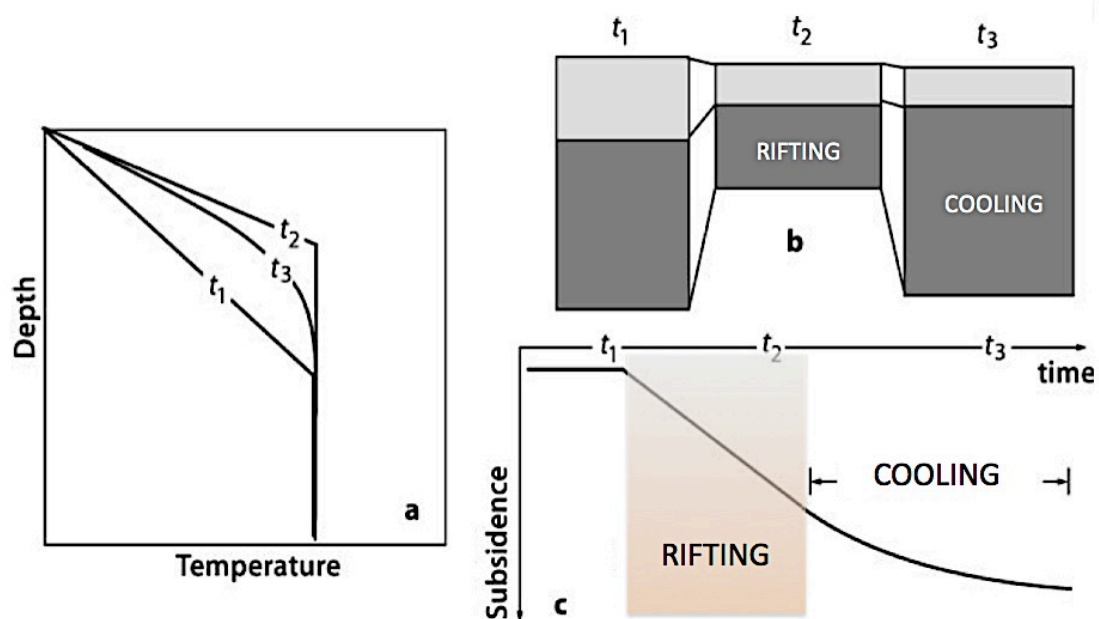


Figure 2.34 Subsidence of sedimentary basins according to the Uniform Stretching Model. (a) Geotherms at three different times: prior to onset of extension ( $t_1$ ), at the end of a rapid stretching phase ( $t_2$ ) and during subsequent thermal equilibration of the lithosphere ( $t_3$ ). (b) Thickness of the crust (light shaded region) and that of the mantle part of the lithosphere (dark shaded region) at these three different time steps, (c) Schematic subsidence curve corresponding to the cartoons in a and b with the rifting phase highlighted in transparent orange. (Modified from McKenzie, 1978).

However, a second group of geological and geophysical observations tell us something different about the modality in which the rifting process evolves in time and space.

Therefore, it is of fundamental importance to take into account these observations when we model the rifting process, in order to fully capture the first order causes leading to the differences found in the rift basins and passive margins.

Outcrop analysis, seismic data, well data, models of subsidence and recovering of strain-rate analysis reveal that lithospheric stretching is not a monophasic process. The evolution of most basins on Earth includes a more *complex rifting histories*. These rifting histories can be described in terms of tectonic activity alternating with quiescence, time-dependent subsidence, and possible rifting migration and melting episodes. Therefore the evidence points to a rifting process that develops with a progression of rifting phases intermitted by tectonic inactivity (cooling stages) of different duration. I identify this type of history with an **R-C-R** (Rifting-Cooling-Rifting) *conceptual model* to the sequence of phases (which is a synthesis of  $R_1 + C_1 + R_2 \dots R_n + C_n$  ideal progression of stretching and cooling events in time). Other rifting events evolve with a sequence of rifting phases in which it is possible to recognise an abrupt change in subsidence rate where cooling is absent. I use to **RR** (Rifting-Rifting) *conceptual model* ( $R_1 + R_2 \dots R_n$ ) to classify this type of rifting history.

One documented case of **R-C-R** is represented by the mid-Norwegian margin ([Gabrielsen et al., 1999](#); [Reemst & Cloetingh, 2000](#)) shown in [Fig. 2.35](#), where a long-lasting rifting history includes several rifting episodes (290-235 Ma, 170-95 Ma, 75-57 Ma), between the first recognized rifting phase and break-up, with oceanisation by ~ 55 Ma. Here, it is possible to see from the Bouguer gravity anomaly map ([Fig. 2.35 top](#)) that the margin opened with a fan-shaped deformation along the rift axis with migration in the depocenters of the basins in space. The subsidence curves ([Fig. 2.35 top](#)) indicates that the deformation is characterized by episodes of rifting intermitted by quiescence periods, which clearly indicates a *polyphase rifting history*, as well as jumps in time in the locus of the extension. Therefore it is possible to say that parts of the same margin underwent different stretching histories.

There are several geological examples in which it is possible to recognize the polyphase rifting signature and therefore the differences in rifting histories. Recovered strain rate data from subsidence curves (methodology implemented by [White, 1993, 1994](#)) helps to picture the variation in rifting history. For example, from the strain-rate inversion data relative to Petrel Sub-basin (Australia), a multiple rift phase evolution of the basin is evident ([Baldwin et al., 2006](#)) ([Fig. 2.36](#)).



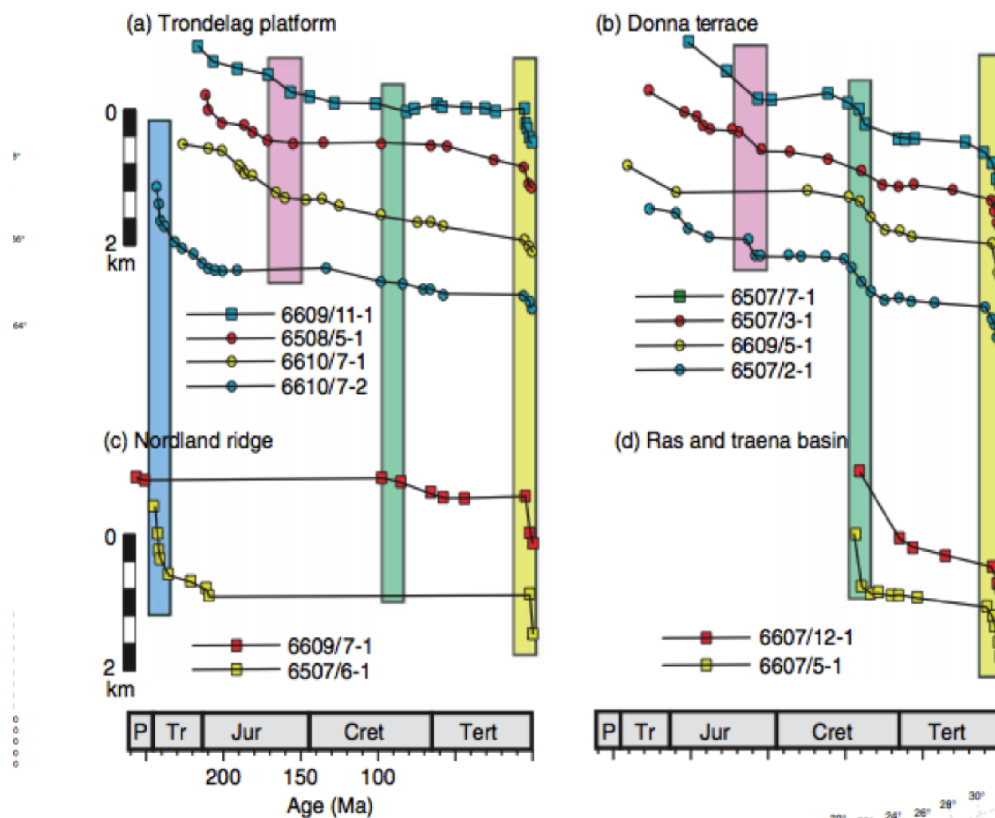
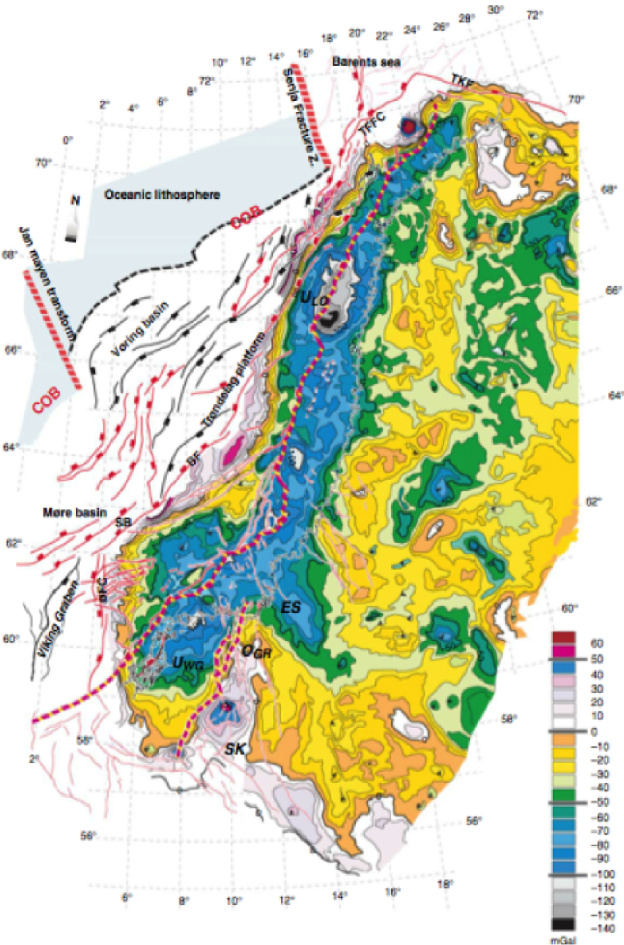


Figure 2.35 (Top) Tectonic subsidence curves for four sub-basins and platforms of the mid-Norwegian margin. Note the simultaneously occurring subsidence accelerations (coloured bars) intermitted by period of tectonic quiescence. The Mesozoic subsidence accelerations reflects pronounced rift-related tectonic phases, whereas the Late Neogene subsidence acceleration (light yellow bar) coincides with a major reorganization of the Northern Atlantic stress field. (Right) Bouguer gravity anomaly map of the onshore parts of the Scandinavian North Atlantic passive margin, showing superimposed rift-related normal faults systems. The width of the passive margin between the continent-ocean boundary (COB), marked by the dashed thick black line, and the innermost boundary fault system (IBF), marked by the dashed thick red line, ranges from 550 km in the south to over 700 km in the Mid-Norway to 165 km north of Lofoten. Note the onshore extension of the rift system. The wiggly black barbed line marks the position of the Caledonian Thrust Front. Modified after Cloetingh (2007)



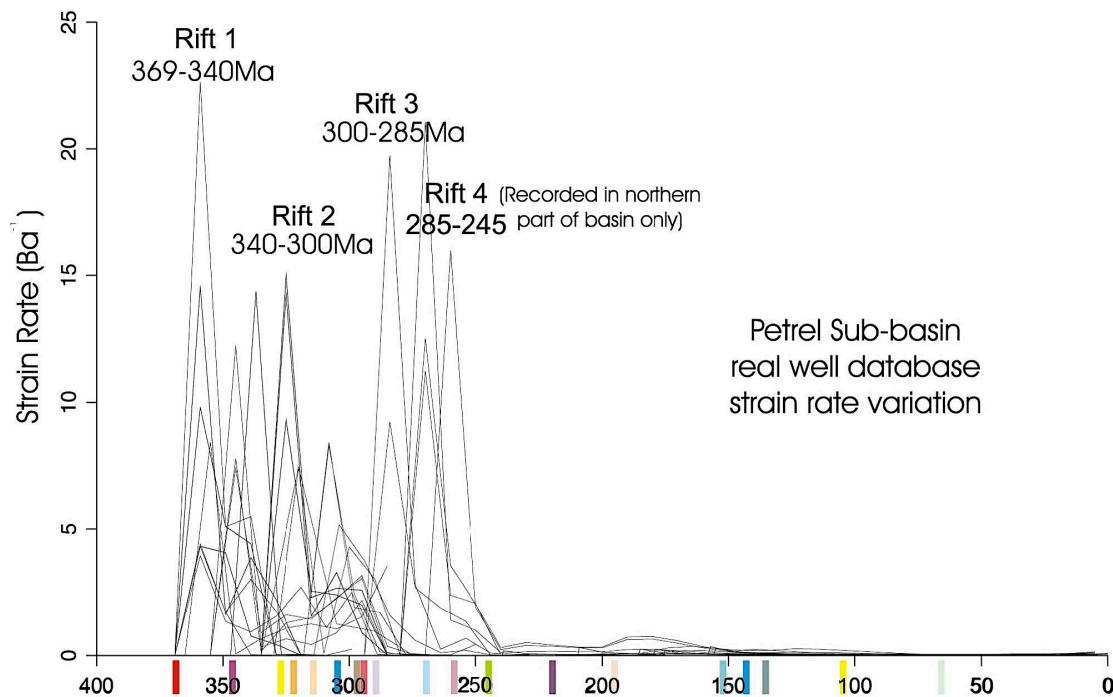


Figure 2.36 Resolving multiple rift phases by strain-rate inversion in the Petrel Sub-basin, northwest Australia. Timing, duration and timing duration and magnitude of strain-rate variation for all actual wells. At least three rift periods occur pre-245 Ma. There is temporal scatter in the timing of rifting between individual wells due to small differences in horizon dating. Wells located in the south of the basin record three distinct early rift events: first from 369 to 340 Ma; second from 340 to 300 Ma; and third from 300 to 285 Ma. Wells further north in the basin also record later rift events as late as 245 Ma. Post-245 Ma, no further rift episodes are recorded (modified after Baldwin *et al.*, 2006).

Using the same process, [Bellingham and White \(2000\)](#) observed similar discontinuities in rifting histories in San Jorge´ basin (offshore Argentina), Pearl River Mouth basin (South China Sea) and Viking graben, (North Sea) ([Fig. 2.37a,b and c](#)). In these examples, the diagrams at the bottom show the spatial and temporal variation of strain rate. For the case of San Jorge´ basin, a localized primary event occurred at ~130 Myr which preceded a more diffuse secondary event with much lower strain rate at 100 Ma. Pearl River Mouth basin shows the variation of strain rate, with two localized primary events at 50–100 km and 150–200 km ranges. At 35 Ma, these events merge to form a widespread and intense secondary event, peaking at 20 Ma. The Viking graben presents instead a main stretching event at ~150 Ma, where the highest strain rate occurs at 100 km range with lower values occurring in a band from 0 to 175 km. Diffuse secondary and tertiary events with low strain rates occur at ~70 Ma and at ~20 Myr.



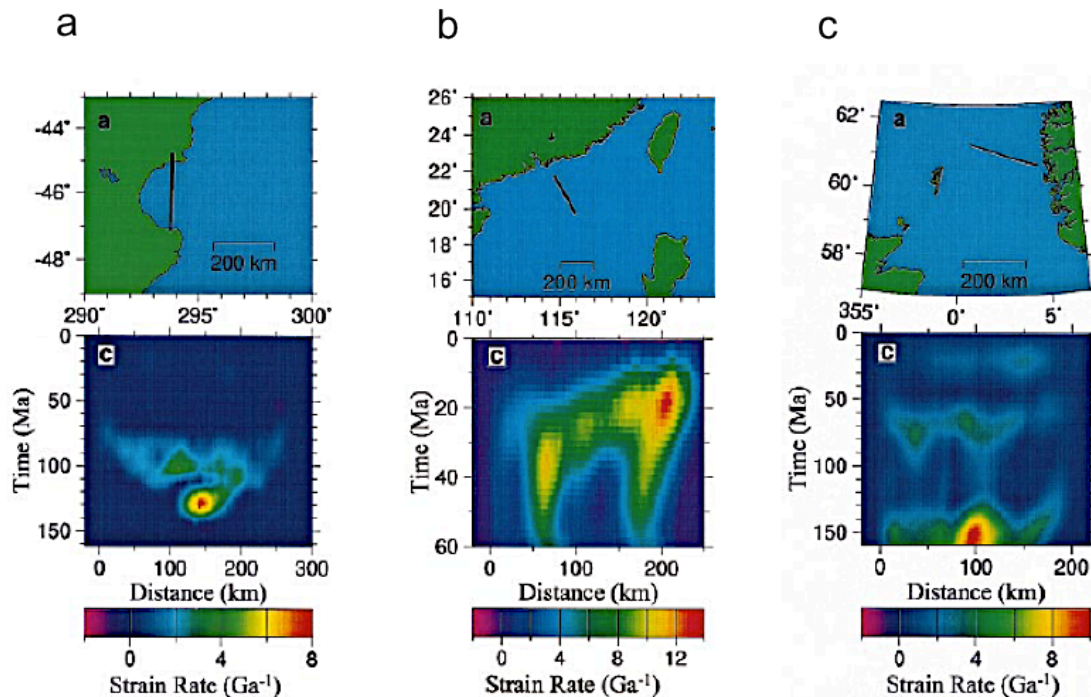


Figure 2.37 (Top) Map showing location of seismic reflection profile. (Bottom) Spatial and temporal variation of strain rate. (a) San Jorge basin, offshore Argentina. Note localized primary event at ~130 Ma and more diffuse secondary events with much lower strain rate at 100 Ma. (b) Pearl River Mouth basin, South China Sea. Note two localized primary events at 50–100 km and 150–200 km ranges. At 35 Ma, these events merge to form a widespread and intense secondary event, peaking at 20 Ma. (c) Viking graben, North Sea. Note primary event at ~150 Ma; highest strain rate occurs at 100 km range with lower values occurring in a band from 0 to 175 km. Diffuse secondary and tertiary events with low strain rates occur at 70 Ma and at 20 Ma (modified after Bellingham and White, 2000).

There are many other examples of basins and passive margins which exhibit complex rifting histories and that can be classified following the **RCR** and **RR** conceptual models. Listing just a few:

- **Rifting history RCR type.** Geological examples of the progression of stretching phases and cooling stages are: Eastern Spain (Fig. 1-35 - van Wees et al., (1998)), Michigan Basin (Bond and Kominz, 1984), Parana Basin (Zalan et al., 1990) Southwest Ordos Basin (Xie, 2007), Illinois Basin, Farley well (Bond and Kominz, 1984), Moroccan Basin (Ellouz et al., 2003), Gippsland Basin (Falvey and Mutter, 1981), Jeanne D'Arc Basin (Stampfli et al., 2002), Baikal basin (Moore et al., 1997) Williston Basin, North Dakota (Bond and Kominz, 1984), Williston Basin, Saskatchewan (Fowler and Nisbet, 1985), Cantarbian Basin (Stampfli et al., 2002), Lusitanian Basin (Stampfli et al., 2002).

- **Rifting history RR type.** Geological example of abrupt changing in strain rate and subsidence rate, without quiescence period in between are: the Red Sea (e.g. [Reilinger and McClusky, 2011](#)), Gulf of Aden ([Fig. 1-36 – Ali and Watts, 2013](#)), South China Sea ([Fig. 1-43 - Chen, 2014.](#)), Lybia's Sirte Basin ([Fig. 1- 39 - Capitanio et al., 2009](#)).

For a more exhaustive classification of rifts that help to infer the type of rifting history see [Sengor, \(2001\)](#).

From the geological/geophysical evidence given above it is possible to state that the *common characteristic* shared by rift basins and passive margin is a variable and complex *rifting history*.

## 6. POLYPHASE MODELS

Over the last 30 years, only a few authors have modelled a polyphase rifting history, trying to explain specific enigmatic geological cases. [Van Wees et al., \(1998\)](#) studied the Iberian Basin (eastern Spain) characterized by several pulsating periods of stretching intermitted by periods of relative tectonic quiescence and thermal subsidence. Through high-resolution backstripping analysis and forward modelling they have accurately assessed the temporal and spatial relations in lithospheric rift dynamics, showing that an increased resolution in subsidence data leads to a better resolution in tectonic signal.

[Tett & Sawyer, \(1996\)](#) have produced a set of multi-stage models based on the Newfoundland and Iberian Margins. They suggest that, under most conditions in which two rift phases occur, the site of the original rift will not be favoured for extension when stretching resumes, because the upper mantle cools and strengthens in the area of the original rift. In [Fig. 2.38a](#) the 5 rifting histories used by the authors, called rifting "paths" are shown. The durations of the path segments were chosen because they approximate the durations of the first (late Triassic) rifting phase, the resting phase, and the second (Late Jurassic to Early Cretaceous) rifting phase on the Newfoundland-Iberian Margins. The extension rate (and hence the amount of extension) for the middle phase was zero in paths 1, 2, 3, and 5; this represented the period in which there is thought to have been no divergent motion between North America and Iberia (about 215 to 160 Ma). The paths

were intended to simulate different distributions of total extension between the first and second rifting phases. Path 4 shows a constant extension rate for the entire duration of rifting. The vertical axis in Fig. 2.38a indicates the cumulative percentage of total extension while the horizontal axis indicates time since the beginning of rifting. The total amount of extension in each generic model is 500 km while the slope of each line is proportional to the relative rate of extension.

Huisman & Beaumon (2007) (Fig. 2.38b) have simulated the cooling stage between two rifting phases, increasing the crustal viscosity by a factor of 100, which results in a localization of the mantle from the crust and the development of an asymmetric basin and exhumation of the mantle lithosphere. This model is compatible with Newfoundland–Iberia natural system.

Armitage, et al. (2010) simulated a polyphase rifting with cooling, shifting the locus of the strain from a location to another in order to explain the difference in magma production between Greenland and the South-West Indian margin. The left end side of Fig. 2-38c shows the models for the Northwest Indian Ocean. The first episode of extension tapped the thermal anomaly, which is associated with the Deccan Traps. This formed the Gop rift and exhausted the thermal anomaly beneath the region of extension. The second episode of extension that led to break-up was above melt-depleted mantle and led to the amagmatic Seychelles/Laxmi ridge margin. The right end side of Fig. 2-38c represents the model for North Atlantic. The first episode of extension formed the Hatton Bank. During the inter-rift period, the thermal anomaly ponded beneath the lithosphere, such that during the second episode of extension this thermal anomaly was tapped, leading to the high volumes of melt generated during the break-up of southeast Greenland and the Hatton Bank. They have demonstrated that the rift history can play a dominant role in the magma production.

Chen (2014), modelled the subsidence the Baiyun Sag in the continent slope of the South China Sea, using a rifting-cooling-rifting model finding a better fit with the backstripping data. Chen (2014) simulated a two-episode rift process. The red shadow regions in Fig. 1-38d denote rifting events, and the gray-shadow areas indicate subsequent cooling. The second rifting cycle (marked by  $\beta_2$ ) is coupled to the first one (marked by  $\beta_1$ ) by succeeding the residual temperature and structural perturbation caused by its former. The stretching factor is estimated by fitting the entire observed subsidence history with model-predicted subsidence. Chen (2014) were able explain only the subsidence pattern as function of rifting history with this technique.

Only a few authors have addressed the role of inter-rifting cooling stages in the evolution of basins [Naliboff & Buiter \(2015\)](#) have simulated both the conditions for the migration and reactivation of rifting. [Fig. 1-38e](#) shows the models that simulate the asymmetry of margins in the mid-Norwegian and mid-East Greenland margins, using models to explain the causes for reactivation of the Northern and Southern Atlantic passive margins.

## **7. ROLE OF BOUNDARY CONDITION VARIATION ON RIFTING HISTORY**

From the previous analysis of the second group of geological and geophysical observables we can say that a common characteristic of rift basins and passive margin is the variation in rifting histories. Few previous authors have introduced rifting history to solve specific problems. They have constrained their models with geological data (for examples the cooling stages in [Naliboff & Buiter, 2015](#)) or simulated cooling by increasing the viscosity of particular layers ([Huismans & Beaumon, 2007](#)) without taking into account that the lithosphere is a Thermal Boundary Layer, prone to variation in thickness according to the stretching intensity and cooling duration. Hence, they only partially addressed the effect of this sequence on the final deformation of the lithosphere and feedback to the basin deformation. This study investigates the influence of strain (deformation) histories on the evolution of rifting basins and passive margins following a range of deformation histories. Previous work has (largely) only modeled polyphase rifting in 1D and for subsidence, neglecting the effect of strain and diffusion in multiple spatial dimensions ([Chen, 2014](#)).

These models are not able to answer to the following questions: what is the dominant factor that allows for the diversity in rifting histories? Does the rifting history have a major influence on the final basin deformation? (with basin deformation the author mean the basin shape and not the infill). Previous works have not explored the polyphase rifting process in the more general frame of physical experiments. A suitable way to answer these questions is to employ a modelling approach that generalises the rifting process, and is then able to explain simultaneously the differences in basin style,

subsidence and magmatism by adopting a multi-disciplinary approach (both geological and geophysical).

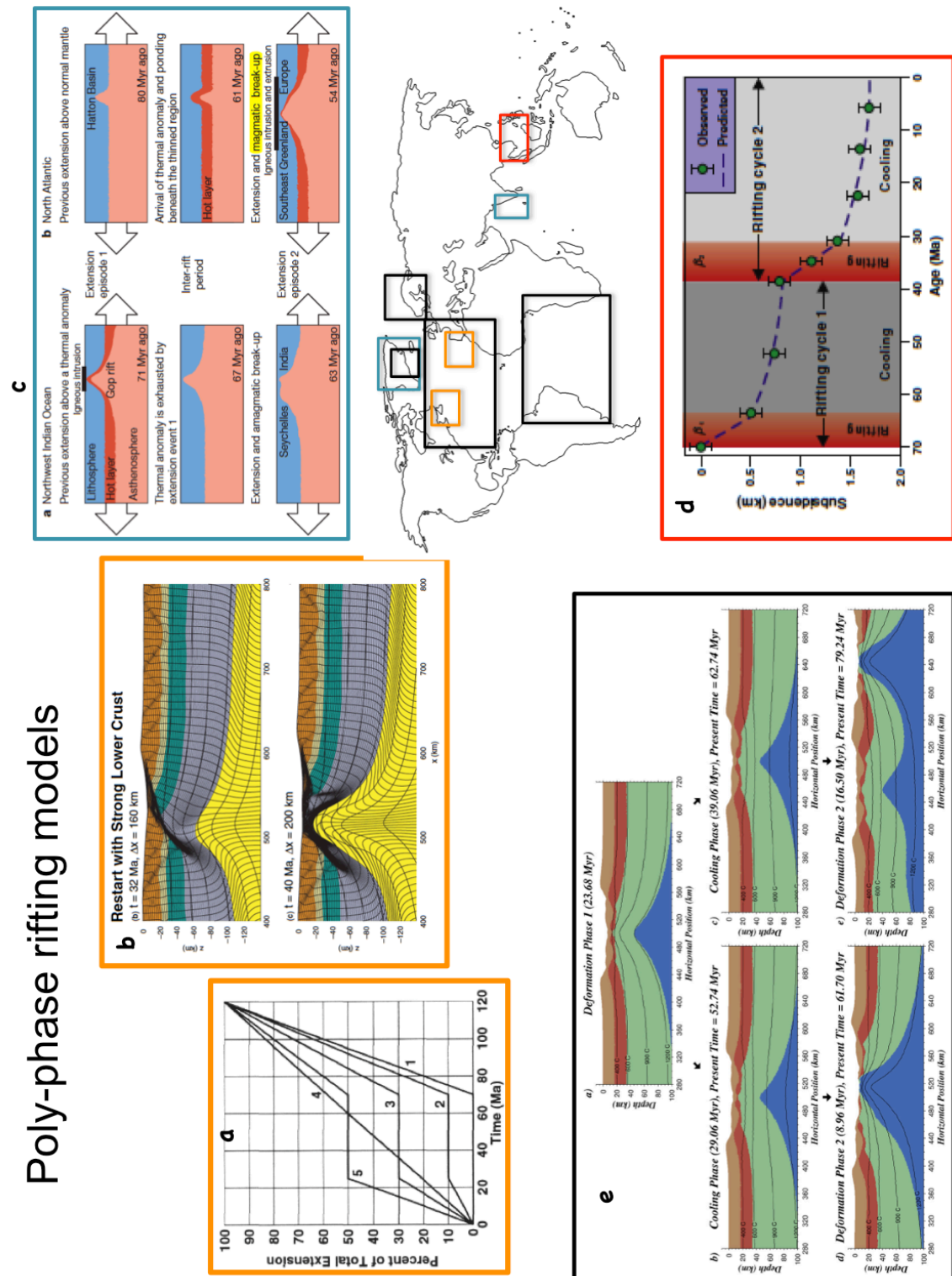


Figure 2.38 Polyphase models: (a) Tett & Sawyer, (1996); (b) Huisman & Beaumont, (2007); (c) Armitage, et al. (2010); (d) Chen (2014); (e) Naliboff & Buiter (2015). See text for a detailed description

## 7.1 General approach hypothesis to test the importance of rifting history

Using a strain rate recovery method (White, 1993, 1994), Capitanio et al., (2009) were able to propose an alternative interpretation of the dynamic context under which the Sirte (northern Africa, Libya) basin opened (Fig. 1-39, top for location and cross section, bottom for recovered strain rates). The main assumption of strain rate recovery method is that the observed syn-rift subsidence variation is a result of variable strain rate during stretching; see White (1993) and White (1994) for a detailed explanation. With this method Capitanio et al., (2009) isolated the boundary force contribution, net thermal and loading effects, and found that the origin and evolution of this wide rift corresponded to Hellenic subduction and lower mantle penetration, recording the development of slab pull forces in the basin's strain history.

The strain rate curves (Fig. 1-39 bottom) are taken from several wells that drilled the Sirte Basin and are interpreted to be representative of the basin dynamics through time. They reveal at first slow deformation ~100-73 Ma with strain rate in the order of  $10^{-16} \text{ s}^{-1}$  and then an increase in the pull force during the ~72–55 Ma phase indicated by an increase of one order of magnitude of strain rate ( $\sim 10^{-15} \text{ s}^{-1}$ ). This induced localized stretching in the Sirte basin. The pull must further increase largely in the following phase, ~55–48 Ma, when all segments of the basin stretch at the same time, recording larger strain rates ( $\sim 10^{-14} \text{ s}^{-1}$ ). Therefore, Capitanio et al. (2009) defined a single event driving Sirte extension, initiated by ~72 Ma, when the boundary force initially grew above the strength of the lithosphere, and then increased abruptly between ~55 and 48 Ma, quickly fading afterwards, when the stress regime inverted. From this observation they inferred that, even though the specific rheological parameters of the region are not constrained, the *variation of the strain rate* in the region gives a *first order constraint* on the *relative evolution of the boundary force magnitude*. In their hypothesis for the case of Sirte Basin the most plausible source of stress and change of boundary condition magnitude can be related to the pull produced by the continuous subducting plate below the Hellenic trench. Dynamics that are compatible with those of lower mantle avalanche models. This piece of work showed, for the first time, how changes in force magnitude generated at depth can manifest on the surface and how these forces control the evolution of basin deformation.



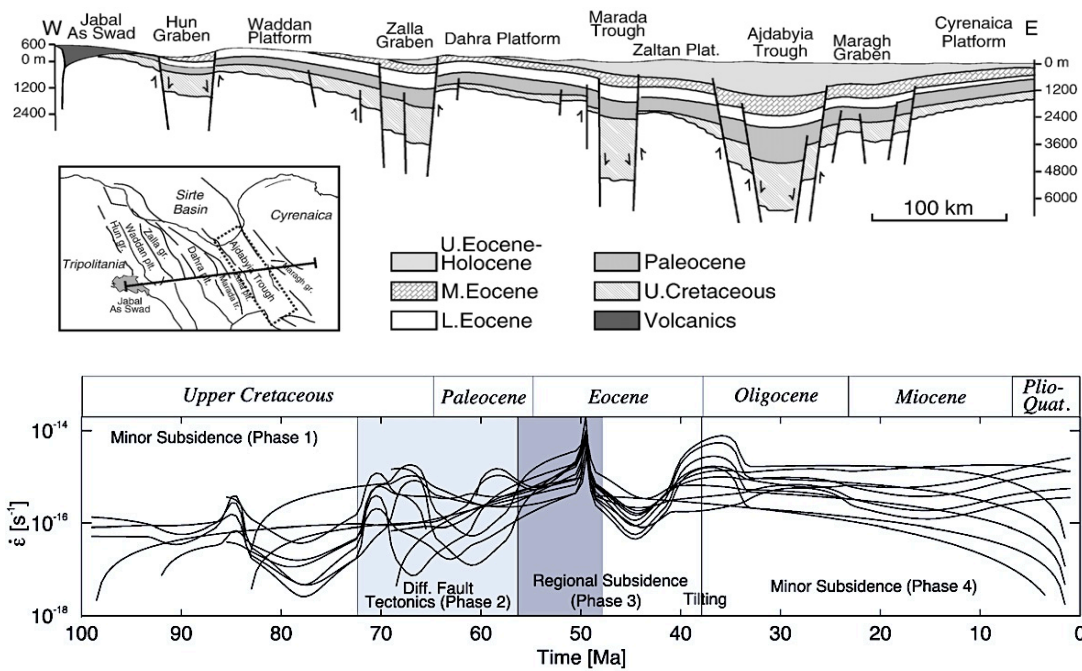


Figure 2.39 (Top) Geological cross section of the Sirte basin, modified after (Roohi, 1996), and tectonic sketch with the location of the section (inset) and location of the wells (dashed). The eastern Ajdabyia trough records the largest subsidence in the Sirte domain. This increases northwards, up to ~10 km, and shallows up towards the south, ~4 km. (Bottom) Strain rates in the Ajdabyia trough, eastern Sirte Basin of 21 selected wells, spanning the basin north to south. Strain rates are recovered following the methodology of White (1993, 1994) and compared with the tectonic phases of (van der Meer and Cloetingh, 1993). In light grey the differential faulting phase, where few fault segment are active, in dark grey the strain rate peak in the regional subsidence phase when all the segments are active at high strain rates. In the last minor subsidence phase, fictitious curves are obtained for tilted segments, where subsidence is not achieved by stretching.

## 7.2 Approach for the present study

This thesis addresses the questions outlined within the context that changes in boundary condition magnitude can be the first order factor generating the switch in deformation mode from one rifting phase to another (e.g. [Capitanio et al., 2009](#)). Specifically, the aim of this thesis is to determine if a variation in boundary conditions can create different rifting histories and how these variations lead to the diversity of deformation found in the rift-drift suite of basins (e.g. basin style - narrow vs wide mode, basin and conjugate margins symmetry/asymmetry - and variations in subsidence patters and melting production).

The role of the rifting history on lithospheric extension has been partially explored in literature. Previous studies preformed by, e.g., [Tett & Sawyer, \(1996\)](#), [Huisman & Beaumont \(2007\)](#), [Armitage, et al. \(2010\)](#), [Chen \(2014\)](#), [Naliboff & Buiter \(2015\)](#), have provided the important and initial insights, useful to understand the role of rifting histories. However, they were focused on specific geological areas, therefore they are not

fully independent and able to explain the rifting process on a frame of a general approach. For example [Tett & Sawyer, \(1996\)](#) and [Huisman & Beaumont \(2007\)](#), used 5 and 2 rifting histories were designed to explain the evolution of the Newfoundland and Iberian Margins; [Naliboff & Buiter \(2015\)](#) used specific duration of cooling (e.g. 30 and 40 Myr) based on estimated quiescence tectonic duration; [Armitage, et al., \(2010\)](#) used numerical models specifically designed (e.g. model with low resolution) to study the role of multiple rifting events on magma production to explain differences found between Greenland and the South-West Indian margins. Therefore, the generality of the research outcomes vanishes and these results can be considered one of the many possibilities to explain the evolution of the specific area under analysis with limited explanation on the physical process. In the present study there is the attempt to maintain this generality considering as common denominator of rifted areas the variation of the rifting history. The aim here is to test that the variation in rifting history plays a simultaneous first order role on different geological features such as basin style, subsidence patterns and melting production. The present study represents just a beginning step and certainly more work needs to be done in the future. Similarly to the previous works on the rifting process, this work has approximations and it cannot resolve all the complexities found in rifted areas (e.g. migration of the basin depocenter along rift axis). Nevertheless, it is an effort to try to study the rifting process with a different perspective.

### **7.2.1 Methodology**

This study is based on a different hypothesis from the one commonly used to model the rifting process (the single-rift event-modelling hypothesis based on [McKenzie, 1978](#)), and has the aim to maintain the generality of the results. For these two reasons the methodology used here is basic and follows the steps suggested by the adaptation of the classical scientific method to contemporary research requirements. It starts with a very simplified conceptual model, adding complexities only once the role of the boundary conditions variation has been fully understood in comparison with traditional modelling approaches (based on [McKenzie, 1978](#)). As consequence, a hierarchical order of experiments was followed for the present research and the modelling methodology is based on both a) scientific method and b) research in technology for practical application.

The methodology applied here can be linked to the one showed by [Barbour & Krahn \(2006\)](#). They describe the design of the scientific investigation and modelling steps in



geoscience using numerical tools, so converting the classical steps of the scientific method into a modelling method with the use of numerical tools. In their work they describe the following steps: 1) conceptualize: geology and the physical processes; 2) define: behavioural processes and material properties; 3) formulate: numerical descriptions and solutions for these processes; 4) solve: obtain an accurate numerical solution; 4) interpret: validate, calibrate and interpret the solutions in the context of the physical system. This is very similar to what is indicated by [Ismail-Zadeh, & Tackley \(2010\)](#),

Here, the investigation methodology is divided in two main phases. In phase one, the rifting process was treated as general problem. This was achieved by doing a series of experiments aimed to investigate the process in its entirety and physical aspect as general case, therefore not investigating any specific geological area. This represents the first part of the modelling methodology used here where a new hypothesis is tested in the context of continuous mechanics. This allows for the correlation of results derived from the general approach of deformation histories of Earth-like materials to the common features found in rifting areas, the effects of a variable rifting history. All the steps relative to this level of generalization of the problem and hypothesis testing are discussed in chapter 3, 4 and 5. In Chapter 3, I present the rationale of the project, formulating the hypothesis and the polyphase history-dependent conceptual model. Here, I show the computational model, explaining the mathematical constraints and numerical techniques needed to operate, and the necessary tests to verify, the model. The numerical model verification imposed the development of a series of monophasic simulations, which allowed for the comparison with models from literature and geological observation. For clarity they are synthetized in a limited number of plots relative to end-members. In Chapter 4, I translate the polyphase history-dependent conceptual model into numerical simulations, showing the 2D results, which demonstrate how rift history influences the final basin deformation, subsidence patterns and magma production.

The second phase of the modelling methodology imposes a validation of the approach by testing it on with a specific geological case, the evolution of Sirte basin, validating the models with independent geological observations. This is presented in Chapter 5.

This work thesis aimed to give a general approach to the modelling of tectonic processes. It can be used on more specific geological cases, taking into account the different initial conditions (crustal thickness, specific rheological parameters etc.) together with the

rifting history of the area (number of rifting phases, variation of strain rate with time, absence of cooling stage or shorter and longer periods of cooling).

Note that in the present work the effect of the strain-induced weakening has not been addressed. I recognise that it is an important process for localising deformation (either in the frictional-plastic or viscous domain, or both – see section 4.2.3.2.5) and is used in many models to replicate natural phenomena linked to a reduction of the cohesion (e.g. [Huismans & Beaumon, 2002, 2007](#)), or grain size transformation/reduction with accumulated strain (e.g. [Gueydan, et al., 2014](#)).

The reason behind this choice is that strain-induced weakening increases considerably the number of parameters to explore, which is outside the aim of the simple and generic models such as those presented here.

For the same reason here sedimentation and melting are not included in the numerical model.

I consider homogenous layers and no pre-existing perturbation in the lithosphere, i.e. no weak/strong seeds or thermal anomalies are introduced ([Fernandez and Ranalli, 1997](#)). Despite being commonly used in numerical modelling ([Peters et al., 2015](#), and references therein) these heterogeneities can constrain the range of lithospheric deformation, favouring the lithospheric necking and localised strain. Although we have performed relevant resolution tests, I am aware that strain localisation of numerical homogenous materials might be affected by the consequences of numerical approximations, introducing numerical heterogeneities ([Peters et al., 2015](#)). Although this is out of the scope of this paper, the inferences on strain localisation vs. diffusion remains valid, as localisation simply occurs at a larger strain/strain rate, with same features (e.g. [Schmeling, 2010](#)). Hence, in this paper we refer to “diffuse” and “localised” deformation meaning the weakly and strongly localised deformation. The absence of initial perturbations in the model setup was adopted by [Crameri and Kaus \(2010\)](#), since they have considered that lithospheric localisation is regulated by the thickness of the plastic field

Nevertheless, the effects of strain-induced weakening, melting, sedimentation and effect of pre-existing heterogeneities together with the variation of rifting history, will be studied in the upcoming work, with the goal to deliver the results in future publications.





## Declaration for Thesis Chapter 3

**Monash University**

### Declaration for Thesis Chapter 3

#### Declaration by candidate

In the case of Chapter 3, the nature and extent of my contribution to the work was the following:

<b>Nature of contribution</b>	<b>Extent of contribution (%)</b>
Presentation of continuum mechanics fundamentals from literature. Development of the research's Rationale as well as Conceptual and Numerical models. Analysis and interpretation of the 1D results. Parts 2 and 3 are going to be the basis for a review paper conjunctly with the structure and revisited information presented in Chapter 2.	85

The following co-authors contributed to the work. If co-authors are students at Monash University, the extent of their contribution in percentage terms must be stated:

<b>Name</b>	<b>Nature of contribution</b>	<b>Extent of contribution (%) for student co-authors only</b>
Dr. Fabio A. Capitanio	Supervisory role.	5
Dr. Rebecca J. Farrington	Supervisory role.	5
Dr. Giovanni Spampinato	Proof reading. Editing.	5

The undersigned hereby certify that the above declaration correctly reflects the nature and extent of the candidate's and co-authors' contributions to this work\*.

**Candidate's  
Signature**

	<b>Date</b> 01/04/2016
---	---------------------------

**Main  
Supervisor's  
Signature**

	<b>Date</b> 01/04/2016
---	---------------------------



# **CHAPTER 3: CONTINUUM MECHANICS**

## **FUNDAMENTALS IN GEODYNAMICS**

### **MODELLING AND PROJECT'S RATIONALE**

#### **1. INTRODUCTION**

In this chapter I present the fundamental physical and mathematical laws used in Geodynamics followed by the assumptions, definitions and ideas that form the rationale of this project.

The conservation and constitutive (rheological) laws are presented to give the reader the continuous mechanics framework used to model natural processes in geodynamics, particularly for the general aspects concerning computational modelling.

A complete polyphase rifting model approach is lacking in the literature. A test of the fundamental hypothesis driving the research is required by using a simple modelling strategy, building the modelling structure step by step. In the second part of this chapter, the second and third steps of the modelling work flow is developed by describing the realization of the 1D conceptual model, the physical assumption and the mathematical formulation. The validation of the rationale against existing models of lithospheric localization is also presented. Here, I have shown how the interplay between initial (e.g. lithospheric temperature distribution, composition, layering) and tectonic boundary conditions ( e.g. initial strain rate), in conjunction with a polyphase rifting (here only 2 phases) and cooling stage, influence the degree of lithospheric localization. With simple 1D experiments and phase-diagrams, the boundary conditions used for a rifting stage are shown to interact in a different way with the cooling stage, creating unique inherited initial conditions for a second rifting phase. This set the stage to further investigation and so for the development of polyphase rifting process in 2D.

The 1D tests allowed for a test of the lithospheric stratification (thickness of rheological layers), rheological parameters, geothermal gradients and range of initial strain rate to be used in later 2D modelling.

## 2. PART 1: FUNDAMENTALS OF CONTINUUM MECHANICS

In order to gather relevant knowledge and understanding about lithospheric and mantle processes, geodynamicists make use of geodynamic models, which are basic scaled examples of nature in the context of the continuous mechanics.

In order to apply continuum mechanics to lithospheric and mantle processes, physical parameters are chosen to imitate natural conditions following the similitude criteria (e.g. [Chanson, 2009](#)). Particularly, a scale model is required to satisfy mechanical similarity ([Heller, 2011](#)). The scale model should be completely similar to its real world prototype and introduces no scale effects. Mechanical similarity requires three criteria ([Chanson, 2009](#); [Heller, 2011](#)):

- Geometric similarity: similarity in shape, i.e. all length dimensions in the model are  $l$  times shorter than of its real-world prototype;
- Kinematic similarity: similarity of motion between model and prototype particle;
- Dynamic similarity: all force ratios are identical.

The relationships between the body's kinematics, mass and forces can be divided in two categories:

- Governing, conservation or fundamental equations, defined as general and common to all bodies regardless of the constitutive material;
- Constitutive laws which help to separate continuous bodies in classes. They define the relation between two physical quantities (kinetic quantities as related to kinematic quantities) that is specific to a material or substance, and approximates the response of that material to external applied fields or forces

The following sections are dedicated to the explanation of these relationships.

### 2.1 Governing equations

The governing equations used in geodynamics include the following conservation laws of physics:

- Conservation of mass;
- Newton's second law: the change of momentum equals the sum of forces on the fluid parcel, conservation of momentum;
- First law of thermodynamics: the rate of change of energy equals the sum of the rate of heat added to and work done on fluid parcel, conservation of energy.



In the following section I describe the mathematical equations. The contents of this section are taken and revised from the work of [Alik Ismail-Zadeh and Paul Tackley \(2010\)](#), [Gerya \(2009\)](#), [Burov \(2007\)](#), [Artemieva \(2011\)](#), [Stüwe \(2007\)](#), [Davies \(2009\)](#) and [Lai et al., \(1996\)](#).

### 2.1.1 The equation of mass conservation

In order to explain the *mass conservation law* (also termed the continuity equation) one needs to consider a fluid in which the density  $\rho$  is a function of position  $x_j$  ( $j = 1, 2, 3$  hereinafter) and where  $u_j$  represents the velocity components.

Conservation of mass states that the rate of change of the mass contained in a fixed volume  $V$  of fluid is given by the rate at which fluid flows across the boundary  $S$  of the volume (Fig. 3.1).

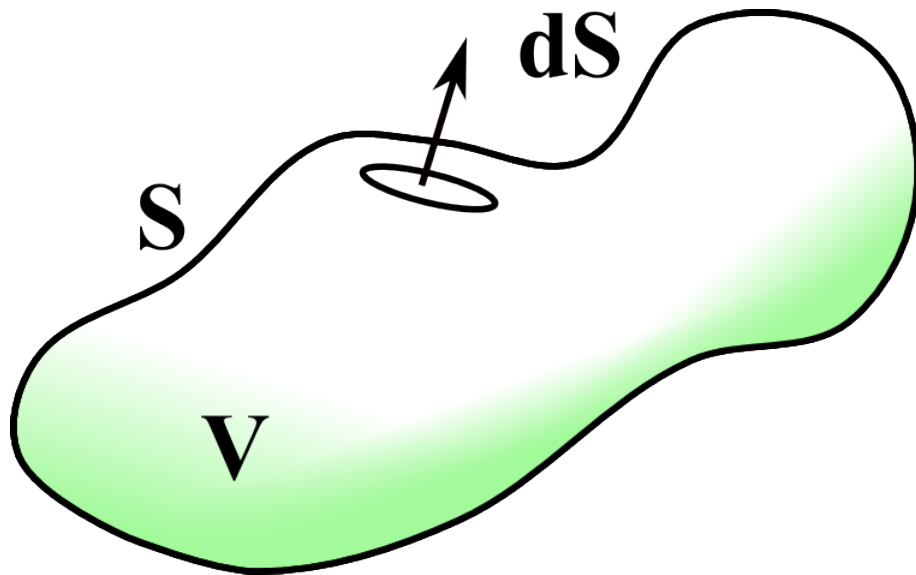


*Figure 3.1 Arbitrary fluid volume,  $V$ , with surface  $S$  and elemental surface normal vector,  $dS$ , within which the fluid properties are to be conserved.*

Mathematically this is expressed as

$$\frac{\partial}{\partial t} \int_V \rho d\tau = - \int_S \rho u_j dS_j \quad (3.1)$$

where  $\tau$  is the volume element and  $dS_j$  the infinitesimal surface element. By means of the divergence theorem (Gauss–Ostrogradsky theorem), conservation of mass can be transformed as:

$$\frac{\partial}{\partial t} \int_V \rho d\tau = - \int_V \frac{\partial}{\partial x_j} (\rho u_j) d\tau \quad (3.2)$$

With the Lagrangian form of the continuity equation:

$$\frac{D\rho}{Dt} \equiv \frac{\partial \rho}{\partial t} + u_j \frac{\partial \rho}{\partial x_j} = -\rho \frac{\partial u_j}{\partial x_j} \quad (3.3)$$

This is because this form is more suitable for numerical analysis.

The corresponding Eulerian notation is:

$$\frac{\partial \rho}{\partial t} = -\frac{\partial}{\partial x_j}(\rho u_j) \quad (3.4)$$

Geodynamics modelling requires the use of an incompressible fluid, reducing the equation of continuity to:

$$\frac{\partial u_j}{\partial t} = 0, \text{ since } \frac{\partial \rho}{\partial t} + u_j \frac{\partial \rho}{\partial x_j} = -\frac{D\rho}{Dt} = 0 \quad (3.5)$$

### 2.1.2 The equation of motion

The *law of momentum conservation* can be stated as follows: the rate of change of the momentum enclosed in a fixed volume  $V$  of the fluid is equivalent to the volume integral of the external body forces acting on the fluid and the surface integral of stresses acting on the bounding surface  $S$  of the volume  $V$  and subtracting the rate at which momentum flows across the boundaries of  $V$  by the motions prevailing on the surface  $S$ .

This is mathematically expressed as:

$$\frac{\partial}{\partial t} \int_V \rho u_i d\tau = \int_V \rho F_i d\tau + \int_S \sigma_{ij} dS_j - \int_S \rho u_i u_j dS_j \quad (3.6)$$

where  $F_i$  ( $= g_i$ ) is the  $i$ th component of external force per unit of mass; and  $\sigma_{ij}$  is the stress tensor.

Considering:

$$\frac{\partial}{\partial t}(\rho u_i) = \rho \frac{\partial u_i}{\partial t} + u_i \frac{\partial \rho}{\partial t} = \rho \frac{\partial u_i}{\partial t} - u_i \frac{\partial}{\partial x_j}(\rho u_j) \quad (3.7)$$

and substituting (3.7) into (3.6), the expression for conservation of momentum can be given by:

$$\int_V \left( \rho \frac{\partial u_i}{\partial t} - u_i \frac{\partial}{\partial x_j} (\rho u_j) \right) d\tau + \int_S \rho u_i u_j dS_j = \int_V \rho F_i d\tau + \int_S \sigma_{ij} dS_j \quad (3.8)$$

The first term can be simplified, giving:

$$- \int_V u_i \frac{\partial}{\partial t} (\rho u_i) d\tau + \int_S \rho u_i u_j dS_j = \int_V \rho u_j \frac{\partial u_i}{\partial x_j} d\tau \quad (3.9)$$

Application of divergence theorem to the last term in (3.8) provides:

$$\int_S \sigma_{ij} dS_j = \int_V \frac{\partial \sigma_{ij}}{\partial x_j} d\tau \quad (3.10)$$

Substituting equation (3.9) and (3.10) into (3.8) gives the equation of motion in a form valid for any arbitrary volume V:

$$\rho \frac{\partial u_i}{\partial t} + \rho u_j \frac{\partial u_i}{\partial x_j} = \rho F_i + \frac{\partial \sigma_{ij}}{\partial x_j} \quad (3.11)$$

Assuming a linear viscous creep, the stress can be related to the strain rate as follows:

$$\sigma_{ij} = -P \delta_{ij} + 2\eta \dot{\epsilon}_{ij} + \left( \eta_B - \frac{2}{3} \eta \right) \delta_{ij} \frac{\partial u_k}{\partial x_k} = -P \delta_{ij} + \eta \left( \frac{\partial u_i}{\partial x_j} + \frac{\partial u_j}{\partial x_i} - \frac{2}{3} \delta_{ij} \frac{\partial u_k}{\partial x_k} \right) + \eta_B \delta_{ij} \frac{\partial u_k}{\partial x_k} \quad (3.12)$$

where P is the pressure,  $\delta_{ij}$  is the Kronecker delta,  $\eta$  is the viscosity,  $\eta_B$  is the bulk viscosity, and  $\dot{\epsilon}_{ij}$  is the strain rate tensor. As compaction or dilation is normally accommodated elastically,  $\eta_B$  is usually assumed to be zero. By substituting relationship (3.12) into the equation of motion (3.11) assuming  $\eta_B = 0$ , the following equation is obtained:

$$\rho \frac{\partial u_i}{\partial t} + \rho u_j \frac{\partial u_i}{\partial x_j} = \rho F_i - \frac{\partial P}{\partial x_i} + \frac{\partial}{\partial x_j} \left\{ \eta \left( \frac{\partial u_i}{\partial x_j} + \frac{\partial u_j}{\partial x_i} - \frac{2}{3} \delta_{ij} \frac{\partial u_k}{\partial x_k} \right) \right\} \quad (3.13)$$

Assuming an incompressible fluid with constant viscosity, equation (3.13) shortens to:

$$\rho \frac{\partial u_i}{\partial t} + \rho u_j \frac{\partial u_i}{\partial x_j} = \rho F_i - \frac{\partial P}{\partial x_i} + \eta \nabla^2 u_i \quad (3.14)$$

The original form of the Navier–Stokes equations (the “original” is taken from [Ismail-Zadeh, & Tackley, 2010](#), and they mean “earliest”)

For geodynamic applications, the Navier–Stokes equations (3.14) can be simplified by assuming Stokes flow for low Reynolds numbers, resulting in Stokes equations. This can be illustrated by scaling for the parameters used in Navier-Stokes equations with geodynamic values. The dimensionless variables and parameters (represented with tilde) are derived using typical values for gravity ( $g = 9.8 \text{ m s}^{-2}$ ), density ( $\rho^* = 4 \times 10^3 \text{ kg m}^{-3}$ ), viscosity ( $\eta^* = 10^{21} \text{ Pa s}$ ), length ( $l^* = 3 \times 10^6 \text{ m}$ ) and thermal diffusivity ( $\kappa^* = 10^{-6} \text{ m}^2 \text{ s}^{-1}$ ) for Earth’s, mantle, respectively:

$$t = \frac{\tilde{t} l^*}{\kappa^*}; \quad \mathbf{u} = \frac{\tilde{\mathbf{u}} \kappa^*}{l^*}; \quad P = \frac{\tilde{P} \eta^* \kappa^*}{l^{*2}}; \quad \rho = \tilde{\rho} \rho^*; \quad \eta = \tilde{\eta} \eta^*$$

Replacement of the variables by their dimensionless form omitting tildes in the Navier–Stokes equations, leads to:

$$\frac{1}{Pr} \rho \left( \frac{\partial u_i}{\partial t} + \rho u_j \frac{\partial u_i}{\partial x_j} \right) = - \frac{\partial P}{\partial x_i} + \frac{\partial}{\partial x_j} \left\{ \eta \left( \frac{\partial u_i}{\partial x_j} + \frac{\partial u_j}{\partial x_i} - \frac{2}{3} \delta_{ij} \frac{\partial u_k}{\partial x_k} \right) \right\} + La \rho \delta_{i3} \quad (3.15)$$

where the dimensionless parameter are defended as following:

$$Pr = \frac{\eta^*}{\rho \kappa^*} = 2.5 \times 10^{23} \text{ Prandtl number;}$$

$$La = \frac{\rho^* g l^3}{\eta^* \kappa^*} \sim 10^9 \text{ Laplace number;}$$

The Laplace number is also given as  $La = Ra/(\alpha \Delta T)$ , where  $Ra$  is the Rayleigh number

controlling the vigor of thermal convection,  $\alpha$  is the thermal expansivity and  $\Delta T$  is the temperature variation. Since the LHS is very small compared to the RHS, (3.15) can be simplified to the following elliptic equations called the Stokes equations:

$$0 = -\frac{\partial P}{\partial x_i} + \frac{\partial}{\partial x_j} \left\{ \eta \left( \frac{\partial u_i}{\partial x_j} + \frac{\partial u_j}{\partial x_i} - \frac{2}{3} \delta_{ij} \frac{\partial u_k}{\partial x_k} \right) \right\} - \frac{Ra}{\alpha \Delta T} \rho \delta_{i3} \quad (3.16)$$

or, in dimensional units,

$$0 = -\frac{\partial P}{\partial x_i} + \frac{\partial}{\partial x_j} \left\{ \eta \left( \frac{\partial u_i}{\partial x_j} + \frac{\partial u_j}{\partial x_i} - \frac{2}{3} \delta_{ij} \frac{\partial u_k}{\partial x_k} \right) \right\} + \rho F_i \quad (3.17)$$

In the case of incompressible flow the term  $\frac{2}{3} \delta_{ij} \frac{\partial u_k}{\partial x_k}$  is neglected. For constant viscosity and incompressible flow the second term reduces to  $\eta \nabla^2 u_i$  as in Eq. (3.14).

### 2.1.3 The heat equation

The conservation of energy law relates the gains and losses of energy that occur in a volume  $V$ , bounded by surface  $S$ , of fluid, per unit time:

$$\frac{\partial}{\partial t} \int_V \rho E d\tau = \int_S u_i \sigma_{ij} dS_j + \int_V \rho u_i F_i d\tau - \int_S k \frac{\partial T}{\partial x_j} dS_j - \int_S \rho E u_j dS_j + \int_V \rho H d\tau \quad (3.18)$$

The equations terms are:

- On the left-hand side of the Eq. (3.18): the rate at which work is done on the boundary;
- On the right-hand side of the Eq. (3.18):
  1. the rate at which work is done on each element of the fluid inside  $V$  by external forces;
  2. the rate at which energy in the form of heat is conducted across  $S$  ;
  3. the rate at which energy is transported across  $S$  ( $k$  is the coefficient of heat conduction);
  4. the rate at which energy is added by internal heat sources.

The term on the right and third term on the right of Eq. (3.18) can be represented as

follows:

$$\int_S u_i \sigma_{ij} dS_j = \frac{1}{2} \frac{\partial}{\partial t} \int_V \rho u_i^2 d\tau + \frac{1}{2} \int_S \rho u_i^2 u_j dS_j - \int_V \rho u_i F_i d\tau + \int_V \Phi d\tau \quad (3.19)$$

$\Phi = \frac{\partial u_i}{\partial x_j} \sigma_{ij}$  , is the viscous dissipation function, and

$$\int_S k \frac{\partial T}{\partial x_j} dS_j = \int_V \frac{\partial}{\partial x_j} \left( k \frac{\partial T}{\partial x_j} \right) d\tau \quad (3.20)$$

The energy E per unit mass of the fluid is quantified as:

$$E = \frac{1}{2} u_i^2 + c_v T \quad (3.21)$$

With  $c_v$  the specific heat at constant volume and T is the temperature. This allows the fourth term of (3.18) to be modified as:

$$- \int_V \rho E u_j dS_j = - \int_S \rho \left[ \frac{1}{2} u_i^2 + c_v T \right] u_j dS_j = \frac{1}{2} \int_V \rho u_i^2 u_j dS_j - \int_V \frac{\partial}{\partial x_j} (\rho u_j c_v T) d\tau \quad (3.22)$$

Replacing Eqs. (3.19)–(3.22) into (3.18), it results in:

$$\int_V \frac{\partial}{\partial t} (\rho c_v T) d\tau = \int_V \frac{\partial}{\partial x_j} \left( k \frac{\partial T}{\partial x_j} \right) d\tau + \int_V \Phi d\tau - \int_V \frac{\partial}{\partial x_j} (\rho c_v T u_j) d\tau + \int_V \rho H d\tau \quad (3.23)$$

Because Eq. (3.23) is valid for any arbitrary volume V, this modifies in:

$$\frac{\partial}{\partial t} (\rho c_v T) + \frac{\partial}{\partial x_j} (\rho c_v T u_j) = \frac{\partial}{\partial x_j} \left( k \frac{\partial T}{\partial x_j} \right) + \Phi + \rho H \quad (3.24)$$

Considering that the left-hand side of the equation is the Lagrangian time derivative D/Dt, operating the derivative separately to T and  $\rho$  results in:

$$\rho \frac{D}{Dt}(c_V T) + c_V T \frac{D\rho}{Dt} = \frac{\partial}{\partial x_j} \left( k \frac{\partial T}{\partial x_j} \right) + \Phi + \rho H \quad (3.25)$$

which brings to the following form after considering thermodynamics simplifications:

$$\rho c_P \frac{DT}{Dt} - \alpha T \frac{DP}{Dt} = \frac{\partial}{\partial x_j} \left( k \frac{\partial T}{\partial x_j} \right) + \Phi + \rho H \quad (3.26)$$

This is a general form of the Conservation of the Energy (or Energy equation), which is valid for compressible flow. For example for incompressible flow, applying the incompressible continuity equation (3.5) to equation (3.24) results in the simplified form:

$$\rho \frac{\partial}{\partial t}(c_V T) + \rho u_j \frac{\partial}{\partial x_j}(c_V T) = \frac{\partial}{\partial x_j} \left( k \frac{\partial T}{\partial x_j} \right) + \Phi + \rho H \quad (3.27)$$

Eq. (3.27) is a parabolic equation.

Equation (3.26) is often written using the ‘nabla’ operator,  $\nabla$ . In this case the equation assumes the following form:

$$\rho c_P \left( \frac{\partial T}{\partial t} + \vec{u} \cdot \nabla T \right) - \alpha T \left( \frac{\partial P}{\partial t} + \vec{u} \cdot \nabla P \right) = \frac{\partial}{\partial t} \nabla \cdot (k \nabla T) + \Phi + \rho H \quad (3.28)$$

#### 2.1.4 The rheological or constitutive law

Over geologic time scales, it can be assumed Earth’s materials have a dual behaviour, deforming as fluids and solids. Therefore the behaviour of Earth’s mantle can be approximated by rheological properties of a fluid or a solid. Thus, to describe the relationship between stress and strain/strain rate of Earth’s geodynamic processes requires consideration of constitutive or rheological laws.

In order to understand the behaviour of geomaterials, some scientists employ the Deborah number (dimensionless), defined as the ratio of the characteristic relaxation time, the time taken for a material to adjust to applied stresses or deformations, and the characteristic time scale of an experiment or observation time probing the response of the material  $De = \frac{t_c}{t_p}$ , where  $t_c$  refers to the stress relaxation time, and  $t_p$  refers to the time scale of observation (Ismail-Zadeh & Tackley, 2010)

If the time of observation is very large (or the time of relaxation of the geomaterial under



observation is very small), the mantle is considered to be a fluid. On the other hand, if the time of relaxation is larger than the time of observation, the mantle is considered to be a solid. The greater the Deborah number, more solid-like behaviour is observed, the smaller the Deborah number the more fluid-like behaviour is observed).

In nature, geomaterials exhibit more complicated rheological behaviour than fluid or solid materials. In the following only the principal rheological relationships used in Geodynamics are addressed.

In geodynamic modelling, a viscous rheology can be used as the mantle behaves as a highly viscous fluid at long geological time scales. The equation describing the relationship between the viscous stress and strain rate can be given in the following form:

$$\tau_{ij} = C \frac{1}{n} \dot{\epsilon}_{ij} \dot{\epsilon}^{\frac{1-n}{n}} \quad (3.29)$$

Where:

- $\tau_{ij}$  is the deviatoric stress tensor,
- $C$  is a proportionality factor defined from the thermodynamic conditions,
- $\dot{\epsilon} = (0.5 \dot{\epsilon}_{kl} \dot{\epsilon}_{kl})^{1/2}$  is the second invariant of the strain rate tensor, and
- $n$  is a power-law exponent.

If  $n = 1$ , Eq. (3.29) describes a Newtonian fluid with  $C/2$  as the fluid's viscosity, which depends on temperature and pressure as discussed below. For  $n > 1$ , Eq. (3.29) represents a non-Newtonian (non-linear) fluid behaviour.

At high temperatures (that are a significant fraction of the melt temperature) the atoms and dislocations in a crystalline solid become sufficiently mobile to result in creep when the solid is subject to deviatoric stresses. At very low stresses diffusion processes dominate, and the crystalline solid behaves as a Newtonian fluid with a viscosity that depends exponentially on pressure and the inverse absolute temperature. The proportionality factor  $C$  in (3.29) can be then represented as:

$$C(T, P) = C^* d^m \exp\left(\frac{E+PV}{RT}\right) \quad (3.30)$$

Where:

- $T$  is the absolute temperature;
- $P$  is pressure;
- $C^*$  is the proportionality factor that does not depend on temperature and pressure;
- $E$  is the activation energy;

- $V$  is the activation volume;
- $R$  is the universal gas constant;
- $d$  is the grain size and  $m$  its exponent.

For dislocation creep, grain size is unimportant and  $m = 0$ , but for diffusion creep  $m$  is between 2 and 3 (Ismail-Zadeh & Tackley, 2010). At higher stresses the motion of dislocations becomes the dominant creep process resulting in a non-Newtonian fluid behaviour described by Eqs. (3.29)–(3.30), with typically  $n = 3.5$  (Ismail-Zadeh & Tackley, 2010). Thermal convection in the mantle and some aspects of lithosphere dynamics are attributed to these thermally activated creep processes. The temperature–pressure dependence of geomaterials is important in understanding the role of convection in transporting heat. During dislocation creep diffusion-controlled climb of edge dislocations is the limiting process. At low temperatures this is extremely slow, but can be bypassed at stresses high enough to force dislocations through obstacles, a process known as low-temperature (Peierls) plasticity. In this case, the exponential proportionality factor  $C$  becomes stress-dependent. A commonly assumed form of the strain rate dependence on stress is:

$$\dot{\epsilon} = A \exp \left[ -\frac{H_0}{RT} \left( 1 - \frac{\sigma}{\sigma_p} \right)^2 \right] \quad (3.31a)$$

Where:

- $\sigma_p$  is the Peierls stress, which is of order 2–9 GPa, and
- $\sigma$  is the second invariant of the stress tensor.
- $H_0 = E + VP$

However, for simplified modelling dislocation creep deformation is more frequently used and approximated by:

$$\dot{\epsilon}_{ij} = A \tau_{ij}^n \exp\left(-\frac{E}{RT}\right) \quad \text{or} \quad \tau_{ij} = \frac{1}{A^{1/n} \dot{\epsilon}_{ij}^{(n-1)/n}} \exp\left(-\frac{E}{RT}\right) \quad (3.31b)$$

where  $\tau_{ij}$  corresponds to  $\tau_c$ , to indicate creep.

Creep processes can relax elastic stresses in the lower lithosphere. Such behaviour can be modeled with a rheological law that combines linear elasticity and linear or non-linear viscosity. A material that behaves both elastically and viscously is referred to as a viscoelastic material. The mantle behaves as a solid on short time scales and a fluid on

long time scales. This can be modeled using a Maxwell viscoelastic rheology with the viscous and elastic stress placed in series to determine the viscoelastic strain (and strain rate). According to the Hooke law of elasticity, the elastic strain  $\epsilon_{ij}$  and the deviatoric stress  $\tau_{ij}$  are related as

$$\tau_{ij} = \mu \epsilon_{ij} \quad (3.32)$$

where  $\mu$  is the shear modulus. For the fluid we assume a linear Newtonian relation between viscous strain rate and the stress (consider Eq. (1.29) with  $n = 1$  and  $C = 2\eta$ )

$$\tau_{ij} = 2\eta \frac{\partial \epsilon_{ij}}{\partial t} \quad (3.33)$$

where  $\eta$  is the fluid viscosity. The Maxwell model for a viscoelastic geometrical assumes that the strain rate of the geometrical is a superposition of the elastic and viscous strain rates, expressed as:

$$\frac{\partial \epsilon_{ij}}{\partial t} = \frac{\tau_{ij}}{2\eta} + \frac{1}{\mu} \frac{\partial \tau_{ij}}{\partial t} \text{ or } \left(1 + 2\tau_r \frac{\partial}{\partial t}\right) \tau_{ij} = 2\eta \frac{\partial \epsilon_{ij}}{\partial t} \quad (3.34)$$

where  $\tau_r = \eta/\mu$  is the viscoelastic relaxation (or Maxwell relaxation) time. Over short time scales compared with the time of relaxation  $\tau_r$  the geomaterial behaves elastically, and on time scales long compared with  $\tau_r$  the material behaves as a Newtonian fluid.

Because the effective viscosity of the shallow lithosphere is very high, its deformation is no longer controlled by dislocation creep; instead it is determined by (at lower pressures) the movement of blocks of the lithosphere along pre-existing faults of various orientations and (at higher pressures) deformation accommodated by distributed micro-cracking.

The dynamic friction along such faults depends only weakly upon the strain rate, and is often idealized using the rheological model of a perfectly plastic material, which does not exhibit work-hardening but flows plastically under constant stress. Hence, the stress–strain relationship for the lithosphere obeys the von Mises equations ([Prager and Hodge, 1951](#))

$$\tau_{ij} = \tau_y \frac{\dot{\epsilon}_{ij}}{\dot{\epsilon}} \quad (3.35)$$

where  $\tau_y$  is the yield limit. The second invariant of the stress,  $\tau = (0.5\tau_{kl}\tau_{kl})^{1/2}$ , equals the yield limit for any non-zero strain rate. When  $\tau < \tau_y$ , there is no plastic deformation and hence no motion along the faults. A comparison of Eqs. (3.29) and (3.35) shows that the perfectly plastic rheology can be considered as the limit of non-Newtonian power-law rheology as  $n \rightarrow \infty$  (and  $C = \kappa$ ). In rocks, the yield stress  $\tau_y$  depends on pressure. If  $\tau_y$  increases linearly with pressure, as is commonly assumed, then this gives the Drucker–Prager yield criterion,  $\tau_y = a + bP$ , where  $a$  and  $b$  are constants and  $P$  is the pressure. Brittle failure may be treated by the Mohr–Coulomb failure criterion, expressing a linear relationship between the shear stress and the normal stress resolved on the failure plane oriented at a particular angle,

$$\tau_y = Co + \sigma_n \tan \Phi = Co + \mu \sigma_n \quad (3.36)$$

where  $\tau_y$  and  $\sigma_n$  are the shear stress and normal stress acting on the failure plane,  $\Phi$  the angle of internal friction,  $Co$  the cohesion and  $\mu = \tan \phi$  the friction coefficient. It is often more convenient to express this in terms of the maximum shear stress  $\tau_{\max}$  and  $\bar{\sigma} = \frac{\sigma_1 + \sigma_3}{2}$ , the average of the maximum and minimum principle stresses:

$$\tau_{y\max} = \bar{\sigma} \sin \phi + c \cos \phi \quad (3.37)$$

In numerical models the Mohr–Coulomb criterion is often approximated by the Drucker–Prager criterion, with  $\tau_{\max}$  equal to the second stress invariant and pressure used in place of  $\bar{\sigma}$ .

In summary the relationships used frequently in geodynamic modelling are.

- fluid behaviour of geomaterials is described by Eqs. (3.29)–(3.31), and (3.33),
- elastic behaviour by Eq. (3.32),
- viscoelastic by Eq. (3.34),
- perfectly plastic by Eq. (3.35) and
- brittle by Eq. (3.36)–(3.37).

### 2.1.5 Byerlee's law

Byerlee (1978) has experimentally demonstrated that for the majority of rocks the Coulomb failure criterion applies in the form (Figure 3.2)

$$\tau = 0.85 \sigma_n, \quad \sigma_n \leq 200 \text{ MPa} \quad (3.38)$$

$$\tau = 50 \text{ MPa} + 0.6 \sigma_n, \quad 1700 \text{ MPa} > \sigma_n > 200 \text{ MPa} \quad (3.38b)$$

or, assuming

$$|\sigma_3| < |\sigma_2| < |\sigma_1| \quad (3.39)$$

$$\sigma_1 = 4.7\sigma_3, \quad \sigma_3 \leq 114 \text{ MPa} \quad (3.40a)$$

$$\sigma_1 = 3.1\sigma_3 + 177 \text{ MPa}, \quad 1094 \text{ MPa} > \sigma_3 > 114 \text{ MPa} \quad (3.40n)$$

[Byerlee \(1978\)](#) has also shown that frictional properties of rocks are weakly dependent on rock type.

This explains why tectonic faults may intersect heterogeneous structures. However, as seen before, brittle strength depends heavily on pressure variations caused by tectonic stress or fluids. The latter are characterized by the fluid pressure factor  $\lambda = \rho_w/\rho$  where  $\rho_w$  is the density of water and  $\rho$  is the rock density (for explanation see [Byerlee, 1978](#)):

$$\Delta\sigma \Rightarrow \sigma_1 - \sigma_3 = \alpha \rho g z (1 - \lambda) \quad (3.41)$$

Where:

- $\alpha = 1-R^{-1}$  for normal faulting,
- $\alpha = R-1$  for thrusting,
- $\alpha = (R-1)/(1+\theta(R-1))$  for strike-slip,

with  $R = [(1 + \varphi^2)^{1/2} - \varphi]^{-2}$  and  $\tan\theta = (\sigma_2 - \sigma_3)/(\sigma_1 - \sigma_3) < 1$ .  $\sigma_1, \sigma_2$  and  $\sigma_3$  are the principal stresses

It is noteworthy that Byerlee's data can be also fitted using a weak power law ([Lockner, 1995](#)):

$$|\tau| = \sigma_n^{0.94} \quad (3.42)$$

where  $|\tau|$  is the absolute value of shear stress and  $\sigma_n$  the normal stress.

Deep drilling has provided direct evidence in support of Byerlee's law for the first few kilometers of the crust (1–14 km) (e.g., [Zoback et al., 1993](#)).

However, this law is probably not applicable for the depths exceeding 30–50 km (e.g., [Kirby et al., 1991](#)). At high depth/pressure or temperature, brittle failure may switch to a semibrittle regime (e.g., [Chester, 1995](#); [Bos and Spiers, 2002](#)). One of discussed possibilities refers to above discussed Peierls' plasticity ([Goetze and Evans, 1979](#)) that takes place at high differential stresses ( $>100$ – $200$  MPa), when mixed dislocation glide and climb occur ([Karato et al., 1986](#); [Karato, 1998](#)).

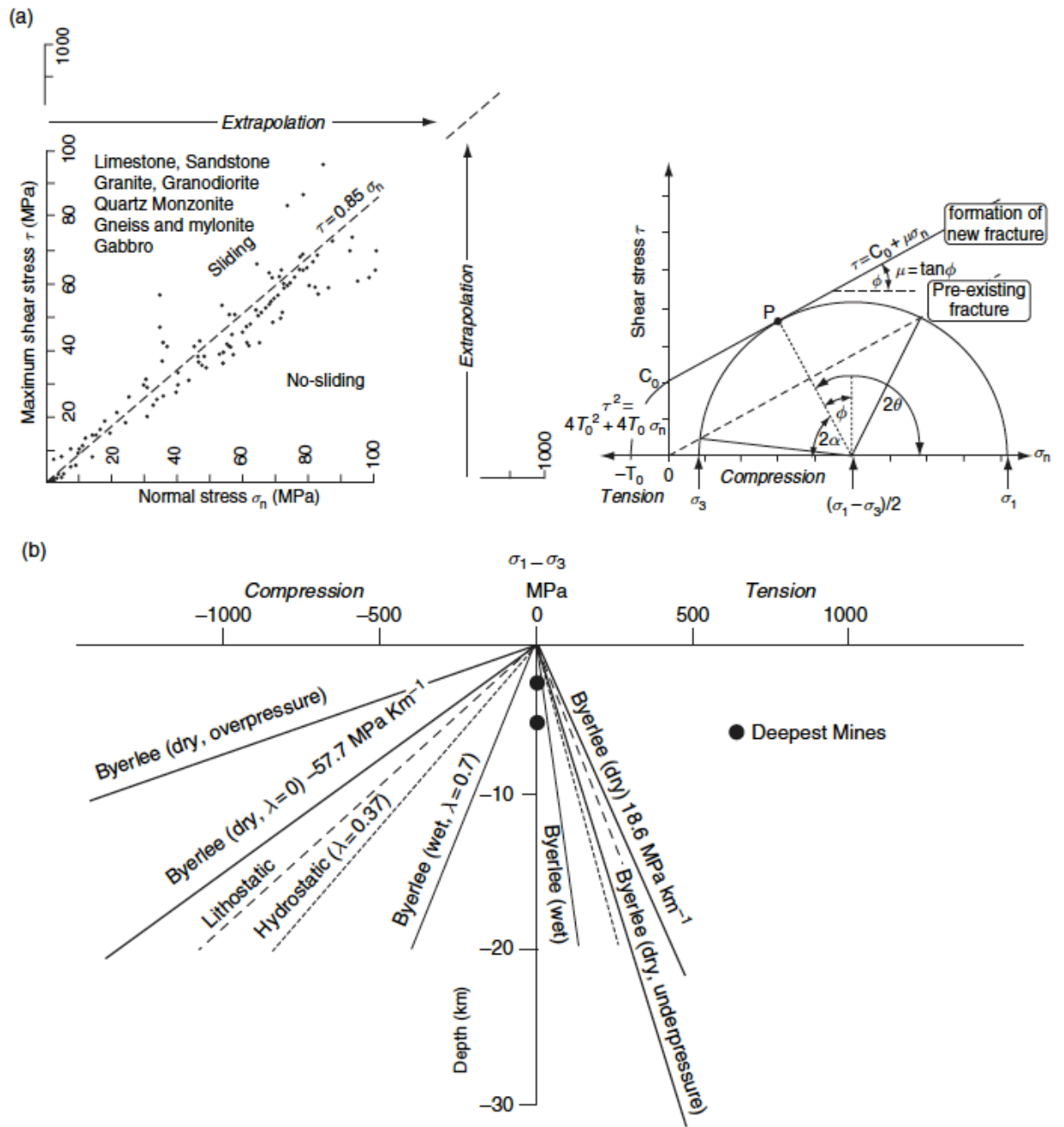


Figure 3.2 a) Right: Experimentally established linear dependence between normal stress and shear stress for compressional failure of various rocks. These data demonstrate the applicability of Mohr-Coulomb failure criterion  $\tau = C_0 + \sigma_n \tan \phi = C_0 + \mu \sigma_n$  and relative independence of the Byerlee's law on rock type. However, this law has been validated only for first several kilometers of the upper crust (pressures of few MPa). It is commonly linearly extrapolated to more important depth/pressure conditions (up to 40–50 km depth or 1–1.5 GPa). Left: Two principal failure criteria (Mohr-Coulomb). Under general compression ( $\sigma_n > 0$ ), Coulomb criterion predicts linear relation between normal stress  $\sigma_n$  and shear stress  $\tau$ . Under general extension ( $\sigma_n < 0$ ), the modified parabolic criterion applies.  $C_0$  is cohesion,  $\tau_0$  is tension cutoff (in here, elsewhere this symbol represents initial temperature),  $\mu$  is friction coefficient, and  $\sigma_1$  and  $\sigma_3$  are principal stresses.  $2\theta$  is angle between two conjugated faults forming under stress  $\sigma_1$ ,  $\phi = \pi/2 - 2\theta$  is friction angle ( $\mu = \tan \phi$ ). For most dry rocks  $\phi = 30^\circ$ . It can be seen that Byerlee's law corresponds to Mohr-Coulomb plasticity with preexisting fractures. (b) Dependence of brittle strength on depth/pressure: lithostatic pressure, fluid pressure, and tectonically induced over- or



*underpressure. Rocks are weaker under extension than under compression, which explains frequent deep seismicity in overall weak rift zones. Tectonic extension or compression may change total pressure, and, consequently, brittle strength, by a factor of, respectively, 0.5–2;  $\lambda$  is pore pressure factor. (after [Byerlee \(1978\)](#), [Burov \(2007\)](#)).*

### 2.1.6 Additional equations

The equations of continuity, motion and heat balance compose the governing equations required to model of mantle and lithosphere dynamics. However, additional equations are necessary to describe the behaviour of mantle rocks, namely, equations of state, rheological law (or equation for viscosity), equation for phase transformations, etc.

In many practical applications, a linear dependence of density on temperature (equation of state) is assumed:

$$\rho = \rho_0[1 - \alpha(T - T_0)] \quad (3.43)$$

Where:

- $\rho_0$  is a reference density;
- $\alpha$  is the coefficient of thermal expansivity;
- $T_0$  is a reference temperature.

If phase transformations of mantle rocks are considered the equation of state is modified. The viscosity of mantle rocks is the least well-known parameter used in numerical modelling of geodynamic problems. The mantle viscosity can depend on temperature, pressure, grain size, content of water or melt, stress, etc. Therefore various representations of viscosity in geodynamic modelling are used depending on circumstances and the modelling requirements. For more insight on pressure dependence in the mantle see [Zlotnik et al, \(2009\)](#)

### 2.1.7 Boussinesq approximation

Heat transfer controls mantle dynamics, therefore, mantle properties are generally functions of temperature ([Ismail-Zadeh & Tackley, 2010](#)). The variations in density due to temperature variations are generally small and yet are the cause of the mantle motion. If the density variation is not large, one may treat the density as constant in the continuity equation (i.e. the fluid is assumed to be incompressible, Eq. 3.5) and in the energy equation, treating density as variable only in the gravitational (buoyancy) term of the momentum equation.

Consider Stokes equation (3.17) and split the term  $\rho \mathbf{F}_i = \rho \mathbf{g}_i$  into two parts:  $\rho_0 \mathbf{g}_i + (\rho - \rho_0) \mathbf{g}_i$ . The first part can be included with pressure and the density variation is retained in

the gravitational term. The remaining term can be expressed as:

$$(\rho - \rho_0)g_i = -\rho_0 g_i \alpha(T - T_0) \quad (3.44)$$

Such simplification of the model is called the Boussinesq approximation. In the strict form of this, all physical properties except viscosity are constant (Ismail-Zadeh & Tackley, 2010). The dimensionless mass and energy conservation equations then become

$$-\frac{\partial P}{\partial x_i} + \frac{\partial}{\partial x_j} \left\{ \eta \left( \frac{\partial u_i}{\partial x_j} + \frac{\partial u_j}{\partial x_i} - \frac{2}{3} \delta_{ij} \frac{\partial u_k}{\partial x_k} \right) \right\} = \frac{Ra}{\alpha \Delta T} \rho \delta_{i3} \quad ; \quad \frac{\partial T}{\partial t} + u_{ij} \frac{\partial T}{\partial x_j} = \frac{\partial^2 T}{\partial x_j^2} + H \quad (3.45)$$

If the fluid is compressible, compressibility is incorporated in a model using either the extended Boussinesq approximation, in which the density is still assumed constant in the continuity equation but extra terms are included in the energy equation, or the anelastic approximation, in which the density is assumed to vary with position but not with time.

## 2.2 Modelling (numerical/analytical) boundary and initial conditions

The equations given above govern the slow movements of the Earth's mantle and lithosphere. They are the same equations whether the movement is, for example, a thermal plume rising beneath a particular region, subduction of the lithosphere, a mid-ocean ridge, convective flow in the upper mantle or whole mantle convection. However, it is the boundary and initial conditions that dictate the particular solutions of the governing equations.

A brief review of the numerical boundary conditions follows. When the condition on the surface of Earth assumes zero relative velocity between the surface and the air immediately at the surface, we refer to the condition as the no-slip (or rigid) condition. If the surface is stationary, then

$$v_1 = v_2 = v_3 = 0 \quad (3.46)$$

When the velocity at the boundary is a finite, non-zero value and there is no mass flow in to or out of the model domain, the velocity vector immediately adjacent to the boundary must be tangential to this boundary. If  $\mathbf{n}$  is a unit normal vector at a point on the boundary and  $\mathbf{v}_\tau$  is the projection of the velocity vector onto the tangent plane at the same point on

the boundary, the condition at this boundary can be given as:

$$\mathbf{v} \cdot \mathbf{n} = 0, \quad \frac{\partial v_{\tau}}{\partial n} \quad (3.47)$$

These conditions are called free-slip conditions. The actual surface of the Earth is free to move up and down. The above conditions, in which the upper boundary of the model domain represents the Earth's surface and there is no vertical motion at the boundary, are idealizations made to simplify the model. Modelling an actual free surface that deflects vertically is more complicated but methods exist.

There is an analogous 'no-slip' condition associated with the temperature at the surface. If the temperature at the surface is denoted by  $T_v$ , then the temperature immediately in contact with the surface is also  $T_v$ . If in a given problem the temperature is known, then the condition on the temperature at the upper boundary of the model domain is

$$T = T_v \quad (3.48)$$

On the other hand, if the temperature at the surface is not known, e.g. if it is changing with time due to heat transfer to the surface, then the Fourier law of heat conduction provides the boundary condition at the surface. If we let  $\dot{q}_v$  denote the instantaneous heat flux to the surface, then from the Fourier law

$$\dot{q}_v = - \left( k \frac{\partial T}{\partial n} \right)_v \quad (3.49)$$

where  $n$  denotes the direction normal to the surface. The surface rocks are responding to the heat transfer on the surface,  $\dot{q}_v$ , hence changing  $T_v$ , which in turn affects  $\dot{q}_v$ . This is a general form of the unsteady heat transfer problems and it must be solved by treating the viscous flow and thermal response at the surface simultaneously ([Ismail-Zadeh & Tackley, 2010](#)). That is,

$$\left( \frac{\partial T}{\partial n} \right)_v = - \frac{\dot{q}_v}{k} \quad (3.50)$$

While the above discussion refers to the top boundary of the domain, similar conditions also apply to the lower boundary, an example from geodynamics is the core–mantle boundary.

At the sides, no-slip or free-slip (mirrored) velocity conditions may be assumed, but if the model is intended to represent the entire mantle then periodic boundaries are most realistic. In local or regional models, which are often used to model the crust and/or lithosphere, it is common for material to flow in or out of the domain, with a prescribed velocity, temperature or some other conditions such as prescribed normal stress. These numerical boundary conditions are set to mimic the physical and tectonic boundary conditions imposed by nature.

### **3. PART 2: MODELLING THE LITHOSPHERE**

Deformation laws described in the previous section allow for the development of

lithospheric strength profiles. These profiles are identified as Brace–Goetze lithosphere profiles, or yield strength envelopes, YSE (see Fig. 3.3 for an example, Burov, 2007). Lithospheric strength is defined as the limiting stress above which the irreversible deformation occurs. Therefore the strength profile represents the total force per unit width required to deform the lithosphere at a given strain rate, temperature and composition.

From the above definition the profiles consist of:

- straight line that correspond to brittle deformation described by a Byerlee's law (Fig. 3.3);
- curve, corresponding to plastic flow described by a power law (Fig. 3.3).

The area under the strength profile provides the vertically integrated lithospheric strength,  $S$ :

$$S = \int_0^z \sigma(z, t, \varepsilon, \dot{p}, T) dz \quad (3.51)$$

where the  $z$ -axis is oriented downwards.

YSE profiles are first order approximations to lithospheric deformation, they are a 1D representation of the system. For real Earth materials, the strain-stress relationship is time-dependent. YSE can therefore be used to test the first order impact of rheological parameters, rheological laws, thermal distribution and velocity boundary conditions.

### 3.1 Yield Strength Envelope profile construction

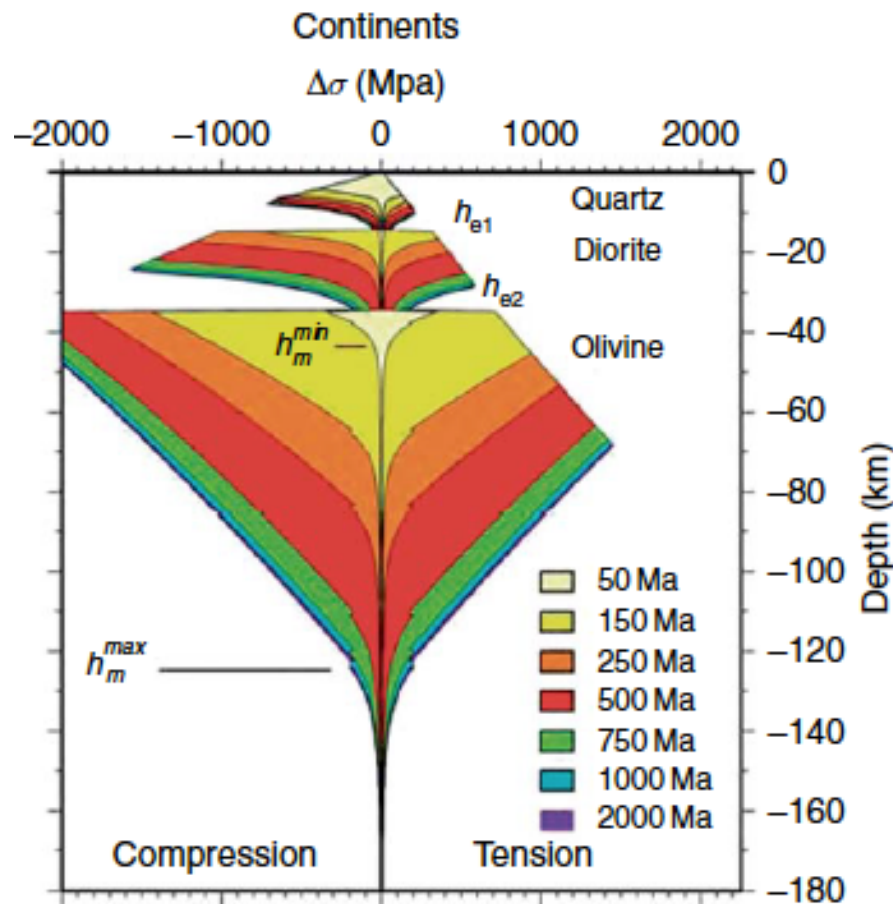
Since rifting initiates in general in continental settings, I will not address the characteristic of the oceanic lithosphere. In general, continental lithosphere is modelled as a system composed by an upper crust, lower crust and lithospheric mantle.

The yield strength envelope outlines at a given depth, the strength of a rock, determined by which deformation mechanism requires the least stress, in this case either viscous flow deformation,  $\tau_c$  ( Eq. 3.31b - which in case of a 3-layered continental lithosphere, gives 3 power laws) and yielding via Mohr-Coulomb / Byerlee's law,  $\tau_y$  (Eq. 3.36):

$$\tau = \min (\tau_y, \tau_c) \quad (3.52)$$

this leads to a “Christmas-tree” pattern of rheological profiles as shown in Fig. 3.3.

Figure 3.3 Examples of rheological YSEs (Goetze and Evans, 1979) for continents. The YSE is shown as a function of the thermo-tectonic age (see legend). Thick crust and multilayered



continental lithosphere could give rise to mechanically decoupled rheological layers as shown by ductile flow portion in the intermediate or lower crust (modified after Burov, 2007).

For the analysis of the YSE shown in Figure 3.3 it is possible to see that the brittle

deformation regime, increases linearly with depth as the normal stress increases (i.e. it also depends on the average density of the overlying lithospheric layers); in this regime rock strength depends also on the pore fluid pressure and pore geometry inside a rock (Burov, 2007), but is insensitive to mineralogy/composition. As discussed previously (section 2.1.5) in brittle deformation, the rock strength (which for the lithosphere is represented by the YSE profile) is different for extension and compression while such a difference does not exist for ductile deformation (Fig. 3.3). Table 3.2 shows mechanical parameters and variables used for the Mohr-Coulomb/Byerlee law and power law. Since, as the first approximation, the rock fails when its rheologically weakest mineral phase fails, and the weakest mineral in the crustal rocks is quartz, upper crustal rheology is commonly approximated by deformation of quartzite. Alternatively, the lower crustal behaviour is described by a diabase or granulite, with olivine used to determine mantle deformation composition (Tab 3.1).

The intersection between the straight line (Byerlee) and the 3 curves (power laws for the

upper crust, lower crust and lithospheric mantle) in Fig. 3.3 defines 3 brittle-ductile transitions (BDT), where strength profiles have 3 maxima. The max strength at the intersection points, increases with depth and migrate vertically (upwards or downwards) for several reasons. For example, Table 3.1 shows the most common power law parameters taken into account for Geodynamic modelling, while Fig. 3.4 shows an example of how the choice of the parameters and the thickness of the plate (different thermal modes) can influence the shape of the YSE and, hence, depth of the 3 transitions. Nevertheless, the plate layering and total thickness as well as composition greatly influence the integrated strength of the lithosphere and the mechanical coupling between the layers.

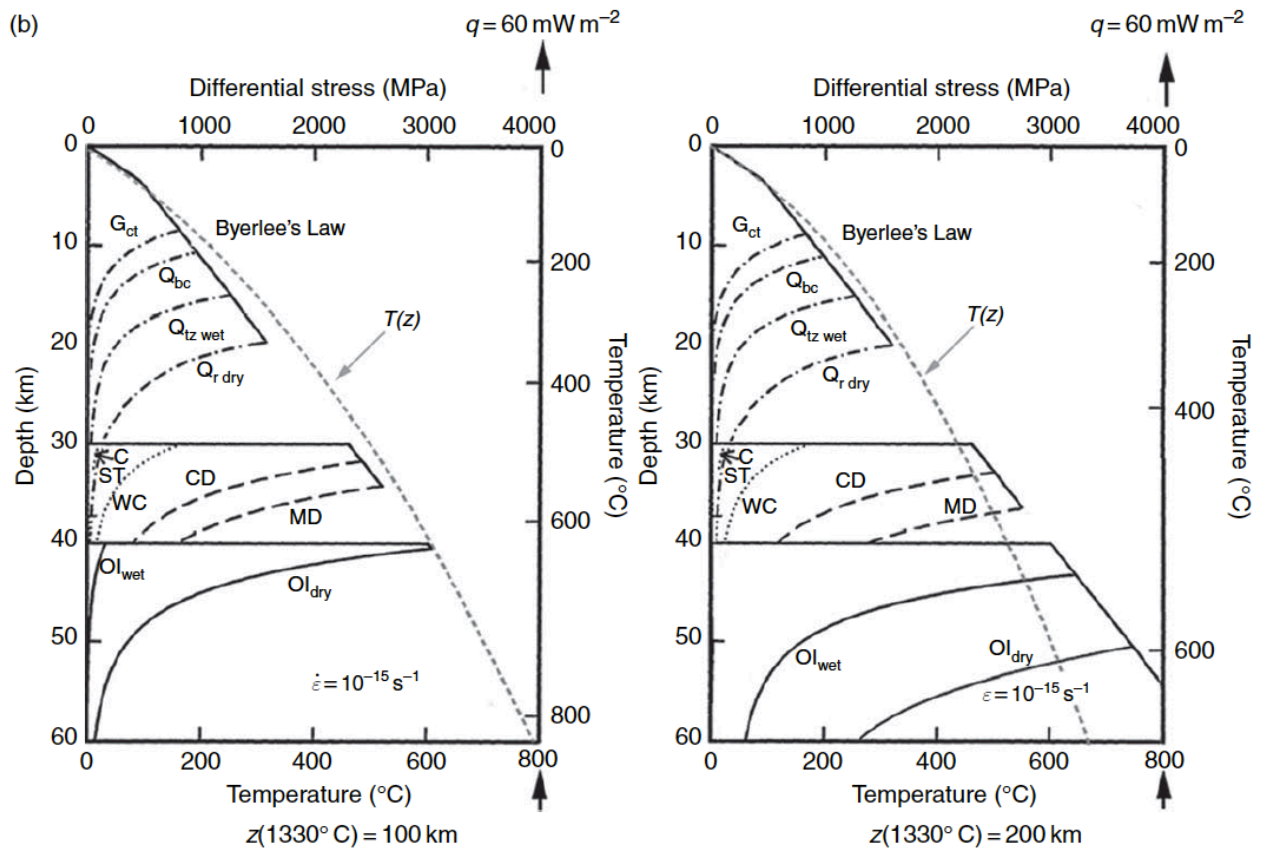


Figure 3.4 Influence of compositional variation, plate thickness  $a = z(1330^{\circ}\text{C})$  and fluid content on continental YSE computed for typical surface heat flow,  $q$ , of  $60 \text{ mW m}^{-2}$  for two different thermal models: equilibrium thermal plate thickness of 100km (left: Champan, 1986)) and of 200km (right: plate cooling model, (Burov and Diament, 1995). CD, dry Columbia diabase; MD, dry Maryland diabase; WC, Pikwitonei granulite; ST and C, diabase from Shelton and Tullis (1981)) and Caristan (1982). See Tab. 3.1) The upper crust is wet quartzite from Gleason and Tullis 1995; Oldry and Olwet, dry and wet dunite from Chopra and Paterson, 1984.  $Q_{bc}$ , dry quartzite from Brace and Kohlstedt (1982).  $G_{gt}$ , wet granite from Carter and Tsenn (1987).  $Q_r$ , extra strong dry quartz from Ranally (1995). Comparison of the YSE computed for two different thermal plate thicknesses demonstrates differences in estimated mantle strength: the continental

heat flux used as a common surface boundary condition mainly affects crustal temperature distribution. The mantle part of the geotherm primarily depends on the position of the thermal bottom of the lithosphere. The left ‘weak’ (for this example) YSE results from the assumption that continents have the same or even smaller thickness than the oceans (Jackson, 2002). The right figure represents a stronger rheology. (after Burov, 2007).

However, not only the rheological parameters can control the YSE width and depth of brittle-ductile transitions. Figure 3.5 shows how transitions in the crust and lithospheric mantle can change as a function of tectonic deformation velocity and/or magnitude of the tectonic forces. The YSE is therefore also a function of the applied boundary condition such as tectonic deviatoric stress,  $\sigma_1$ - $\sigma_2$ , horizontal velocity,  $v_{xx}$ , or initial strain rate,  $\dot{\epsilon}_{in}$ . In general for 1D modelling it is straightforward to use as boundary condition the initial strain rate,  $\dot{\epsilon}_{in}$ . For example, at a given depth and for a given composition and geothermal gradient, a higher strain rate will produce a YSE with greater strength (Fig. 3.5). This implies that, in such an approach, the depth of the brittle–ductile transition is strain rate dependent. For strain rates of  $10^{-17}$ – $10^{-14}$  s $^{-1}$ , typical of the continental lithosphere, the brittle–ductile transition occurs at  $\sim 300$ – $400$  °C in quartz and at  $600$ – $700$  °C in olivine.

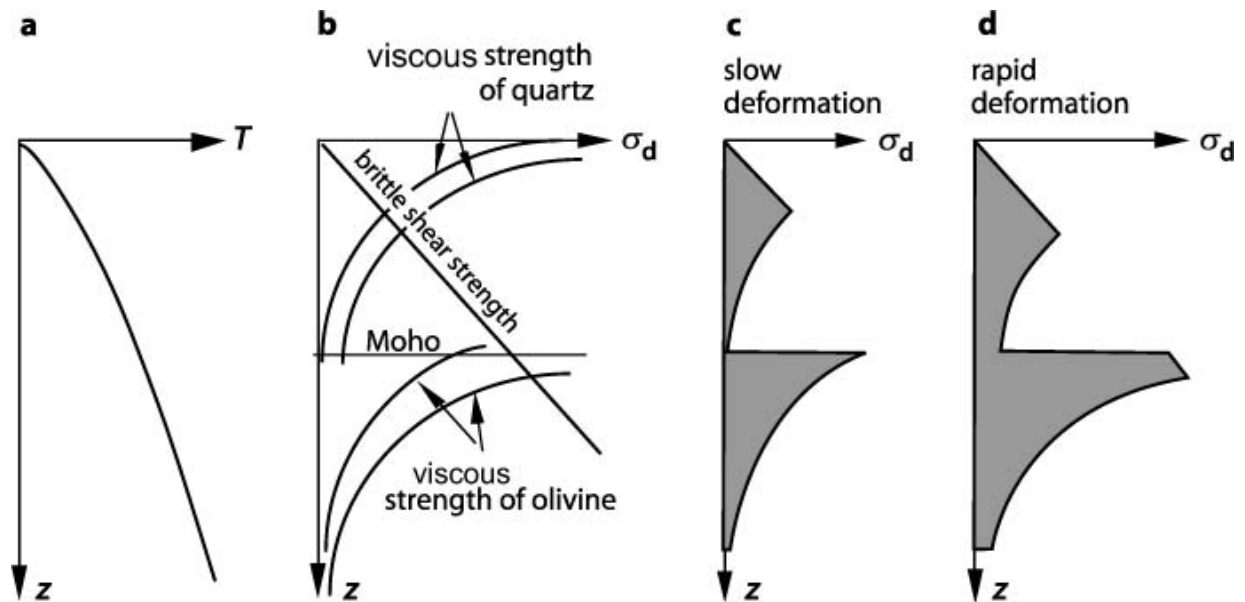


Figure 3.5 Schematic illustration of a Brace-Goetze lithosphere. (a) Temperature  $T$  as a function of depth  $z$ . This curve has the shape of a typical continental geotherm. (b), (c) and (d) show shear strength (labeled as  $\sigma_d$  corresponding to  $\tau = \min(\tau_y, \tau_c)$  in this work) as a function of depth. (b) Shear strength due to brittle failure (straight line (constant, non-zero gradient) and viscous deformation (curved lines) for two different strain rates and the material constants for quartz and olivine. At any given depth, the curve with the higher viscous strength corresponds to the higher strain rates, (c) and (d) are strength profiles constructed from (b) for low and high strain rates. Integrating the shaded area yields the integrated strength in units of Nm $^{-1}$ . This integrated



*strength may be interpreted as the force per meter length of orogen applied in the direction normal to the orogen (assuming the orogen is uniformly deforming). Note the cartoon indicates that, at high strain rates (profile d), the upper mantle will deform in a brittle fashion just below the Moho (After Stüwe (2007)).*

For a given composition, there will be a synergistic effect on lithospheric strength when the variation of the initial strain rate is combined with a change in heat flow (temperature distributions). Figure 3.6 shows an example where slow deformation (low strain rate) and/or high heat flow (temperatures), the BDT is shallow, while for fast deformation and/or low heat flow has a deeper BDT.

In summary, the brittle-ductile transition may migrate depending on:

- Initial Conditions:
  - Temperature gradient (i.e. Moho temperature and basal lithosphere temperature);
  - Composition and rheological layering (in particular, the presence of melts and fluids).
- Tectonic boundary conditions
  - E.g. Initial strain rates

As seen in this section, lithosphere strength is controlled by a large number of thermodynamic and structural parameters. As a result, rheological models and lithospheric strength profiles constrained for different tectonic settings could be very different (e.g. compressional vs extensional tectonic settings).

In particular for the continental lithosphere the analysis of initial and boundary conditions affecting the strength of continental lithosphere shows that:

- Continental lithosphere is stronger under compression than under extension;
- Cold lithosphere is significantly stronger than hot lithosphere;
- Strength increases with increasing strain rate;
- Fluids reduce crustal and mantle strength dramatically.

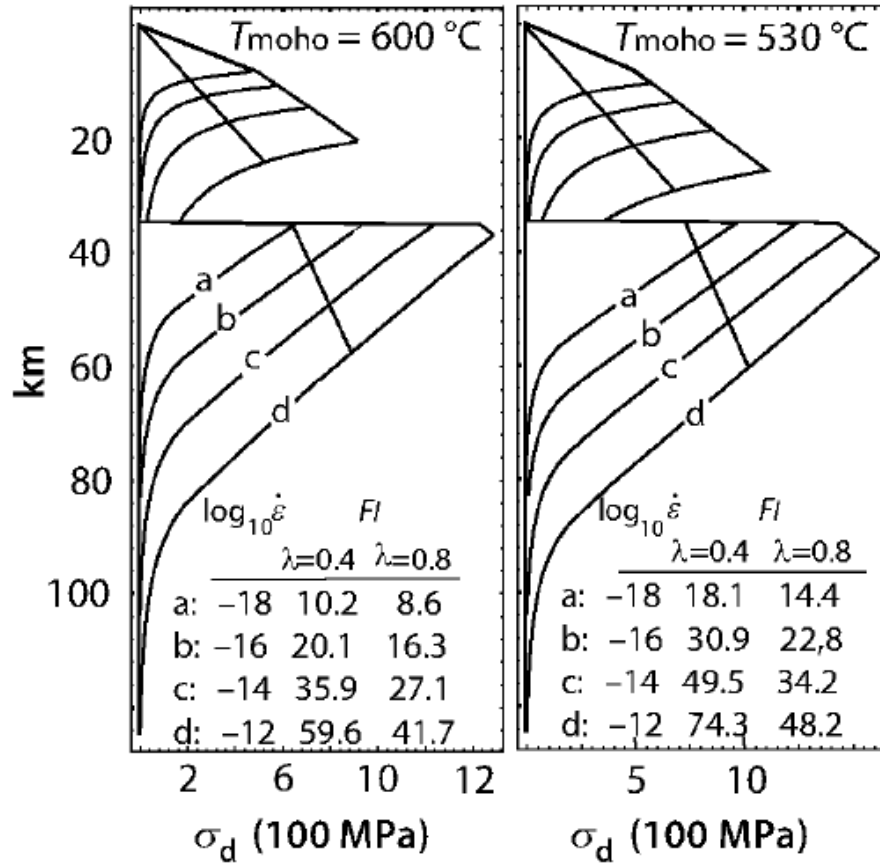


Figure 3.6 Strength profiles for the continental lithosphere as calculated with the model for a Brace-Goetze lithosphere (After Stüwe (2007)). (a), (b), (c) and (d) are profiles for four different geologically relevant initial strain rates. The two diagrams show the strength profiles for two different Moho-temperatures that result from assumptions for the radiogenic surface heat production of  $So = 5 \times 10^{-6} \text{ Wm}^{-3}$  and  $So = 7 \times 10^{-6} \text{ Wm}^{-3}$ . In each diagram two linear curves for brittle failure for extension (steeper one) and compression are plotted.

\

Table (3.1) Commonly inferred parameters of dislocation creep (power law). 1- Mackwell et al. (1998); 2 - Gleason and Tullis (1995) ; 3 - Ranalli and Murphy (1987); 4 - Brace and Kohlstedt (1980); 5 - Kirby and Kronenberg; 6 - Wilks and Carter (1990); 7 - Chopra and Paterson (1984); 8 - Chopra and Paterson (1981);

Rock name	Rock symbol	Pre-exponent constant: A [MPa <sup>-n</sup> s <sup>-1</sup> ]	Exponent: n [Dimensionless]	Activation Energy [KJ mol <sup>-1</sup> ]	References
<u>Upper Crust</u>		A <sub>UC</sub>	n <sub>UC</sub>	E <sub>UC</sub>	
Wet Granite	G <sub>ct</sub>	2x10 <sup>-4</sup>	1.9	140	1
Wet Quartzite		1.1x10 <sup>-4</sup>	4	223	2
Dry Quartzite	Q <sub>bc</sub>	6.3x10 <sup>-6</sup>	2.4	156	3
Wet Quartzite	Q <sub>ztWet</sub>	1.1x10 <sup>-4</sup>	4	223	2
Extra Strong Dry Quartzite	Q <sub>rdry</sub>	10 <sup>-4</sup>	2.4	160	4; 5; 6
<u>Lower Crust</u>		A <sub>LC</sub>	n <sub>LC</sub>	E <sub>LC</sub>	
Columbia diabase (weak)	C	190	4.7	485	1
Maryland diabase (strong)	MD	8	4.7	485	1
Undried Pikwitonei granulite	WC	1.4x10 <sup>-4</sup>	4.2	445	6
<u>Lithospheric Mantle</u>		A <sub>LM</sub>	n <sub>LM</sub>	E <sub>LM</sub>	
wet Anita Bay dunite	Ol <sub>Wet</sub>	955	3.4	444	7
Dry Anita Bay dunite	Ol <sub>dry</sub>	4.5	3.6	535	8
Dry Olivine	Ol <sub>Dry</sub>	4.85x10 <sup>4</sup>	3.5	535	8

Table (3.2) Thermal and mechanical parameters of the lithosphere used in model simulations

Parameter	Abbreviation	Unit	Range
<b>Geometrical parameters</b>			
Upper crust thickness	UC	km	15
Lower crust thickness	LC	km	15
Lithospheric mantle	LM	km	70
<b>Thermal parameters and variables</b>			
Thermal conductivity	K	$\text{Wm}^{-1} \text{K}^{-1}$	2.6
Thermal diffusivity	K	$\text{m}^2 \text{s}^{-1}$	$10^{-6}$
Crust radioactive production	H	$\text{mW m}^{-3}$	0-1-2
Lithosphere-Asthenosphere Boundary	$T_{\text{LAB}}$	$^{\circ}\text{C}$	1300
Moho temperature (Rifting onset)	$T_{\text{m}}$	$^{\circ}\text{C}$	400 - 850
Initial Moho temperature depth (Rifting onset)	----	km	30
Thermal expansion	$\alpha$	$10^{-5} \text{K}^{-1}$	3
<b>Mechanical parameters and variables</b>			
<i>Byerlee law</i>			
Upper crust density	$\rho_{\text{UC}}$	$\text{kg m}^{-3}$	2700
Lower crust density	$\rho_{\text{LC}}$	$\text{kg m}^{-3}$	2900
Lithospheric mantle density	$\rho_{\text{LM}}$	$\text{kg m}^{-3}$	3300
Cohesion	$C_0$	MPa	60
Friction coefficient	M	Dimensionless	0.6
Initial strain rates	$\dot{\epsilon}_{\text{in}}$	$\text{s}^{-1}$	$10^{-18} - 10^{-12}$
Gravity constant	g	$\text{m s}^{-2}$	9.81
Extensional regime coefficient	---	Dimensionless	0.65
Deviatoric stress	$\tau$	MPa	Calculated
Lithostatic pressure	P	MPa	Calculated
<i>Power law</i>			
Universal gas constant	R	$\text{J(mol K)}^{-1}$	8.314
Viscosity	$\eta$	Pa s	Calculated
<b>Localization parameters and variables</b>			
Brittle thickness on YSE	$th_b$	km	Calculated
Localization index	I	Dimensionless	Calculated

### 3.2 Conceptual models and project rationale

As introduced in Chapter 2, the necessity to model rifting as a polyphase process arises from geological evidences that:

- Tectonic divergent forces acting on the lithosphere fluctuate in time and space;
- Rifting generally develops through a series of stretching phases and tectonic quiescence.

Due to the approach outlined here, proof of the concept is required firstly using a simple methodology and subsequently increasing the numerical model complexity. Therefore, the aim of this section is to provide a conceptual model which:

- Describes the underlying physics of polyphase rifting;
- Explains and tests model assumptions;
- Provides an indication on the most appropriate initial condition from experimental and geological/geophysical data (rheological parameters, initial geothermal gradients, rheological layering) and set of kinematic (i.e. velocity or initial strain rate) and dynamic boundary conditions, to be used in later 2D modelling;
- Verifies and validates the approach against literature models.

At present, there are no polyphase models developed that are constrained as physical experiments (i.e. series of simulations/tests with several rifting phases and intermitted cooling stages allowing the full recovery of the lithospheric thickness). For example, [Tett et al., \(1995\)](#) tested 5 rifting ‘paths’, by varying the duration, rate of the deformation and duration of the cooling according to the evolution of the Newfoundland-Iberia margins, thus providing an explanation for the evolution of just that particular area without providing an understanding of the underlying physics of polyphase rifting. [Nalibof and Buiter \(2015\)](#) made substantial improvement taking into account a duration of the quiescence period on a statistical bases, however limited the experiments to cooling periods between 30 Myr and 40 Myr, which, in their modes, allows for minor lithospheric thickness recovering, less than the original thickness.

Therefore, the novelty of this studies approach necessitates an initial screening of the compositional parameters, temperatures distribution etc., in a 1D monophase setting, validating the hypothesis against existing models. The 1D simulations are developed with the selected parameters in Tab. 3.2 and 3.3 and are compared with the monophase results and literature models to evaluate first order model predictions. The 1D simulations are limited at a single dimension and cannot give a complete spectrum of the possible lithosphere evolution and basins formation, which will be explored in 2D.

Here, using methodology described in literature (Kaus and Podladchikov, 2006 and Cramer and Kaus, 2010), I first explain how it is possible to quantify the ability of the lithosphere to localize strain and how this is connected to a prediction of the final sedimentary basin geometry (e.g. Lu et al., 2011), and the meaning and importance of localization index.

Then the monophasic 1D models are presented with calculated localization indexes. The 1D polyphase models are subsequently developed.

### 3.2.1 Parameterisation of rifting histories

The most evident difference between rifted basins is their width. In fact rifts are often classified as wide or narrow. This geometrical feature is an indication (or “symptom”) of the ability of the lithospheric strain to localize within a limited area or distribute across a much wider region. This is also associated with the asymmetry of sedimentary basins and the uppermost part of the lithosphere. The localization/delocalization of strain is also a characteristic of compressive tectonic settings. Hence, many studies have been interested in understanding the dominant factors leading to localization in the lithosphere. In particular, several studies have focused on the mechanisms that favor lithospheric localization, for example grain size reduction (Kameyama et al., 1997; Jin et al., 1998; Braun et al., 1999), two phase damage (Bercovici et al., 2001a,b; Landuyt and Bercovici, 2009), lattice preferred orientation of olivine (Tommasi et al., 2009), or shear heating (Schubert and Turcotte, 1972; Bercovici, 1996; Regenauer-Lieb and Yuen, 2004). With these mechanisms involving many elements, Kaus and Podladchikov (2006) performed a systematic analysis to unravel the first order parameter leading to lithospheric localization. They were able to derive a scaling law for the onset of localization showing that this occurs when:

$$\dot{\epsilon}_{in} \geq \frac{1.4}{\Delta L} \sqrt{\frac{\kappa \rho c_p}{\eta_0 \gamma}} \quad (3.53)$$

Where:

- $\kappa$  is the thermal diffusivity,
- $\eta_0$  the viscosity at temperature  $T_0$ ,
- $\Delta L$  an heterogeneity length scale, and
- $\gamma$  the temperature-dependence of viscosity in the Frank-Kamenetskii approximation ( $\eta = \eta_0 \exp [-\gamma(T - T_0)]$ ) which can be computed from a power-

law creep rheology by  $\gamma = E/nRT_0^2$  (e.g., [Solomatov and Moresi, 1996](#)).

Therefore, in order for the lithosphere to localize deformation, the presence of an heterogeneity of a scale greater than a threshold value is required, calculated using the following relationship:

$$\Delta L = \frac{1.4}{\dot{\epsilon}_{in}} \sqrt{\frac{k}{\eta_0 \gamma}} \quad (3.54)$$

where  $k$  is the thermal conductivity.

The onset of localization is a strong function of this length scale  $\Delta L$ . Hence, it is possible to derive a localization condition and calculate the relative localization index as following:

$$I = \frac{\dot{\epsilon}_{in} \Delta L}{1.4} \sqrt{\frac{\eta_0 E}{nRT_0^2 k}} \quad (3.55)$$

From their study, localization is predicted when  $I > 1$ . For a given simulation, all parameters in equation (3.55) are known, except the length scale  $\Delta L$ . [Kaus and Podladchikov \(2006\)](#), used the width of the heterogeneity placed in their 2D numerical model as the characteristic length scale.

[Crameri and Kaus \(2010\)](#) further extended the parameter study by taking into account the rheological stratification of the lithosphere as well as non-linear power law rheologies for a lithosphere under compression. As the characteristic length they considered the thickness given by the sum of the Coulomb/Byerlee and Peierls layers on the yield envelope strength profile (which corresponds to the thickness of the brittle portion of the YSE profile). The 1-D models derived in this latter study were capable of predicting whether lithospheric localization occurs or not. Using a 1- D deformation code they computed the time-dependent  $\Delta L$  and localization index  $I$ , using  $\eta_0 = \tau_{II} / (2 \dot{\epsilon}_{in})$  in the upper crust and  $\eta_0 = \eta_{eff}$  elsewhere. Using a semi-analytical method, employing the comparison of the 1-D and 2-D results, they were able to establish  $I=1$  as the threshold value between lithospheric localization and non-localization.

[Lu et al. \(2011\)](#) applied this approach to study the formation of rifting basin in cratons. They further developed [Crameri and Kaus \(2010\)](#) approach to better constrain the prediction from 1D models and reduce the discrepancy between the onset strain rate

required in the 1D and those needed to realize localization in the 2D models. In addition, these authors were able to determine when localization is symmetric or asymmetric.

Crameri and Kaus (2010) and Lu et al. (2011) have produced phase diagrams from 1D simulation results (respectively Figs. 3.9 a1 a2 and Figs. 3.9 b1 b2) in which the localization indexes are plotted in a temperature versus initial strain rate space. They have subsequently compared these phase diagrams with results from 2D numerical models confirming that 1D predictions corresponded to final 2D results. It is important point out that these authors found the combination of strain rate, temperature (thermal age in the case of Lu et al., 2011 and lithosphere-asthenosphere boundary (LAB) temperature for Crameri and Kaus (2010)) and lithospheric layering/composition at the *onset* of tectonic deformation provides a *diagnostic tool* to predict localization in the lithosphere. These outcomes reinforced the fact that localization can be anticipated at the onset of the simulation, offering a method to physically quantify it. When comparing their findings with previous models and phase diagrams, as for example Buck (1991) (Fig. 3.9 c1 e c2) there is a satisfactory agreement. Clearly, comparing different phase diagrams necessitates taking the equivalent and correct intervals of temperatures and strain rates.

Here, I have used the Crameri and Kaus (2010) approach to predict localization in 1D, for a given set of rheological parameters, Moho and LAB temperatures, as a function of applied initial strain rates in a conceptual model mimicking polyphase rifting scenarios (Tab. 3.2 and Tab. 3.3). The aim is to first produce phase-diagrams for 1D monophasic rifting simulations, validate against the results of previous authors and then procure phase-diagrams for polyphase cases (RR and RCR), establishing how the change in tectonic boundary conditions and increase in number of stretching phases, can influence the shifting of the limit ( $I = 1$ ) between localization and no-localization regimes in the lithosphere and hence predict, in first approximation as shown by Lu et al. (2011) for the monophasic case for the North China Craton, if, and how much, polyphase rifting predictions deviates from monophasic cases.

### 3.3 Monophasic 1D experiments: parameter choice and validation of reference model for polyphase simulation

In order to optimise the modelling procedure, semi-analytical model developed by Crameri and Kaus (2010) has been used, combining a 1D lithospheric deformation code with previously derived scaling laws for the onset of localization (Kaus and Podladchikov



(2006)).

Similarly to Crameri and Kaus (2010) work, the characteristic length,  $\Delta L$ , has been defined as the thickness of the brittle field calculated from 1D YSE models. I have indicated this brittle thickness as  $th_b$  and calculated it for a lithospheric column composed of 15 km of thickness of upper crust, 15 km of thickness of lower crust and 70 km of thickness of lithospheric mantle for a given set of strain rates, Moho temperatures and rheological parameters representing a wet, a mixed and a dry lithosphere (Tab 3.3). The localization indices evaluated for the three compositions are used to generate 3 phase diagrams with the aim of comparing them with those produced by the previous authors. I assume that the deformation is completely described by Byerlee and Creep laws, neglecting the Peierls mechanism.

Table (3.3) Previous page. Dislocation creep parameters used in 1D parameters of the lithosphere, simulating the deformation of a weak, mixed (average) and strong lithosphere. In bold are the parameters used in the polyphase simulation for 1.

Power law	Pre-exponent constant: A [MPa <sup>-n</sup> s <sup>-1</sup> ]	Exponent: n [Dimensionless]	Activation Energy [KJ mol <sup>-1</sup> ]
Upper Crust (UC)	A <sub>UC</sub>	n <sub>UC</sub>	E <sub>UC</sub>
Wet/soft <sup>1</sup>	2x10 <sup>-4</sup>	1.9	140
Mixed/Average <sup>2</sup>	<b>1.1x10<sup>-4</sup></b>	<b>4</b>	<b>223</b>
Dry/Hard <sup>3</sup>	10 <sup>-4</sup>	2.4	160
Lower Crust (LC)	A <sub>LC</sub>	n <sub>LC</sub>	E <sub>LC</sub>
Wet/soft	1.4x10 <sup>-4</sup>	4.2	445
Mixed/Average	<b>190</b>	<b>4.7</b>	<b>485</b>
Dry/Hard	10 <sup>-4</sup>	2.4	160
Lithosphere Mantle (LM)	A <sub>LM</sub>	n <sub>LM</sub>	E <sub>LM</sub>
Wet/soft	955	3.4	444
Mixed/Average	<b>4.5</b>	<b>3.6</b>	<b>535</b>
Dry/Hard	4.85 10 <sup>4</sup>	3.5	535

The YSE calculated and plotted in Fig, 3.7 a show the correspondence between increased  $th_b$  and localization index for the mixed lithosphere in Tab.3.3 (in bold), generated for low, medium and high strain rates ( $\dot{\epsilon}_{in2} = 1 \times 10^{-16}$ ;  $\dot{\epsilon}_{in2} = 1 \times 10^{-15}$ ;  $\dot{\epsilon}_{in1} = 1 \times 10^{-14}$  s<sup>-1</sup>) If the initial strain rate at the onset of rifting is low ( $\dot{\epsilon}_{in2} = 1 \times 10^{-16}$  s<sup>-1</sup>), the brittle fields are confined in the first few kilometers of the upper part of each lithospheric layer (Fig.3.7 a in green ~5km for the upper crust, in red ~ 2 km for the lower crust and in blue ~1 km for the

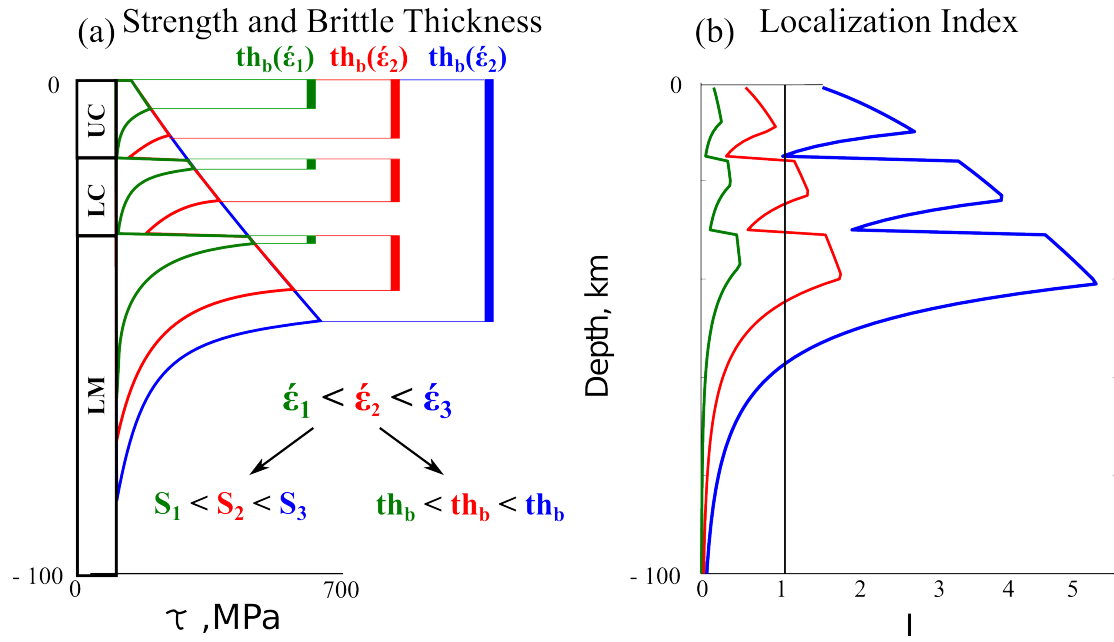


Figure 3.1 (a) Yield strength envelope profiles and (b) localization numbers calculated by the semi-analytical model for  $\dot{\epsilon}_{in2} = 1 \times 10^{-16}$ ;  $\dot{\epsilon}_{in2} = 1 \times 10^{-15}$ ;  $\dot{\epsilon}_{in1} = 1 \times 10^{-14} \text{ s}^{-1}$ . The black line in (b) shows the critical value for the localization number.

lithospheric mantle). In this case, the deformation is dominated by the ductile behaviour and the rheological layers are severely decoupled. With the increase of applied initial strain rate (average,  $\dot{\epsilon}_{in2} = 1 \times 10^{-15} \text{ s}^{-1}$ ),  $th_b$  expands reaching  $\sim 8$ ,  $\sim 5$  and  $\sim 7$  km respectively for UC, LC and LM, with the layers still decoupled but with a reduced ductile thickness. Different scenarios are presented when the deformation starts with a high initial strain rate ( $\dot{\epsilon}_{in1} = 1 \times 10^{-14} \text{ s}^{-1}$ ); UC and LC are completely coupled with the uppermost part of the mantle (between  $\sim 30$  and  $50$  km), which responds in a brittle way. From Figure 3.7a it is evident that brittle thickness  $th_b$  increases with strain rate. This is a direct consequence of the enlargement of brittle fields and shifts the brittle-ductile transitions to greater deep. This leads to a progressive coupling between upper crust, lower crust and lithospheric mantle, which favor the tendency of the lithosphere to focus deformation at depth, reaching complete involvement of the crust and uppermost part of the lithospheric mantle.

With the characteristic length scale  $th_b$  defined and the stress profile calculated, it is possible to compute  $I$  as a function of depth for the given setup. As established by Crameri and Kaus, (2010), I consider that if the maximum of  $I$  is greater than 1, localization is expected to occur. A conjunct analysis of the YSE (Fig. 3.7 a) and the

Localization Index (Fig. 3.7 b) profiles provides more constraints on lithospheric localization. What is depicted by strength profiles is partially confirmed by the maximum localization index profile, which mimics the shape of the YSE profile. Likewise, the localization index is greatly influenced by an increase in strain rate.

However Fig.3.7 gives more information when we compare the localization index profile with the threshold value for localization,  $I = 1$ , indicated with a vertical line in Fig.3.7 b. In particular, when the initial strain rate is very low, even though the strength envelop profile suggests that there is a minimal portion of the UC, LC and LM layers which behaves in a brittle fashion (Fig. 3.7 a, green profile), the localization index profile clearly indicates that such systems will not localize deformation (Fig. 3.7 b, green profile and vertical black line). If the deformation starts with an average strain rate, localization will be focused in the LC and LM, as indicated by the red profile and black line,  $I$ , in Fig. 3.7 b. In the case of the highest initial strain rate, the entire system will localize deformation (blue line vs black line Fig. 3.7 b) even though the YSE suggests a ductile flow in the lower parts of the UC and LC.

In summary, for a given composition, rheological stratification and Moho temperature the localization number is a function of the strain rate. The plot in Fig. 3.7 b:

- Reveals that there is a unique initial strain rate that gives as max localization Index  $I_{\max} = 1$ ;
- Quantifies precisely at what depth localization occur. The maximum of  $I$  appears in the upper most mantle, which show that localization is typically initiated below the Moho.

### 3.3.1 Localization phase diagrams for monophasic stretching: R or M history type

Based on the discussion above, it is possible to use the 1D models to compute phase-diagrams of localization for the wet, mixed and dry compositions (Tab 3.3). Moho temperatures and initial strain rate ranges are given in Tab 3.2. These phase diagrams are interpolated on points representing localization indexes derived from the combination of particular strain rates and Moho temperature for a given composition. Consequently, these diagrams reveal a unique initial strain rate gives as max localization Index  $I_{\max} = 1$  for a given combination of parameters (black solid line in Fig. 3.8 a, b and c), with a linear relationship between increased Moho Temperatures and initial strain rate, which is lost partially in the case of the Dry lithospheric composition.

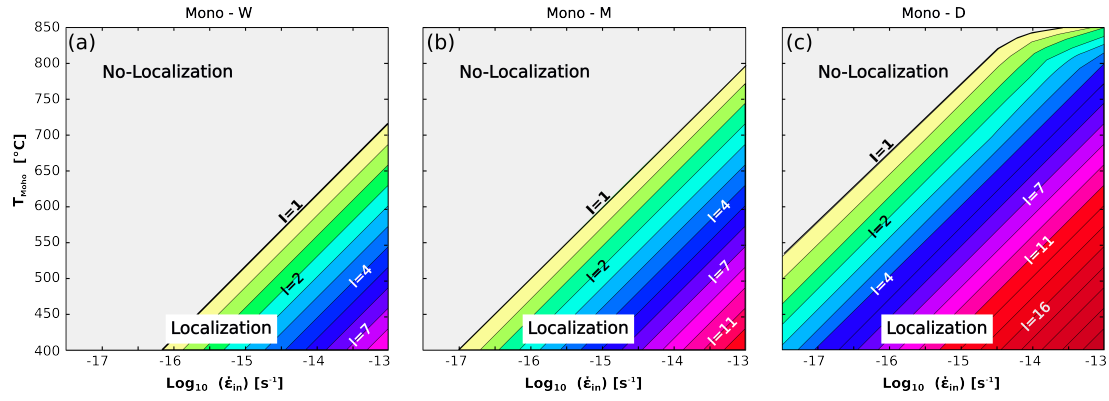


Figure 3.2. Phase diagrams representing the localization for a) wet, b) mixed and c) dry rheology for Moho temperatures and initial strain rate ranges in Tab. 3.2 and 3.3.

The light grey area shows all localization indexes for the delocalized regime,  $I_{\max} < 1$ , while the coloured bands indicates the system's combination of conditions that will lead to localization, with indices increasing with decreasing Moho temperature and increasing initial strain rate. Taking the mixed composition as a reference, the main difference between the plots consists in the shifting of  $I_{\max} = 1$  towards a lower strain rate and higher Moho temperatures in the case of dry composition instead of wet composition. For example, considering a mixed composition (Fig. 3.8 b), it is possible to obtain  $I_{\max} = 1$  when combining  $T_m = 600$  °C with strain rate  $\dot{\epsilon}_{in} = 1 \times 10^{-15}$ . Therefore, for the same  $T_m$  lithospheric localization will occur for all  $\dot{\epsilon}_{in} > 1 \times 10^{-15}$ . Alternatively, if the lithosphere is characterized by weaker rocks (Fig. 3.8 a) this previous combination of  $T_m$  and  $\dot{\epsilon}_{in}$  is not sufficient to reach the threshold value  $I_{\max} = 1$ . It will give fall within the no-localization regime area. Conversely, this particular  $T_m - \dot{\epsilon}_{in}$  combination will give  $I_{\max} = 7$  when modelling a dry lithosphere, indicating lithospheric localization will occur even in conditions of higher geothermal gradient and lower strain rate. For example, a combination of  $T_m = 600$  °C and a  $\dot{\epsilon}_{in} > 1 \times 10^{-16}$  will give an  $I_{\max} = 1.5$ . This result shows how the no-localization regime prevails in the case of very high  $T_m$  ( $T_m > 800$  °C) even for extremely high initial strain rates.

These three phase diagram clearly show in the case of a monophase rifting that localization depends on rheological parameters, initial temperature assign at Moho depth and initial strain rate. 1D models can predict, at least in first approximation, which combination of initial ( $T_m$ , composition X) and boundary conditions ( $\dot{\epsilon}_{in}$ ), localization will occur.

Faster deformation is favored to initiate a narrow rift by lithospheric localization while it

is more likely the lithosphere may deform uniformly without localization under very slow extension or under water-rich conditions.

In summary, the conditions that predict localization occur in compressive and extensional tectonics settings:

- A cold thermal state tends to develop lithospheric localization in comparison to hot thermal state.
- Strong lithosphere with dry rheologies promotes the occurrence of localization.
- Faster deformation is favoured to initiate narrow rifts by lithospheric localization while it is more likely lithosphere may deform uniformly without localization under very slow extension or in water-rich conditions.

### 3.3.2 Comparison of localization index phase diagrams present in literature and 1D conceptual monophasic model verification

Crameri and Kaus (2010) have modeled a weak (Fig. 3.9 a1) and a strong lower crust rheology (Fig. 3.9 a2) using methods employed by Burg and Schmalholz (2008). Localization indexes are plotted as a function of LAB Temperature ( $T_{\text{bot}}$ ) using  $\dot{\epsilon}_{\text{in}} = (\sim 1 \times 10^{-16}; \sim 1 \times 10^{-14}) \text{ s}^{-1}$  for strain rates. By applying the semi-analytical method, comparing the 2D with the 1D result and scaling to derive the localization indexes, they have shown that the lithosphere is able to generate shear zones in a compressive tectonic setting, which are typically initiated in the mantle lithosphere and preferentially occur in cold and rapidly deforming lithospheres. If the thickness of the plastically deforming (Peierls or Peierls/Coulomb) part of the lithosphere is employed as the characteristic length scale, excellent agreement was obtained between 1D predictions and 2D numerical simulations.

Lu et al., (2011), used a standard model (wet quartzite for UC, diabase for the LC and wet olivine for the LM) with a Dry Mantle (with dry olivine). The plotting has as y-axis the thermal age of the lithosphere and as x-axis strain rate with the  $\dot{\epsilon}_{\text{in}} = (\sim 1 \times 10^{-15}; \sim 1 \times 10^{-13}) \text{ s}^{-1}$  interval (Figs. 3.9 b1 and b3). Analyzing 2D numerical results by means of the semi-analytical method Lu et al., (2011) concluded, for a given extension strain rate, lithosphere with an old thermal age (cold thermal state) tends to develop localization and so a narrow rift ( $I_{\text{max}} > 1$ ). Conversely, a lithosphere with a young thermal age, a hot thermal state, is more prone to deform in a homogeneous manner favoring the formation of a wide rift. Moreover, those authors have established that faster deformation and colder thermal state are required to form lithospheric

asymmetric localization in comparison with symmetric localization for both dry and wet mantle.

The conditions for localization predicted by these studies, and that are presented here, are in good agreements with the initial thermal and strain rate conditions that form narrow rifts, as indicated by [Buck, 1991](#) (Figs. 3.9 c1 and c2). [Buck \(1991\)](#) showed that narrow rifts could not be formed in a hot lithosphere, and so that wide rift and core- complex are the most likely manner of deformation. This study associated wide rifts/core-complex with heat flows higher than  $40 \text{ mWm}^2$  and  $60\text{--}70\text{mWm}^2$  respectively for a normal 40 km thick crust and a 60 km pre-rifting thickened crust, corresponding to an initial Moho temperature of  $750\text{--}800^\circ\text{C}$ . The hot thermal state is caused by thicker crust, which leads to an increase in radiogenic production. However, he also indicated that when a certain thermal Moho interval ( $\sim 400 - 800^\circ\text{C}$ ) is combined with initial strain rates between  $\sim 1 \times 10^{-16}$  and  $\sim 1 \times 10^{-12} \text{ s}^{-1}$ , this increases the chance that a narrow rift will develop.

Overall, there is good agreement to the present study with trends revealed by both previous works concerning the ability of the lithosphere to localize strain. The 1D phase diagrams presented in this chapter confirm that localization is a strong function of applied strain rate and the range of parameter chosen for the mixed rheology can be used as a starting point for a polyphase rifting conceptual model in addition to the initial assumptions chosen for specific cases.

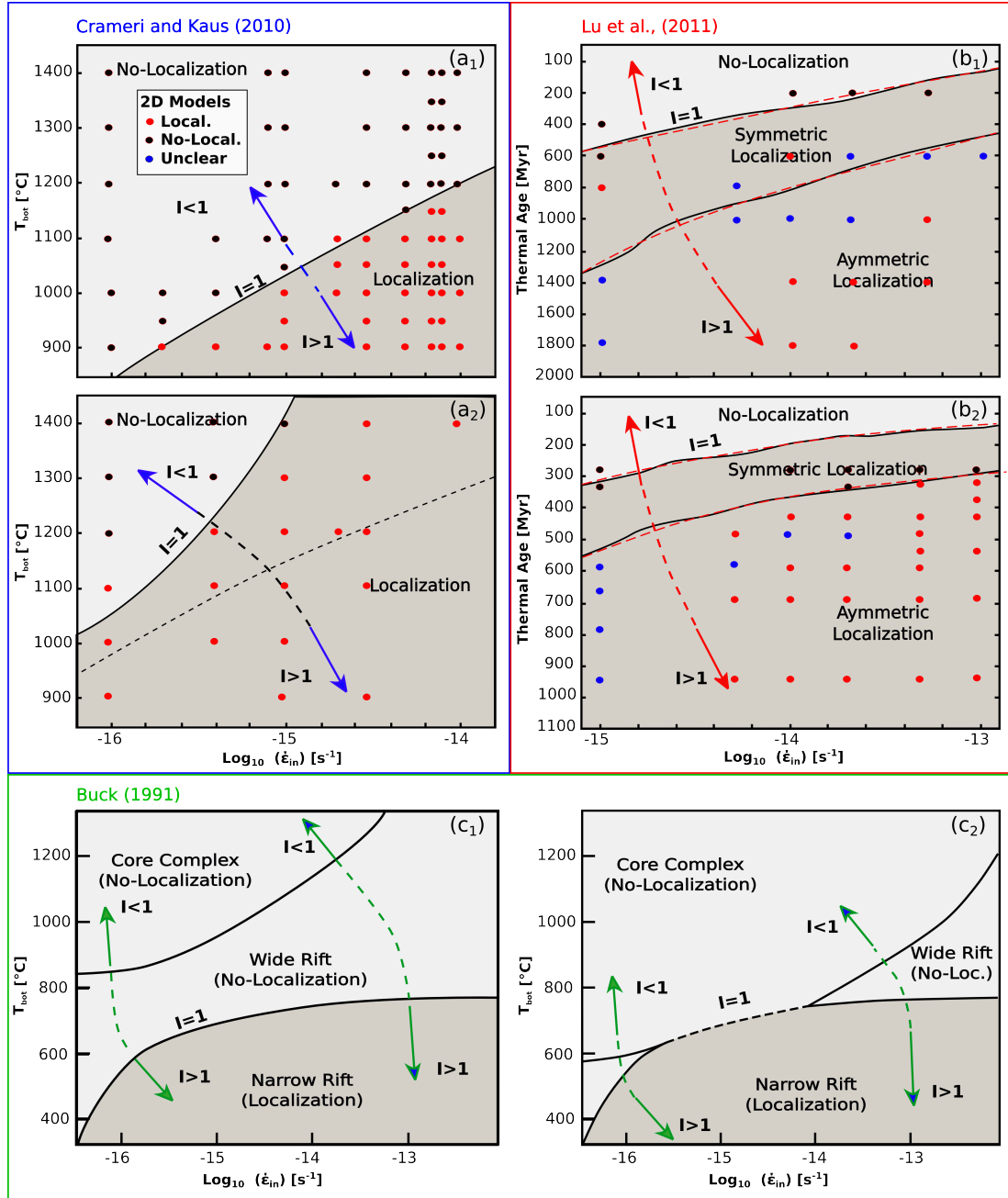


Figure 3.3. Comparison of existing literature models for lithospheric localization.  $a_1$ - $a_2$  Crameri and Kaus (2010): overlap of 2D numerical models (dots) with the 1D models interpreted using a semi-analytical method. This work was done for a compressive tectonic setting changing the rheology of the lower crust (soft  $a_1$ , strong  $a_2$ ),  $b_1$ - $b_2$  Lu et al., (2001): as before but for an extensional setting. Wet Olivine for  $b_1$  and Dry Olivine for  $b_2$ .  $c_1$ - $c_2$  phase diagrams from Buck (1991) for the formation of narrow, wide and core complex rift types with a 40 km ( $c_1$ ) and 60 km thick crust ( $c_2$ ). Grey areas represents localization (localization Index  $I_{max} > 1$ ), light grey is for no-localization ( $I_{max} < 1$ ). (see text for full explanation)

### 3.4 Conceptual model for polyphase rifting

#### 3.4.1 Lithosphere definitions

The study and modelling of polyphase rifting requires prescribing a definition of the lithosphere and a description of the most appropriate thermal boundary layers, TBL. The

reason is that It remains difficult to find a universal definition of the lithosphere, mostly because physical parameters, such as temperature or density, change continuously beneath the Moho and that the transition from the rigid outer shell of the earth (the so-called mechanical boundary layer) to the more viscous hot asthenosphere is continuous. This transition is often identified as the thermal boundary layer, TBL, even though it is also used to define the entire lithosphere. Later in this section, it will be discussed which definition of TBL is used in the preset study.

The lithosphere can be defined in several ways depending on what parameters are used to describe it and the boundary to the asthenosphere ([Artemieva, 2011](#)), for example:

- Mechanical: *Sensu stricto* is the elastic (flexural) lithosphere defined as the elastic plate overlying the viscous mantle. In a more general sense the mechanical lithosphere can be defined by the plastic/ductile behaviours when the elastic limit is exceeded;
- Seismic: seismic high-velocity layer above the low-velocity zone (LVZ) or above a zone of high velocity gradient in the upper mantle, presumably caused by partial melting ([Artemieva, 2011](#));
- Thermal: based on the temperature-dependent physical properties of mantle rocks measured indirectly in geophysical surveys ([Artemieva, 2011](#)). The base of the thermal lithosphere is commonly defined either by the depth to a constant isotherm (e.g. 1300 °C), or by the depth where a linear downward continuation of the geotherm reaches some predefined fraction of the ambient mantle temperature or mantle solidus (~0.9 of the melting mantle temperature).
- Rheological: defined as the boundary layer and commonly interpreted as being associated with mantle zones of reduced viscosity and asthenospheric flow. Mantle zones of reduced viscosity cause alignment of minerals, such as highly anisotropic olivine, and are thus associated with changes in seismic and electrical anisotropy. Mantle flow also causes variation in the texture of xenoliths brought to the surface from different depths in the mantle, and in petrologic studies the base of the rheological lithosphere can be constrained by the transition from non-sheared to sheared xenolith ([Artemieva, 2011](#)).
- Chemical or petrologic lithosphere: defined using mantle-derived xenoliths.

Consequently, the lithosphere definition depends on the type the techniques used to acquire the data/geophysical properties, on the purpose of the study that is being



conducted and on the timescale considered. Essentially the definition of the lithosphere depends on the scientific question that is being asked. This leads to different lithospheric thickness for each of lithospheric definition or depending on the time scale of the process being analyzed. For example, it can be shown that the thickness of the lithosphere is a function of the observed time scale. Seismic motion, isostatic uplift and ductile deformation occur on time scales of seconds,  $10^4$  y and  $> 10^6$  y, respectively (Stüwe, 2007). The larger the time scale of the process, the smaller the thickness of the lithosphere and a different definition for the lithosphere is to be used (i.e. small time scale → mechanical lithosphere *sensu stricto* (e.g. Artemieva, 2011; Burov, 2007); large timescale → rheological lithosphere (Artemieva, 2011)). Seismically, the lithosphere is of the order of 200 km thick, while the elastic thickness of the lithosphere is only some tens of kilometers thick.

Here, I have taken into account the general definition of mechanical lithosphere along with the thermal lithosphere and thermal boundary layer definitions.

### 3.4.2 Assumptions for the present study

#### 3.4.2.1 Mechanical lithosphere

When the lithosphere is defined mechanically in a general sense, it represents the outer part of the earth in which stresses can be transmitted on geological time scales (i.e. McKenzie 1967) and the deformation is described using the elastic/brittle behaviour. However, in this work I consider a mechanical deformation that derives from viscous flow/ductile behaviour. I do not address the role of elastic deformation. Therefore, the mechanical lithosphere is defined as the portion of the lithosphere that deforms in brittle and viscous way and I consider only non-recoverable deformations, which in mechanics occur when the elastic limit is exceeded. For example, in case of tectonic extension once the crust has been thinned due to stretching it preserves deformation even when divergent tectonic forces cease.

#### 3.4.2.2 Thermal lithosphere and thermal boundary layer

According to a thermal definition the lithosphere is the part of Earth where thermal energy is mainly transferred by heat conduction, in contrast to the asthenosphere, where heat is transported primarily by convection. Thus, the lithosphere itself is nothing but a thermal boundary layer of the Earth, although some scientists define the thermal boundary layer as the transition zone from the rigid outer shell (the mechanical boundary

layer) into the more viscous hot asthenosphere. (Fig. 3.10 for the 2 definitions)

This boundary layer loses heat through Earth's surface, with the average continental heat flow of  $0.065 \text{ Wm}^{-2}$ . The total surface area of the continents is about  $A_c = 2 \times 10^8 \text{ km}^2$ . Thus, the total heat loss of earth from the continents is  $1.3 \times 10^{13} \text{ J s}^{-1}$ . This heat loss is balanced by radioactive heat production within the lithosphere and by heat flow into the lithosphere from the asthenosphere, with the thermal boundary layer maintaining a largely constant temperature profile, if it is not disturbed by orogenesis or stretching (Stüwe, 2007).

In some ways the thermal definition encompasses the mechanical definition because many of the mechanical properties of rocks depend on the ratio of temperature to melting temperature. In stable continental lithosphere, thermal and mechanical definitions indicate thickness of 100- 200 km (Pollack and Chapman 1977).

### 3.4.3 Schematic model for Monophase versus Polyphase 1D thinning

Whichever of the two of thermal boundary layer definition is used, the thermal boundary between the lithosphere and asthenosphere is represented by the  $1300^\circ\text{C}$  isotherm and is called the lithosphere-asthenosphere boundary (LAB). Assuming that the composition of asthenospheric and lithospheric mantle is the same and the only difference is marked by the geothermal gradients (average of  $25^\circ\text{C/Km}$  far from tectonic boundaries in the lithosphere (Lowrie, 2007) while the geothermal gradient within the bulk Earth's mantle is of the order of  $0.5^\circ\text{C/Km}$ , and is determined by the adiabatic gradient associated with mantle material (peridotite in the upper mantle - Turcotte, and Schubert, (2002)), it is possible that during tectonic extension

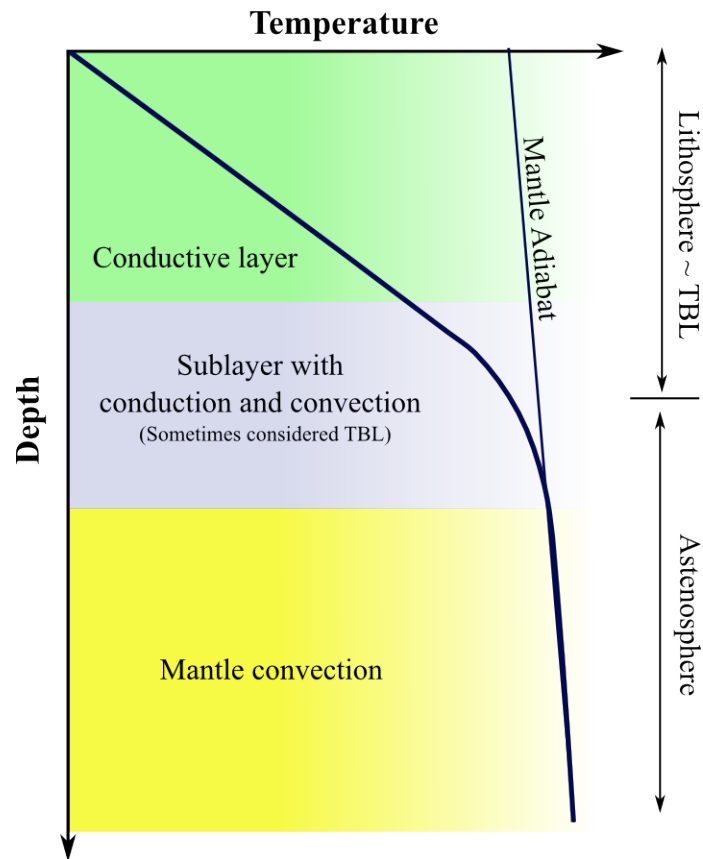


Figure 3.4 Schematic representation of the lithospheric system with indication of two possible definitions for Thermal Boundary Layer (TBL).

deformation of the lithospheric mantle can be described by thermal thinning. Here, the part that deforms thermally (e.g. thermal thinning means that the isotherms are moving upwards and the geothermal gradient increases) is considered the lithospheric mantle. The LAB is thermally destabilized by stretching and rises upwards with a consequent increase of geothermal gradient. The crust thins mechanically and the Moho, which is a compositional boundary, moves to a shallower level. In the case of the monophase rifting, with a given initial  $\dot{\epsilon}_{in}$ , mechanical thinning of the crust and thermal thinning of the lithospheric mantle is schematically represented in Fig. 3.11 a. This is not in scale because it serves to provide the idea of the lithospheric evolution in the case of a monophase and polyphase rift in Fig. 3.11 b. Here,  $thL_{tot}$  is the original total thickness of the lithosphere while  $thC_o$  and  $thLm_o$  are respectively the initial crust and lithospheric mantle thickness. At the end of the rifting the layers are reduced by a Beta factor ( $th_o/th_f$ ), to final thickness  $thC_{fl}$ ,  $thLM_{fl}$  and  $thLm_{fl}$ .

Fig. 3.11 b (lower part) represents the case of two-phase rifting intermitted by a cooling stage. Starting rifting has the same setting as the monophase case, with the same  $thC_o$ ,

$thLm_o$ , original lithosphere total thickness ( $thL_{tot}$ ) and initial  $\dot{\epsilon}_{in}$ . The first rifting phase is similar to the monopase case with thermal and mechanical thinning of the crust and lithospheric mantle. When rifting ceases or pauses (tectonic quiescence and cooling), thermal diffusivity equilibrates temperatures and the lithosphere can recover thickness lost during previous rifting phases (Fig. 11 b), allowing the lithosphere to regain its original thickness with a varied rheological layering. In fact, the lithospheric column at the onset of Rifting 2 has less crust a thicker and colder lithospheric mantle. This is possible because of the thermal nature of the lithospheric mantle, during cooling the only heat transfer mechanism is diffusion. The crust maintains the deformation previously acquired. Assuming simple 1D time-dependent heat conduction and thermal diffusivity ( $\kappa$ ) of  $1 \times 10^{-6} \text{ m}^2 \text{ s}^{-1}$  it is possible to calculate the time,  $t = l^2 / \kappa$ , if  $l$  is the thickness to be recovered (Fig. 3.11 b). The maximum recoverable lithospheric mantle thickness is capped at the original lithospheric thickness due to the effect of underlying convecting mantle preventing further grow. This is indicated in Fig. 3.11 b, where the blue dashed line represents the hypothetical continuation of thickening. If the same  $\dot{\epsilon}_{in}$  is used for the second rifting phase, final thinning is less than the monopase case, with  $thC_{f2} < thC_{f1}$ ,  $thLM_{f2} < thLM_{f1}$  and  $thLm_{f2} < thLm_{f1}$ .

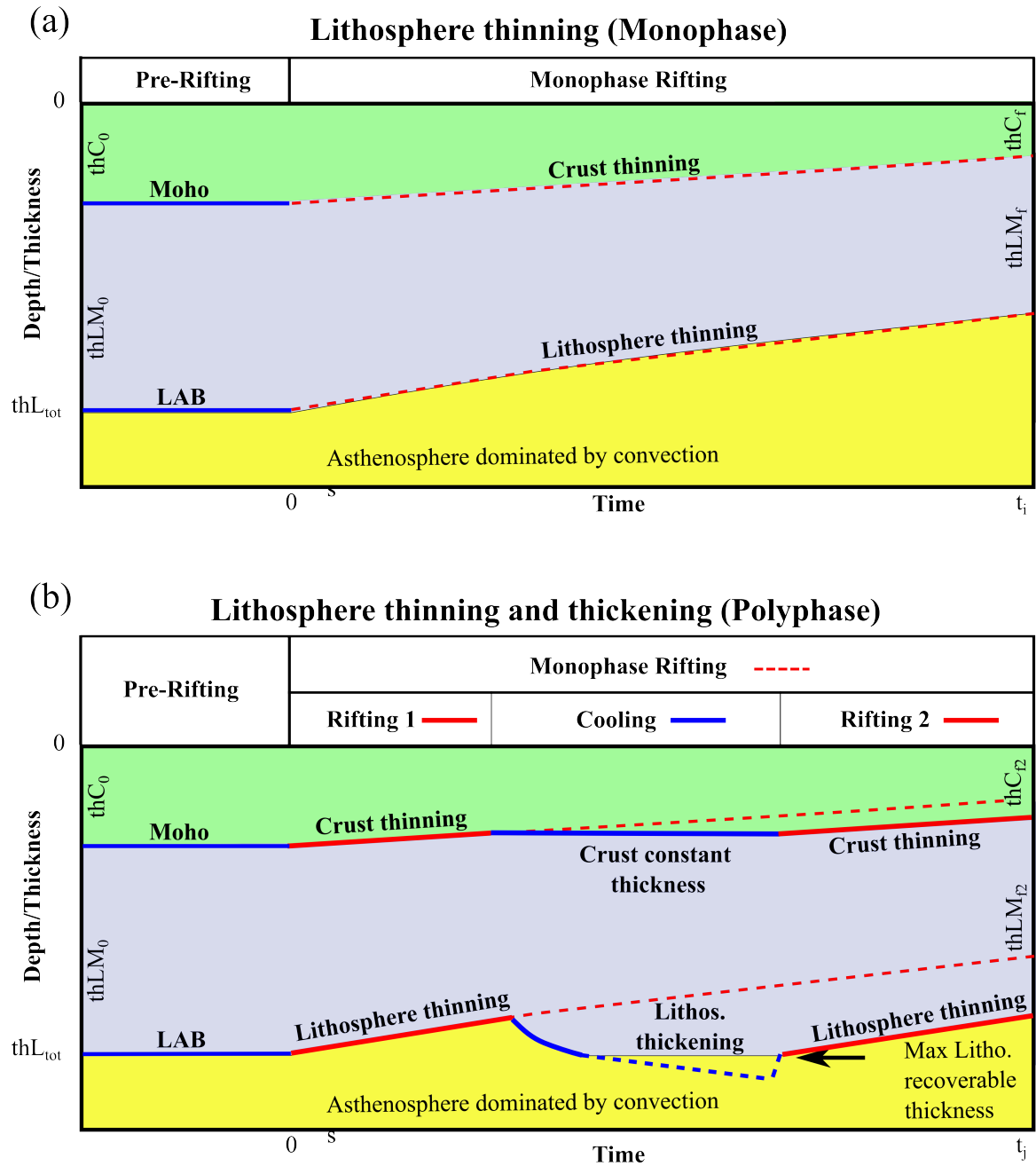


Figure 3.5. Schematic (not to scale) evolution of monophase (a) and polyphase (b) rifting. Green, light purple and yellow are respectively upper crust (UC), lower crust (LC) and lithospheric mantle (LM) thickness. LAB (Lithosphere-Asthenosphere Boundary) is indicated for the evolution in time for both cases. Note that monophase and polyphase rifting are compared for the same horizontal extension, therefore  $t_i \neq t_j$ . Red lines represent rifting phases. Blue lines are indicative of tectonic quiescence, during which conductive cooling allows for recovery of original lithosphere thickness through lithospheric mantle thickening. Note how the crust remains undeformed during cooling.

### 3.5 Polyphase 1D experiments: RCR history type

As seen in the previous section for a given lithospheric composition, a change in initial

strain rate can affect the plastic thickness,  $th_b$ , and integrated strength,  $S$ , leading to either lithospheric localization or no-localization regimes. Consider the lithosphere setting of a monophasic case (geothermal gradient, composition and rheological stratification). Several questions arise for what concerns the polyphase rifting and the ability of the lithosphere to localize strain. These questions can be summarized as following:

- What are the consequences in terms of the lithospheric response when combining different initial strain rates (changing boundary conditions) and polyphase rifting?
- Can the cooling phase, in interplay with variation of boundary conditions, influence the ability of the lithosphere to localise deformation in the second rifting phase (does it decrease or increase the possibility of localization)?
- How much can this evolution differ from the monophasic case?

To answer these questions in first approximation I have performed a series of 1D models, using the setting of the monophasic experiments the same initial strain rate range (Tab. 3.2) and  $T_m$  = same as for monophasic). As the experiments are in 1D, there is no horizontal stretching only thinning of the lithospheric column, a situation analogous to pure shear stretching, where the horizontal and vertical deformation are the same as the lateral and upward rate of strain. Thinning in first and second phases are respectively rifts 1 and 2. Fig. 3.10 shows a synthesis of the 1D polyphase experiments where 3 initial strain rates (low  $\dot{\epsilon}_{in} = 1 \times 10^{-16} \text{ s}^{-1}$ , average  $\dot{\epsilon}_{in} = 1 \times 10^{-15} \text{ s}^{-1}$  and high  $\dot{\epsilon}_{in} = 1 \times 10^{-14} \text{ s}^{-1}$ ) have been used alternatively in two rifting phases. Strain rates are indicated by the following colours:

- Yellow for lowest  $\dot{\epsilon}_{in}$ ,
- Amber for average  $\dot{\epsilon}_{in}$ , and
- Orange for highest  $\dot{\epsilon}_{in}$ .

Due to the 1D nature of the model, it is possible to make two type of comparison:

- To stop the rifting phase when the lithospheric column was thinned for the same beta factor,  $\beta = thC_o/thC_f$ , and delta factor,  $\delta = thLM_o/thLM_f$ , for all the simulations or;
- To use the same duration,  $t$ , for all the first rifting phases.

The second option has been used here to compare the simulations, with the resulting  $\beta$  and  $\delta$  at the end of the first rifting phase are functions of the initial strain rate  $\dot{\epsilon}_{in}$ . Given the same duration of rifting, a higher initial strain rate leads to greater  $\beta$  and  $\delta$  at the end

of rift 1. Consequently, after cooling occurs (which allows for the regrowth of lost thickness), rifting 2 starts with the same total lithospheric thickness as rifting 1, with a diminished crustal layer and more lithospheric mantle ( $th_{LMo2}/th_{Co2} > th_{LMo1}/th_{Co1}$ ). In this simulation the lithospheric mantle essentially recuperates its original thickness plus the crustal portion that was lost in the prior stretching phase (Fig. 3.11 and Fig. 3.12a). This produces  $\beta$  values  $> 1$ , with  $\delta$  after cooling  $< 1$ .

The option of running the rifting phases for the same amount of time, allows for better evidence on the interplay between the rifting and cooling phase for the case of 1D.

The red box in Fig. 3.10a represents the strength envelope profile at the onset of rifting 1 for the same initial lithospheric column showing the effect of the 3 strain rates on:

- Coupling/decoupling of the lithospheric layering
- Progressive increase of  $th_b$  proportionally to the initial strain rate
- Increase of the integrated strength as a function of strain rate.

The green box represents the strength envelope profiles calculated at the onset of the second rifting phase, hence after cooling has allowed for complete recovering of the original lithospheric thickness. Looking at Figs. 3.12 b, e and h,  $\beta$  and  $\delta$  are respectively 1.25 and 0.92. These thinning factors are generated if  $\dot{\epsilon}_{in} = 1 \times 10^{-17} \text{ s}^{-1}$ , it is used for rift 1. The connection between lithospheric stratification at the start of rift 2 and the boundary condition is given by YSE colour in both the red and green boxes. Therefore, in the case of Figs. 3.12 b, e and h, yellow indicates the lower initial strain rate. The temperatures are re-equilibrated but the Moho temperature is lower compared to the start of the process ( $T_{m2} = 490 \text{ }^\circ\text{C} < T_{mo} = 580 \text{ }^\circ\text{C}$ ).

From the example discussed, it is possible to consider the lithospheric columns and new Moho temperature, as inherited initial conditions originated by the interplay between the boundary condition used in the first rifting phase and the cooling stage.

So, how do these inherited conditions interact with 3 different initial strain rates? Analysing again the same set of figures, it is possible to see that:

plastic thickness and coupling between rheological layers increases proportionally to strain rate.  $th_b$  in Fig. 3.12 a, e and h is respectively  $18 \text{ km} < 29 \text{ km} < 39 \text{ km}$ . All  $th_b$  are greater than the ones in the first rifting phase (8 km).

Integrated Strength,  $S$ , gets gradually larger with increasing  $\dot{\epsilon}_{in}$ . In Fig. 3.12 b, e and h,  $S$  is  $6.54 \times 10^{12} \text{ N/m}$  (yellow YSE),  $1.24 \times 10^{13} \text{ N/m}$  (amber YSE) and  $1.88 \times 10^{13} \text{ N/m}$  (orange

YSE) respectively. Integrated strength for the lowest  $\dot{\epsilon}_{in} = 1 \times 10^{-16} \text{ s}^{-1}$  (yellow) in the rift 1 is  $3.8 \times 10^{12} \text{ N/m}$ .

Analysing in the same way [Fig.s 3.12 c, f and i](#) and [Fig.s 3.12 d, g and l](#), the same trends are evident with maximum values of  $th_b$ ,  $S$  and complete coupling when the highest initial strain rate in the second rifting phase is combined with the inherited conditions derived from the same  $\dot{\epsilon}_{in} = 1 \times 10^{-14} \text{ s}^{-1}$  used in rift 1.

This set of experiment proves it is possible to creates different rifting histories by only changing the boundary conditions in a rifting-cooling-rifting cycle, classified here as RCR type.



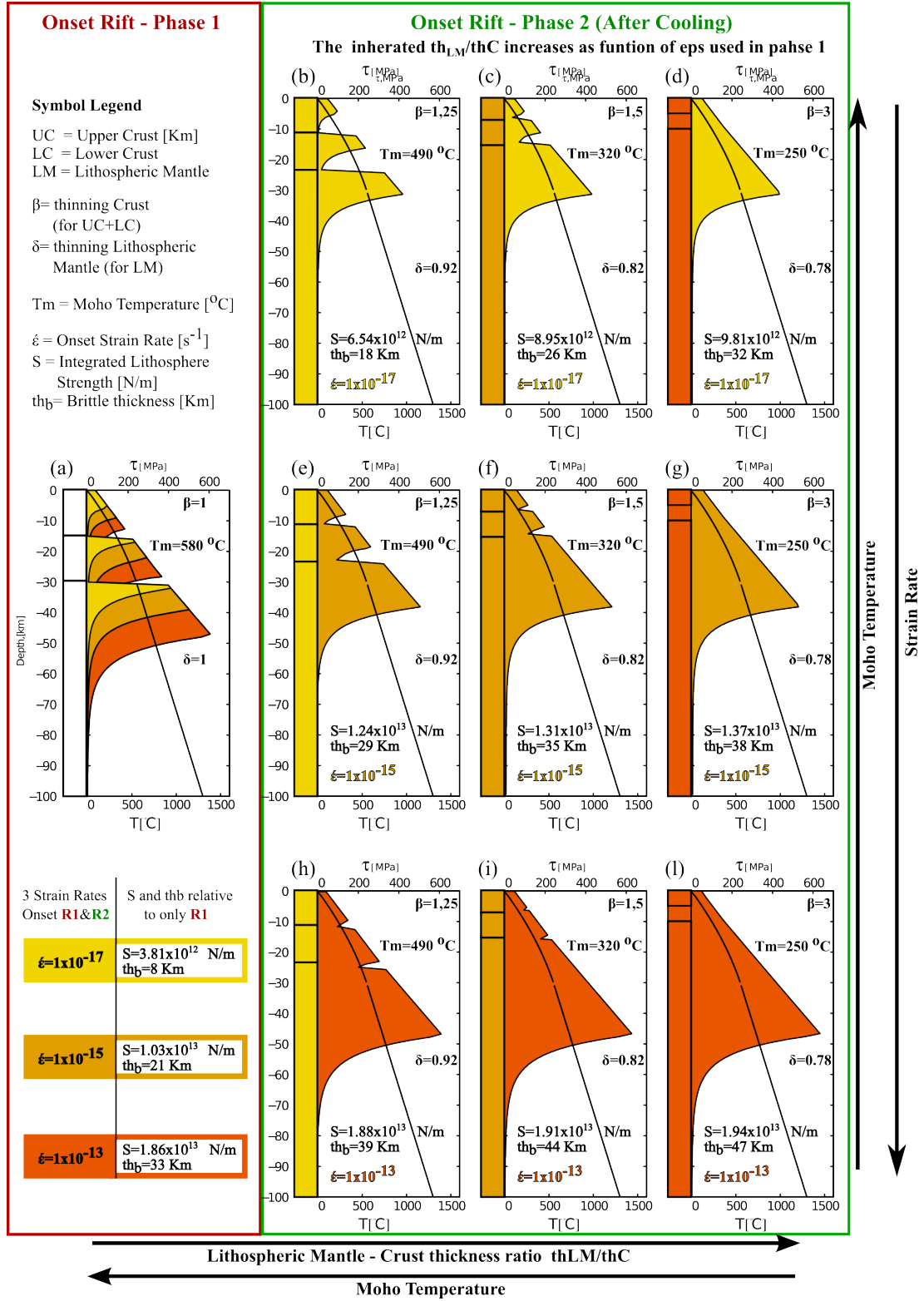


Figure 3.6. 1D polyphase experiments used to test the role of boundary condition at the start of the rifting 1 (red box) and the start of rift 2 (green box). Yellow, amber and orange colours indicate YSE and lithospheric column produced respectively by low, average and high initial strain rate. See text for explanation.

### 3.5.1 Localization phase diagrams for polyphase stretching

To analyze how polyphase rifting evolution can affect lithosphere localization, a calculation of the localization indexes for each 1D model is required similar to the monophase case seen in section 3.7a. I first plot the data relative to the case discussed (RCR histories type) and then consider a case where the conductive cooling stage is completely absent with just the change in initial strain rates between two rifting phases (RR type histories).

#### 3.5.1.1 RCR and RR

Data deriving from Strength envelope profiles of polyphase rifting allows for the computation of phase-diagrams of localization index for mixed lithospheric composition (Tab 3.3), Moho Temperatures and initial strain rate ranges in Tab 3.2. Due to the presence of 2 rifting phases, there is a phase diagram plot relative to the first rifting phase (Fig 3.13 a1 and a1 respectively for the RCR and RR case) and two plots representing the second rifting phase (Fig 3.13 a2 and a2 respectively).

It is better to remind the reader that these plots show only the localization indexed calculated for the same composition, range of  $T_m$  and initial strain rate relative only to the onset of the rifting phases.

Therefore, given the same composition and IC/BC ranges, the diagrams for rifting phase 1 of RCR and RR rifting histories are identical to plotting the monophase case (see Fig 3.8 b and below Fig. 3.13 a<sub>1</sub>, a<sub>2</sub>).

The inherited condition in Fig. 3.13 a<sub>1</sub>, is represented by the  $\beta$  factor at the end of R1, which is a function of  $\dot{\epsilon}_{in}$  and remains preserved after cooling. For RCR histories, only  $\beta$  factors are shown on Fig. 3.13 a<sub>2</sub> for simplicity since, as demonstrated in the previous section, rifting in phase 2 restarts with the same total lithospheric thickness but with an increased mantle as a consequence of cooling. Thus, in case of RCR,  $\delta$  is always  $< 1$ , with  $thLM_{o2}/thC_{o2} > thLM_{o1}/thC_{o1}$ . This is equivalent to changing the initial lithospheric composition at the start of R2: as  $\beta$  becomes larger at the end of R1, the lithosphere is proportionally dominated by the cold olivine at the end of cooling and onset of R2, therefore shifting the critical value  $I = 1$  toward higher  $T_m$  and lower  $\dot{\epsilon}_{in}$ . For example, given a  $T_m = 600^\circ\text{C}$  at the onset of Rift 1, the critical value  $I = 1$  is found for  $\dot{\epsilon}_{in} = 1 \times 10^{-15} \text{ s}^{-1}$ , just as for the monophase case. For Rift 2 instead the same  $T_m = 600^\circ\text{C}$  requires  $\dot{\epsilon}_{in} = 5 \times 10^{-16}$  for inherited condition  $\beta = 2.35$ ,  $\dot{\epsilon}_{in} = 1 \times 10^{-16} \text{ s}^{-1}$  for  $\beta = 3$  and

$\dot{\epsilon}_{in} = 5 \times 10^{-17} \text{ s}^{-1}$  for  $\beta = 3.45$ .  $I_2 = 1$  (Fig. 3.13 a,g) is always the same threshold value between localization and no-localization regimes.

In the case of RR history (Fig. 3.13 b<sub>1</sub>, b<sub>2</sub>), the onset of Rift 2 results in  $\beta = \delta$  due to the absence of the cooling stage, so the lithosphere preserves the total thinning acquired at the end of Rift 1 when Rift 2 starts. I assumed that rifting restarts soon after the previous phase terminated and that there is a sudden increase in boundary condition magnitude ( $\dot{\epsilon}_{inR2} > \dot{\epsilon}_{inR1}$ ). The inherited condition is a function only of the previous rifting phase and, in the RR case, consists of:

- A thinned lithosphere ( $\beta = \delta > 1$ ) compared to the original thickness;
- A  $T_{mR2} > T_{mR1}$  so a softer lithosphere.

The consequence is that, even though the second rifting phase  $\dot{\epsilon}_{inR2} > \dot{\epsilon}_{inR1}$ , the integrated strength  $S$  is always lower compare to the initial one. Therefore, the localization regime is represented by a smaller area respect to the RR case (Rift 1) the RCR case (Rift 2). However,  $th_b$  still increases proportionally to of  $\dot{\epsilon}_{inR2}$ , shifting the critical value  $I = 1$  similarly to the previous RCR case. The difference is that for the same  $T_m = 600 \text{ }^\circ\text{C}$ , the localization indexes  $I = 1$  needs a much greater interval of initial strain rate. Comparison between Fig 3.13 a<sub>1</sub>, a<sub>2</sub> and Fig. 3.13 b<sub>1</sub>, b<sub>2</sub>, shows how different rifting histories correlate with changes in lithosphere response to the applied divergent forces.

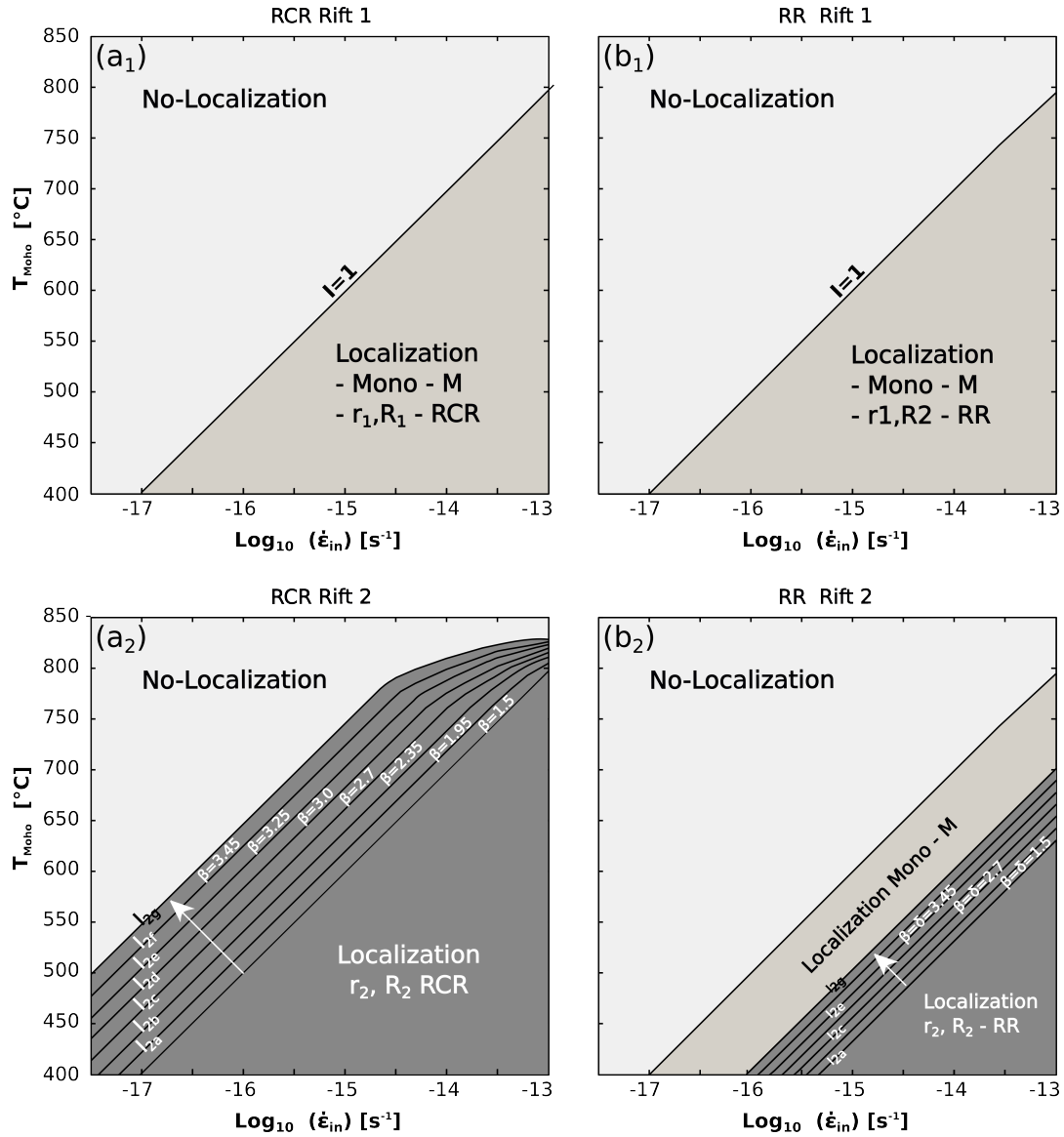


Figure 3.7. Phase diagrams representing the localization for a mixed rheology (Tab. 3.3), Moho temperatures and initial strain rate ranges in Tab. 3.2.

#### 4. DISCUSSION ON 1D MODELLING

A series of 1D rifting simulations have been performed in order to analyze as a first approximation the role of polyphase rifting on the ability of the lithosphere to localize strain.

The experiments consisted of:

- A monophase rifting 1D models (M) used to:
  - Choose rheological parameters, range of Moho temperature and initial strain rate for subsequent polyphase conceptual model and,
  - Verification and validation of the conceptual monophase model against

literature models

- A polyphase model represented by a rifting-cooling-rifting (RCR) and rifting-rifting (RR) cycles representing two families of rifting histories.

From the comparison of 3 rifting types (M, RCR and RR) it is possible to see how the rifting history has a first order effect on the response of the lithosphere in terms of localization. In particular, the difference in rifting histories derives from the interplay between boundary conditions at the onset of the rifting phases, here represented by the initial strain rate, and the initial and inherited conditions, are  $T_m$ , composition and rheological layering.

Previous studies conducted of 1D and 2D models ([Kaus and Podladchikov, 2006](#); [Cramaeri end Kaus, 2010](#); and [Lu et al., 2011](#)) have proven the relationship between localization and no localization regimes with, respectively, formation of narrow shear zones and wide distributed deformation areas. This was done both for Earth-like materials, with a more general and global understanding of underlying physics of the localization process (both for compression and extension) and for the specific case of North China Craton Rift System. Reading these results in the light of recent findings ([Cramaeri end Kaus, 2010](#); and [Lu et al., 2011](#)) and to previous results (i.e., [Buck, 1991](#)) it is possible to conclude that, at least at first approximation, the variation in boundary conditions exerts an important influence on lithospheric localization, almost comparable to rheological parameter chosen in the start of the monophase rifting phase ([Fig. 3.8 a, b and c](#)).

Due to the limit of 1D, a 2D model for both monophase and polyphase rifting is required with verification of any differing outcome or improvement in understanding of the rifting process. Next section briefly shows the development of a 2D monophase model, used as a comparison tool with the 2D polyphase model developed in chapters 4 and 5. I will address just the thinning of the crust and the lithospheric mantle, showing the localization and delocalization of the strain in monophase 2D models. As 1D experiments have served as a screening for initial and boundary conditions, the following chapter shows a few tests linked to numerical procedures in building the 2D model and some tests testing specific 2D features (e.g. influence of pre-existing heterogeneities) that are not possible to be properly analyzed in 1D.

## 5. PART 3: 2D MODELLING MONOPHASE LITHOSPHERIC STRETCHING

### 5.1 Generalities on numerical modelling procedure

In the previous sections I have presented the initial stage of numerical modelling which consists in the simplification of a more complex geodynamic reality.

A conceptual 1D model has been developed for the polyphase rifting. By comparison with observations the 1D model has been validated and the mathematical/conceptual model was found to be adequate to support an implementation of monophasic and polyphasic rifting in 2D.

The 1D conceptual models need to be then transformed in a computational model containing discrete equations to be solved by adequate computational means. In this step the accuracy of the computational model solution needs to be assessed by comparison with analytic or numerical known solutions.

The design and realization of a numerical model requires several steps, which are aimed to the verification of the model.

The general procedure includes:

- 1) The choice and testing of the physical parameters (e.g. density, temperature profile, rock properties) and numerical domain geometries;
- 2) Detection of inaccuracies in the implementation of the specific model algorithm (e.g. multiphasic deformation), including incompatibilities between plugins, inappropriate choices of discretization resolution, and inappropriate choice between algorithms and the nature of the mathematics;
- 3) Identification of the inaccuracy of the science (e.g. the hypothesis of the conceptual model is inappropriate for the numerical etc.).

It is possible to verify the physical 2D model by comparing results with simple analytic solutions, experimental observations, other models results performed with the same or similar codes.

When the computational model is verified, the model can be computed and numerical results obtained can be tested against observations. If there is good agreement between the numerical results and observed (field or experimental) data, the model results can be considered as the model predictions.

## 5.2 Underworld, modelling set-up and boundary conditions

The 2D lithospheric extension was modelled using Underworld, a geodynamic modelling software framework (Moresi et al., 2003, 2007), which solves the equations of mass, momentum and energy conjunctly with the rheological laws presented in part 1 on this chapter.

It is a parallel, Particle-In-Cell Finite-Element-Method code with a modular structure allowing for highly complex and mechanical models to be implemented. Underworld is the specialized geodynamics modelling part of the code. It describes the initial and boundary conditions, the material properties, and rheological laws specific geodynamics, along with processing of the numerical solution to relevant geophysical outputs. It uses a plugin environment base on a scientific-neutral finite element modelling framework that includes five separate packages: (i) 'PICellator' provides the Particle-In-Cell integration schemes, (II) 'StgFEM' provides the finite element codes achieved by utilizing the (iii) 'PETSc' linear solver package, (iv) 'StGermain' provides the base for the framework and 'gLucifer' provides the run time visualization.

The code has been widely used in several geodynamic application such as extension tectonics and passive margins (e.g. Farrington et al., 2010, Sharples et al., 2015), subduction (e.g. Stegman et al., 2010; Capitanio & Replumaz, 2013; Capitanio, 2014; Mason et al., 2010; Farrington et al., 2014) and for the study of the Stokes flow and problems arising in computational geodynamics. (e.g. May & Moresi, 2008).

Therefore, here I have performed only the grid independency test (Resolution test) on a 2D computational domain 400 km deep and 400 km. The test is summarized in Fig. 3.14. The numerical domain test shown in Fig. 3.14 is 400 by 400 km, therefore the resolutions are expressed as 25x25, 50x50, 100x100, 400x400, 500x500 and 800x800 elements which correspond respectively to a cell element of 16x16, 8x8, 4x4, 1x1, 0.8x0.8 and 0.5x0.5 km. The appropriate numerical spatial resolution for the testing domain was found to be of 1x1 km elements mesh, with an error of 5%. This corresponds in a 700 x 400, km for the model domain, with 20 particles for element and it is stretched by imposing moving boundaries at left and right hand sides.

The lithosphere model is composed of three layers (Fig. 3.15). The two layers on the top are each 15 km thick, respectively upper and lower crust, and reproduce the properties of the crust. Beneath the crust lies the mantle, extending to the bottom of the computational domain, where the properties are homogeneous, yet differentiated into lithospheric mantle and asthenosphere by the temperature-dependent viscosity. Although the mechanical

stiffness of the lithosphere is, thus, loosely constrained, I define the lithosphere-asthenosphere boundary (LAB) as the isotherm 1300 °C, at 100 km of depth in the setup. Atop the lithosphere there is 5km of incompressible air and an compressible air layer 35 km thick, mimicking the “sticky air” layer to allow for a quasi-free surface and self-consistent evolution of topography (Cramer & Kaus, 2012).

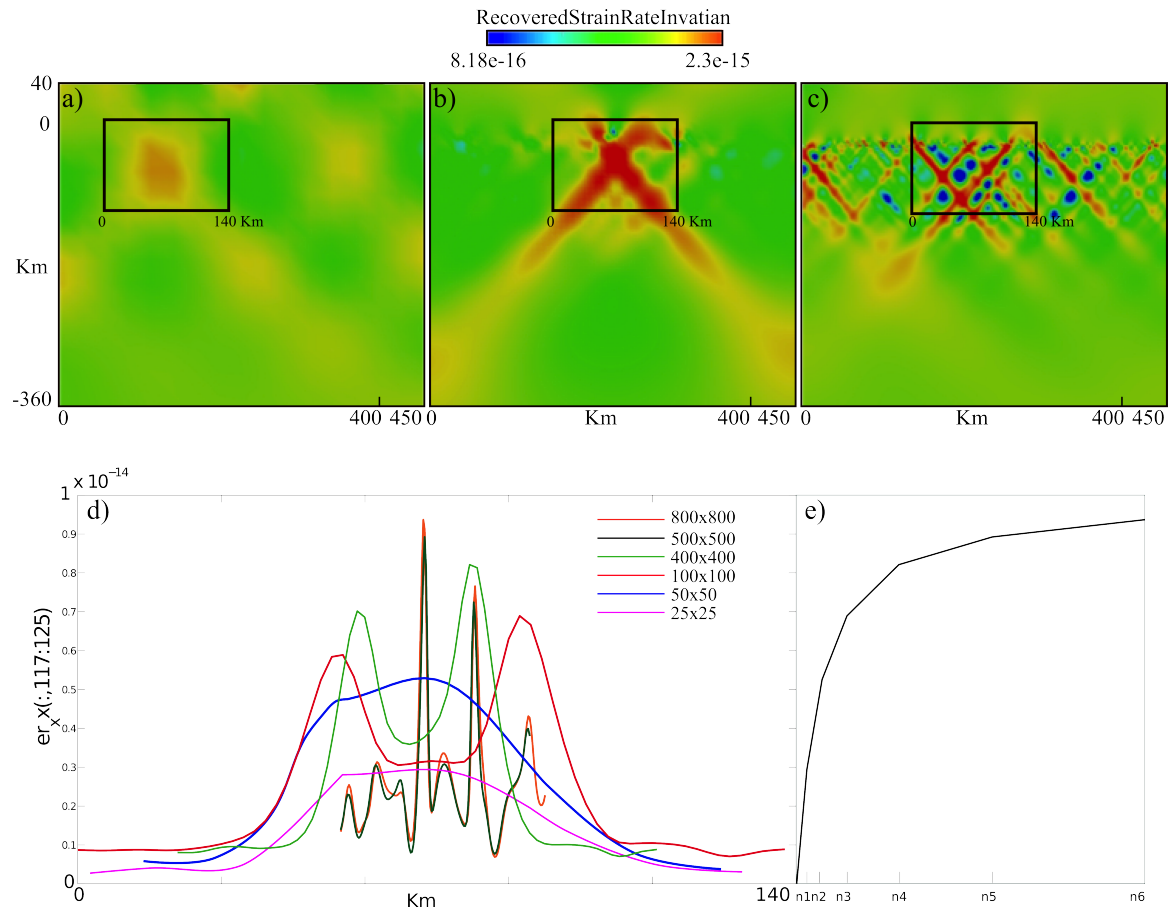


Figure 3.14 Grid independency test (Resolution test) performed on a testing domain at 400km depth by 400 km wide. This does not change the size of the elements of the resolution test. Numerical domain for increasing resolution mesh of  $n1=25 \times 25$ ,  $n2=50 \times 50$ ,  $n3=100 \times 100$ ,  $n4=400 \times 400$ ,  $n5=500 \times 500$  and  $n6=800 \times 800$  elements. a), b) and c) show only 25x25, 100x100 and 500x500 respectively, for a second invariant of the strain rate as example. The appropriate numerical spatial resolution for the testing domain is 1x1 km elements mesh, with an error of 5%. This corresponds to a 700 x 400 cells, km for the model domain, with a cell element of 1x1 km. c) Values of Strain rate invariants from the 6 model runs with the 6 resolution indicated above and taken. From the areas similar to the one delimited with the black square on Fig. a), b) and c), where the maximum value of strain rate invariant is achieved. e) Plot of the maximum value of strain rate invariant for each the 6 model runs vs resolution.



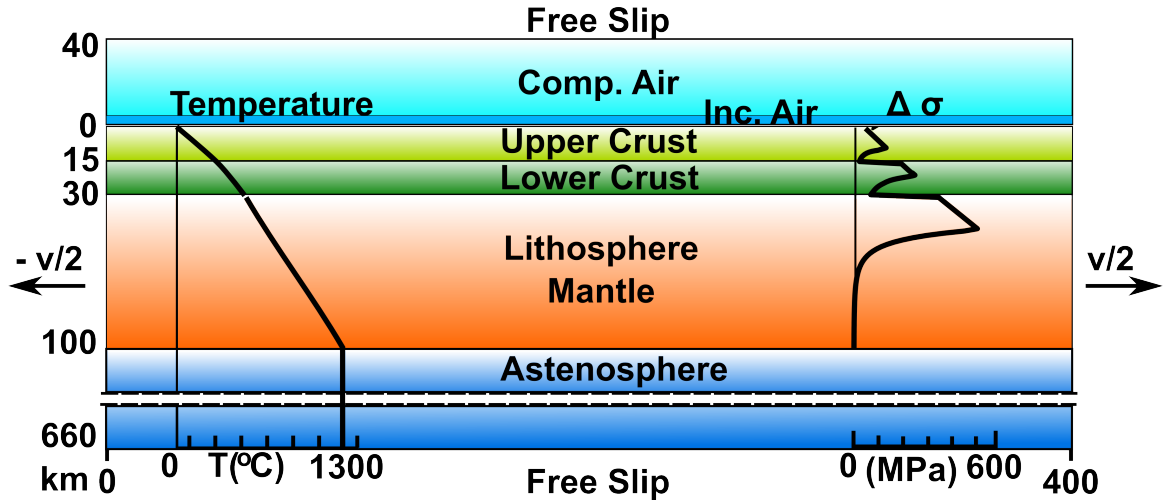


Figure 3.15 Numerical model setup. The lithosphere is 100 km thick, defined by the 1300 °C isotherm, with upper crust and a lower crust of 15 km thick each, and a “sticky air” layer on top (see text). Beneath the lithosphere, the asthenosphere extends to the bottom of the computational domain, 700 km deep. Horizontal velocity boundary conditions of  $\pm v/2$  are applied at the right and left sides of the numerical domain. All the model boundaries are free slip. Temperatures profile is depth-dependent, constant laterally. No initial perturbations are added. Stress profile is calculated for a strain rate  $\dot{\epsilon} = 1 \times 10^{-15} \text{ s}^{-1}$ . Comp. = Compressible air and Inc. = Incompressible air

To track precisely the thicknesses of the lithospheric layers in time, we have embedded Lagrangian passive tracers in the models for the surface (upper crust top), the top and base (Moho) of the lower crust, and the initial 1300 °C isotherm, the lithosphere-asthenosphere boundary.

The initial temperature distribution in the model follows that of an equilibrated continental geotherm (Allen & Allen, 2013) with temperature boundary conditions of  $T_0 = 0 \text{ °C}$  at surface and  $T_m = 1300 \text{ °C}$  at the base of the model lithosphere, and Moho temperature of 600° C. The temperature in the crust  $T_c$  and beneath are defined as:

$$T_c = T_0 + \left( \frac{Q_m + Ah}{k} \right) a - \frac{A}{2k} h^2 \quad (3.56)$$

$$T = T_c + \left( \frac{Q_m}{k} \right) (a - h) \quad (3.57)$$

where  $Q_m$  is the heat flux from the mantle,  $A$  is the radiogenic heat production,  $k$  is the thermal conductivity,  $h$  is the thickness of the whole crust and  $a$  is the thickness of the lithosphere  $a = h + H$ , with  $H$  the lithospheric mantle thickness. Deeper, the temperature is kept constant.

On the top and bottom of the model space we enforce free-slip boundary conditions,

whereas on the side we apply kinematic boundary conditions. The right and left sides of the model domain are pulled with a constant velocity  $v_x$ , applying  $v_x/2$  at the right side and  $-v_x/2$  at the left side. These are consistent with the range of present-day plate velocities derived from GPS data (e.g. [Argus & Hefin, 1995](#); [Reilinger R., & McClusky, 2011](#); [McClusky et al., 2010](#)) and from plate kinematic models (i.e. [Heine et al., 2013](#)). All the models runs stop when the domain length reaches 528 km, for a total horizontal strain  $\epsilon_{xx}=1.32$ , achieved in one phase. Also, to provide a more general understanding, I will express the velocity boundary conditions as initial strain-rates,  $\dot{\epsilon}_i = v_i / L_i$ . For the velocity range of 0.1 to 6 cm/yr and domain's initial width of 400 km at the beginning of the modelling we get strain rates of  $7.9 \times 10^{-17} \text{ s}^{-1}$  to  $4.7 \times 10^{-15} \text{ s}^{-1}$ , comparable with the strain-rates recovered from rifting on Earth ([Newman and White, 1993](#)). In the present work we use the strain-rate  $\dot{\epsilon}_{in}$ , to indicate the initial strain rate imposed by the constant velocity boundary condition  $v_i$ . For constant velocities boundary conditions this varies inside the lithosphere as  $\dot{\epsilon}_{in}(t) = \dot{\epsilon}_{in} \exp(-t\dot{\epsilon}_{in})$  ([England, 1983](#)), which implies the strain rates remain significant for times  $\dot{\epsilon}^{-1}$ .

I have performed additional tests changing horizontal size of the domain, resolution, initial crustal layering thicknesses, rheological parameters, radiogenic heating and adding weak/strong seeds in order to investigate their impact on the modelling results. Only models with an initial perturbation, such as weak seeds, result in earlier strain localization, which strongly constrains the evolution of the models, while none of the other parameters resulted in significant deviation from the outcomes, so that I will present a reduced set of models, for clarity.

### 5.2.1 Lithospheric thinning and rifting: the “diagnostic” tool for comparison between different rifting histories

To format our outcomes to usual basins analysis data, we measure the thinning factor in the crust and the lithospheric mantle (e.g. [van Wijk et al., 2001](#); [van Wijk & Cloetingh, 2002](#)), and define  $\beta$  the ratio between the initial thickness of the crust and that during the modelling,  $h_0$  and  $h(x,t)$ , respectively, and  $\delta$  the ratio between the initial thickness of the lithospheric mantle and that during the modelling,  $H_0$  and  $H(x,t)$ , respectively:

$$\beta(x, t) = h_0/h(x, t) \quad (3.58)$$

$$\delta(x, t) = H_0/H(x, t) \quad (3.59)$$

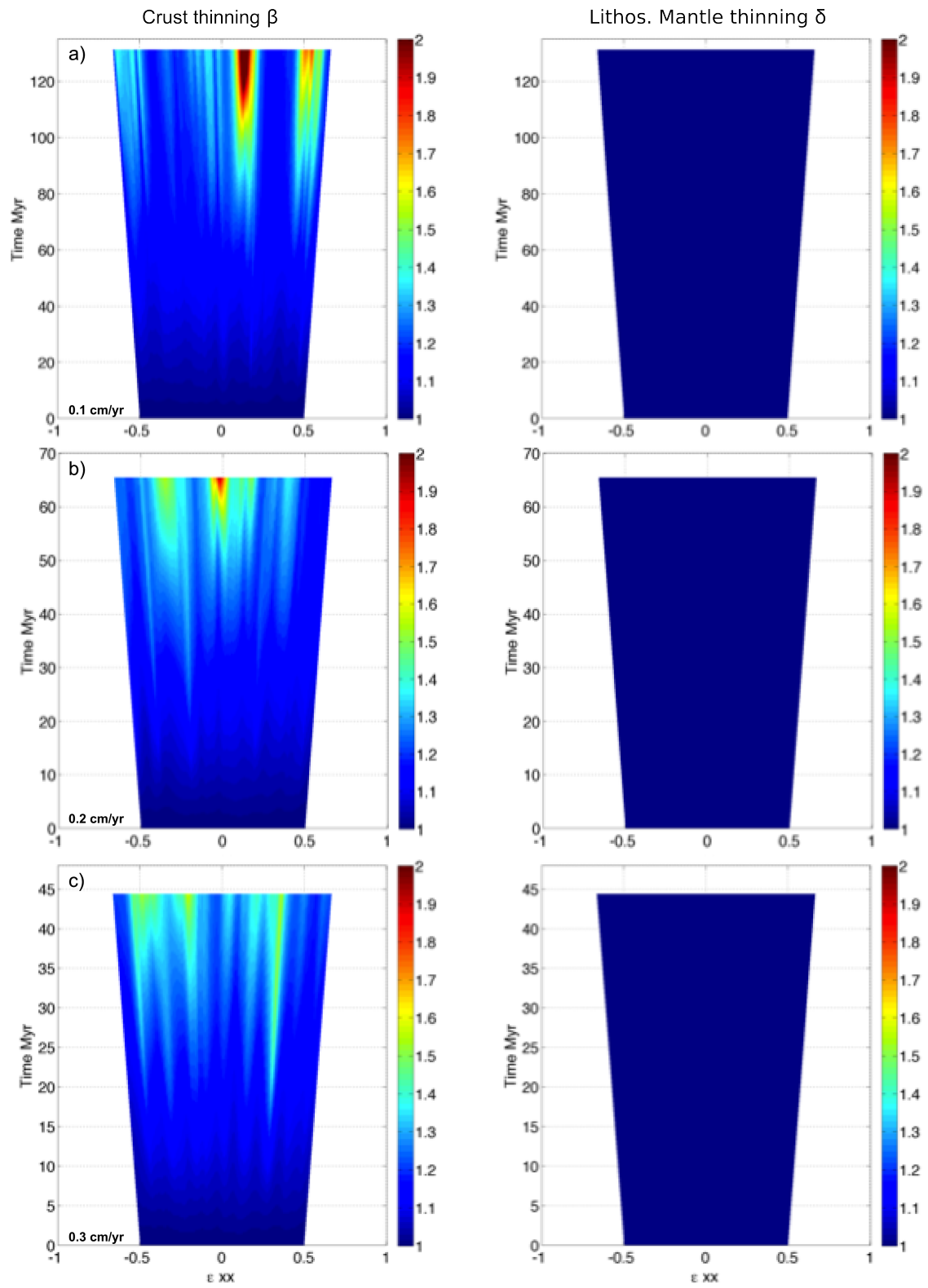
Although the models embed upper and lower crust, we present the thinning factor of whole crust and do not focus on details of intra-crustal structures. Presenting the thinning

factors of crust and lithospheric mantle versus time allows visualising the evolution of the basins, and provide insights in the evolution of the basin. We define the break-up of the crust when  $\beta > 22$  and the break-up the lithosphere when both crust and lithospheric mantle have  $\beta$  and  $\delta > 22$ , in agreement with [Frenke, \(2013\)](#).

[Fig. 3.16](#) shows how applying faster horizontal velocity at the domain sides, allows the development of a wide rift, with no coupling between crust and mantle ([Fig. 3.16a](#),  $v_{xx}=0.1$  cm/yr) to a well developed narrow rift with complete coupling of the deformation between crust and mantle ([Fig. 3.16m](#),  $v_{xx}=5$  cm/yr).

[Van Wijk and Cloetingh \(2002\)](#) modelled monophasic lithospheric stretching using crust and lithospheric mantle thinning to show the results. They found that a wide rift and rift migration was favoured by a velocity below 0.8 cm/yr, while a velocity above 0.8 cm/yr allows for development of a narrow rift, with strong crust/lithospheric mantle coupling. Analysing the models in [Fig. 3.16](#), it is possible to understand that the critical value between the lithospheric delocalization (wide rift) and localization (narrow rift) is around 0.8 cm/yr. Comparing these results with the [Van Wijk and Cloetingh \(2001\)](#), one can observe that there is a good match and, therefore, the model is validated for the rheological parameters, geometries, resolution, temperature distribution and range of velocity boundary conditions adopted. This model can then be used to build the polyphase 2D numerical models.

*Figure 3.16 (next page) Crustal ( $\beta$ ) and lithospheric mantle ( $\delta$ ) thinning vs time showing the formation of the wide and narrow rift end members (respectively models a) and m) ) and all the intermediate cases. The following horizontal velocities have been used to stretch the lithospheric domain. The velocities from a) to m) are  $v_{xx} = 0.1, 0.2, 0.3, 0.4, 0.5, 0.8, 1, 2, 3, 4$  and  $5$  cm/yr. the threshold velocity value between lithospheric strain delocalization and localization is found at  $v_{xx} = 0.8$  cm/yr . Time is the vertical axis and is scaled for every model.*



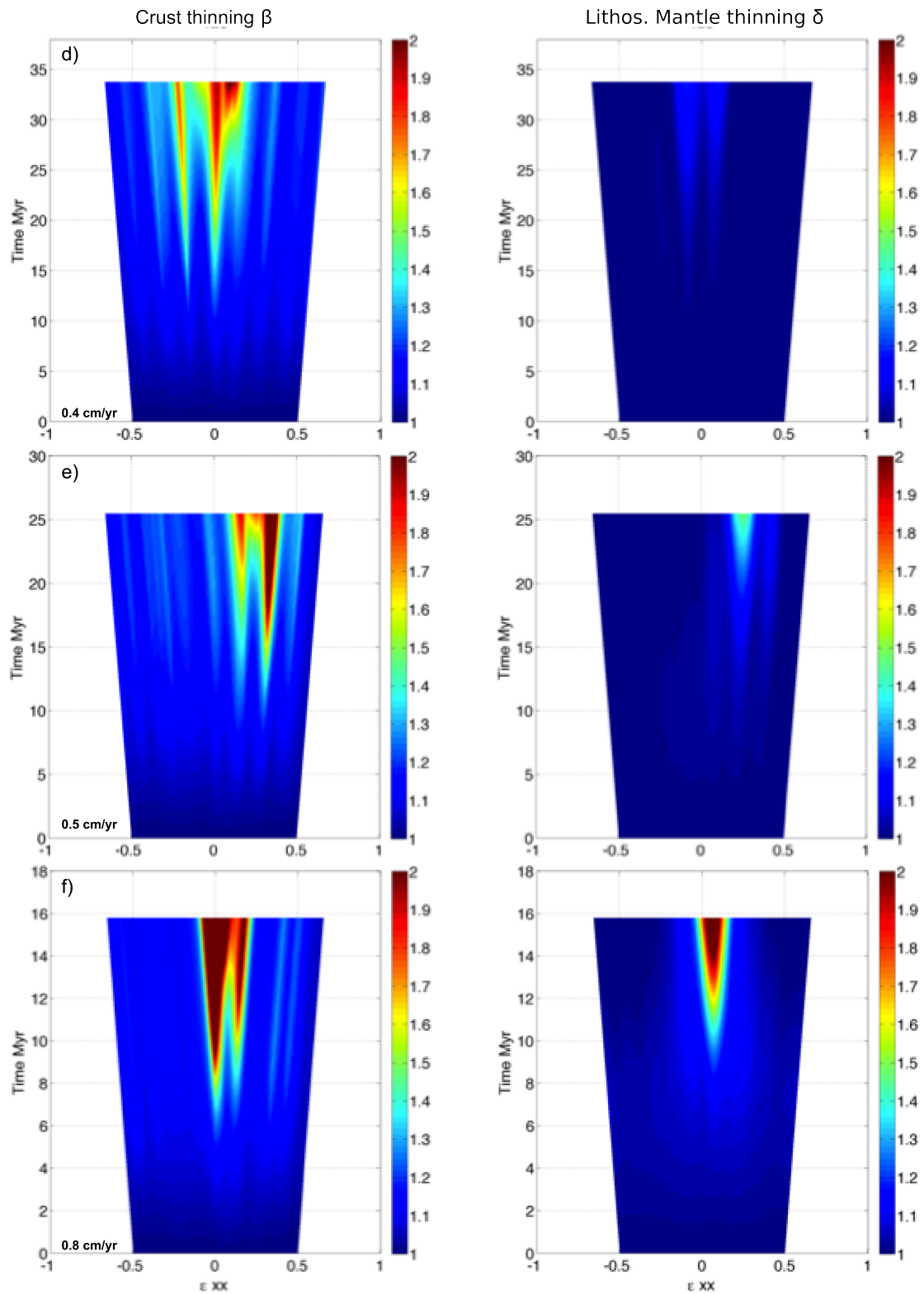


Fig. 3.16 continued

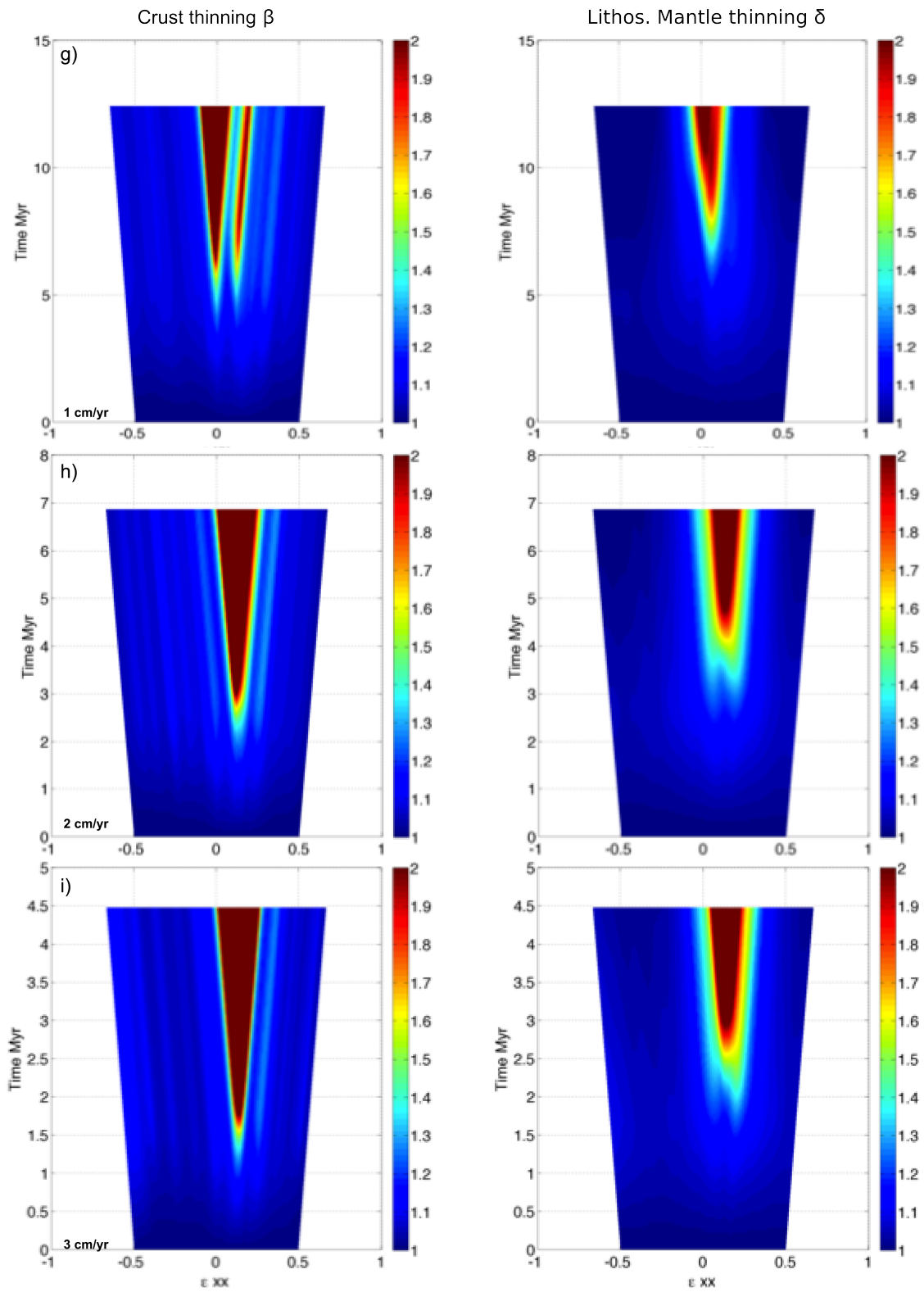


Fig. 3.16 continued

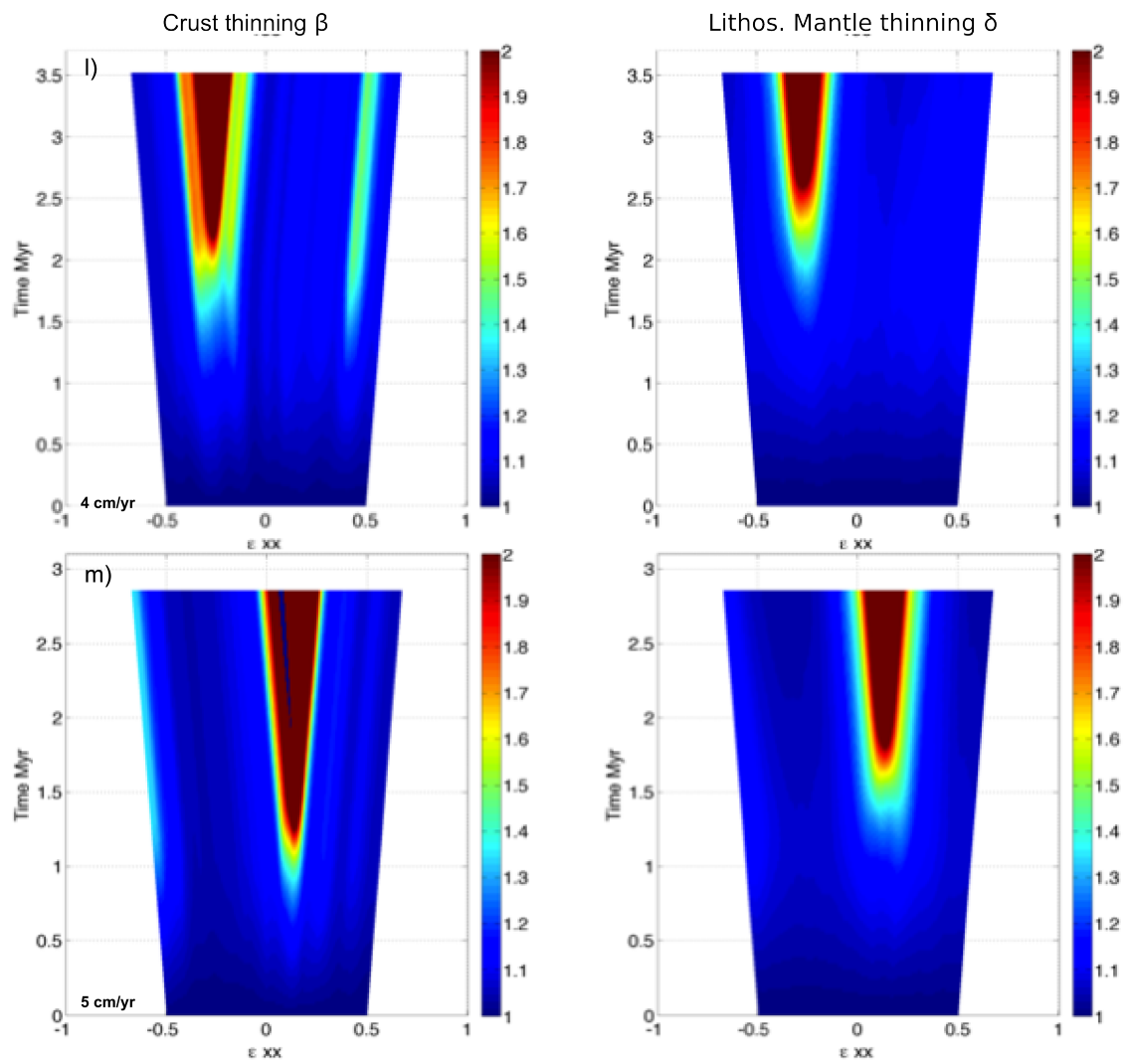


Fig. 3.16 continued





## Declaration for Thesis Chapter 4

**Monash University**

### Declaration for Thesis Chapter 4

#### Declaration by candidate

In the case of Chapter 4, the nature and extent of my contribution to the work was the following:

<b>Nature of contribution</b>	<b>Extent of contribution (%)</b>
Development of the Rationale as well as Conceptual and Numerical modelling; Analysis and interpretation of the results.	90

The following co-authors contributed to the work. If co-authors are students at Monash University, the extent of their contribution in percentage terms must be stated:

<b>Name</b>	<b>Nature of contribution</b>	<b>Extent of contribution (%) for student co-authors only</b>
Dr. Fabio A. Capitanio	Supervisory role; Rationale; Modelling strategy.	5
Dr. Rebecca J. Farrington	Supervisory role; Numerical modelling.	3
Dr. Nicolas Riel	Melting post-processing coding.	2

The undersigned hereby certify that the above declaration correctly reflects the nature and extent of the candidate's and co-authors' contributions to this work\*.

**Candidate's  
Signature**

	<b>Date</b> 01/04/2016
---	---------------------------

**Main  
Supervisor's  
Signature**

	<b>Date</b> 01/04/2016
---	---------------------------



# **CHAPTER 4: MODELLING COMPLEX RIFTING EVOLUTION EXEMPLIFIED THROUGH RIFT- COOLING-RIFT (RCR) HISTORY TYPE**

The role of the strain history on the modes of continental extension

V. Morena Salerno \*, Fabio A. Capitanio, Rebecca J. Farrington and Nicolas Riel<sup>1</sup>

School of Earth, Atmosphere and Environment, Monash University, Clayton, 3800 VIC, Australia

<sup>1</sup> Now at Department of Earth Sciences, Durham University, UK

## **ABSTRACT**

Continental rifts evolve through deformation episodes into a variety of diverse basins with complex structural styles, subsidence and thermal histories, which may include melting. Existing models have probed the role of initial lithospheric rheological layering, geothermal gradients and stretching rates on continental rifting, however continental rifts often evolve through several extensional phases, which are not explained by a single rifting approach. Here, we address the role of episodic stretching on the long-term evolution of continental rifts. By means of numerical modelling we investigate the development of rifting patterns as a consequence of distinct phases of lithospheric extension under different stretching rates, modifying the lithosphere's rheological layering, and intervening cooling, when the lithosphere regains its original thickness, and their effect on subsequent rifting. The models showed that early rifting stages have a fundamental control on lithospheric-scale strain localization/delocalization and, consequently, on the tectonic rifting style and its evolution. The combination of diverse rifting velocities results in a variety of basins ranging from narrow to wide rifts to hyper-thinned, with different degree of symmetry and melt yield in time, reproducing the first-order features of major basins on Earth. We propose a classification that support the interpretation of rift basins and passive margins and illustrate the cases in which the previous rifting history cannot be neglected.

## 1. INTRODUCTION

The major effect of divergent forces on continental lithosphere is rifting, where lithosphere undergoes stretching, faulting, subsidence and sedimentary basin formation, with possible episodic magmatism (e.g. [Mckenzie, 1978](#); [Wernicke, 1985](#); [Buck, 1991](#); [Kusznir & Park, 1987](#); [Brun, 1999](#); [Lister & Davis, 1898](#); [Whitmarsh et al., 2001](#); [van Wijk et al., 2001](#); [Manatschal, 2004](#); [Péron-Pinvidic et al., 2007, 2013](#); [Sutra et al, 2013](#); [Bell et al., 2014](#)). Different deformation styles are observed on Earth's rifts, ranging from narrow to wide rift basins, or basins on hyper-stretched crust, eventually developing asymmetric structures (e.g. [Brun, 1999](#); [Buck, 1991](#); [Huismans & Beaumont, 2007, 2011, 2014](#); [Keen, 1987](#); [Keen, 1985](#); [Kusznir & Park, 1987](#); [Perez-Gussinye et al., 2006, 2012](#); [Peron-Pinvidic & Manatschal, 2010, 2015](#); [Brune, 2014](#); [Lavie & Manatschal, 2006](#)). Among many classification criteria, a common one is based on the lithospheric-scale deformation mode. It is acknowledged that localised faulting throughout the whole lithosphere couples the crust and mantle deformation, thus resulting in symmetric narrow basins (e.g. [Buck, 1991](#); [Gueydan et al., 2008](#); [Mckenzie, 1978](#)); when instead the deformation is diffuse across a larger area, a wide rift can form, usually associated with uncoupled tectonic styles in the crust and the lithospheric mantle (e.g. [Buck, 1991](#); [Wernicke, 1985](#)). The uncoupled tectonics style also applies to basins where strongly thinned crust overlies unroofed lithospheric mantle, referred to as hyper-stretched basins (e.g. [Whitmarsh et al., 2001](#); [Hopper et al., 2004](#); [Unternehr et al., 2010](#); [Aslanian & Moulin, 2010](#); [Aslanian et al., 2009](#); [Huismans & Beaumont, 2011](#); [Manatschal et al., 2015](#)). The record of these basins may include episodes of melting during rifting, identified as deep bodies by seismic surveys, such as along the northern Iberian continental margin ([Zelt et al., 2003](#)) and northern Angolan margin ([Moulin et al., 2005](#)) or also volcanism, as found in the African Rift System ([Corti et al., 2012](#) and references therein; [Baker et al., 1972](#)) and several other volcanic margins along the Atlantic Ocean (e.g. [Franke 2013](#)).

Our understanding of how lithosphere deforms into sedimentary basins relies greatly on the physical modelling of rifting processes. The rifting of the lithosphere is understood through a single, major phase of extension, during which the surface subsides forming a sedimentary basin, followed by a cooling stage, during which the subsidence is strictly related to thermal thickening ([Mckenzie, 1978](#)). Using this approach, the role of lithosphere's initial and boundary conditions during rifting have been emphasised,

revealing that the initial lithospheric 1) rheological layering and 2) geothermal gradients (e.g. [Buck, 1991](#); [Gueydan et al., 2008](#); [Weinberg et al., 2007](#)), and 3) the stretching rates compete in the determination of the basins' deformation style (e.g. [Wijk & Cloetingh, 2002](#); [England, 1983](#); [Porth, 2000](#)). Because lithosphere-forming rock's rheology is temperature-dependent, [Buck \(1991\)](#) proposed that a wide rift is the result of stretching of a thickened lithosphere with an elevated initial surface heat flow,  $Q = 80 \text{ mW/m}^2$ , thus defined as hot and weak lithosphere. Instead, lithosphere with a lower initial heat flow,  $Q = 60 \text{ mW/m}^2$ , is cold and thus strong and undergoes narrow rifting when stretching. However, similar results are achieved when the compositional layering within the lithosphere, hence the temperature at the Moho, varies. Several geological cases can be explained by this modelling approach, such as the wide rifts of the Aegean Sea and North Basin and Range, or the narrow rifting in the Rio Grande, Northern Red Sea, Gulf of Suez, East African Rifts, Rhine Graben and Baikal Rift ([Buck, 1991](#)). Alternatively, the formation of narrow and wide rifts is explained through varying the rheological layering thicknesses, leading to similar strain coupling of crust and lithospheric mantle. This offered an understanding of the Basin and Range and Corinth basin wide rifts as well as the deep crustal décollement along the Atlantic-type non-volcanic passive margins and the narrow rifting in the Limagne-Bress-Rhine system, Rio Grande, East African Rift and Baikal basins ([Gueydan et al., 2008](#)). Finally, [Van Wijk & Cloetingh, \(2002\)](#) showed that the velocities of stretching at the lithosphere's boundary also exert a similar control on the rift width and localisation, with a wide rifting forming through basin migration under slow stretching rates, as opposed to narrow rifts when stretching velocities are instead fast. Similar evolutions are found along the mid-Norwegian, Galicia and South Alpine margins.

The trade-off between these parameters has been addressed by [Crameri & Kaus \(2010\)](#) and [Kaus and Podladchikov \(2006\)](#), who explain the conditions necessary for strain localisation through a non-dimensional localisation number which explicitly accounts for the initial temperature-dependent rheological layering and boundary conditions, as an initial strain rate (in their work this is referred to as background strain rate). In [Lu et al., \(2011\)](#) this approach is applied to the North China Craton province, where the emergence of narrow and wide rift basins is illustrated. This body of work allows the elegant synthesis of the controls on rifting evolution as a function of plastic thickness, temperature-dependent viscosity, Moho temperature and initial strain-rates, thus emphasising the role of initial lithospheric temperatures and strain rates evolution.

Therefore, the interpretation of rifting on Earth remains strongly dependent on the initial temperatures and the boundary conditions under which rifts develop. However, some of the constraining data might suffer from significant uncertainties. While the strain rates during rifting can be recovered from burial histories (e.g. [White, 2002](#); [Bellingham & White, 2000](#); [Baldwin et al., 2006](#); [Capitanio et al., 2009](#)) the initial temperature distribution and rheological layering are not easily constrained. In fact, the evolution of most basins on Earth includes more complex rifting histories with tectonic activity alternating with quiescence, time-dependent subsidence, stretching velocities and possible rifting migration and melting episodes. Hence, no single rifting event occurs on a pristine lithosphere, so that the initial conditions are hardly determined with precision. Therefore, their large variability over time and space limits the applicability of single-phase rifting model ([Mckenzie, 1978](#)). One such case is the Norway margin ([Gabrielsen et al., 1999](#); [Reemst & Cloetingh, 2000](#)), where a long-lasting rifting history includes several rifting episodes (290-235 Ma, 170-95 Ma, 75-57 Ma), between the initial rifting and break-up, with oceanisation by ~ 55 Ma. Similar episodic rifting histories can be observed in the Iberian Basin ([Van Wees et al., 1998](#)), West Antarctic Rift System ([Huerta and Larry, 2007](#); [Corti et al., 2013](#)), Michigan Basin ([Bond and Kominz, 1984](#)), Parana Basin ([Zalan et al., 1990](#)) Southwest Ordos Basin ([Xie, 2007](#)), Illinois Basin, Farley well ([Bond and Kominz, 1984](#)), Moroccan Basin ([Ellouz et al., 2003](#)), Gippsland Basin ([Falvey and Mutter, 1981](#); [P. Yin, 1985](#)), Jeanne D'Arc Basin ([Stampfli et al., 2002](#)), Baikal Basin ([Moore et al., 1997](#)), Williston Basin, North Dakota ([Bond and Kominz, 1984](#)), Williston Basin, Saskatchewan ([Fowler and Nisbet, 1985](#)), Cantabrian Basin ([Stampfli et al., 2002](#)), Lusitanian Basin ([Stampfli et al., 2002](#)). For simplicity, these basins can be classified as rift-cooling-rift history basins (**RCR**). Other basins, instead show abrupt changes in strain rate and subsidence rate during long-term rifting, such as the Petrel Sub-basin, Australia ([Baldwin et al., 2006](#)), the Red Sea (e.g. [Reilinger and McClusky, 2011](#), [Almalki et al., 2014](#)), Lybia's Sirte Basin ([Capitanio et al. 2009](#)), South China Sea ([Chen, 2014](#)), and many others (see [Sengor, 2001](#)). They can be classified as rift-rift history basins (**rr**) basins. Interpreting these complex histories through a single rifting – cooling model has eventually led to incongruities.

In this frame, the final basins architectures are better described as the interplay of the earlier rifting and quiescence phases, defining through thinning and cooling the ever-changing conditions for subsequent stages, and lithospheric stretching rates. Several authors have modelled poly-phasic rifting histories of RCR type addressing specific

geological cases. [Van Wees et al. \(1998\)](#) studied the Iberian Basin characterised by several pulsating periods of stretching intermitted by periods of relative tectonic quiescence and thermal subsidence. [Chen \(2014\)](#) modelled the subsidence the Baiyun Sag in the continent slope of the South China Sea, using a rifting-cooling-rifting model to better fit the subsidence data. [Armitage et al. \(2010\)](#) simulated a poly-phasic rifting with intervening cooling, resulting in the strain localisation shift, in order to explain differences in magma production between Greenland and South-west Indian margins. The cooling stage between rift episodes has been addressed also by [Huisman & Beaumont, \(2007\)](#), who have shown how this favours deeper strain localization in the mantle, the development of an asymmetric basin and exhumation of the mantle lithosphere, compatible with what observed in the Newfoundland–Iberia margins system. Similar results were originally proposed by [Tett & Sawyer, \(1996\)](#), who showed through multi-stage rifting models inspired to the Newfoundland and Iberian Margins, that when episodic rifting repeats, the basin centre will not be favoured for further extension, because cooling of the upper mantle strengthens significantly the lithosphere beneath the previously thinned lithosphere (England, 1983). Additionally, the role of inter-rifting cooling on the basin migration of margin asymmetry has been also addressed by [Naliboff & Buiter, \(2015\)](#), with applications to the mid-Norwegian and mid-East Greenland margins and Northern and Southern Atlantic passive margins, and by [Petersen et al. \(2015\)](#), who illustrated the cooling stage's impact on the subsidence patterns in long-term rifting cases. While there is growing evidence that accounting for the several episodes of rifting and possible intervening quiescence (cooling) leads to a better explanation of rifts, a more general understanding of the role of rifting history on the mode of continent deformation remains lacking.

In this study we focus on the role of complex rifting history, addressing under which conditions previous deformation phases and cooling affect the subsequent rifting evolution. We use numerical modelling to reproduce different rifting histories, with combined stretching rates and cooling, and analyse how the different modes of lithospheric extension affects the final basin style. The results illustrate that the combination of two rifting phases achieved under a range of stretching rates, and intervened by cooling when thinning is severe, eventually leads to a variety of basin structures such as wide and narrow rifts, with different degrees of symmetry, or basins on hyperextended crust. We illustrate the cases in which the initial rifting stage has a strong control on the following evolution (Slow Early Control Phase group) and cases in which

the rifting is independent of the early rift history (part of Fast Early Control Phase group). The diversity of these basins are characterised by quantifying thinning factors, tectonic subsidence and melting histories to provide comparative tools to the geological observations. We conclude by discussing the insights into the interpretation of key features of rifts and basins, and their relevance for the understanding of the rifting evolution and the basins reconstructions.

## 2. NUMERICAL MODELLING

### 2.1 Modelling approach

Here, we model the deformation of the lithosphere under stretching imposed through moving boundaries. The rifting process is here approximated to a 2D problem (when we think at the opening of the Atlantic, the rifting process can be approximated as 2D). We focus on the role of the varying boundary conditions during rifting, i.e. various strain rates and quiescence, to derive the conditions under which the model is dependent on lithosphere's initial state. Therefore, we use the same initial lithospheric model with an equilibrium continental geotherm and normal-thickness crust. We do not investigate the role of various crustal compositions here, affecting the rheology, and instead use the same crustal rheological parameters (Table 1). To better illustrate the role of the complexities during rifting, we consider no pre-existing perturbation in the lithosphere, i.e. no weak/strong seeds or thermal anomalies are introduced ([Fernandez and Ranalli, 1997](#)).

The modelled rifting history includes three stages: an initial rifting, a cooling stage and a second rifting phase. For both rifting phases we have tested the effect of different stretching velocities in each phase, varied between  $v = 0.1$  and  $6$  cm/yr, for a total of 289 models combinations. All models are run until the same finite strain is achieved, and are split evenly in the two phases, each of  $\Delta\epsilon_{xx} = 0.16$ , which runs until  $\epsilon_{xx} = 1.16$  in the first and reaches the total  $\epsilon_{xx} = 1.32$ , in the second. The duration of each stretching phase depends on rifting velocity  $t_r = L_i \Delta\epsilon_{xx} / v_i$ , with  $L_i$  initial models' length and stretching velocity at the rifting phase  $i$ , yielding 66 to 1.2 Myrs, for the range of velocity used here.

In the cooling phase, the stretching velocity vanishes, and only heat diffusion occurs. This is run until the lithospheric mantle isotherms relax to the initial thickness. Thus, the cooling time has a duration that depends on the thinning of the thermal boundary layer  $\delta$ , achieved during the first rifting phase, defining the thickness to be recovered. The initial thickness  $a$  of a thermal boundary layer (the lithosphere), defined as the depth of the



isotherm 1300 °C, is  $a = c (\kappa t)^{1/2}$  (Turcotte & Schubert, 2014), with  $\kappa$  the thermal diffusivity and  $t$  the time. Thus, the cooling time  $t_c$  needed to restore this isotherm depends on its displacement, the thermal lithospheric thinning factor  $\delta$  (see below):

$$t_c = \frac{h^2}{c^2 \kappa} \left(1 - \frac{1}{\delta}\right)^2 \quad (4.1)$$

with the nondimensional constant  $c = 0.85$  here determined empirically. Because stretching under very slow velocities does not lead to thermal perturbations, in a range of models the cooling phase vanishes and the two rifting phases are replaced by a long-term deformation until the finite strain is achieved.

To address the interaction of mechanical extension and heat diffusion in our modelling we resort to the Peclet number, which allows expressing the relation between the efficiency of the advection against the diffusivity, and has been used in lithospheric extensional modelling (e.g. England, 1983; Allen & Armitage, 2012; Allen & Allen, 2013). This non-dimensional number is defined as  $Pe = ua^2/\kappa$  (Turcotte & Schubert, 2014) where  $u$  is the vertical velocity,  $a$  is the thickness of the thermal lithosphere. In general, when  $Pe \gg 1$  upward advection dominates and when  $Pe \ll 1$  the process is dominated by heat diffusion. Yet, different authors have proposed a modified Peclet number. Allen & Allen, (2013) and Allen & Armitage, (2012) introduce the strain rate  $\dot{\epsilon} = du/dl$ , such that  $Pe = \dot{\epsilon} a^2 / 2\kappa$ , whereas in England, (1983) the horizontal initial length of the model  $L_0$  is introduced  $Pe = ua^2/\kappa L_0$ . Hence, the critical Peclet number indicating the transition from diffusion- to advection-dominated processes is less constrained, and occurs for  $1 < Pe < 10$  according Allen & Allen (2013). For larger (smaller) values advection (diffusion) dominates.

In these two domains clearly dominated by diffusion or advection, the lithosphere deformation changes behaviour, being deformed at small or large strain rates, respectively, resulting in two deformation modes, wide and narrow rifts (Buck, 1991). Hence, although we have modelled a wide range of velocities, in the remainder of the paper we refer to two stretching velocities as  $v_{\text{slow}} = 0.3$  cm/yr, and fast  $v_{\text{fast}} = 5$  cm/yr, indicating two values that clearly lead into one of the two deformation modes.

This simplification allows discussing four cases, only, that is the models with same velocity on both rifting phases,  $v_{\text{fast}} - v_{\text{fast}}$  and  $v_{\text{slow}} - v_{\text{slow}}$ , and models when the rifting rates is different in the two phases, slower followed by faster stretching, and vice-versa. Using a nomenclature for the models based on the applied velocity relative to the rifting

phase, where  $r$  is for slow rifting at  $v_{\text{slow}}$  and  $R$  is for fast rifting at  $v_{\text{fast}}$ , the four models are 1)  $r_1$ - $r_2$ , 2)  $r_1$ - $R_2$ , 3)  $R_1$ - $r_2$  and 4)  $R_1$ - $R_2$ , where the subscript indicates the rifting phase.

## 2.2 Governing equations

We have modelled the 2D lithospheric extension, using Underworld, which solves the incompressible Stokes flow on an Eulerian finite element mesh embedding Lagrangian particles, which allows to track movements of the materials points relative to the mesh for high deformation in visco-plastic flow (Moresi et al., 2007; Moresi et al., 2003).

The code solves the governing equations of mass (Eq.4.2), momentum (Eq.4.3), and energy conservation (Eq.4.4) for an incompressible flow:

$$\frac{\partial u_i}{\partial x_i} = 0 \quad (4.2)$$

$$\frac{\partial \tau_{ij}}{\partial x_j} + \frac{\partial p}{\partial x_i} = -\alpha \rho \mathbf{g} T \lambda_i \quad (4.3)$$

$$\frac{\partial T}{\partial t} + u_i \frac{\partial T}{\partial x_j^2} = \kappa \frac{\partial^2 T}{\partial x_j^2} + H_r \quad (4.4)$$

where  $\tau_{ij}$  is the deviatoric stress tensor,  $p$  the total pressure,  $x_i$  are the spatial coordinates,  $u_i$  is the velocity,  $T$  is the temperature,  $\alpha$  is the thermal expansivity,  $\rho$  is the fluid density,  $\lambda_i$  is the unit vector in the direction of gravity,  $\mathbf{g}$  is the gravitational acceleration and  $H_r$  radiogenic heat.

The details of the numerical method, software implementation and relevant numerical benchmarks are described in Moresi et al., (2007), Moresi et al., (2003). The code has been widely used in several geodynamic application such as extension tectonics and passive margins (e.g. Farrington et al., 2010, Sharples et al., 2015), subduction (e.g. Stegman et al., 2010; Capitanio & Replumaz, 2013; Capitanio, 2014; Mason et al., 2010; Farrington et al., 2014) and for the study of the Stokes flow and problems arising in computational geodynamics. (e.g. May & Moresi, 2008).

The constitutive equation relating the stress with the strain rate is given by the generalised non-Newtonian model of the form:

$$\tau^n = 2\eta \dot{\epsilon} \quad (4.5)$$

where  $\eta$  is the dynamic viscosity and  $\dot{\epsilon}$  is the strain rate tensor:

$$\dot{\epsilon} = \frac{1}{2} [\nabla \mathbf{u} + (\nabla \mathbf{u})^T] \quad (4.6)$$

We use non-linear, temperature-dependent flow laws for the viscous deformation of rocks according with the following equation:

$$\tau_{II} = \frac{1}{A\eta_{eff}^{n-1}} \exp\left(\frac{E}{nRT}\right) \quad (4.7)$$

where  $T$  is the temperature,  $R$  is the gas constant,  $A$  is a pre-exponent,  $E$  the activation energy and  $n$  the power-law exponent. The material parameters vary in the models according the rock type (Tab. 1), that is we use rheological parameters of a wet quartzite for the upper crust (Gleason & Tullis, 1995), wet diabase parameters for the lower crust Mackwell et al. (1998) and a dry olivine for the mantle (Chopra and Paterson (1981).

To account for the brittle deformation, we used a Drucker-Prager frictional-plastic pressure-dependent law:

$$\tau_y = C_0 + \tan(\varphi) \sigma_n \quad (4.8)$$

where  $C_0$  is the cohesive strength,  $\tan(\varphi)$  is the internal friction coefficient,  $\varphi$  is the internal friction angle,  $\tau_y$  and  $\sigma_n$  are, respectively, the brittle shear and normal stress to the plane of failure within material.

The composite visco-plastic flow law used in the models is implemented through the effective viscosity:

$$\eta_{eff} = \min\left(\eta; \frac{\tau_y}{2\dot{\epsilon}_{II}}\right) \quad (4.9)$$

where  $\dot{\epsilon}_{II} = \sqrt{\dot{\epsilon}_{ij}\dot{\epsilon}_{ij}/2}$  is the strain rate tensor's second invariant, i.e. the effective strain rate. Similarly, the stress tensor's second invariant is defined as  $\tau_{II} = \sqrt{\tau_{ij}\tau_{ij}/2}$ .

### 2.3 Model set up and boundary conditions

The governing equations are solved on a 2D computational domain 660 km deep and 400 km wide, with numerical resolution of 700 x 400 elements, for a spatial resolution of 1 km (Fig. 4.1), with 20 particles per element. The lithosphere model is composed of three layers (Fig.4.1). The two layers on the top are each 15 km thick, henceforth the upper and lower crust, and reproduce the properties of the crust. Beneath the crust lies the

mantle, extending to the bottom of the computational domain, where the properties are homogeneous, yet differentiated into lithospheric mantle and asthenosphere by the temperature-dependent viscosity eq. (4.7). Although the mechanical stiffness of the lithosphere is, thus, loosely constrained, we define the lithosphere-asthenosphere boundary (LAB) as the isotherm 1300 °C, at 100 km of depth in the setup. Atop the lithosphere we use an air layer 40 km thick, mimicking the “sticky air” layer to allow for a quasi-free surface and self-consistent evolution of topography (Cramer & Kaus, 2010).

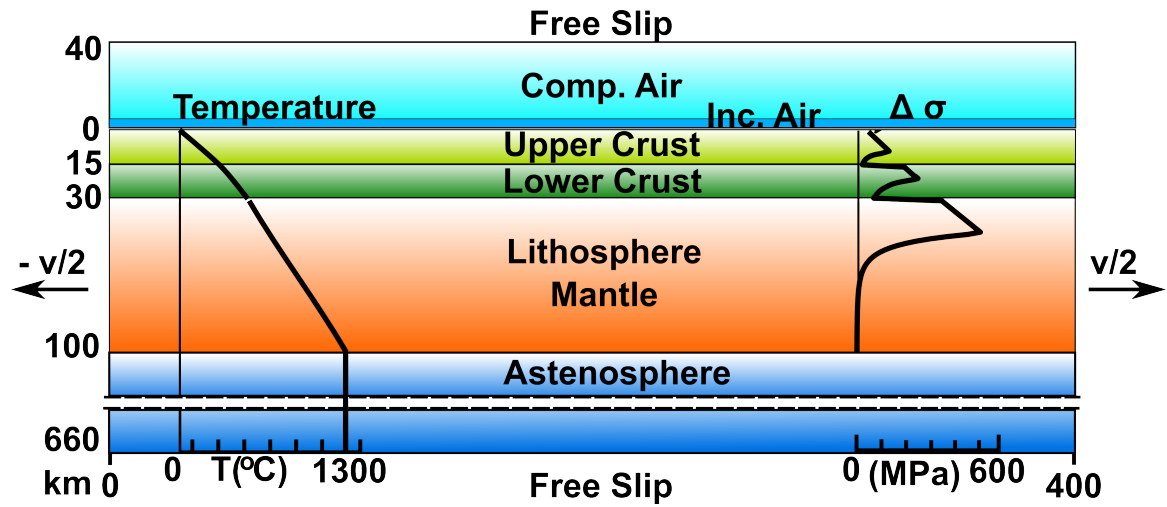


Figure 4.1 Numerical model setup. The lithosphere is 100 km thick, defined by the 1300 °C isotherm, with upper crust and a lower crust of 15 km each, and a “sticky air” layer on top (see text). Beneath the lithosphere, the asthenosphere extends to the bottom of the computational domain, 660 km deep. Horizontal velocity boundary conditions of  $\pm v/2$  are applied at the right and left sides of the numerical domain. All the model boundaries are free slip. Temperatures profile is depth-dependent, constant laterally. No initial perturbations are added. Stress profile is calculated according Eqs. 4.7, 4.8, 4.9 with  $\dot{\epsilon} = 1 \times 10^{-15} \text{ s}^{-1}$ .

To track precisely the thicknesses of the lithospheric layers in time, we have embedded Lagrangian passive tracers in the models for the surface (upper crust top), the top and base (Moho) of the lower crust, and the initial 1300 °C isotherm, the lithosphere-asthenosphere boundary.

The initial temperature distribution in the model follows that of an equilibrated continental geotherm (Allen & Allen, 2013) with temperature boundary conditions of  $T_0 = 0$  °C at surface and  $T_m = 1300$  °C at the base of the model lithosphere, and Moho temperature of 600° C. The temperature in the crust  $T_c$  and beneath are defined as:

$$T_c = T_0 + \left( \frac{Q_m + Ah}{k} \right) a - \frac{A}{2k} h^2 \quad (4.10)$$

$$T = T_c + \left(\frac{Q_m}{k}\right)(a - h) \quad (4.11)$$

where  $Q_m$  is the heat flux from the mantle,  $A$  is the radiogenic heat production,  $k$  is the thermal conductivity,  $h$  is the thickness of the whole crust and  $a$  is the thickness of the lithosphere  $a = h + H$ , with  $H$  the lithospheric mantle thickness. Deeper, the temperature is kept constant.

On the top and bottom of the model space we enforce free-slip boundary conditions, whereas on the side we apply kinematic boundary conditions. The right and left sides of the model domain are pulled with a constant velocity  $v_x$ , applying  $v_x/2$  at the right side and  $-v_x/2$  at the left side. These are consistent with the range of present-day plate velocities derived from GPS data (e.g. [Argus & Hefin, 1995](#); [Reilinger R., & McClusky, 2011](#); [McClusky et al., 2010](#)). All the models runs stop when the domain length reaches 528 km, for a total horizontal strain  $\epsilon_{xx}=1.32$ , achieved in two phases of same strain  $\Delta\epsilon_{xx}=1.16$ . Also, to provide a more general understanding, we will express the velocity boundary conditions as initial strain-rates,  $\dot{\epsilon}_i = v_i / L_i$ , for each rifting phase  $i$ . For the velocity range of 0.1 to 6 cm/yr and domain's initial width of 400 km at the beginning of the modelling we get strain rates of  $7.9 \times 10^{-17} \text{ s}^{-1}$  to  $4.7 \times 10^{-15} \text{ s}^{-1}$ , comparable with the strain-rates recovered from rifting on Earth ([Newman and White, 1993](#)). In the present work we use the strain-rate  $\dot{\epsilon}_i$ , to indicate the initial strain rate imposed by the constant velocity boundary condition  $v_i$ . For constant velocities boundary conditions this varies inside the lithosphere as  $\dot{\epsilon}(t) = \dot{\epsilon}_i \exp(-t\dot{\epsilon}_i)$  ([England, 1983](#)), which implies the strain rates remain significant for times  $\dot{\epsilon}^{-1}$ .

We have performed additional tests changing horizontal size of the domain, resolution, initial crustal layering thicknesses, rheological parameters, radiogenic heating and adding weak/strong seeds in order to investigate their impact on the modelling results. We note that only models with an initial perturbation, such as weak seeds, result in earlier strain localization, which strongly constrains the evolution of the models, while none of the other parameters resulted in significant deviation from the outcomes, so that we will present a reduced set of models, for clarity.

## 2.4 Lithospheric thinning and rifting

To format our outcomes to usual basins analysis data, we measure the thinning factor in the crust and the lithospheric mantle (e.g. [van Wijk et al., 2001](#); [van Wijk & Cloetingh, 2002](#)), and define  $\beta$  the ratio between the initial thickness of the crust and that during the

modelling,  $h_0$  and  $h(x,t)$ , respectively, and  $\delta$  the ratio between the initial thickness of the lithospheric mantle and that during the modelling,  $H_0$  and  $H(x,t)$ , respectively:

$$\beta(x,t) = h_0/h(x,t) \quad (4.12)$$

$$\delta(x,t) = H_0/H(x,t) \quad (4.13)$$

Although the models embed upper and lower crust, we present the thinning factor of whole crust and do not focus on details of intra-crustal structures. Presenting the thinning factors of crust and lithospheric mantle versus time (Fig. 4.3) allows visualising the evolution of the basins, and provide insights in the evolution of the basin. We define the break-up of the crust when it  $\beta > 22$  and the break-up the lithosphere when both crust and lithospheric mantle have  $\beta$  and  $\delta > 22$ , in agreement with [Frenke, \(2013\)](#).

## 2.5 Basin Subsidence

Under the assumption of isostatic equilibrium, we have calculated the tectonic subsidence in our models. This is done following the methodology suggested by [Steckler & Watts, \(1978\)](#).

$$S = \frac{a[(\rho_l - \rho_c) \frac{h}{a} (1 - \frac{\alpha T_m h}{2a}) - \frac{\rho_l \alpha T_m}{a}] (1 - \frac{1}{\beta})}{\rho_l (1 - \alpha T_m) - \rho_w} \quad (4.14)$$

where  $S$  is the tectonic subsidence (depth of the basement in absence of surface loads),  $\rho_l$ ,  $\rho_c$  and  $\rho_w$  are respectively the lithospheric, crust and water averaged densities,  $T_l$  is the lithosphere-asthenosphere boundary temperature,  $\alpha_v$  the coefficient of volume expansion and  $\beta$  is the stretching factor of the whole crust. The depth of the basin is measured taking the initial surface as reference, advected as the lithospheric model stretches, and is calculated on the models only in the point where the maximum stretching is measured. Using eq. (4.14) allows accounting for the water filling of the basin, which is not explicitly modelled. No sedimentation is considered in these models since we derived the tectonic subsidence. We recognised that sedimentation could have an important contribution for basins evolutions, ([Sandiford et al., 2006](#)). However, we do not consider it since the aim here is to isolate only the contribution of the boundary conditions.

## 2.6 Melting

We have calculated the magma production using a benchmark model for peridotite formulated by Katz et al., (2003). The solidus and liquidus curves for given pressure

calculated as:

$$T_{sol} = A_1 + A_2 + A_3 p^2 \quad (4.15)$$

$$T_{liq} = B_1 + B_2 + B_3 p^2 \quad (4.16)$$

where A and B are fitting parameters (see [Katz et al., 2003](#))

As  $T_{sol}$  and  $T_{liq}$  are computed in each element, we quantify the melt fraction  $D$  of peridotite at the temperature  $T$  as:

$$D = \left( \frac{T - (T_{sol} - \Delta T_{H2O})}{T_{liq} - T_{sol}} \right)^{\beta_1} \quad (4.17)$$

For an extensive explanation of parameterization used to calculate the melt fraction ( $T_{H2O}$ ,  $A_n$ ,  $B_n$  and  $\beta_n$ ) see [Katz et al., \(2003\)](#). Integration over the melt-generating area provides an estimate of melt and potential magma production.

### 3. RESULTS

#### 3.1 Lithospheric rifting modes

In this section we present the lithospheric stretching and rifting modes emerging from the models. The models are presented at the end of the first and second rifting phases ([Fig 4.2](#)), when half of the total strain has been achieved ([Figs. 4.2a, b](#)). The slow stretching velocity used during the first rifting phase ([Fig. 4.2a](#)) results in a series of small shear zones/faults where strain-rates are as large as  $1.2 \times 10^{-15} \text{ s}^{-1}$  and rather diffuse in the model. The LAB (red line) is displaced upward respect to the original position (black line) rather uniformly across the domain, with a slight doming in the centre of the model. Similarly, the crust is rather uniformly thinned, and crustal  $\beta$  factors reach a value of 1.35 in the centre of the domain, for crust thickness of 22.3 km, and a rather uniform thinning across the domain ( $\beta \sim 1.2$ ). Thinning in the lithospheric mantle is instead smaller with maximum value  $\delta = 1.08$ , corresponding to a lithospheric mantle thickness of about 65 km, slightly smaller compared to the original one. The different values are explained through the slow stretching rates allowing for cooling during extension, which compensate partly the loss of thickness due to rifting. This deformation style is commonly referred to ‘diffuse’ and associated with wide rifting formation ([Buck, 1991](#))

The model undergoing fast stretching rate ([Fig. 4.2b](#)) is significantly different with strong strain localisation along two major conjugate shear zones/faults cross-cutting the whole lithosphere, where large strain rates of  $5.3 \times 10^{-15} \text{ s}^{-1}$  are measured. Beneath the major shear

zones, the LAB is drawn up by  $\sim 20$  km and the lithosphere mantle is thinned of a maximum  $\delta \sim 1.5$ . Similar thinning localisation is observed in the crust, atop the location of lithosphere thinning with  $\beta \sim 1.75$ . As opposed to the previous model, this deformation style is rather localised, in agreement with published models, leading to a ‘narrow’ basin formation (Buck, 1991).

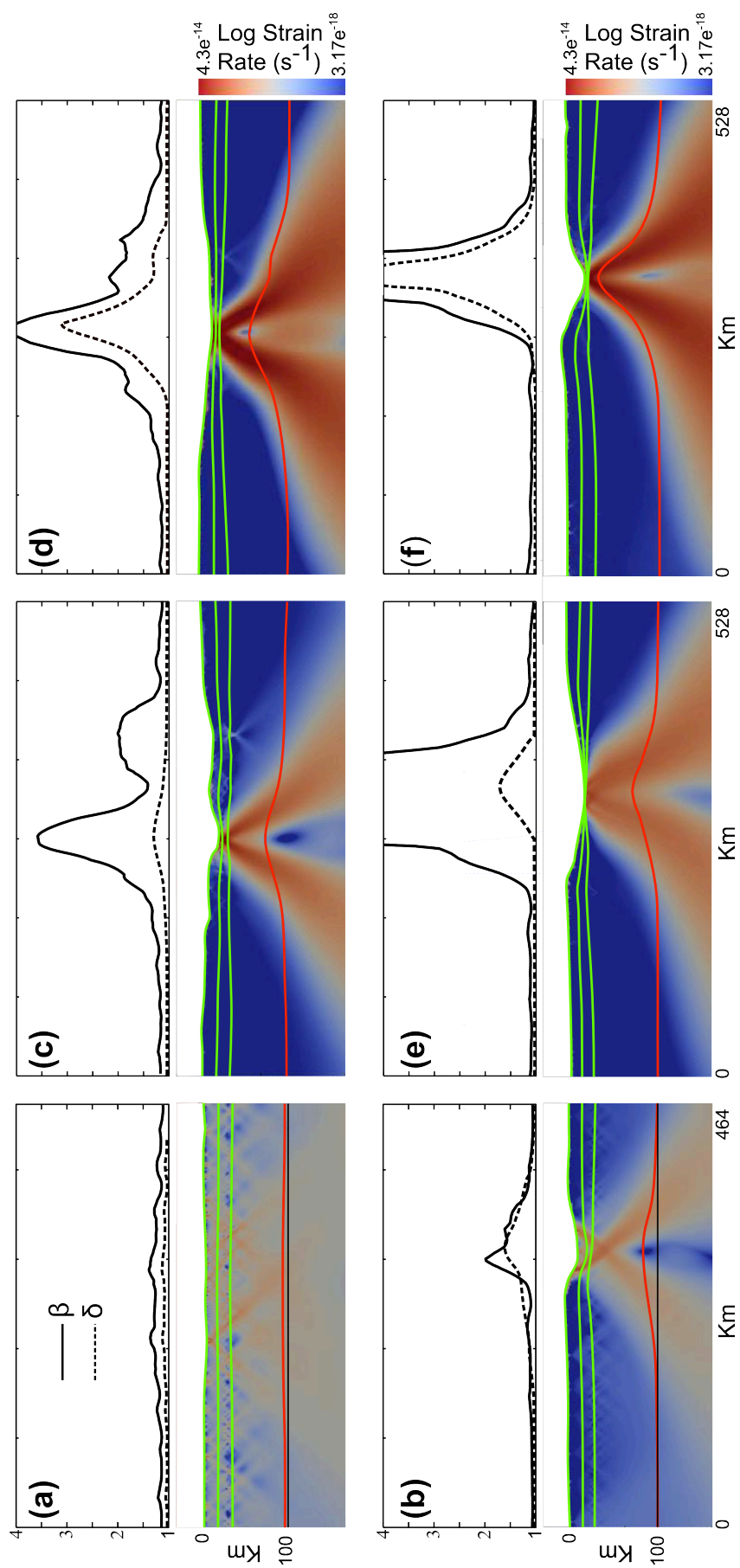
In the subsequent stage the models undergo thermal equilibration, when the LAB is restored to its original position. Despite the geotherms at the end of the cooling phase are almost identical to that of the initial conditions, there is a different inherited rheological structure when the second rifting phase onsets. During thinning, the crust is replaced by lithospheric mantle, which overall increases the integrated strength of the lithosphere (England, 1983). Since the thinning is variable along the lithosphere, both vertical and horizontal strength distributions are affected. While the temperature profile is fully recovered to that of an equilibrium geotherm, the new rheological layering is the result of the previous rifting phase.

Under renewed stretching in the second rifting phase, four different modes are determined, allowing illustration of the history-dependence. In all the models, the second rifting phase leads to a more pronounced localisation, however the characteristics of the resulting rifting basins and lithospheric thinning are different.

In the model with slow rates in both rifting phases  $r_1$ - $r_2$ , the thinning in the LAB is rather minor, the smallest of the all the models (Fig. 4.2c) and large thinning occurs in the crust. The lithospheric thinning is rather localised compared to the first rifting phase (Fig. 4.2a), in spite of the horizontal stretching and stretching rates being exactly the same. A LAB doming is found in the centre of the lithosphere, coupled at the surface with a thinning in the crust, where deformation is accommodated by two shear zones joining at surface, and strain rates are in excess of  $9 \times 10^{-15} \text{ s}^{-1}$ . Average  $\beta$  factors of 1.2 are found across the domain, and reaches 3.5 in the main basin.

*(Next page) Figure 4.2 Results from numerical models. (a) Models at the end of the first slow-rifting phase  $r_1$  and (b) at the end of fast-rifting phase  $R_1$ . (c) Model with repeated slow rifting  $r_1$ - $r_2$ , and (d) slow-fast rifting  $r_1$ - $R_2$ . (e) Model with fast-slow rifting phases  $R_1$ - $r_2$  and (f) with repeated fast rifting  $R_1$ - $R_2$ . Slow stretching velocity  $0.15 \text{ cm yr}^{-1}$  are used in  $r_1$  and  $r_2$ ,  $2.5 \text{ cm yr}^{-1}$  are used in fast rifting phases  $R_1$  and  $R_2$ . Top panel shows thinning factors for crust,  $\beta$  (black solid line), and lithospheric mantle,  $\delta$  (black dashed line). Second invariant of the strain rate with top Upper Crust (surface), top Lower Crust and Moho (green), initial (black) and perturbed (red) asthenosphere -lithosphere boundary (LAB).*





The thinning here is co-located with the maximum thinning in the lithospheric mantle where  $\delta = 1.6$ . The crustal rift basin is  $\sim 210$  km wide, wider than the thinned lithospheric width, and strongly asymmetric. Besides the major basin where lithospheric and crustal thinning are co-located, we find a secondary basin where maximum  $\beta = 2$  is measured, which, however, develops over thick, i.e. non-thinned, lithosphere, unlike the main basin. This mode is called here Asymmetric Wide Rift (AWR).

In models with a slow first phase and a fast second phase  $r_1$ - $R_2$  (Fig. 4.2d) the crustal thinning achieved is similar to the prior model, although the fastest stretching rate results in larger thinning in the lithospheric mantle. While the localisation of strain in this model is similar to the previous model, with two shear zones joining at surface, the thinning of this one is rather different. The measured stretching factors in the two lithospheric layers are similar here, with  $\beta$  in excess of 4 and  $\delta = 3$ . Furthermore, the distribution of thinning is rather similar in the two lithospheric layers, with a co-located maximum stretching factor and a rather symmetric and wide thinning distribution, with a resulting basin  $\sim 350$  km wide. We call this mode Symmetric Wide Rift (SWR).

In the model undergoing slow stretching following an initial fast stretching phase ( $R_1$ - $r_2$ ) the thinning of the lithosphere and crust are co-located, however strongly vertically heterogeneous (Fig. 3e). The shear zones develop here in a similar way to the others models, with two conjugated faults joining in the centre of the basin, along which strain rate of  $7 \times 10^{-15} \text{ s}^{-1}$  are measured. However, in this model, while lithospheric mantle thinning is  $\delta < \sim 1.7$ , the stretching in the crust is much larger, with  $\beta$  in excess of  $\sim 20$ . In this case the crust, which was already consistently locally thinned, becomes here hyper-thinned, with the creation of a basin  $\sim 200$  km wide where it overly a possible unroofed lithospheric mantle if the thinning increases leading to the break-up of only crust (Frenke, 2013). We refer to this mode Hyper-Thinned Rifting (HTR).

The fourth mode is characterised by fast rate of stretching in both the second and the first rifting phases,  $R_1$ - $R_2$  (Fig. 4.2f). Here, the thinning in the crust and lithosphere is highly coupled, with eventual breakup reached at the same finite horizontal stretching of previous models. Under these conditions the resulting narrowest basin is created,  $\sim 125$  km wide, while high similar attenuation is found in the crust and lithospheric mantle, with  $\beta \sim \delta > 4$ , with almost same spatial distribution. This deformation mode is referred to as Narrow Rifting (NR).

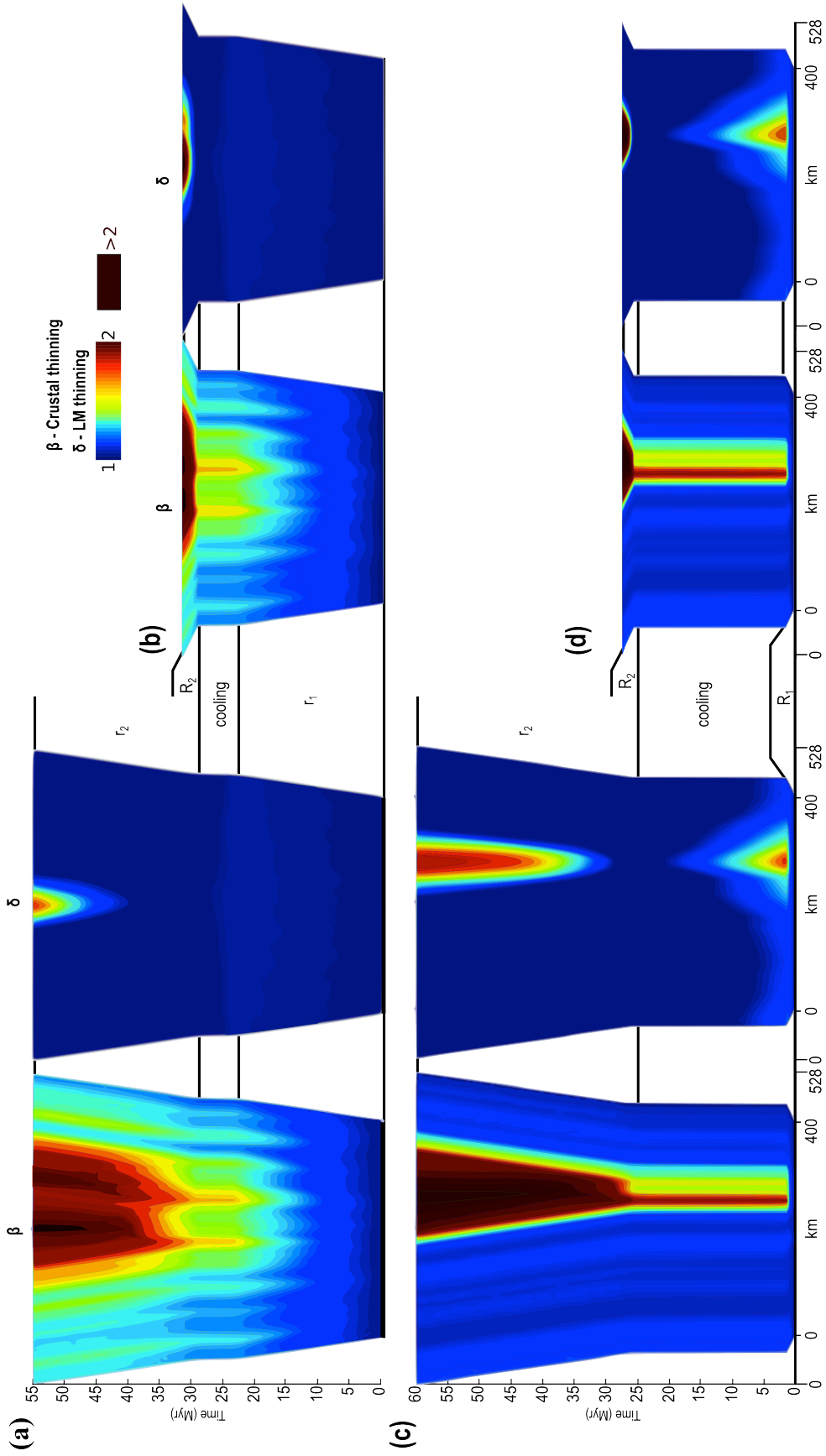
### 3.2 Lithospheric thinning and basin evolutions

To characterise the evolution of the different rifting modes, we present here the crustal and lithospheric mantle thinning factors on a horizontal strain vs. time plot. In Fig. 4.3a and b we show the models with an initial slow stretching phase. The end of this rifting phase is reached in 22 Myr. Throughout this stage the stretching is uniformly distributed in the crust and lithospheric mantle, in a consistent diffuse mode across the domain, increasing almost uniformly. At the end of this phase the thinning factor in both the crust and lithosphere are rather diffused, although in the crust two points have slightly larger  $\beta$ . According eq. (4.1) the cooling phase lasts 6 Myr to recover almost completely the thinning in the lithospheric mantle, and restore  $\delta = 1$ . The crustal thinning, instead, is not recovered during cooling, since it is compositionally defined. Thus, while both the crust and the lithosphere lose strength in the initial rifting, this is completely regained and enhanced in the mantle lithosphere only during cooling.

When rifting resumes in the model  $r_1$ - $r_2$ , i.e. with same slow velocity of the first phase, the deformation is still distributed across the domain (Fig. 4.3a), however, the two points where crustal stretching factor was slightly higher help localising deformation in this phase, eventually developing a wide basin with two deepest points, while the whole width of the model's crust is mildly thinned. The onset of localised thinning occurs rapidly upon stretching in the second phase. The lithospheric thinning remains mostly negligible at the beginning, and only in the final stage of this rifting phase,  $\sim 10$  Myr after stretching (total time  $\sim 38$  Myr) the lithosphere localises and thins beneath the major basin, only, hence the rifting attains a wide asymmetric structure.

In model  $r_1$ - $R_2$  extension in the second rifting phase is driven by a stretching velocity of 5 cm/yr and leads to a wide rift basin ( $\sim 200$  Km) similar to the one in the previous model, although symmetric. The same heterogeneities created at the end of the first rifting phase (is the same for both  $r_1$ - $r_2$  and  $r_1$ - $R_2$  models), become more relevant under fast stretching, so that in this model the two sites of largest crustal thinning localise deformation in the crust and the lithosphere as soon as the lithosphere undergoes stretching.

*(Next Page) Figure 4.3 Plot of crust and lithospheric mantle thinning factors  $\beta$  and  $\delta$  for the whole domain vs. time. Horizontal axis is the domain width in km. The width of the model domain increases as the lithosphere is extended in time. (a) Models with repeated slow rifting  $r_1$ - $r_2$ , (b) slow and fast rifting phases  $r_1$ - $R_2$ , (c) fast and slow rifting  $R_1$ - $r_2$  and (d) repeated fast rifting  $R_1$ - $R_2$ . See text for discussion. Note that the colours for  $\beta$  and  $\delta$  are scaled for a  $\delta = 1$  as minimum value, therefore values of  $\delta < 1$  are not shown.*



Here, the lithospheric mantle thinning is distributed along an area comparable to the crust's showing a vertical strain coupling at lithospheric scale throughout the second rifting phase.

In models  $R_1$ - $r_2$  and  $R_1$ - $R_2$  extension was driven with 5 cm/yr in the first rifting phase. The second phase stops when the horizontal extension is  $\epsilon_{xx} = 1.16$ , in just 3.5 Myr. As shown in Fig. 3 the deformation is concentrated in narrow lithospheric segment, where large thinning is measured in both the lithospheric mantle and the crust. Negligible thinning is measured away from this centre. The factors  $\beta$  and  $\delta$  reach maximum values of respectively 2 and 1.55 (from 30 km to 15 km and from 70 km to 45.16 km) in this phase. Consequently a larger thickness reduction is recovered in the cooling phase, which thus lasts 21 Myr, according eq. (4.1).

When rifting restarts at slow rates in the model  $R_1$ - $r_2$  (Fig. 4.4c) the crust thins rapidly, reaching large  $\beta$  factors, in excess of 4, and up to  $\beta = \sim 20$  in  $\sim 10$  Myr. Thus, the crust is severely attenuated to a thickness of 0.75 km. However, the thinning in the lithospheric mantle, although co-located with the crust's, remains consistently low, reaching maximum values of  $\delta = 1.7$ , thinning to 50 km. This configuration has a hyper-thinned crust on an unroofed cold lithospheric mantle.

The fourth model presented is that of lithosphere stretched at a fast rate in both phases,  $R_1$ - $R_2$ , lasting 3 Myr each. In this case there is a strong thinning coupling between crust and lithospheric mantle with same maximum values of  $\beta$  and  $\delta$  ( $\sim 20$ ), leading to a narrow basin. This basin develops as soon as the rifting resumes. Deformation outside of this basin is negligible. For the extreme thinning, to 0.75 km and 4.25 km in the crust and thinning lithosphere, respectively, this model reaches lithospheric break up.

### 3.3 Subsidence patterns and melting production

#### 3.3.1 Subsidence Analysis

Figure 4.4 shows the patterns of tectonic subsidence for the rifting models presented in the previous sections. For comparison, the subsidence curves of the poly-phasic rifting models are presented with subsidence curves calculated for three numerical models where a single rifting stage is modelled with a constant stretching rate. We indicate the breakup, when occurring, to better characterise the full rifting history. After breakup, the isostasy assumption implies that the surface uplifts (Watts, 2001; Watts & Burov, 2003), however, this stage is not interpreted here.

In the case of a single rifting phase, i.e. boundary velocities do not vanish until final stretching 1.32 is achieved, with a velocity of  $v = 0.1$  cm/yr, the lithospheric deformation results in the formation of 900 meters of subsidence in 70 Myr (Fig. 4.4, model M<sub>0</sub>, black thin dashed line). This model does not reach the breakup neither in the crust nor in the lithospheric mantle, and extreme attenuation of the lithosphere is achieved through protracted stretching in time with potentially larger subsidence. No breakup occurs also in the model driven with  $v = 0.3$  cm/yr, and the deepest basin subsidence reaches ~1250 m in approximately 52 Myr (Fig. 4.4 model M<sub>1</sub>, black thick dashed line). When velocity is as high as  $v = 5$  cm/yr, full breakup occurs (Fig. 4.4 model M<sub>2</sub>, black solid line). Here the maximum tectonic subsidence reaches ~ 1950 m in less of 3 Myr, before reaching breakup (black star). While the latter develops with a quite straight trajectory and a sharp subsidence gradient, the

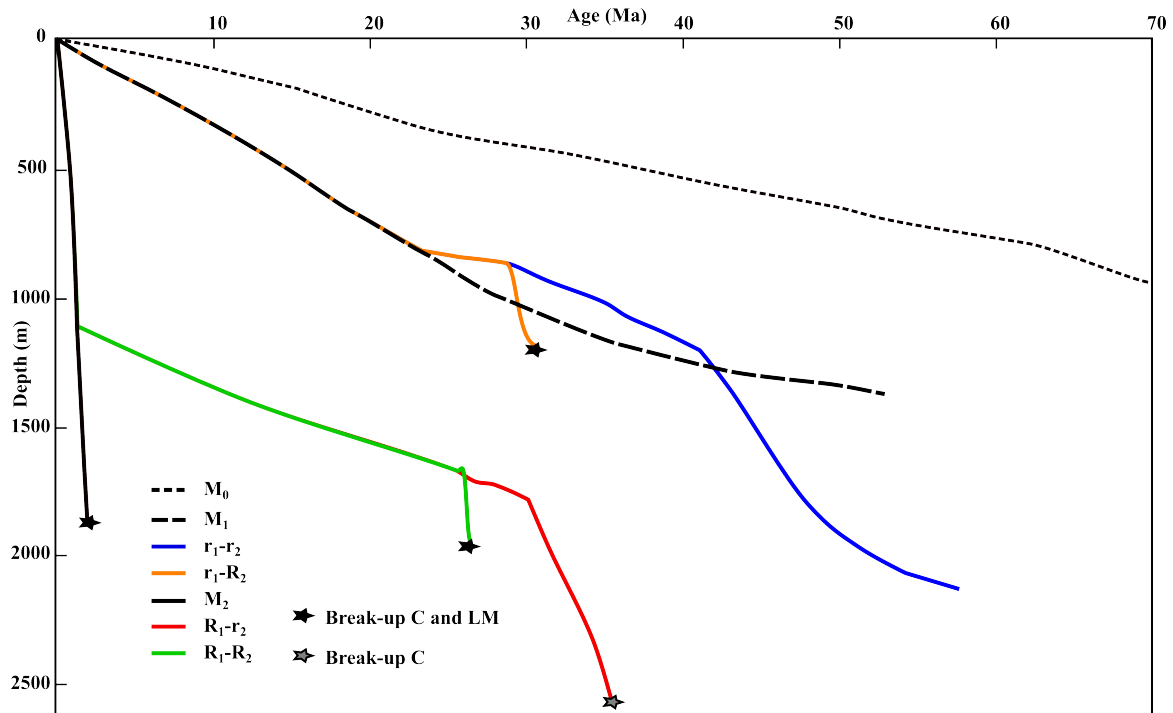


Figure 4.4 Subsidence curves for 3 monophasic ( $M_0, M_1$  and  $M_2$ , black lines) and 4 polyphase end-members ( $r_1-r_1$ ,  $r_1-r_2$ ,  $R_1-r_2$  and  $R_1-R_2$ ) models. Break-up is indicated with stars for crust (C, white star) and lithospheric mantle (LM, black star).  $M_0$  model deforms with low velocity  $v = 0.1$  cm yr<sup>-1</sup> (black dotted line).  $M_1$  with  $v = 0.3$  cm yr<sup>-1</sup> (black dashed line);  $M_2$  with high velocity  $v = 5$  cm yr<sup>-1</sup> (solid black line). Polyphase models are achieved combining fast and slow velocities intervened by cooling. Tectonic subsidence is calculated until break-up.

model in M<sub>1</sub> instead reaches ~1100 m in the first 30 Myr, then gently deflect reducing the subsidence gradient in such a way that it needs 20 Myr more to reach the maximum subsidence of ~ 1250 m. This is because under slower stretching the effect of the thermal

diffusion and, thus, thermal thickening in the lithosphere becomes more relevant, breaking the relation between horizontal stretching and thinning.

The models with a slow stretching-early phase ( $r_1$ - $r_2$  and  $r_1$ - $R_2$  respectively represented with blue and orange solid curves in Fig. 4.4) share the subsidence pattern of model  $M_1$  in their first rifting phase, leading to  $\sim 800$  m of accommodation space in 22 Myr, reaching horizontal stretching of 1.16. This is then followed by cooling (6 Myr) when subsidence becomes thermally controlled. Then, the models diverge in the second rifting phase when the stretching velocities are different. For model  $r_1$ - $r_2$ , the second rifting is resumed with  $v=0.3$  cm/yr and it continues its subsidence path with a subsidence rate similar to the previous rifting phase, until  $\sim 42$  Myr (subsidence value  $\sim 1100$  m) where the gradient increases for  $\sim 10$  Myr allowing the basin depth to reach  $\sim 2100$  m. Then, the subsidence curve deflects upward, possibly because of the thermal diffusion as before, reaching a maximum subsidence value at 58 Myr, while no lithospheric breakup occurs.

Instead, when the second stretching stage occurs under fast stretching  $r_1$ - $R_2$  (Fig. 4.5, orange solid curve)  $v = 5$  cm/yr, the maximum subsidence here is of  $\sim 1150$  m, reached in less than 3 Myr, then eventually breaking up (31 Myr, black star).

In the fast stretching-early phase models ( $R_1$ - $r_2$  and  $R_1$ - $R_2$  respectively represented with red and green solid curves in Fig. 4.5), the subsidence patterns and breakup timing change dramatically.

In the first rifting phase these models' subsidence overlaps model  $M_2$ 's, owing to the same boundary velocity imposed (5 cm/yr). At the end of this rifting phase, 1100 m of subsidence are measured. The tectonic quiescence stage of the cooling is much longer here (22 Myr) than the previous models, to recover larger lithospheric mantle thinning. By the end of the cooling stage, the thermal subsidence has reached a total depth of  $\sim 1700$  m. The two models develop separate patterns, instead, during the second stretching phase, when rifting restarts with  $v = 0.3$  cm/yr and  $v = 5$  cm/yr respectively for model  $R_1$ - $r_2$  and  $R_1$ - $R_2$ . The fast stretching model reaches a maximum subsidence of  $\sim 2000$  m at 27 Myr, where full breakup occurs (Fig 4.5, black star; see also Fig. 4.2f and Fig. 4.3d at 27 Myr).

The subsidence rate in model  $R_1$ - $r_2$  is similar to the one for the cooling phase until 30 Myr, when the rate increases dramatically arriving at  $\sim 2650$  m in less than 5 Myr. Here, at 35 Myr the crust breaks up (grey star) while the lithospheric mantle is still thinning (Fig. 4.2e, Fig. 4.3c).



### 3.3.2 Melting production

In figure 4.5 we present the models at the end of each rifting phase and the P-T profiles against the solidus to illustrate the melting production during rifting.

No melt is produced at the end of the slow stretching first phase ( $r_1$ - $r_2$  and  $r_1$ - $R_2$ ) (Fig. 4.5a). The profile beneath the maximum thinning, taken at the end of this rifting phase (Fig. 4.5c), shows that the P-T curve (dashed red line) does not cross the solidus (solid black line). A comparison with the original equilibrium geotherm (blue dashed line) shows that this curve has been mildly elevated by thinning.

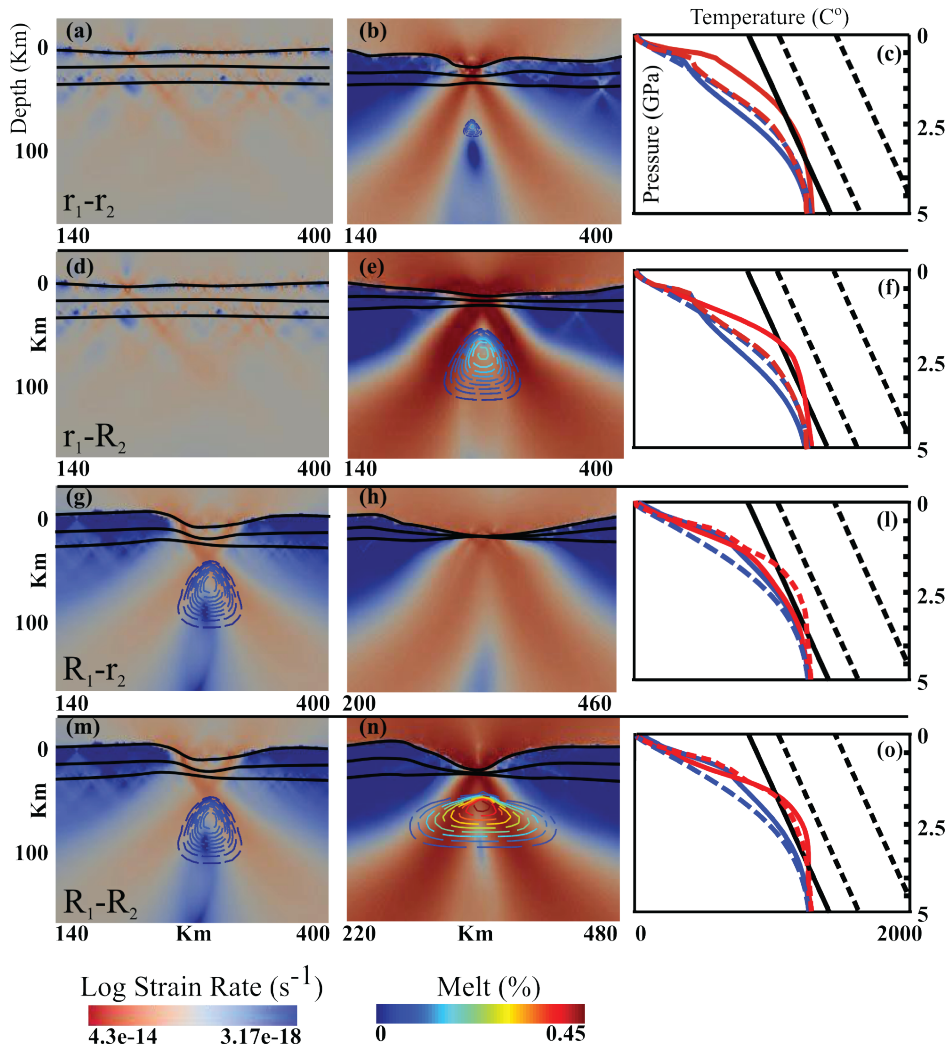


Figure 4.5 Strain rate, melting percentage contours and T-P profiles. Upper crust top, lower crust top and Moho in black lines. Model strain rates and melting at the end of slow rifting phase  $r_1$  (a) and phase  $r_2$  (b). (c) Pressure–Temperature profiles at the end of first and second rifting phase (blue and red lines), and initial and re-equilibrated curve at the end of the cooling phase (blue and red dashed lines). Solidus (Black solid line), 1% wet solidus (left dashed black line) and liquids (right dashed black line) after Katz et al., 2003. Model strain rates and melting at the end of (d)  $r_1$  and (e)  $R_2$ , and (f) P-T profiles. Strain rates and melting at the end of (g)  $R_1$  and (h)  $r_2$ , and (i) P-T profiles, and at the end of (l)  $R_1$  and (m)  $r_2$ , and (n) P-T profiles.



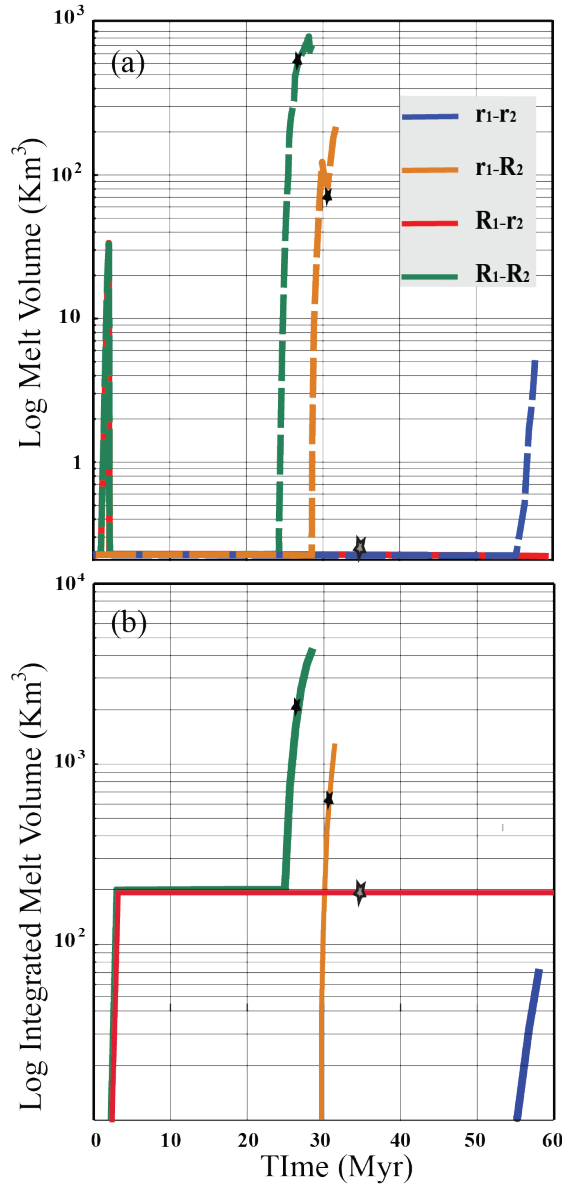


Figure 4. 6 Melting production in time. Values from models  $r_1-r_2$  (blue curve),  $r_1-R_2$  (orange),  $R_1-r_2$  (red) and  $R_1-R_2$  (green). (a) Melt volume rates and (b) Integrated melt volume.

This is caused by the slow rate of stretching which does not lead to large thinning (Fig. 4.5a) and favours heat diffusion, so that the isotherms do not rise sufficiently to yield decompression and melting. The blue solid line in the P-T plot (Fig. 4.5c) represents the distribution after the conductive cooling stage for both  $r_1-r_2$  and  $r_1-R_2$  models. At the end of the second rifting phase under the slow velocity (model  $r_1-r_2$ ;  $v_1 = 0.3$  cm/yr) a minimum production of melting is measured of 0.012 %, (Fig. 4.5b) located beneath the major shear zones location ( $\sim 75$  km), which affects an area  $\sim 10$  km wide, with the P-T curve just crossing the solidus (Fig. 4.5c). If instead the rifting is resumed with a fast stretching velocity of 5 cm/yr ( $r_1-R_2$  model), the melt percentage reaches larger values of  $\sim 0.1\%$ . The melt develops between  $\sim 40$  and 100 km affecting an area of  $\sim 30$  km wide (Fig. 4.5e), where the major lithospheric attenuation occurs and where the P-T

profiles crossed more clearly the solidus conditions (Fig. 4.5f).

Different scenarios are shown for the models developing after a fast stretching first phase (models  $R_1-r_2$  and  $R_1-R_2$ ) Due to the greater strain localization and consequent local rise of isotherms, the first rifting phase leads to a  $\sim 0.2\%$  maximum percentage of melt production (Fig. 4.5g and m). In terms of depth interval and width, the area affected by the melting is compatible with the one at the end of second rifting phase for model  $r_1-R_2$ , which is the location of maximum lithospheric thinning (Fig. 4.5g and m) and where the P-T profile (red dashed line) intersect the solidus (Fig. 4.5l and o). During cooling stage, the P-T profiles migrate towards the original position (Fig. 4.5l and o).

When rifting is resumed at velocity of  $v_2 = 0.3$  cm/yr (model  $R_1$ - $r_2$ ), no melt is produced by the end of the rifting phase two (Fig. 4.5l), where the P-T curve by this time (red solid line) is the closest of the model presented to the original P-T curve (dashed blue line – P-T after cooling). Instead, if rifting resumes at fast rate  $v_2 = 5$  cm/yr, the melt percentage increases dramatically reaching maximum value of  $\sim 0.45$  % (Fig. 4.5n). This is also showed on P-T plot, where the curve (red solid line) intersects the solidus, and gets closer to the 1% wet solidus (Fig. 4.5o). The area affected by the melting is between  $\sim 40$  and 90 km and is much wider beneath the rift,  $\sim 100$  km.

Additional insights are provided by the melt production rates (Fig. 4.6a) and the integrated melt volumes (Fig. 4.6b). The measurements here refer to the volume per unit width parallel to the rift axis.

In model  $r_1$ - $r_2$  (blue dashed line Fig. 4.6a) melt production starts as late as 56 Myr, reaching the maximum value of  $8 \text{ km}^3/\text{Myr}$ , and an integrated melt volume of  $70 \text{ km}^3$  (Fig. 4.6a, blue solid line). Note that the stretching of  $\varepsilon_{xx}=1.32$  in this model is achieved by 55 Myr, and we only illustrate the melt production for reference.

Model  $r_1$ - $R_2$  (orange dashed line) starts melt production soon after the second rifting phase starts ( $\sim 30$  Myr) with high rates, reaching  $102 \text{ km}^3/\text{Myr}$ . After breakup occurs, by 31 Myr, lithospheric breakup occurs (black star), and the melting production reaches a maximum rate of  $\sim 110 \text{ km}^3/\text{Myr}$ . Here, the total volume produced at breakup is  $\sim 500 \text{ km}^3$  (grey star, Fig. 4.6a,b) and  $\sim 1050 \text{ km}^3$  at the end of phase two.

Both models  $R_1$ - $r_2$  (Fig. 4.6a, red solid line) and  $R_1$ - $R_2$  (Fig. 4.6a, green dashed line) have a peak of melt during the first rift phase. This starts as early as  $\sim 1$  Myr after the onset of the rifting with a steep rate reaching a maximum of  $27 \text{ km}^3/\text{Myr}$  at the end of rifting phase one. Total potential integrated volume of melt is  $200 \text{ km}^3$ . The effect of the cooling is reflected in the decrease in rate production (Fig. 4.6a) with melt/depleted lithosphere remaining embedded as the thermally boundary layer grows.

In model  $R_1$ - $R_2$ , melting restarts at 25 Myr, at the same time of the initiation of the second rifting phase. Here, the rate production reaches  $150 \text{ km}^3/\text{Myr}$  when the lithosphere breaks up (27 Myr), with an integrated melt volume of  $2000 \text{ km}^3$ . Melting production continues until 29 Myr where it reaches the maximum volume of  $4500 \text{ km}^3$  (Fig. 7C, green solid line).

Models  $R_1$ - $r_2$  instead do not present any melting during the second rifting phase. This is explained also by the crust breakup at 35 Myr (see Fig. 4.2e, Fig. 4.3c and Fig. 4.4 red solid curve).

### 3.4 Controls on the modes of lithospheric extension

In Fig. 4.7 we present a regime diagram based on the 289 models and present the diverse basin styles. In order to evidence the controlling role of the two phases' velocity boundary conditions, the models plot on first-stage vs a second-stage initial strain rate, that is  $\dot{\epsilon}_2$  vs.  $\dot{\epsilon}_1$ .

We classify the first rifting phases in two groups: “slow early rifting-controls”, where the deformation at the end of rifting phase one is distributed and similar to figure 3a, and “fast early rifting-controls” with models that localise, as shown in Fig. 4.3b. In Fig. 4.7 this limit is indicated on the horizontal axis with  $I_1$ . The meaning of this symbol is explained later in the Discussion section.

On the basis of the second rifting strain rates, we delimit four domains, represented by the end-members models presented before,  $r_1$ - $r_2$ ,  $r_2$ - $R_2$ ,  $R_1$ - $r_2$  and  $R_1$ - $R_2$  (larger dots in Fig. 4.7), called here Asymmetric wide rift (AWR), Symmetric wide rift (SWR), Hyper-thinned Rift (HTR) and Narrow Rift (NR) domains. Additionally, the plot allows to illustrate an additional domain characterised by very low strain rates and rifting, henceforth intracratonic basins (IC), and transitional behaviour between the main domains.

For initial strain rates between  $7.9 \times 10^{-17}$  and  $2.78 \times 10^{-17} \text{ s}^{-1}$ , the models reproduce very long-lasting evolutions under slow stretching. In these models undergoing small strain rates of  $O(10^{-17} \text{ s}^{-1})$  the bulk thinning in the crust is low ( $\beta < \sim 1.06$ ) and distributed (e.g. Fig. 4.3a), however, no thinning in the lithospheric mantle occurs, as this the isotherms restore during stretching, and instead this increases overall, as that the thickness lost in the crust is simultaneously replaced by mantle material. As a consequence, in these models there is no cooling phase between the two rifting stages, and they undergo a longer single rifting phase.

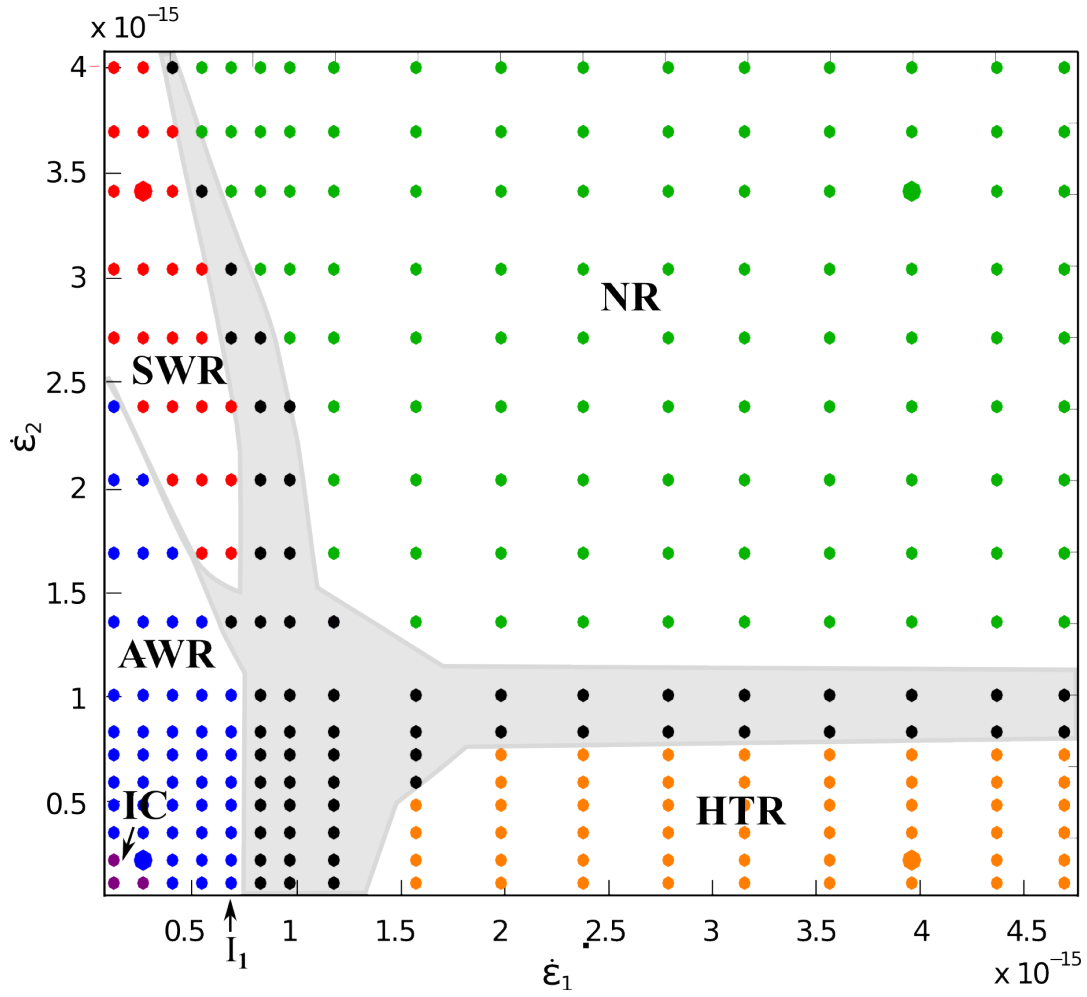


Figure 4.7 Phase diagram for the 289 numerical models of two rifting phases intervened by cooling, on a  $\dot{\epsilon}_{in1}$  -  $\dot{\epsilon}_{in2}$  space, i.e. initial strain rate in the first and second rifting phases, respectively. The following domains are defined (see text): Intracratonic (IC), Asymmetric Wide Rifts (AWR), Symmetric Wide Rifts (SWR), Narrow Rifts (NR) and Hyper Thinned Rifts (HTR). In grey, the rift style is transitional and has mixed features. Larger dots are the reference models disused before:  $r_1$ - $r_2$ ,  $r_1$ - $r_2$ ,  $R_1$ - $r_2$  and  $R_1$ - $R_2$ .

The evolution of these models is similar also when velocities change in the two – continuous – phases, and crustal stretching is  $\beta < \sim 1.09$ . Similar evolutions are observed in intra-cratonic and sag-stage basins (e.g. Chad Basin, Eyre Basin - Modern examples - Palaeozoic Michigan and Illinois basins or Permian–Mesozoic West Siberian Basin - Ancient examples. [Allen et al., 2015](#)) and although the comparison to the models here remains purely speculative, we refer to this domain as Sag Basin-like.

Under chosen parameters, models develop into an AWR when initial strain rates are in the range  $\dot{\epsilon}_1 = 7.90 \times 10^{-17}$  to  $6.35 \times 10^{-16} \text{ s}^{-1}$  (0.1 to 0.8 cm/yr), followed by strain rates  $\dot{\epsilon}_2 = 7.90 \times 10^{-17}$  to  $2.38 \times 10^{-15} \text{ s}^{-1}$  in the second phase. At low background strain-rates in both rifting phases, the formation of a wide asymmetric basin follows the continuous growth in

both phases of diffuse heterogeneities, resulting in an AWR. For increasing initial strain rates  $\dot{\epsilon}_1$  in the first phase, the models transition from AWR to SWR with decreasing strain rates  $\dot{\epsilon}_2$ . For example, if the rifting-cooling-rifting cycle starts with a very low strain rate  $\dot{\epsilon}_1 = 7.9 \times 10^{-17} \text{ s}^{-1}$ , the AWR model transition to SWR at values of  $\dot{\epsilon}_2 = 2.38 \times 10^{-15} \text{ s}^{-1}$ , instead, if strain rate  $\dot{\epsilon}_1 = 6.35 \times 10^{-16} \text{ s}^{-1}$  is used in the first rifting phase, the transition occurs at values of  $\dot{\epsilon}_2 = 1.19 \times 10^{-15} \text{ s}^{-1}$ . This illustrates the role of the slow early rifting-controls.

The models develop a SWR under low strain rates in the first rifting phase, and high strain rate in second rifting phase. At these low background strain-rates in the first rifting phase, the formation of a wide symmetric basin is explained by the localisation in the second phase on the diffuse heterogeneities inherited by the first rifting phase. While the transition to AWR has been discussed previously, we note that the transition to the NR domain occurs at smaller first rifting phase's strain rates so that the models become less dependent on the initial rifting phase, although for the maximum – Earth-like – strain rates used here the dependence has weakened but not vanished. Also, we note here that the transition to a different regime, where mixed behaviour is observed, narrows with increasing strain rates in the second rifting phase. For limit strain rates in the first rifting phase of  $\dot{\epsilon}_1 = 5.55 \times 10^{-16} \text{ s}^{-1}$  the transition to localised NR occurs until strain rates  $\dot{\epsilon}_2 = 3.17 \times 10^{-15} \text{ s}^{-1}$  are reached (Fig. 4.7, vertical black line). For increasing values of  $\dot{\epsilon}_2$  the transition to the NR domain occurs at smaller  $\dot{\epsilon}_1$ , and the NR domain expands. The negative slope of the transition between the SWR and NR indicates a weaker dependence on the early rifting phases as strain rates in the second phase increase.

The narrow rift NR domain is characterised by the largest strain-rate interval occurring for strain rates  $\dot{\epsilon}_1 > 5.55 \times 10^{-16} \text{ s}^{-1}$ . However, this field expands to lower values with increasing  $\dot{\epsilon}_2$ . These models show an increasing coupling between crust and lithospheric mantle and become dependent on the first rifting phase for  $\dot{\epsilon}_2 > \sim 3 \times 10^{-15} \text{ s}^{-1}$ .

The hyper-thinned rifting HTR domain is defined by background strain rates for the first rifting phase being  $\dot{\epsilon}_1 > 1.58 \times 10^{-15} \text{ s}^{-1}$ , although a transitional mode is observed for  $\dot{\epsilon}_1 > 5.55 \times 10^{-15} \text{ s}^{-1}$ , while the second rifting phase this occurs for  $\dot{\epsilon}_2 > 7.90 \times 10^{-17} \text{ s}^{-1}$  although it extends to smaller  $\dot{\epsilon}_1$  with increasing  $\dot{\epsilon}_2$ , as illustrated before.

The area where transitional domains (black dots) are found is largest for small strain rates, although this is clearly wider in the  $\dot{\epsilon}_1$  direction and slightly smaller in the  $\dot{\epsilon}_2$ . This mixed domain maximum extension is from  $\dot{\epsilon}_1$  of 5.55 to  $\sim 15 \times 10^{-16} \text{ s}^{-1}$ , instead it narrows

down to  $0.7$  to  $13 \times 10^{-16} \text{ s}^{-1}$  when these strain rates are imposed in the second rifting phase. This further supports the idea that the rifting in the second phase is dependent on the previous rifting history.

## 4. DISCUSSION

### 4.1 Rifting histories and deformation modes

The deformation mode of lithospheric rifts is commonly addressed as achieved completely during a single rifting phase (McKenzie, 1978). England (1983) and van Wijk and Cloetingh (2002) illustrated the role of the stretching velocities on the evolution of rifting, showing that when boundary velocities are below a threshold value, cooling and stiffening of the lithospheric mantle portion occurs, which forces the deformation to migrate laterally, while necking and strain localisation is the result of stretching velocities above the threshold, possibly culminating into a breakup. Because the lithospheric rheology is strongly temperature-dependent, England (1983) used the Peclet number to quantify rifting mechanics, measuring the ratio of the two competing heat variation mechanisms, conduction and advection. In the case a low velocity-rifting event- low Peclet number, heat diffusivity prevails over advection allowing for the lithosphere to remain relatively cold, increasing lithospheric strength and promoting migration of the strain laterally, were the lithosphere is weaker and hotter (e.g England 1983, van Waijk & Cloetingh 2002). Conversely, a higher stretching velocity facilitates advection over diffusivity, with upward shifting of isotherms, which promotes focalization of the deformation in a narrow area (e.g England 1983, van Waijk & Cloetingh 2002).

The evolution of these lithospheric rifting modes has been categorized using a criterion of localisation by Crameri & Kaus (2010), Lu, Kaus, & Zhao (2011) and Kaus & Podladchikov (2006). These authors proposed an index that accounts for the initial or background strain rates, the rheology as well as the strain. Crameri & Kaus (2010) propose a localization index  $I$  for a lithospheric deformation under compression:

$$I = \frac{\dot{\epsilon}_{in} \Delta l}{1.4} \sqrt{\frac{\eta_0 E}{n R T^2 k}} \quad (4.18)$$

where  $\dot{\epsilon}_{in}$  is the initial strain rate,  $\eta_0$  is effective viscosity,  $E$  is activation energy  $n$  is power law exponent,  $R$  is gas constant,  $T$  is temperature distribution,  $k$  thermal diffusivity and  $\Delta l$  is a characteristic length. A transition to diffuse deformation (strain localisation) is found when  $I < 1$  ( $I > 1$ ). Kaus & Podladchikov (2006) proposed that the characteristic length  $\Delta l$  is the radius of a circular body enclosed in the lithosphere, favouring stress

localisation. [Crameri & Kaus \(2010\)](#) used a setup with no pre-existing heterogeneities and propose that lithospheric localization is primarily controlled by the thickness of the plastic field ( $th_p$ ), measured from 1D yield strength profiles and 2D numerical models. In their work the characteristic length is calculated using the gradient of Moho morphology's deflection, with localization occurring when steep gradients of  $dy/dx > 4$  are found. [Lu et al., \(2011\)](#), used the same approach applied to the evolution of North China Craton and proposed, instead, the Moho temperature deflection caused by lithospheric extension as characteristic length  $\Delta l$ .

Here, it is useful to use the same approach to illustrate the role of rifting history on the deviation from the insights the single-rift analysis has yielded. Following [Crameri & Kaus \(2010\)](#), we have calculated the plastic thickness in 1D models using the parameters of our simulations and varying background strain-rates and illustrate in [Fig. 4.8](#) and [Fig 4.9](#) the scaling between the plastic thickness and the maximum crustal thinning  $\beta$  in the 2D models after a minimum strain is achieved of  $\epsilon_{xx}=1.05$ . Additionally, we note that the crustal thinning is similarly a measure of the Moho deflection ([Fig.4.8](#)), with respect to the original depth, caused by the early rifting phase, in agreement with [Lu et al., \(2011\)](#). Hence, we use the Moho displacement as a characteristic length for the localisation index and replacing in eq. (4,18)  $\Delta l = h_0 (1 - 1/\beta) - S$ , using the initial crustal thickness  $h_0$ , the maximum thinning  $b$  and the subsidence  $S$  achieved in the first rifting stage ([Fig. 4.8](#)). This can be interpreted as an inherited crustal heterogeneity, which implies localization of early rifting for large  $\beta$  and diffused rifting-induced smaller heterogeneities when  $\beta$  is small. In the results

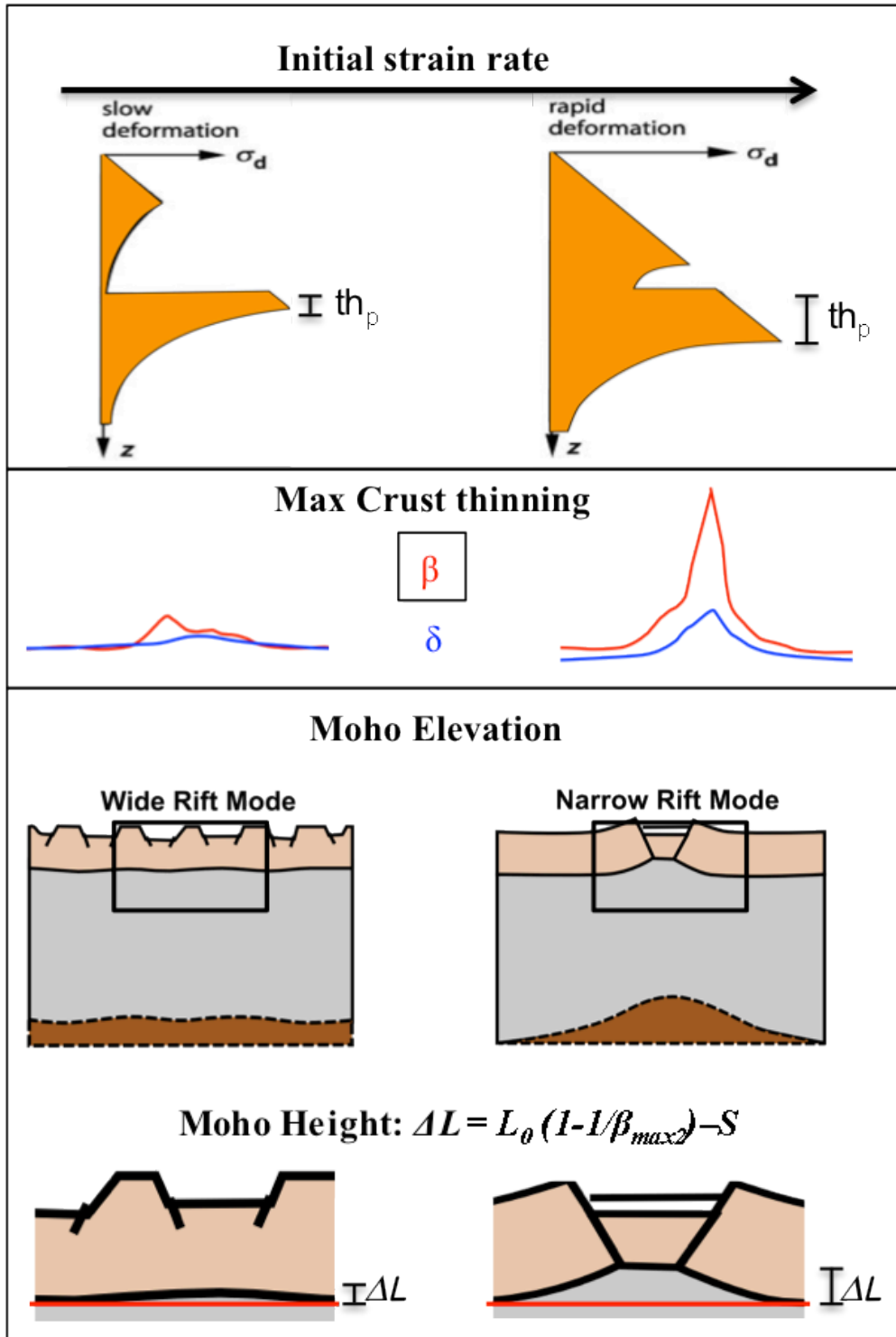


Figure 4.8. a) Schematic representation of changing of plastic thickness,  $th_p$ , on the yield envelope profile as function of increasing initial strain rate,  $\dot{\epsilon}_{in}$ . b) Crustal thinning factors,  $\beta$  (red curves) soon after the onset of rifting. On the left the  $\beta$  factor derived from a low initial strain rate; right,  $\beta$  factor relative to high initial strain rate. c) Cartoon showing the Moho deflection as a consequence of the initial strain rate applied to the rifting. The figure shows the role exerted by initial boundary condition (initial strain rate), on the response of the lithosphere (plastic thickness,  $th_p$ ), which feeds back into the degree of thinning of the crust  $\beta$  and Moho deflection.



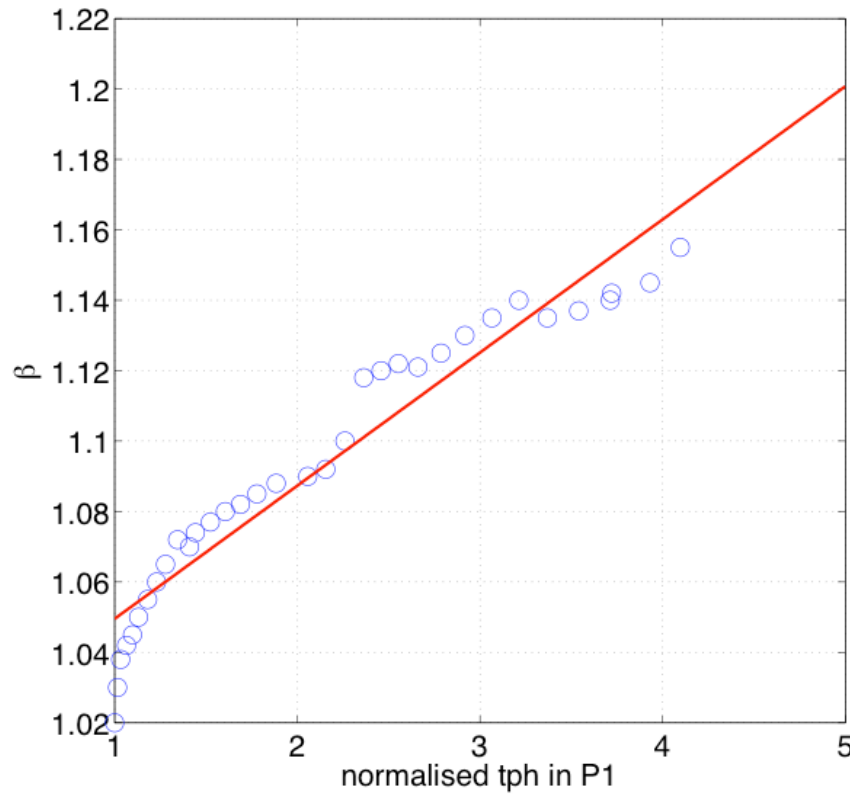


Figure 4.9. Linear fitting of crustal thinning factor  $\beta$  at the onset of the rifting phase and the thickness of the plastic portion of the lithosphere. Each point on the red line represent the stretching phase soon after the onset of rifting with different initial strain rates, therefore showing the link between thinning of the crust  $\beta$ , the response of the lithosphere to the initial boundary condition (initial strain rate).

section we have shown how these both eventually strongly favour localisation in the following rifting phases, thus implying that the evolution of multi-phase rifting must be different from single rifting evolution. Note that the localisation index here is only calculated for the last rifting phase, thus allowing a direct comparison with the prediction of single rifting modelling.

In Fig. 4.10 we present the contouring of the localisation index  $I$  calculated for all the 289 models in a phase diagram of strain  $\dot{\epsilon}_{in1}$  vs.  $\dot{\epsilon}_{in2}$ . The dashed lines indicate the values corresponding to the analytical calculation for  $I = 1$  in the first rifting phase.

As a general feature, in models with  $I > 1$  localised lithospheric strain is favoured in the first rifting phase while for models with  $I < 1$  diffuse lithospheric strain is predominant. This corresponds to the limit between  $I_1$  on Fig 4.7 between the “slow early rifting-controls” and fast “fast early rifting-controls” basin groups.

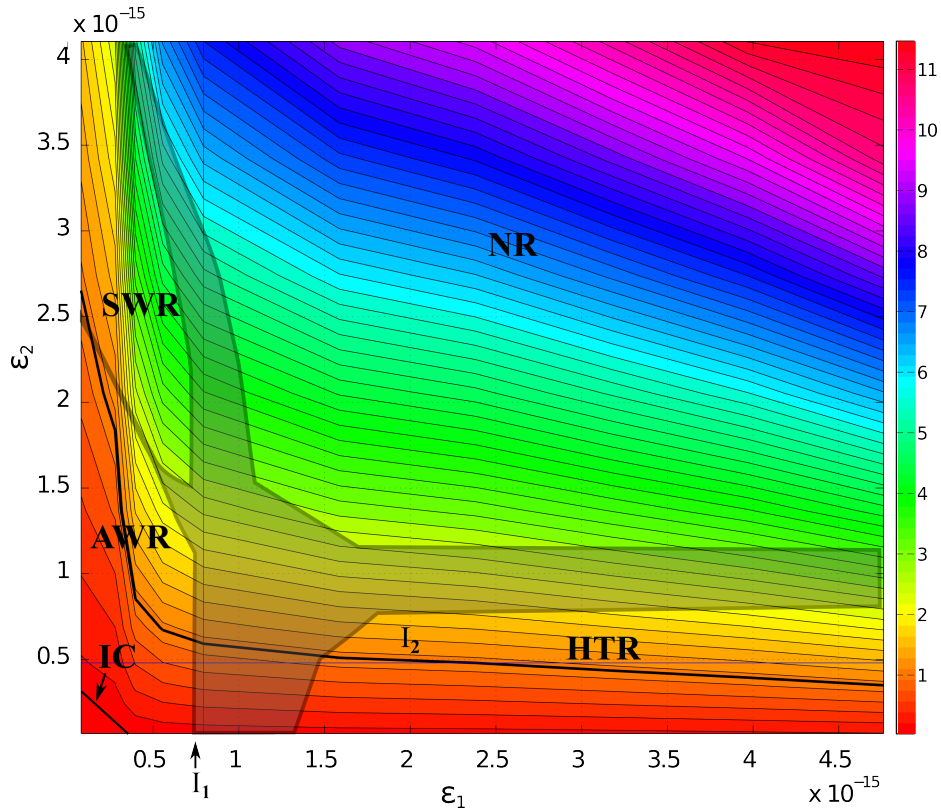


Figure 4.10 Localization indexes for the 289 numerical models and the rifting mode domains, on a  $\dot{\epsilon}_1$  -  $\dot{\epsilon}_2$  space, i.e. initial strain rate in the first and second rifting phases, respectively. In colorscale the localization index  $I$  in the second phase calculated for each model. Vertical black solid line and horizontal dashed lines for analytical localisation index  $I=1$  assuming each rifting phase is independent and deforms a pristine lithosphere (see text). The comparison between the analytical and the model localisation indexes illustrates the domains where the rifting history, that is the previous rifting events, has a control on the evolution.

The coloured isolines indicate values of localization index  $I_2$  increasing moderately from IC, AWR and HTR basin style domains toward SWR and more abruptly towards NR. The black solid isoline ( $I_2=1$ ) indicate limit between lithospheric strain localization and delocalization regions. Basin style domains that have a  $I_2 < 1$  are SB, part of AWR, the majority of HTR and partially SWR. The lower branch of transitional domain (grey area) also falls in the delocalization region. The upper part of the HTR domain, all the rest of transitional domain (grey area) and NR are above the lithospheric localization limit for the second rifting phase. The analysis of the trend of isoline  $I_2=1$  helps to understand the relationship between the rift history and the final basin style. This isoline is almost vertical on the left hand side of the line  $I_1=1$  while changes abruptly when it approaches the  $I_1=1$ , to become quasi-horizontal at the right hand side of  $I_1=1$ .

This demonstrates that final basin style of models that belong to the slow first rifting phase group (left hand side of  $I_1=1$ ), depend strongly on the background strain-rate used during the first rifting phase. For example, for the same  $\dot{\epsilon}_{in2} = 1.5 \times 10^{-15} \text{ s}^{-1}$  in the second

rifting phase we should expect strain distribution and a wide asymmetric rift if the stretching of the lithosphere in first rifting phase is driven with  $\dot{\epsilon}_{in1} < 3.2 \times 10^{-16} \text{ s}^{-1}$ . It is still possible have the same basin style for very high second rifting phase background strain-rate,  $\dot{\epsilon}_{in2} = 3.2 \times 10^{-15} \text{ s}^{-1}$  provided that the first rifting phase is very slow. In SWR the strain diffusion is only possible for the same very low range of first rifting phase background strain rate. A different scenario is represented at right hand side of the black line  $I_1=1$ . The models located in the lower part of the plot are almost independent of the first rifting phase. In fact, to generate HTR models that allows for a distribution of the strain in the lithospheric mantle we need a restricted range of a  $\dot{\epsilon}_{in2}$  between  $6.2 \times 10^{-16} \text{ s}^{-1}$  and  $3.2 \times 10^{-16} \text{ s}^{-1}$ , which matches with a larger  $\dot{\epsilon}_{in1}$  interval for the first rifting phase (from  $1.58 \times 10^{-15} \text{ s}^{-1}$  to  $4.76 \times 10^{-15} \text{ s}^{-1}$ ). With increasing second rifting phase background strain-rate there is a similar situation of independency from the early rift history for the horizontal branch of the transitional domain and for the NR domain.

From the analysis of the isolines and the domains we can see that it is the mode of lithospheric stretching in the earlier rifting phase that exerts a paramount influence on the final basin style. It is easy to see that models produce wide rifts are very sensitive to the rifting history since it can lead to a different degree of symmetry. Narrow rift and basins on hyper-thinned crust instead are sensitive only the boundary condition used in the last rifting phase. If that is represented by an high initial strain rate,  $\dot{\epsilon}_{in2}$ , the resultant basin is a narrow rift with well developed lithospheric necking and lithospheric breakup. If  $\dot{\epsilon}_{in2}$  is low this triggers the severe thinning of the crust with possible crustal breakup and unroofing of the lithospheric mantle portion.

For a SWR basin probably the early history was a slow stretching and so it is important when modelling this particular case to take into account the previous rifting phase.

## 5. CONCLUSION: INFERENCES ON RIFTING EVOLUTION INTERPRETATIONS

### 5.1 Basin Style and rifting mode

When compared to previous modelling, our outcomes provide self-consistent and better explanation for the evolution of wide rift and narrow rifts basins, when comparing our results with the general features found in rift-drift suites such as complex histories shown

by subsidence curves. Our study supports the idea that the diversity in deformation mode is controlled by the variation of boundary conditions in time, and therefore the rifting history.

The implication of the work presented here are likely far reaching. In fact, the application of the uniform rifting model by [McKenzie \(1978\)](#) is limited to a single major subsidence phase. Here, we have shown that last rifting phase, although providing useful insights in this phase (e.g. [Allen and Armitage, 2012](#); [MacKenzie, 1978](#)), cannot explain the variety of rifting basins, found on Earth. For example, the Norwegian rifted margin presents a complex evolution made by episodic stretching and intervening cooling stages or the margins of South Atlantic (asymmetric) among many others (see introduction for list of geological examples).

Models based on the monophasic approach (e.g. [Buck, 1991](#); [Kusznier & Park, 1987](#); [van Wijk & Cloetingh, 2002](#); [England, 1993](#); [Chenin & Beaumont \(2013\)](#); [Gueydan et al., 2008](#)), have reproduced fundamental features, such as the wide or narrow rift, however they cannot address many complexities found in the structures and the evolutions of the basins. However they needed to strongly differentiate the initial conditions (e.g. Moho Temperature (high for wide and low for narrow), initial lithospheric layering thicker crust for wide and thinner for narrow), different rheologies – weak or strong lower crust respectively for wide and narrow basin) between the models to be able to reproduce a wide or narrow rift. Here, upon quantification of lithospheric strain localization and interrelation basin style through crust and mantle thin evolution, we have shown that a deeper understanding of the basin evolution and predictions on the overall structure can be achieved when the whole lithospheric history is considered.

## 5.2 Subsidence

The interpretation of subsidence patterns and geological evolution of various rifting settings is usually focused on the main rifting phase ([McKenzie, 1978](#)). Although successful, many geological cases have shown anomalous evolutions, through their subsidence history, structural complexities and magmatic evolution, which are not always explained by this single-rift model. Models explaining these anomalies include the role of magmatic intrusions during the initial extensional phase ([Buck, 2004](#)), phase changes linked to increasing overburden (e.g. [Artyushkov, 2007](#); [Kaus et al., 2005](#); [Kaus et al., 2005](#); [Petrini et al., 2001](#)), protracted negative dynamic topography effects (e.g. [Flament et al., 2013](#); [Heine et al., 2008](#)) or stress variations in the far-field (e.g. [Birt et al., 1997](#);

[Lyngsie et al., 2007; Marotta et al., 2000](#)).

Here we have showed that although (minor or higher) subsidence is a consequence in the first and second rifting phases, the modification the lithosphere undergoes (i.e., geothermal gradients and diffusion of deformation), constrains strongly the structure of the lithosphere at the inception of the following rifting phase. This demonstrates that the interplay between the inherited initial conditions from previous rifting phases and intervening cooling, with the boundary conditions at the onset the second rifting phase, exert a fundamental role on the creation of different rifting histories. In other words, the previous rifting phase provides evidence of the initial conditions during the major rifting phase, which cannot be neglected, nor can be inferred unambiguously.

### 5.3 Melting production

Previous rifting models such as van Wick and Cloetingh 2001 have shown that the boundary conditions applied to driven the lithospheric stretching, together with the mantle temperatures, represent the main the controlling factors on the melting production. They have modeled a parameterized lithosphere that fit best the physical state of mid-Norwegian margin, finding that the melt production occurred in late synrift stage, and the amounts of melt are consistent with the observations. They have concluded that mantle plumes (e.g. [White and McKenzie, 1989](#)) or small scale convection (induced by either rifting or discontinuities in lithosphere thickness, e.g. [Buck, 1986; Anderson, 1994; Boutilier and Keen, 1999; Keen and Boutilier, 1995; 2000](#)) are not always a prerequisite to generate a volcanic margin while dynamical processes related to lithospheric rifting may enhance the produced melt volumes sufficiently to explain the sometimes enigmatic amounts of melt observed at volcanic rifting provinces such as the African Rift System ([Corti et al., 2012](#) and references therein; [Baker et al., 1972](#)) and several other volcanic margins along the Atlantic Ocean (e.g. [Franke 2013](#)).

Our work confirm [van Wik & Cloetingh \(2001\)](#) results, that the boundary conditions play a fundamental role on the amount of melt produced, however we expand their results by introducing the effect of the rifting history on the melt production and its variation over time. We have shown that the influence of the boundary condition can be multiplied or reduced as a function the particular rifting history. Figs. 4.5 and 4.6 illustrate in detail 4 end-members cases belonging the RCR rifting history. As indicated in the introduction there are many deep, high velocity bodies in passive margins area such as along the northern Iberian continental margin ([Zelt et al., 2003](#)) and northern Angolan margin

(Moulin et al., 2005). Even if it needs a more rigorous investigation, our models could provide, as first approximation, an explanation the origin of deep, high velocity bodies revealed by seismic surveys,

#### 5.4 Conclusion

In conclusion, we have shown here that the lithospheric deformation history is of fundamental importance when modelling the rift basin evolution. Variations to tectonic boundary forces and resulting stretching rates, exert a dominant control on the deformation of lithospheric-scale rifted basin. In particular, when stretching is fast, breakup is rapidly achieved, so that the rifting is much less sensitive to the previous history. When stretching is slow, then rifting episodes can repeat without leading to break-up. Although we have modelled only two phases, these latter are the conditions under which the rift can be long-lasting and allows for several rifting episodes, and thus refer to these as poly-phasic.







## Declaration for Thesis Chapter 5

**Monash University**

### Declaration for Thesis Chapter 5

#### Declaration by candidate

In the case of Chapter 5, the nature and extent of my contribution to the work was the following:

Nature of contribution	Extent of contribution (%)
Development of the Rationale as well as Conceptual and Numerical modelling; Analysis and interpretation of the results.	90

The following co-authors contributed to the work. If co-authors are students at Monash University, the extent of their contribution in percentage terms must be stated:

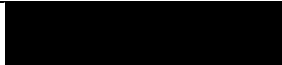
Name	Nature of contribution	Extent of contribution (%) for student co-authors only
Dr. Fabio A. Capitanio	Supervisory role, Rationale, Modelling strategy, Data interpretation.	10

The undersigned hereby certify that the above declaration correctly reflects the nature and extent of the candidate's and co-authors' contributions to this work\*.

**Candidate's  
Signature**

	<b>Date</b> 01/04/2016
---	---------------------------

**Main  
Supervisor's  
Signature**

	<b>Date</b> 01/04/2016
---	---------------------------



# CHAPTER 5: MODELLING GEOLOGICAL CASE: RIFT-RIFT (RR) HISTORY TYPE

Strain history controls on the Sirte widest narrow rift basin, Libya

V. Morena Salerno \*, Fabio A. Capitanio, Rebecca J. Farrington and Nicolas Riel<sup>1</sup>

School of Earth, Atmosphere and Environment, Monash University, Clayton, 3800 VIC, Australia

## 1. INTRODUCTION

One of the most common classifications of rift basins is based on their width, i.e. wide and narrow rifts, depending on the distribution of crustal and mantle lithospheric thinning diffused over a wide area or localized in a narrow highly deforming zone, respectively. In wide rifts, the width of the deformed area is greater than the lithospheric thickness (Brun & Choukroune 1983; Buck, 1991), with formation of listric faults and widespread extension. Narrow rifts instead, develop as discrete basins with steep normal faults as the consequence of localized lithospheric necking. Natural examples of the wide rift basins are the Basin and Range, Aegean Sea and West Antarctic Rift System while Rhine Graben, North Sea, Red are geological cases of narrow rifts, among many others.

Due to the bimodal occurrence of the deformation in these basins, workers have studied the evolution of rifting using these two end member models, referred to as wide and narrow rift modes. The two end members rifting modes are understood result from a single rifting phase, where different initial and boundary conditions are imposed in the crust thickness (Buck, 1991) and rifting velocity, and yield a narrow or a wide rift basin as the result of a single stretching event.

While this approach has helped enormously to understand the physics of the single rifting phase, it does not capture the complex evolutions of many rift areas, which often comprises time varying stretching history, and, hence, the lithospheric stretching/rifting process as developed through several rift events. However, during the evolution of rifts, changing boundary conditions, such as varying stretching rates or vanishing stretching and lithospheric cooling, might be of paramount importance for the rift evolution. These, in fact, change dramatically the rheology or the distribution of strain within the lithosphere and, as a consequence, the rifting mode. As a consequence, the single rift approach might fail to explain the diversity in lithospheric stretching histories as revealed by geological and geophysical data. In particular, the single rifting approach cannot

explain the spatial transition between wide and narrow rift modes, which is found in basins such as the Gulf of California ([Lizarralde et al., 2007](#)) or Eastern Australia ([Bryan et al., 2012](#)), or the switch between the two modes during their evolution, which is an observed characteristic of rift basins such as Rio Grande, ([Philippon et al., 2012](#)), Tisza rift in the Békés basin (Pannonia Basin, [Tari et al., 1999](#)) and West Antarctic Rift System ([Huerta and Larry, 2007](#); [Corti et al., 2013](#)) as well as in Iberia-Newfoundland (e.g., [Huisman & Beaumont, 2007](#)).

An interesting example of such rift system is the Sirte Basin ([Fig. 5.1](#)), Libya, which, although has been thoroughly investigated because of hydrocarbon resources (e.g. [Conant and Goudarzi, 1967](#); [Goudarzi, 1981](#); [Gumati and Nairn, 1991](#); [van der Meer and Cloetingh, 1993a.b](#), [Abadi et al., 2008](#); [Galushkin et al., 2014](#), [Abdunaser and McCaffrey, 2015](#); see wells in [Fig. 5.5](#)), presents peculiar features that cannot be easily explained. In fact, this is one of the widest basins in the world, ~500 km wide, however, most of the deformation was achieved in as short as ~10 Myrs during the Paleocene and is localized in its easternmost graben ([Fig. 5.1](#)), which suggests it should be classified as a narrow rift mode.

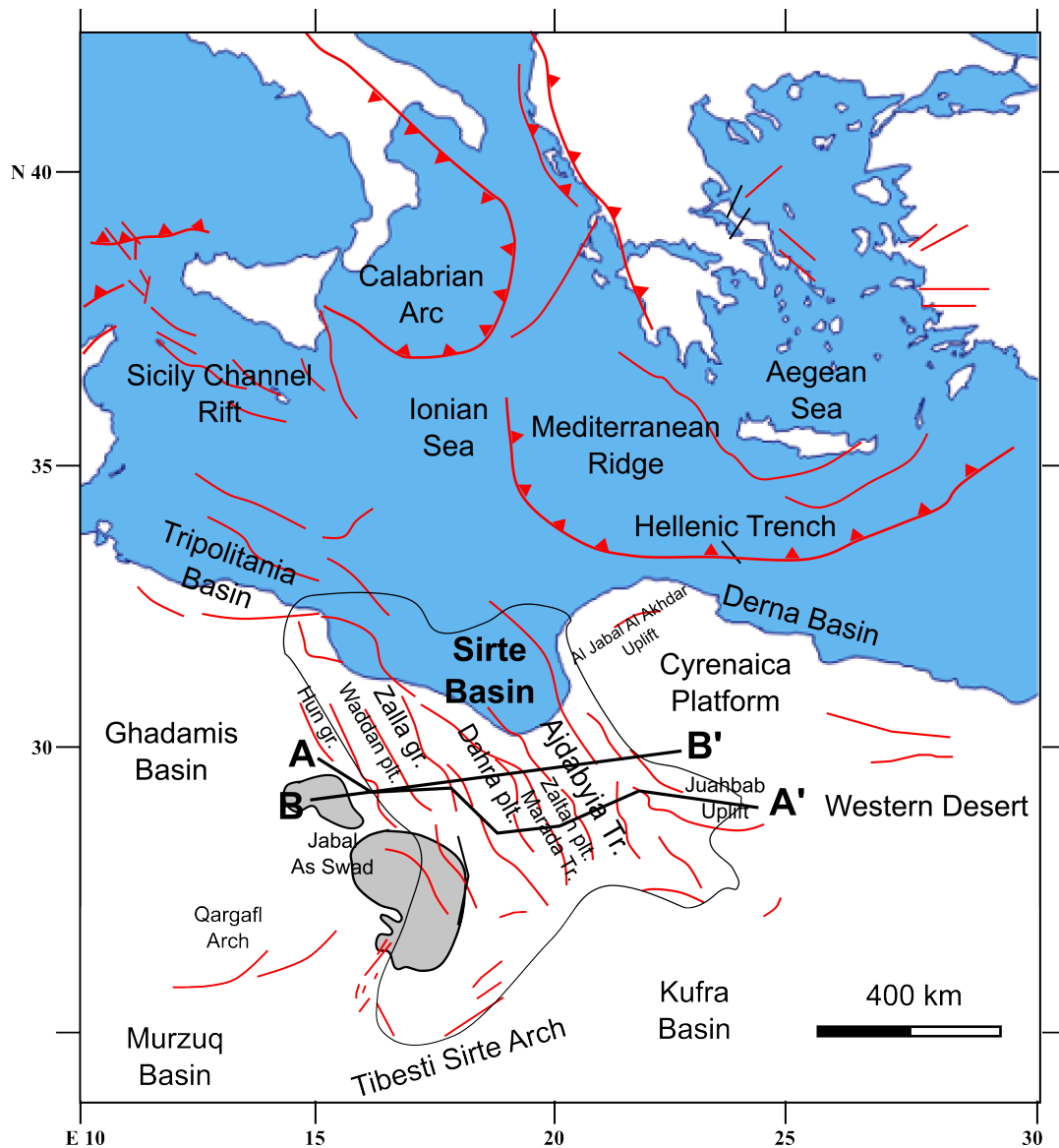


Figure 5.1 Tectonic sketch of the Central Mediterranean–North Africa area with the Sirte Basin located in the northern African margin (modified after Capitanio et al., 2009; Rusk, 2001). Black contour defines the Sirte Basin area onshore and offshore A-A' and B-B': cross sections on Figs. 5.3a and b. Yellow box indicates the deepest basin in the Sirte area, Ajdabyia Trough.

The structure of this basin from seismic lines and geological data (Abdunaser and McCaffrey, 2015; ), illustrates the distribution of horsts and grabens over a width of ~ 500 km width (Fig. 5.2a-b), where the basin-filling Cretaceous sediments are of comparable thicknesses.

However, other results focused on the Paleogene rifting (Ghanoush et al., 2014; Abadi et al., 2008; Capitanio et al., 2009) illustrate a different later evolution of the Sirte basin:

1) The sharp change in subsidence pattern occurs by ~ 55 Myr, when the largest sedimentary cover thickness are deposited.

2) The depth of the Cretaceous unconformity and the Moho show strong localization beneath the easternmost graben, the Ajdabyia Trough, where average sedimentary covers are ~5000-7000 m thick, and reach 11 km in the northernmost basin.

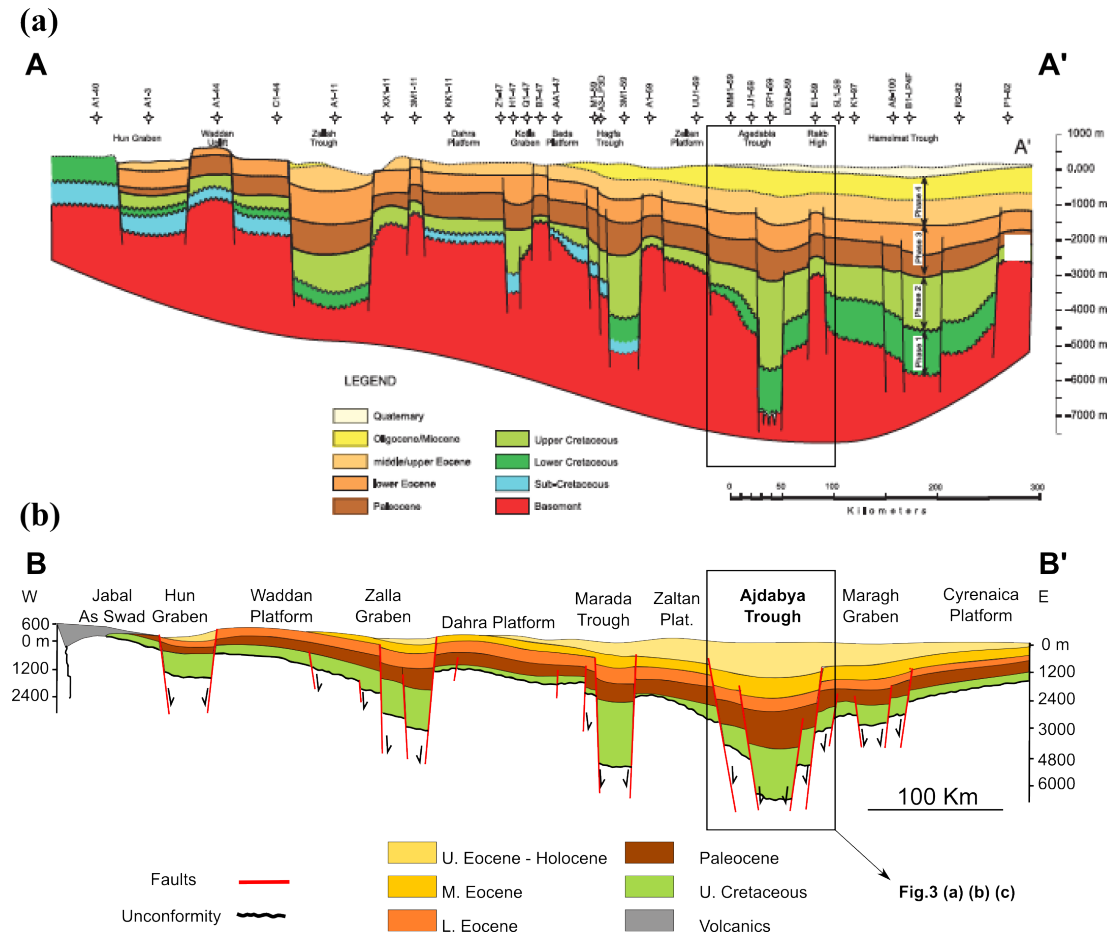


Figure 5.2 Evidence of wide rift. Two geological cross sections semi-parallel which combined together 1) show the entire sedimentary succession and 2) show that there is a minimum of difference in structures along strike (eastern part of the two sections). (a) Cross section modified after Abadi et al., (2008) and (b) modified after Roohi (1996). Black box indicates the Ajdabyia Trough, the most representative for the entire history of Sirte basin since it records the largest subsidence in the domain. This increases northwards, up to ~ 10 km, and shallows up towards the south, ~ 4 km. In the Ajdabyia Trough are located the wells used to calculate the total subsidence in Fig. 4a, the tectonic subsidence in Fig. 4b and the inversion of the strain rate in Fig. 4c in Capitanio et al. (2009). A-A' and B-B' locations are shown on figure 5.1

Goudanzi, 1980, and more recently Abadi et al., 2008 and Ghanoush et al., (2014) report that the crust is thinned to ~26 km in beneath the deepest structure (this comprises the thickness of the crust – 18 km – and the sediments – 8 km), the Ajdabyia Trough (Fig. 5.3 bottom), where crustal thinning factors of  $\sim \beta = 1.3$  have been estimated (Abadi et al., 2008, Fig. 5.3 top). The  $\beta$  for the crust is then 2, if we do not consider the sediment column. Therefore while the Sirte rift is still very wide (Fig. 5.1 and Fig. 5.2a-b), the deeper lithosphere presents local rise of the Moho, which is a feature typically found in

narrow rifts (i.e. North Sea). Additionally, the switch between the two modes can be attributed to a time-variation, which led the Paleocene narrow rifting event to be superimposed on the Cretaceous wide rift.

Our current understanding of how and why the two modes superpose remains unclear. Generic rifting modeling, thus far, has illustrated the controls on emergence of narrow as opposed to wide rifts (e.g. van Wijk and Cloetingh, 2002; Kusznieir and Park, 1987; Lu et

al., 2011). Authors such England (1983) and Lu et al. (2011) have shown that, the relatively large deflection of the Moho when rifting is limited to a narrow area, is linked to lithospheric strain localization and to the localized deflection of the lithosphere-asthenosphere boundary (LAB). This opposes to the typical features of the lithosphere beneath wide rift basins. This latter is best described by lithospheric strain distributed on a large area, semi-flat Moho and LAB and a small (or absent) deflection of the LAB parallel to the width model domain (Kusznieir & Park, 1987; England, 1983; Sawyer, 1985a; an Wjik & Cloetingh.

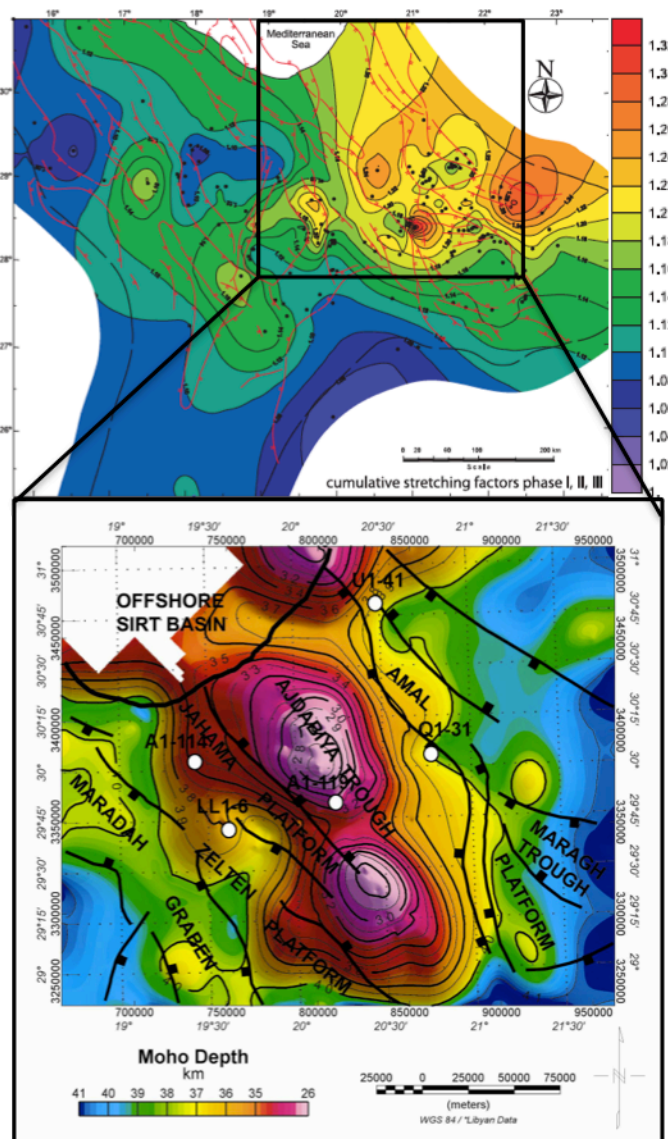


Figure 5.3 Evidence of narrow rift. Top Contour map of the total crustal stretching distribution (144.0–0 Ma) (modified after Abadi et al., 2008). Bottom: Moho depth map for the Ajdabiya Trough and adjacent areas inferred from gravity and magnetic modelling (modified after Ghanoush et al., 2014).

subsidence. They have correlated the abrupt change in magnitude of vertical strain rates to variation of divergent basin boundary forces at ~ 55 Myr. In their work, these authors



proposed that these change in boundary forces intensity could have been the response to the development of the Hellenic subduction system, attached to the African plate further north. This is indicated by the change in subsidence patters of the Ajdabyia Trough (Fig. 5.4a-c), between Early and Middle Eocene and from the related recovered strain rates curves, which allow them to infer a variation of one order of magnitude (Capitanio et al. 2009, and Fig. 5.4c). Although their analysis is focused on the Ajdabyia Trough, this is the structure that has recorder the largest and entire subsidence history of the Sirte basin, thus offering the most significant estimates of its stretching history. In general, these results are in agreement with many other studies of subsidence histories relative to this area. Although many results od studies focused on Sirte basin area, show similar features (Abadi et al., 2008; Conant and Goudarzi, 1967; Goudarzi, 1981; Gumati and Nairn, 1991; van der Meer and Cloetingh, 1993, Galushkin et al., 2014, Abdunaser & McCaffrey, 2015), they all agree on the different distribution of the two main tectonic phases between  $\sim 90 - 45$  Myr, and the widespread diffusion of Cretaceous deformation as opposed to the strongly localized Paleocene deformation.

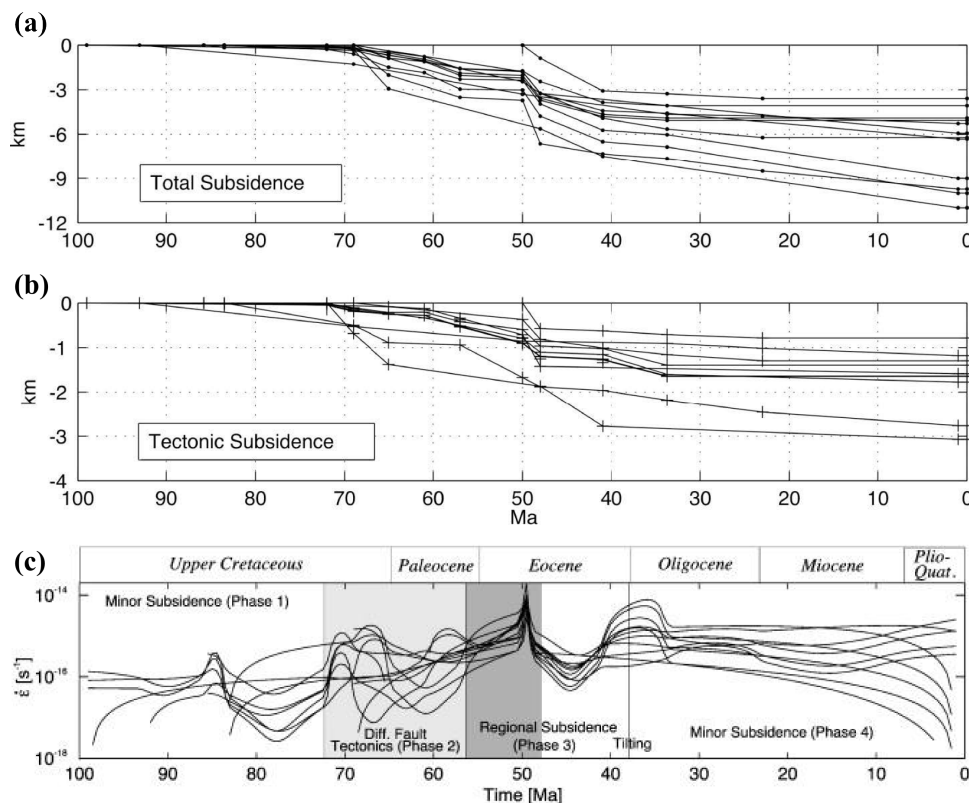


Figure 5.4 (Previous page) The tectonic subsidence in Fig. 4b and the inversion of the strain rate in in Fig. 4c (after Supplementary information in Capitanio et al., 2009; (d) Capitanio et al., 2009). Because the boundary forces exert a first order control on the rifting mode, the variation in time of these might provide an explanation for the switch in time from diffuse to



*localized lithospheric stretching. Hence, in this study, we focus on the time variation of boundary forces and investigate how this can explain the switching from a wide to narrow rift mode the Sirte, explaining the formation of the widest narrow basin in the world.*

Investigations on the rifting modeling in the Sirte Basin are few. [Van der Meer & Cloetingh \(1993a, b\)](#) have proposed 1D subsidence models using an uniform instantaneous stretching model, with a stretching phases of finite duration ([Jarvis and McKenzie, 1980](#)). This approach finds an agreement with the recovered characteristics of the tectonic subsidence pattern in the Paleocene rift.

In this work I approach the modelling of this rift from a 2D perspective, modelling the section of the lithosphere applying different single rift (monophase) and more complex rift event (polyphase) histories. This leads to clarify the link between lithospheric strain localization/delocalization and magnitude of the initial boundary conditions driving the monophase rifting. In general the monophase approach leads to narrow rift and lithospheric necking when stretching velocities,  $v_{xx}$ , (or initial strain rates,  $\dot{\epsilon}_{in}$ ) are above a critical value, while the deformation is distribute along the numerical domain when velocities  $v$  (or  $\dot{\epsilon}_{in}$ ) are below this value (e.g. [Van Wijk and Cloetingh, 2002](#); [Kusznier and Park, 1987](#); [Lu et al., 2011](#)). This physical constraint along with observables such as subsidence, thinning factors (for all the Sirte basins and for the deepest Ajdabyia Trough) and recovered strain rate data from literature, allows us to build a polyphase history to constrain and eventually compare with the numerical models. Here, the polyphase model is reduced to a two-phase rifting, contiguous phase in which the velocity of rifting is varied from a slow one to a faster one, following the work of [Capitanio et al., \(2009\)](#), where a change in tectonic forces of one order of magnitude was inferred at  $\sim 55$  Myr.

In the following section, I review the geological setting of the Sirte basin region with focus on the structural and stratigraphic features and the evolution of the subsidence (Fig. 5.6 and 5.7) based on the work of [Adabi et al., \(2008\)](#) and [Weegar \(1972\)](#).

Subsequently, I briefly present the numerical methodology used to build the model and illustrate the modeling of monophase and two-phases simulations, and present the results of subsidence patterns and thinning factors evolution.

Finally I discuss the model outcome, and an explanation of the rifting switch, from wide to narrow mode, and the inferences on the behavior of the lithosphere that can be drawn.

The example of Sirte Basin demonstrates that the different lithospheric histories affect the evolution of the deformation (monophase fast, monophase slow or different two-phase lithospheric stretching), and that they are of paramount importance for the final basin

architectures, providing a novel frame for the interpretation of rifted basins. Furthermore, this example points to the hidden deeper lithospheric process, which should not be neglected when addressing the evolution of crustal scale basins.

## **2. GEOLOGICAL SETTING AND LITERATURE REVIEW ON SIRTE BASIN OPENING**

### **2.1 The Sirte Basin System: Geological Setting**

Sirte Basin is NW-SE oriented ~500 km wide by ~500 km long intraplate rift system of Meso-Cenozoic age, situated in Libya, North Africa. The southern part of the Sirte Basin is onland while it extends offshore into the Mediterranean with a regional plunge toward the North. The Sirte Basin is bounded, from north-west to north-east, by Sicily Channel rift, Calabrian and Hellenic subduction zones ([Fig. 5.1](#)). To the west, Sirte Basin is bounded by Ghadamis Basin, Quargafli uplift and Murzuc Basin. At south it is limited by the Tibesti-Sirte Arch and Kufra Basin, and borders the structures belonging to Cyrenaica platform to the East.

Rifting in the Sirt Basin is typical of a Tethyan-realm extensional rift system that initiated in the Early Cretaceous and peaked in the Late Cretaceous ([Harding, 1984](#); [Gras and Thusu, 1998](#); [Ambrose, 2000](#)). A series of NW–SE trending horsts and grabens were created that imparted the dominant structural trends seen in the basin today ([Abdunaser and McCaffrey, 2014](#)). The grabens progressively deepen eastwards giving a regional asymmetry to the structural form of the basin when viewed in cross section. ([Fig. 5.3a-b](#)).

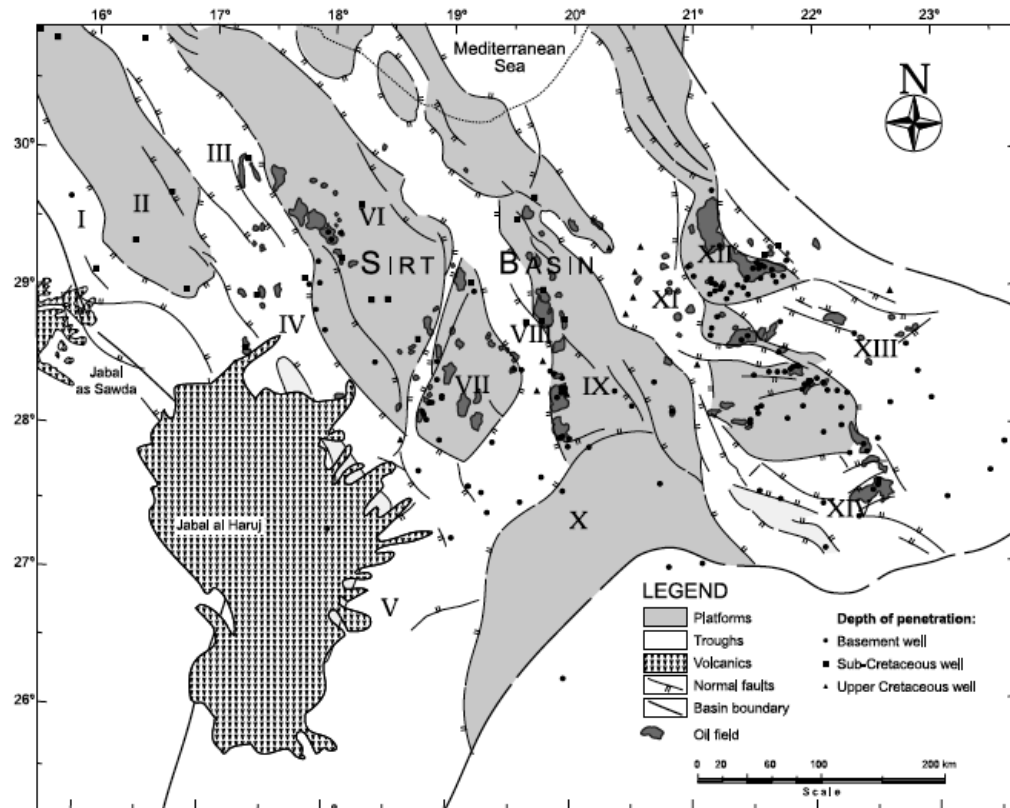


Figure 5.5 Generalized structural map of the Sirte Basin (modified from Mouzoughi and Taleb, 1981). The main structural elements of the Sirt Basin are Hun graben (I), Waddan uplift (II), Dor El Abid trough (III), Zallah trough (IV), Bu Tamaym trough (V), Dahra platform (VI), Beda platform (VII), Hagfa trough (VIII), Zelten platform (IX), Southern shelf (X), Agedabia trough (XI), Rakk high (XII), Hameimat trough (XIII), and Sarir trough (XIV) (after Abadi et al., 2008)

## 2.2 Basin Stratigraphy and tectonic subsidence

This section presents of the structuring of Sirte Basin on the basis of the analysis of cross sections (Fig. 5.2a-b), structural mapping (Fig. 5.5, stratigraphic correlations (Fig. 5.6) and tectonic subsidence maps (Fig. 5.7 a-h), plus available literature data (i.e. Klitzsch and Squyres, 1990; Goudarzi, 1980; Abadi et al., 2008; Van der Meer and Cloetingh, 1993a, b; Abdunaser and McCaffrey, 2014; Galushkin et al., 2014; Guiraud et al., 2005; Rusk, 2001; Saheel et al., 2010; Skuce, 1996).

The Sirte Basin horst and graben system began to develop in the latest Jurassic. The basin structure evolved as a rifted embayment on the northern margin of the African plate, following a sequence of tectonic events that led to the breakup of the supercontinent Pangaea. These events were marked elsewhere by rift occurrences along the present northwestern margin of Africa, from the Middle Triassic onward.

Crustal separation and sea-floor spreading commenced in the Early Jurassic, probably linked with the creation of central Atlantic between northwest Africa and North America (Gumati and Kanes, 1985; Gumati and Nairn, 1991; Van der Meer and Cloetingh, 1993a, b; Baird et al., 1996; Schroter, 1996), followed by the opening of the central Tethyan Basin during the Middle Jurassic (Laubscher and Bernoulli, 1977; Cavazza et al., 2004). The first phase of basin formation is recorded in a limited number of wells (Fig. 5.2). The eastern part of the basin shows rapid subsidence in the Hameimat and Sarir troughs (Section A-A' in Fig. 5.1 and Fig. 5.2a) and Ajdabyia Trough. (Section B-B' in Fig. 5.1 and Fig. 5.3b) The western part of the basin shows less intense subsidence, located in the Gattar Ridge (western rim of the Dahra platform, bordering the Zallah Trough, Hun graben, and Waddan uplift. Spatially, the wells that show subsidence align along an east to west trend and form local troughs in the eastern part of the basin. The pattern in the middle and the western parts of the basin is less clear, mostly caused by a lack of wells penetrating the Lower Cretaceous succession. Early Cretaceous rifting in the Sirte area occurred as a result of an extension along a separation zone between two African crustal blocks (Fig. 5.2a, phase 1), which led to the collapse of the preexisting Sirte Arch (Burke and Dewey, 1974). It is suggested that the drift of the African plate over a fixed mantle hotspot/plume triggered this event (Van Houten, 1983).

## **Phase II: Upper Cretaceous (Cenomanian–Maastrichtian, 98.9–65 Myr)**

The upper Cretaceous basin evolution is marked by major basin subsidence the Sirte Basin. The maps for this period show that subsidence is highly variable in space and time. Spatial variations are related to the formation and evolution of horst and graben structures and the reactivation of these structures.

Temporal variations reveal that subsidence occurred in pulses and is diachronously distributed. In some areas, conditions of non-deposition and unconformities suggest the presence of topographic relief. The strong variations in subsidence most likely reflect changes in the stress field interacting with the basin-fault framework.

Biju-Duval et al., (1977), Duncan (1981) and Morgan (1980, 1983) proposed that during the Upper Cretaceous a change from the northward to westward motion of the African plate in the Late Cretaceous promoted the thinning of the cratonic lithosphere and fragmentation in north Africa. This was marked by basin subsidence (Fig. 5.3a-b, the phase 2), crustal extension, and reactivation of faults (Gumati and Kanes, 1985; Gumati and Nairn, 1991). In the Santonian and Coniacian (89.8 - 86.3 Myr), subsidence slowed





*Figure 5.6 Generalized stratigraphic lithologic correlation chart of the Upper Cretaceous and Tertiary successions of the Sirte Basin (modified from Barr and Weegar, 1972).. Subphases a–h correspond to subphases in the subsidence curves in Figure 5.7. LS = limestone; FM = formation (modified after Abadi et al., 2008).*

During the Cenomanian (Fig 5.4b), rapid subsidence was most pronounced in the western part of the Sirte Basin. This indicates that a new rifting phase started in the western Sirte Basin, leading to the development of a new northwestern structural trend, whereas in the east, some Early Cretaceous depocenters continued to be aligned east–west.

In the Turonian, (Fig 5.4c) rapid continuous subsidence shifted to the eastern part of the basin, creating the Hagfa, Agedabia, and Hameimat troughs. By this time, the dominant northwestern horst and graben system of the Sirte Basin was well established.

During the Coniacian and Santonian (Fig 5.4d), high subsidence local depocenters were formed in the southeast. Interestingly, high local rates of subsidence are shifted in position relative to the Cenomanian to the southeast of the Sirte Basin, marked by very fast subsidence in the Sarir Trough.

The Campanian (Fig 5.4e) is characterized by widespread subsidence over the entire basin, except for the platform areas (Dahra platform. In comparison to the previous stage, the more intense subsidence in the east had shifted northward (Agedabia Trough,) and toward the center of the basin (Hagfa Trough), whereas in the Hameimat Trough, less intense, broader subsidence prevailed, suggesting thermal subsidence. In the west, renewed subsidence in the northern Zallah Trough is evident. Interestingly, some highs (e.g., Zelten platform and Rakb high ) also show considerable subsidence at this stage, whereas the Dahra and Beda platforms were already established.

During the Maastrichtian (Fig 5.4f), subsidence patterns in the region became spatially less differentiated. Subsidence still occurred in the northern parts of the Dahra and Beda platforms, Hagfa Trough, Zallah and Agedabia troughs, and Waddan uplift, of which the Agedabia Trough subsided most intensively.

The Kalash Limestone covered both troughs and submerged horst regions, with relatively little change in facies. It is the first formation to cover the whole study area by transgressing the last remnants of the sub-Sirt relief (Hofra Formation or granite highs on the Dahra platform).

### **Phase III: Paleocene–Early Eocene (Danian–Ypresian, 65–49 Myr, Fig 5.4g)**

In the Danian–Ypresian phase there is rapid subsidence (Fig. 5.2a phase 3, and Fig. 5.2b),

which is most in the northeast. This indicates that a renewed phase of rifting had now commenced. This phase was widespread, particularly toward the northeast, where the Upper Cretaceous depocenter deepened and widened, accommodating the deposition of Paleocene shales. The Paleocene rifting phase (65–49 Ma) marked an abrupt deepening of the basin, separated from the Late Cretaceous subsidence by a period of tectonic quiescence in the Maastrichtian. This phase of high subsidence was followed by the deposition of lower Eocene evaporate and dolomite. In the late Eocene, progressive collisional coupling of Africa and Europe, under approximately north-northwest–south-southeast compressional stresses ([Ziegler et al., 1998](#); [Cloetingh et al., 2005](#)), resulted in a renewed inversion of the Al Jabal al Akhdar area ([Guiraud et al., 2001](#)).



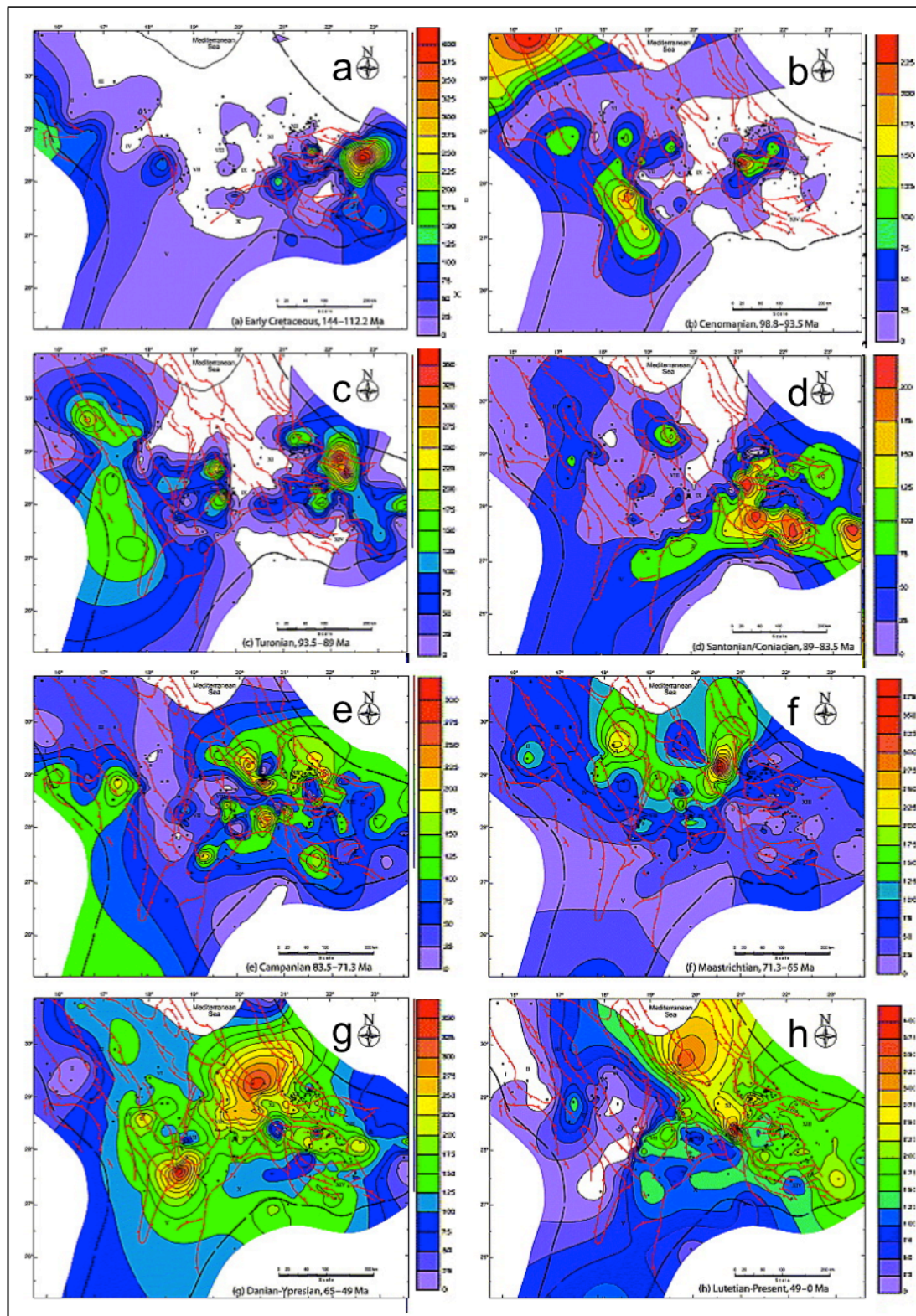


Figure 5.7 Contour maps of tectonic subsidence (m) of (a) Early Cretaceous, 144.0–112.2 Ma; (b) Cenomanian, 98.9–93.5 Ma; (c) Turonian, 93.5–89 Ma; (d) Santonian or Coniacian, 89–83.5 Ma; (e) Campanian, 83.5–71.3 Ma; (f) Maastrichtian, 71.3–65 Ma; (g) Danian–Ypresian, 65–49 Ma; and (h) Lutetian–Present, 49–0 Ma. (modified after Abadi et al., (2008)).



The Sirte Basin seems not to be affected by inversion, however, being marked by a thick succession of post-rift sediments filling it from the late Eocene until the Miocene (Fig. 5.3a, phase 4). In the western part of the basin, large parts of the Tertiary sequence have been eroded. Erosion is interpreted to have occurred from the late Miocene onward (e.g., Gumati and Schamel, 1988), which is contemporaneous with the widespread volcanic activity recorded in the western part of the Sirte Basin area (Fig. 5.1). Jabal as Sawda is the nearest major volcanic eruption center and is dated 10.5–12.3 Ma (Ade-Hall and Reynolds, 1975). A second major eruption center is Jabal al Haruj in the southern part of the Sirte Basin, dated as late Pliocene (2.2 Ma; Ade-Hall et al., 1974).

Late Oligocene to Holocene magmatism within the African plate and Cenozoic rift system of Europe is widespread and reflects a change in the plate tectonic regime, most likely associated with the changing patterns of mantle convection and changing stress fields (Guiraud and Bellion, 1995; Janssen et al., 1995; Cloetingh and Van Wees, 2005; Cloetingh et al., 2005). At the same time, large-scale mantle plumes appear to be the main cause of the flood basalt volcanism (Wilson and Guiraud, 1998).

#### **Phase IV: Middle Eocene–Present Day (Lutetian–Present Day, 49 Myr–Present Day, Fig 5.4h)**

Super-Eocene spatial patterns show that continued subsidence occurred in the northeast, where the Ajdabyia Trough and eastern flanks of the Zelten platform formed a single large elongated depression that coincided with the main northwest–southeast trend. In map view, the basin subsidence patterns reveal a tilting to the northeast toward the Mediterranean Sea. However, no fault activity in this interval is observed, which indicates that the basin subsided because of sediment loading and thermal relaxation (see also Fig. 5.3a phase 3, and Fig. 5.3b). Sedimentation was limited, and large areas in the west and the fringes of the Sirte Basin suffered from strong erosion (e.g., Gumati and Schamel, 1988), revealing a large-scale up warding of these areas.

Underplating related to mantle upwelling can explain a significant amount of relative uplift (e.g., Skogseid, 1994), which for the Sirte Basin may possibly explain the highly anomalous uplift in the west and the resulting asymmetry. The broad-scale up warding and down warding patterns, in the absence of faulting, may also suggest a component of lithospheric folding (cf. Cloetingh et al., 1999) in the late-stage post-rift evolution, superposed on thermal relaxation. This folding may be related to mantle upwelling as found for large areas in Europe (Cloetingh and Van Wees, 2005).

### 3. NUMERICAL MODELLING

#### 3.1. Modelling approach

We have modelled rifting evolution in single and two-phase stretching simulations. The monophasic models, where a single rifting phase is modelled allow the comparison with published results such as [Kusznier and Park \(1987\)](#) or [Buck, \(1991\)](#), and benchmark our reference boundary conditions for the lithospheric localization. Localization is defined when lithosphere necking occurs in a discrete, small area, producing a narrow rift. As shown by other authors (i.e. [van Wijk & Cloetingh, 2002](#)), the higher the applied stretching velocity (or initial strain rate), the higher the coupling between the lithospheric rheological layers and this will promote lithospheric localization which, in turn, facilitates the creation of narrow shear bands. Below a critical velocity value, instead lithosphere deformation is instead distributed on a large area given rise to wide rifts (i.e. [Lu et al., 2011](#)).

The polyphase models, where two stretching phases are simulated, allow the comparison with the single rifting simulations, in order to highlight the role of the time-dependent boundary conditions and their effect on the final rift history.

We focus on the role of the varying boundary conditions during rifting, considering the range of velocities  $\frac{1}{2} v = 0.05\text{-}3 \text{ cm/yr}$  to derive the conditions under which the model is dependent on the lithosphere's initial state. Therefore, we use the same initial lithospheric model with an equilibrium continental geotherm and normal-thickness crust. We do not investigate the role of various crustal compositions here, affecting the rheology, and instead use the same crustal rheological parameters (Table 1). To better illustrate the role of the complexities during rifting, we consider no pre-existing perturbation in the lithosphere, i.e. no weak/strong seeds or thermal anomalies are introduced ([Fernandez and Ranalli, 1997](#)).

#### 3.2. Governing equations

Here, the extension of the lithosphere is simulated using a 2D numerical domain and the Underworld code ([Moresi et al., 2003](#); [Moresi et al., 2007](#)) which solves the governing equations of mass (Eq.1), momentum (Eq.2), and energy conservation (Eq.3) for incompressible Stokes flow:

$$\frac{\partial u_i}{\partial x_i} = 0 \quad (5.1)$$

$$\frac{\partial \tau_{ij}}{\partial x_j} + \frac{\partial p}{\partial x_i} = -\alpha \rho g T \lambda_i \quad (5.2)$$

$$\frac{\partial T}{\partial t} + u_i \frac{\partial T}{\partial x_j} = \kappa \frac{\partial^2 T}{\partial x_j^2} + H_r \quad (5.3)$$

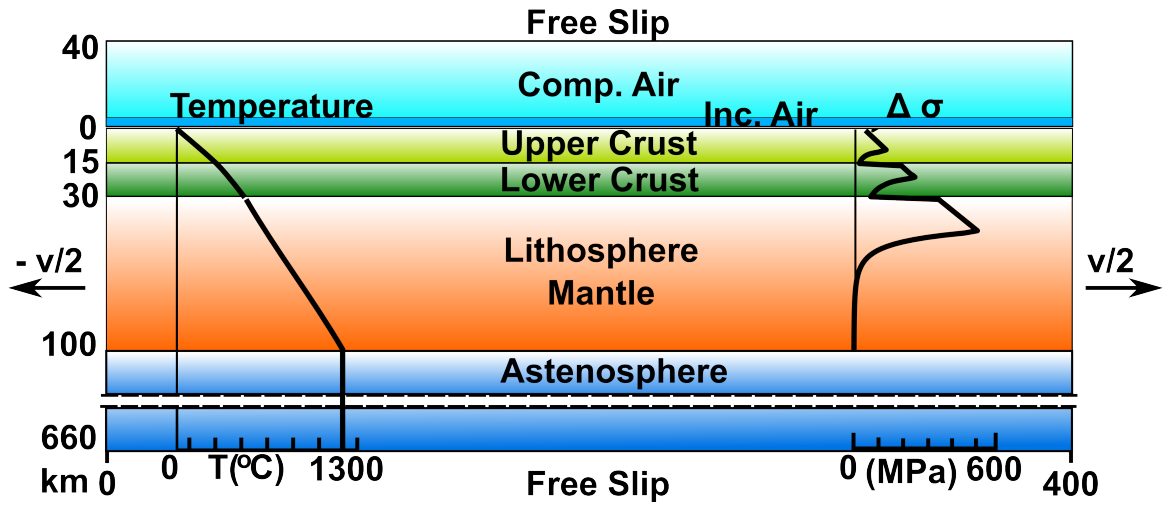


Figure 5.8 Model Setup. All the models have a standard lithosphere 100 km thick, an upper crust and a lower crust thickness are 15 km each, and an asthenosphere, which expands to a depth of 660 km. The model is laterally uniform without weak/strong seeds or thermal anomalies. Horizontal velocity boundary conditions of  $\pm v/2$  (where  $v$  ranges between  $\frac{1}{2}v_{xx}=0.05$  cm/yr and  $\frac{1}{2}v_{xx}=3$  cm/yr) are applied at the right and left sides of the numerical domain. The top is a incompressible 5km thin layer above which there is a compressible 35 km air layer with top free slip condition. The base is a horizontal free slip boundary. Temperatures and rheological constitutive laws and rheological parameters are discussed in the text and summarised it le1.

where  $\tau_{ij}$  is the deviatoric stress tensor,  $p$  the total pressure,  $x_i$  are the spatial coordinates,  $u_i$  is the velocity,  $T$  is the temperature,  $\alpha$  is the thermal expansivity,  $\rho$  is the fluid density,  $\lambda_i$  is the unit vector in the direction of gravity,  $g$  is the gravitational acceleration and  $H_r$  radiogenic heat.

The incompressible Stokes flow is calculated in an Eulerian finite element mesh embedding Lagrangian particles, which allows to track movements of the materials points relative to the mesh for high deformation in visco-plastic flow (Moresi et al., 2003; Moresi et al., 2007).

The code has been widely used in several geodynamic applications such as extension tectonics and passive margins (e.g [Farrington et al., 2010](#); [Sharples et al., 2015](#)) and subduction (i.e. [Stegman et al., 2010](#); [Capitanio & Replumaz, 2013](#); [Farrington et al., 2014](#); [Capitanio, 2014](#)).

We use non-linear, temperature-dependent flow laws for the viscous deformation of rocks with the following form:

$$\tau_{II} = \frac{1}{A\eta_{eff}^{n-1}} \exp\left(\frac{E}{nRT}\right) \quad (5.4)$$

where  $T$  is the temperature,  $R$  is the gas constant,  $A$  is a pre-exponent,  $E$  the activation energy and  $n$  the power-law exponent. The material parameters vary in the models according the rock type (Tab. 1), that is we use rheological parameters of a wet quartzite for the upper crust ([Gleason & Tullis, 1995](#)), wet diabase parameters for the lower crust ([Mackwell et al. \(1998\)](#)) and a dry olivine for the mantle ([Chopra and Paterson, 1981](#)) (Tabs. 5.1 and 5.2)

To account for the brittle deformation, we used a Drucker-Prager frictional-plastic pressure-dependent law:

$$\tau_y = C_0 + \tan(\varphi) \sigma_n \quad (5.5)$$

where  $C_0$  is the cohesive strength,  $\tan(\varphi)$  is the internal friction coefficient,  $\varphi$  is the internal friction angle,  $\tau_y$  and  $\sigma_n$  are, respectively, the brittle shear and normal stress to the plane of failure within material.

The composite visco-plastic flow law used in the models is implemented through the effective viscosity:

$$\eta_{eff} = \min\left(\eta; \frac{\tau_y}{2\dot{\epsilon}_{II}}\right) \quad (5.6)$$

where  $\dot{\epsilon}_{II} = \sqrt{\dot{\epsilon}_{ij}\dot{\epsilon}_{ij}/2}$  is the strain rate tensor's second invariant, i.e. the effective strain rate. Similarly, the stress tensor's second invariant is defined as  $\tau_{II} = \sqrt{\tau_{ij}\tau_{ij}/2}$ .

### 3.3. Model set up and boundary conditions

The numerical domain is 700 km deep and 400 km wide, with numerical resolution of 700 x 400 elements, for a spatial resolution of 1 km (Fig. 5.8), with 20 particles per element. The lithosphere model is composed of two layers on the top are each 15 km, hereafter the upper and lower crust, and reproduce the properties of the crust, and mantle portion, ranging to the bottom of the computational domain, where the properties are homogeneous, still differentiated into lithospheric mantle and asthenosphere by the temperature-dependent viscosity eq. (5.4). Although the mechanical stiffness of the lithosphere is, thus, loosely constrained, I describe the lithosphere-asthenosphere boundary (LAB) as the isotherm 1300 °C, at 100 km of depth in the setup. Atop the lithosphere I have placed a thin incompressible layer of air and 35 km of compressible air. This allows for a quasi-free surface and self-consistent evolution of topography.

To track precisely the thicknesses of the lithospheric layers in time, I have embedded Lagrangian passive tracers in the models for the surface (upper crust top), the top and base (Moho) of the lower crust, and the initial 1300 °C isotherm, the lithosphere-asthenosphere boundary.

The initial temperature distribution in the model follows that of an equilibrated continental geotherm (Allen & Allen, 2013) with temperature boundary conditions of  $T_0 = 0$  °C at surface and  $T_m = 1300$  °C at the base of the model lithosphere, and Moho temperature of 600° C. The temperature in the crust  $T_c$  and beneath are defined as:

$$T_c = T_0 + \left( \frac{Q_m + Ah}{k} \right) a - \frac{A}{2k} h^2 \quad (5.7)$$

$$T = T_c + \left( \frac{Q_m}{k} \right) (a - h) \quad (5.8)$$

where  $Q_m$  is the heat flux from the mantle,  $A$  is the radiogenic heat production,  $k$  is the thermal conductivity,  $h$  is the thickness of the whole crust and  $a$  is the thickness of the lithosphere  $a = h + H$ , with  $H$  the lithospheric mantle thickness. Deeper, the temperature is kept constant.

On the top and bottom of the model space we enforce free-slip boundary conditions, whereas on the side we apply kinematic boundary conditions. The right and left sides of the model domain are pulled with a constant velocity  $v_x$ , applying  $v_x/2$  at the right side and  $-v_x/2$  at the left side. These are consistent with the range of present-day plate velocities derived from GPS data (e.g. Argus & Hefin, 1995). Also, to provide a more general

understanding, we will express the velocity boundary conditions as initial strain-rates,  $\dot{\epsilon}_i = v_i / L_i$ , for each rifting phase  $i$ . For the velocity range of 0.1 to 6 cm/yr and domain's initial width of 400 km at the beginning of the modelling we get strain rates of  $7.9 \times 10^{-17} \text{ s}^{-1}$  to  $4.7 \times 10^{-15} \text{ s}^{-1}$ , comparable with the strain-rates recovered from rifting on Earth (Newman & White, 1997; Newman et al., 1999). In the present work we use the strain-rate  $\dot{\epsilon}_i$ , to indicate the initial strain rate imposed by the constant velocity boundary condition  $v_i$ . For constant velocity boundary conditions this varies inside the lithosphere as  $\dot{\epsilon}(t) = \dot{\epsilon}_i \exp(-t \dot{\epsilon}_i)$  (England, 1983), which implies the strain rates remain significant for times  $\dot{\epsilon}^{-1}$ .

Several parameters, domain and grid size, rheological stratification and initial temperature distribution initial perturbations (e.g., group of weak-seeds and single one placed in the crust and lithospheric mantle), were tested. The initial heterogeneities lead to earlier lithospheric strain localization, which strongly constrains the evolution of the models, while none of the other parameters resulted in significant deviation from the outcomes. I will present only the key models useful to understand the Sirte basin evolution.

### 3.4. Lithospheric thinning and rifting and Basin Subsidence

In order to compare the results with both existing general models on narrow and wide rifts (e.g. van Wijk & Cloetingh, 2002; Kuszner & Park, 1987; Buck, 1991; Gueydan et al., 2009; Chenin & Beaumont, 2013) and with basin analysis results (e.g. backstripping curves and maps – i.e. Abadi et al., 2008 - gravity and magnetic models - i.e Saheel et al., 2010; Ghanoush et al., 2014) specifically obtained for the Sirte Basin, I calculate and measure the subsidence of the basin and the thinning of the lithosphere of the numerical models.

#### 3.4.1. Basin Subsidence

Under the assumption of isostatic equilibrium, I have calculated the tectonic subsidence of the models. This is done following the methodology suggested by Steckler & Watts, (1978) .

$$S = \frac{a[(\rho_l - \rho_c) \frac{h}{a} (1 - \frac{\alpha T_m h}{2a}) - \frac{\rho_l \alpha T_m}{a}] (1 - \frac{1}{\beta})}{\rho_l (1 - \alpha T_m) - \rho_w} \quad (5.9)$$

where  $S$  is the tectonic subsidence (depth of the basement in absence of surface loads),

$\rho_l$ ,  $\rho_c$  and  $\rho_w$  are respectively the lithospheric, crust and water averaged densities,  $T_l$  is the lithosphere-asthenosphere boundary temperature,  $\alpha_v$  the coefficient of volume expansion and  $\beta$  is the stretching factor of the whole crust. The depth of the basin is measured taking the initial surface as reference, advected as the lithospheric model stretches, and is calculated only at the point where the maximum stretching is measured. Using eq. (5. 9) allows us to account for the water filling of the basin, which is not explicitly modelled.

### 3.4.2 Lithospheric thinning

I measure the thinning factor in the crust and the lithospheric mantle, and define  $\beta$  the ratio between the initial thickness of the crust and that during the modelling,  $h_0$  and  $h(x,t)$ , respectively, and  $\delta$  the ratio between the initial thickness of the lithospheric mantle and that during the modelling,  $H_0$  and  $H(x,t)$ , respectively:

$$\beta(x, t) = h(x, t)/h_0 \quad (5.10)$$

$$\delta(x, t) = H(x, t)/H_0 \quad (5.11)$$

I present the thinning factor of whole crust, even though the models embed upper and lower crust, and do not focus on details of intra-crustal structures. Presenting the thinning factors of crust and lithospheric mantle versus time (Fig. 5.10) allows us to visualise the development of the basins, and provide insights in the evolution of the basin. As general criterion, I define the break-up of the crust when  $\beta > 22$  and the break-up the lithosphere when both crust and lithospheric mantle have  $\beta$  and  $\delta > 22$ , in agreement with Frenke, 2013, although Sirte Basin did not reach the stage of breakup and the maximum thinning factor for the crust is estimate  $\sim 1.3$  (Abadi et al., 2008).

### 3.5 Localization index of the lithosphere

In order to link the lithospheric deformation with the subsidence data, the style of the basin (narrow or wide), and the thinning factors of the basins I need to quantify the ability of the lithosphere to localise and delocalise strain. The evolution lithospheric localization can be summarised by a criterion of localisation, which accounts for the initial strain rates, the rheology as well as the strain history. In order to identify these controlling parameters we follow the approach of Crameri & Kaus (2010), Lu, Kaus, & Zhao (2011) and Kaus & Podladchikov (2006). Crameri & Kaus (2010) have calculated a localization index for a lithospheric deformation under compression:

$$I = \frac{\dot{\epsilon}_{in} \Delta L}{1.4} \sqrt{\frac{\eta_0 E}{nRT_0^2 k}} \quad (5.12)$$

where  $\dot{\epsilon}_{in}$  is the background strain rate,  $\eta_0$  is effective viscosity,  $E$  is activation energy  $n$  is power law exponent,  $R$  is gas constant,  $T$  is temperature distribution and  $k$  is the thermal conductivity, and  $\Delta L$  is a characteristic length.

The only undefined parameter is the characteristic length,  $\Delta L$ . [Crameri and Kaus \(2010\)](#) have proven that lithospheric localization is primarily controlled by the thickness of the plastic field ( $th_p$ ), which they have measured from 1D yield strength profiles. For the same rheology, lithospheric localization occurs when  $I > 1$ , while strain is diffuse when  $I < 1$ . In a second step, they compare the 1D results with the 2D numerical models. The localization/non-localization in the 2D models was calculated using the first derivative of Moho morphology (localization occurs when  $dy/dx > 4$ , where  $dy$  is the height of the Moho from the original horizontal position). They have found a good agreement between the 1D and 2D models, so they were able to constrain physically the nucleation and development of localised lithospheric shear zones in the 2D models. [Lu et al. \(2011\)](#) have used a similar approach to model the North China Craton evolution and found that narrow and wide rifts develop respectively when  $I > 1$  and  $I < 1$ .

Here, I propose that the variation of the plastic thickness is proportional to the thinning of the crust and, similarly to [Crameri and Kaus \(2010\)](#) The Moho morphology in the 2D depends on the initial strain rate. I use this approach to calculate the lithospheric localization indexes,  $I$ , for the 2D monophase and two-phasic models in this work. This helps to interpret the subsidence and thinning results in the framework of lithospheric stretching history.

## 4. RESULTS AND DISCUSSION

### 4.1 Subsidence curves and lithospheric thinning

Tectonic subsidence curves have been calculated from 2D numerical models for monophase rifting cases ([Fig. 5.9a](#)) and two-phase rifting simulations ([Fig. 5.9b](#)). They are calculated in where the maximum crustal thinning occurs, therefore can be compared with subsidence curves of the deepest trough (Ajdabyia) in the Sirte Basin. I have used two time scales in [Fig. 5.9b](#): the first one is the relative running time of the models while



the grey time scale represents the geological interval in Fig. 5.4. This is necessary in order to compare the models with the data.

#### 4.1.1 Monophase tectonic subsidence (M rifting history type)

The tectonic subsidence curves in Fig. 5.9a are calculated from the monophase lithospheric stretching models where the deformation was driven with horizontal half velocities,  $\frac{1}{2}v$ , between 0.05 cm/yr and 3 cm/yr as boundary condition. There is an evident correlation between the subsidence ratio and the magnitude of the boundary condition used. In fact the subsidence ratio increases from a minimum of  $\sim 800$  m in 70 Mr with  $\frac{1}{2}v=0.05$  cm/yr, to a minimum of  $\sim 2000$  m when  $\frac{1}{2}v=3$  cm/yr is used.

I have calculated the lithospheric localization Index for each of these models for the onset of the rifting and use it to divide the tectonic subsidence curves in two groups:

- Dashed lines represent models with  $I < 1$  and that, according to section 3.6 (in this chapter) and Crameri & Kaus (2010) and Lu et al., (2011), predict that the strain is distributed over the modelled lithospheric domain. This group of curves are diagnostic of a wide rift mode;
- Solid lines denote simulation with  $I > 1$  which indicates lithospheric strain localization and, as suggested by literature (e.g. van Wijk & Cloetingh, 2002; Kusznieir & Park, 1987; Buck, 1991), relates to a narrow rift mode.

It is evident that none of this curves can be related to the increase in subsidence ratio occurring at  $\sim 50$  Myr (Fig. 5.4b). This confirms the 1D model results of van der Meer and Cloetingh, (1993a). Yet, these monophase tectonic subsidence curves (Fig. 5.9a) can be used for two aims in this study:

- They highlight the strong correlation between the magnitude of the boundary condition used to stretch the model, the ability of the lithosphere to localise the strain (lithospheric localization = narrow rift mode = narrow basin and lithospheric delocalization = wide rift mode = wide basin; e.g. Lu et al., 2011) and the subsidence ratio. From this it is possible to state that higher subsidence ratios are diagnostic of a narrow rift mode while low subsidence ratios can indicate a wide rift mode. Obviously this need to be quantified, as I did here, calculating which curve corresponds to the threshold value,  $I=1$ , between lithospheric localization and non-localization.
- More specifically, they help to choose the half stretching velocities,  $\frac{1}{2}v_{xx}$ , needed to simulate the first rifting phase of Sirte two-phase model. This is a necessary

step since my model is driven using horizontal velocities and from my knowledge, there are no indications of specific stretching velocity range for Sirte Basin. Therefore, comparing the backstripping data of Ajdabiya Trough (Fig. 5.4a,b) and the tectonic subsidence curves for monopase models, curve 1 in Fig. 5.9a seems to best represent the subsidence between the  $\sim 85$ -55 Myr. According to Abadi et al. 2008, this time interval represents phase II and III of the Sirte opening. However, since I want to study the effect of the abrupt change in tectonic forces, as suggested by Capitanio et al., 2009 (Fig. 5.9c), I approximate the subsidence between  $\sim 85$ -55 Myr with a single phase. The  $\frac{1}{2}v_{xx}=0.05$  cm/yr seems appropriate since the relative tectonic subsidence curve reaches  $\sim 500$  m in 35 Myr, therefore this is the starting point for Sirte two-phase model.

#### 4.1.2 Two-phase tectonic subsidence (RR rifting history type)

Fig. 5.9b shows two groups of models tests (group 1 is composed by 1, 1-a, 1-b and 1-c curves; group 2 comprises curves 3, 3-a, 3-b and 3-c curves. N.B. the number represent the first rifting phase  $R_1$  and corresponds to the same  $\frac{1}{2}v$  used in monopase model, while the letters indicate the second rifting phase  $R_2$ ). Group 1 represent the Sirte Basin models while group 2 serves for a more general understanding of this particular family of rifting histories (RR, see Ch. 2, paragraph 5).

Analysing the group 1 curves, it is evident the lithospheric response can change depending on the rifting history. For example curve 1- a results from the combination of  $\frac{1}{2}v = 0.05$  cm/yr in  $R_1$  with  $\frac{1}{2}v = 0.1$  in  $R_2$ , which are both velocities that in the monopase case leads to a  $I < 1$  and so to a lithospheric delocalization. Curve 1-a preserves this mode of deformation with the only difference that the final subsidence at the 48 Myr (grey time-scale and 30 on withe time scale) is  $\sim 650$  m while the monopase model run with the same velocity reached  $\sim 400$  m for the same time. The monopase model run with the same velocity reached  $\sim 1000$  m of max tectonic subsidence reached at the end of the model (17 Myr grey time-scale and 0 on withe time scale). Curve 1-b shows that the lithospheric deformation mode shift from a distributed deformation in  $R_1$  to a localised strain in  $R_2$ , even though the velocity  $\frac{1}{2}v = 0.25$  cm/yr in this second phase, was leading to a no-localization of the strain in the monopase case. The subsidence history represented by curve 1-c also attains this shift in lithospheric deformation modes from delocalised to localised as well, with velocity  $\frac{1}{2}v = 1.5$  cm/yr in  $R_2$  that leads to localization.

In-group 2 I have uses a slightly higher velocity,  $\frac{1}{2}v_{xx}=0.1$  cm/yr, in  $R_1$  but for a shorter time ( $\sim 13$  Myr). This was deliberate chosen to reach the same thinning factors and tectonic subsidence in crust at the end of  $R_1$  in the 2 models groups. Group two confirm that same shift in deformation mode.

Form this analysis it is possible to summarise that:

- The ability of the lithosphere to localise the strain is strongly depended on the type of rifting history. In particular, it depends on the interplay between the onset new boundary condition in rift phase 2 ( $R_2$ ) and the inherited deformation achieved in rift phase 1 ( $R_1$ ).
- The curves that best represent the Sirte Basin backstripping data is 1-c. In fact, from the comparison between [Fig. 5.4b](#) and [Fig. 5.9b](#), it can be seen that the first part of 1-c curve reaches the 500 m of subsidence in  $\sim 35$  Myr ( $\sim 85$ -55 Myr on grey scale) while the second part well matches the subsidence ratio between 55-48 Myr.

The RR model represented by the tectonic subsidence curve 1-c, ( $R_1 \frac{1}{2}v = 0.05$  cm/yr and  $R_2 \frac{1}{2}v = 1.5$  cm/yr) is the one that will be exanimated in the next section. A comparison is made with the monophase curves 1 and c.

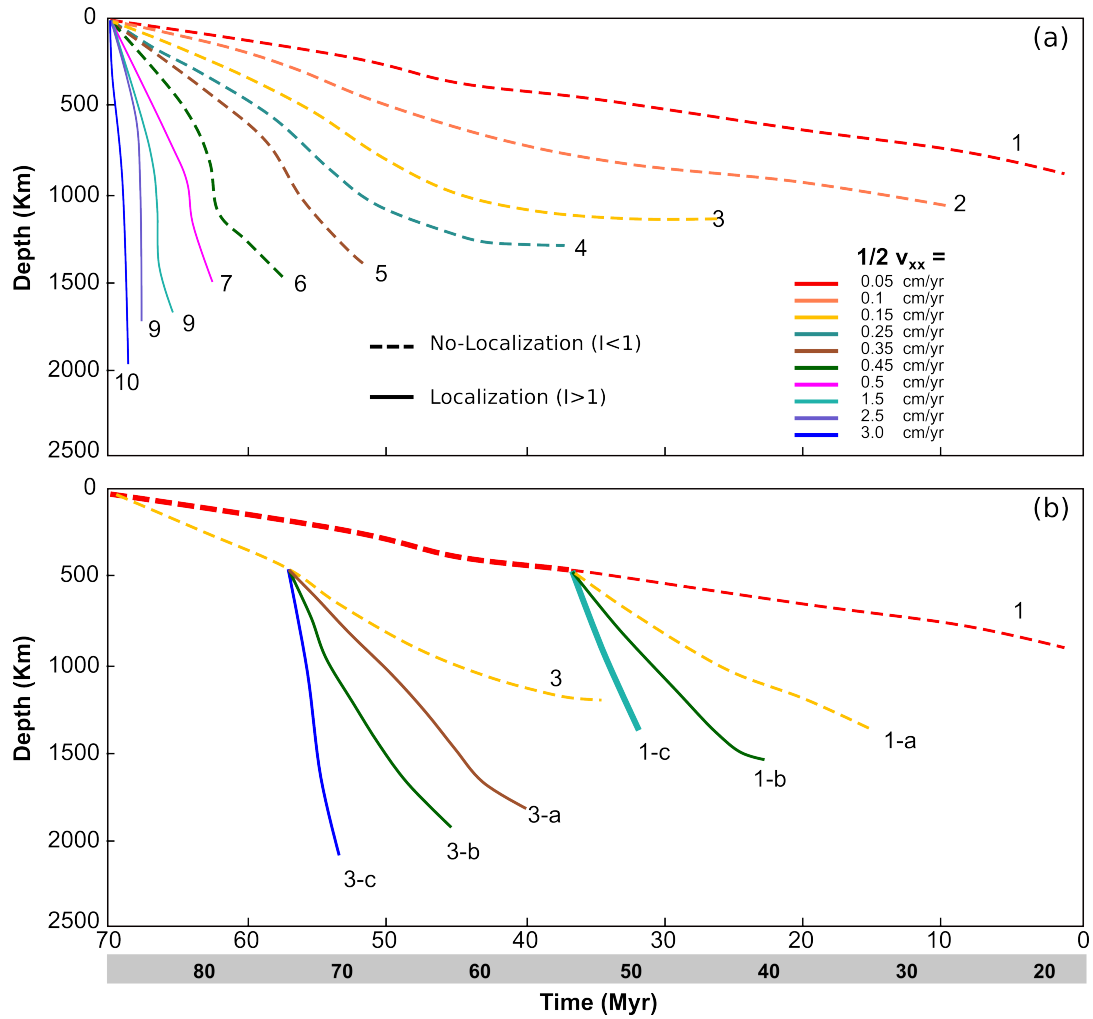


Figure 5.9 (a) Tectonic subsidence curves calculated from 2D numerical model simulations for monophase rifting with half stretching velocities between  $1/2 v = 0.05 - 3$  cm/yr. Each velocity has a specific colour (see legend for details). The time scale represents the numerical model time in Myr while the grey one corresponds to Capitanio et al., (2009) useful for comparison. Dashed lines represents models that have realized necking and so, lithospheric localization with strong ( $1/2 v = 3$  cm/yr) and moderate ( $1/2 v = 0.5$  cm/yr) coupling between upper, lower crust and lithospheric mantle. The largest velocities lead to breakup both in the crust and lithospheric mantle. For this family of monophase models advection heat transfer mechanism predominates over diffusion heat transfer mechanism. Solid lines indicate models deforming in a diffuse mode without often allows for breakups and, therefore, with crust and lithospheric mantle layers decoupling from moderate ( $1/2 v = 0.45$  cm/yr) to strong ( $1/2 v = 0.05$  cm/yr). Here, the diffusivity heat transfer mechanism dominates progressively as the stretching velocities decrease. (b) Tectonic subsidence for two-phase rifting. The Sirte Basin history (Ajdabyia Trough) is represented by the union of the thicker red dashed line ( $R_1$  = rifting phase, which matches roughly  $\sim 80$  and  $\sim 52$  Myr interval on grey timescale) and the sea green solid thick line ( $R_2$  = rifting phase, which is about  $\sim 52$  and  $\sim 46$  Myr interval on grey timescale). The other two-phase models curves (group 1 = 1, 1-a, 1-b, 1-c and group 2 = 3, 3-a, 3-b) are to facilitate the comparison between different rifting histories.

#### 4.1 Crust and mantle lithospheric thinning for Sirte Basin model

To characterise the evolution of the different rifting modes (wide, narrow and the transition from wide to narrow, the latter characteristic of the Sirte Basin), I present here

the crustal ( $\beta$  on the left) and lithospheric mantle thinning ( $\delta$  on the right) factors on a horizontal strain vs. time plot. Separating the thinning of the crust and lithospheric mantle helps to analyse the degree of lithospheric coupling during rifting evolution and, therefore its influence on the final basin architecture. Note that here I use a mixed definition of the lithosphere, considering lithosphere as thermal boundary layer for the part represent by the lithospheric mantle while a mechanical definition for the crust. The consequence of this is that if rifting stops (or is very low) the crust preserves the deformation acquired previously while the lithospheric mantle regains the thickness previously lost. In fact the LAB is able to rise or move downwards according to the efficiency of advection over diffusion. For very slow rifting or cooling, diffusion prevails (e.g. [England, 1983](#)).

According to result of the previous section I have chosen the slow monophasic rifting, where the stretching velocity was  $\frac{1}{2}v=0.05$  cm/yr ([Fig. 5.10a1 and a2](#)) while [Fig. 5.10b1 and b2](#) simulates the faster rifting with  $\frac{1}{2}v=1.5$  cm/yr. Those two velocities are found to be representative respectively of the first and second rifting phases characteristic for the modelling of the Sirte Basin, which is presented in [Fig. 5.10c1 and c2](#).

The colours in [Fig. 5.10a2](#) and [Fig. 5.10c2](#) are scaled to a maximum of  $\beta = \delta = 1.5$  while the colours in [Fig. 5.10b2](#) are scaled to a maximum of  $\beta = \delta = 1.2$ . This is to highlights the strong difference in thinning between the models. The plots on the top provide stretching factor values of the final rifting phases, giving the topography of the Moho (red line) and the LAB (blue line).

The monophasic models clearly show the control exerted by the boundary condition used to drive extension on the evolution of the basin. [Fig. 5.10a2](#) shows a short-lived extension with a final well-developed narrow basin ([Fig. 5.10a2](#) left), and a lithospheric mantle necking, with  $\beta_{\max} = \delta_{\max} > 22$ . This indicates a strong coupling between the two lithospheric layers. As indicated previously, I consider lithospheric breakup when the thinning factor are  $> 22$ . The lithospheric strain localization affects an area  $\sim 80$  km wide. The sides of this area are thinned at value of  $\beta = \delta \sim 1.02-1.05$ .

The opposite situation is shown in [Fig. 5.10 b1 and b2](#) where the deformation in the crust is very low for the first 20 Myr, gradually increased value of  $\beta \sim -1.1$  with two depocenters of respectively 1.3 and 1.2 with the formation of a wide basin. Interestingly, the lithospheric mantle does not show any evidence of deformation, due to the LAB remaining at rather constant depth during the slow rifting process, pointing out that diffusion in the thermal boundary layer is the predominant heat transfer mechanism in this model and that the lithospheric layers are completely decoupled.

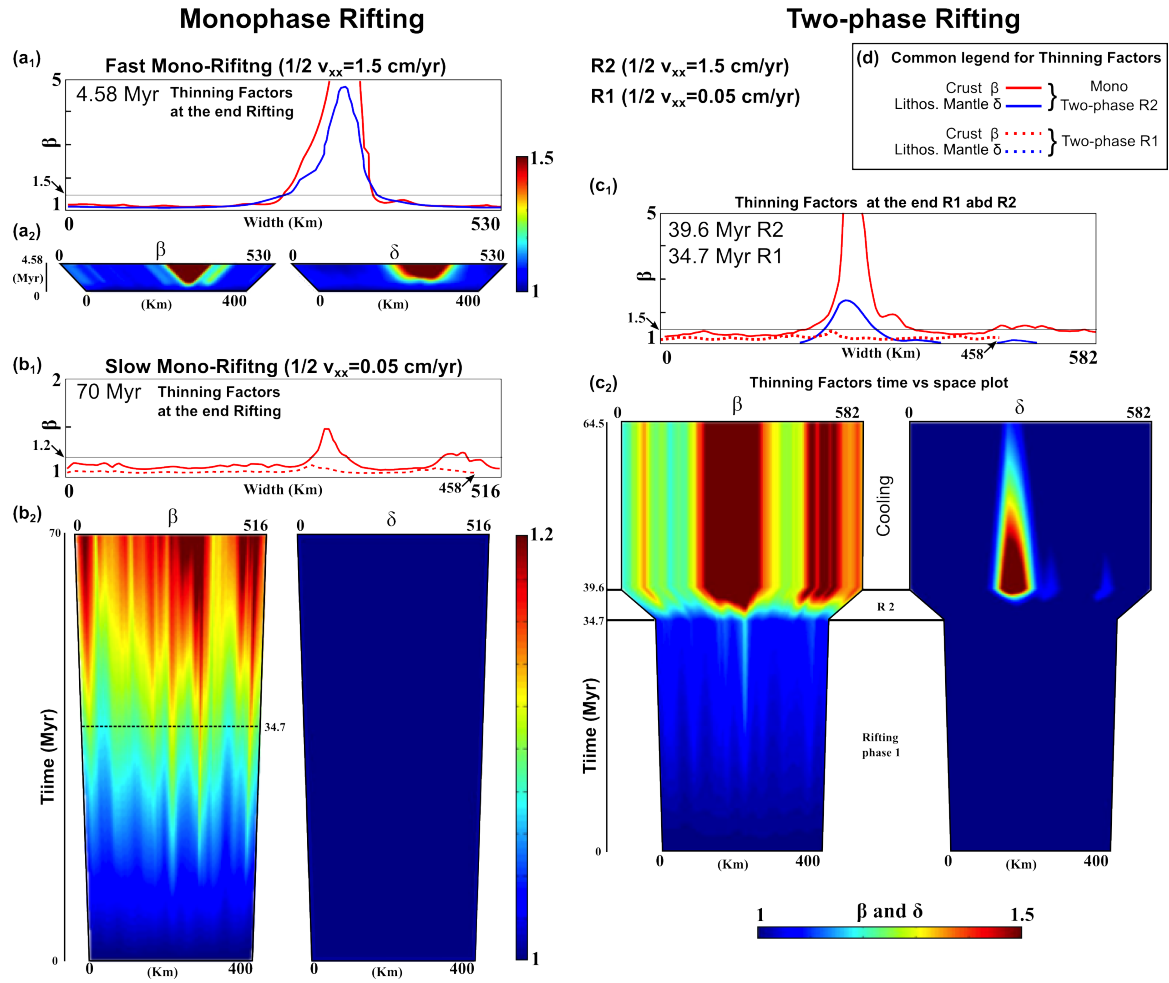


Figure 5.10 Thinning factors for crust,  $\beta$ , and lithospheric mantle,  $\delta$ , plotted at the end of the rifting (top panel,  $\beta$  red line and  $\delta$  blue line) and as function of time and horizontal size variation (bottom panels: left  $\beta$  and right  $\delta$ ). Monophase model end members: (a<sub>1</sub>) and (a<sub>2</sub>) thinning factors produced at large stretching velocity  $1/2 v = 1.5$  cm/yr while (b<sub>1</sub>) and (b<sub>2</sub>) same but with smaller  $1/2 v = 0.05$  cm/yr. (c<sub>1</sub>) and (c<sub>2</sub>) show two-phase rifting model representing Sirte basin rifting history realized with the same velocities of before:  $1/2 v = 0.05$  cm/yr for R1  $1/2$  and  $v = 1.5$  cm/yr for R2.

The model in Fig. 5.10 c<sub>1</sub> and c<sub>2</sub> represents the Sirte Basin evolution. Here, it is evident that the model starts as a wide rift with no coupling between crust and mantle and then, when the boundary condition changes from  $1/2 v = 0.05$  cm/yr to  $1/2 v = 1.5$  cm/yr, the switch between the two modes occurs. In fact, in the second rifting phase the thinning of the crust continues with larger thinning factors, yet always distributed over the model width (from 0-458 to 0-92 km) and a focalisation of the thinning in a small basin where the thinning reaches  $\beta > 5$ , while in the lithospheric mantle strain localised in a narrow area ( $\sim 60$  km), just below the crustal major depocenters. In this sense, the two layers start to couple. As shown before for the faster rift model, a high and local rise of the LAB

corresponds to a comparable rise of Moho, resembling the local high topography of the Moho beneath the Ajdabyia Trough (Fig. 5.3 bottom). As suggested in the literature (Fig. 5.4 and 5.6), this second phase is relatively short and therefore I stop the model after  $\sim 5$  Myr, continuing the deformation with a cooling stage. This is just for convenience of showing the effect of the reducing drastically the extension velocity. In fact the Fig. 5.4 shows a decrease of strain rate of 1 order of magnitude but still indicating an active stretching from 55 Myr to  $\sim 10$  Myr in some part of the Sirte Basin.

Fig. 5.10c1, c2 demonstrated how the variation of tensile forces can determine in the Sirte Basin a transition from diffuse to focused extension, and how the “footprint” of this evolution can be understood when considering the specific rift history of the basin, here a function of varying boundary conditions.

## 1. Discussion and Conclusion

The occurrence of transitions from a diffused to focused extension in many geological examples a model has been explained as the result of a rifting phase where either initial conditions, such as initial mantle/Moho temperature or initial perturbations are varied at the onset each rifting phase.

For example, Huerta and Larry (2007) explain the switch from wide to narrow rift only as the consequence of an initial upper mantle temperature of  $\sim 730 \pm 50$  °C beneath the rift and sufficient crustal heat production to account for 40– 50% of the mantle temperature. This was based on the case study of West Antarctica. Simulations with less heat from the crust, led to a cooler upper mantle and the rapid development of focused rifting at the edge of the model domain. Larger heat production in the crust, instead lead to high upper mantle temperatures and the lithosphere experiences a much longer diffuse extension stage with no evolution into a focused rift. Their work emphasizes that the extensional rate has a minimal or negligible role.

Similarly, a change in rifting mode was found by Huismans & Beaumont (2007) when they have simulated a first rifting with and initial weak lower crust and distributed crustal mechanical perturbation, followed by a second rifting phase where the lower crust was instead stronger, mimicking the effect of thermal cooling on the rheology. This model addresses the evolution of Iberia–Newfoundland conjugate margin system, although the causes that originate the viscous stiffening of the lower crust are not addresses, and a viscosity increase of a factor 100 is chosen.

More in general, the change in rheological response invoked by these authors is best



understood as the by-product of rheological properties and background strain rates. In fact, for strongly temperature- and strain rate-dependent dislocation creep rheology of the lithospheric mantle, the deformation mode is either defined by initial properties, such as rock type composition, or by time-dependent boundary conditions, such as the diffusion of heat (with re-equilibration of the temperatures) and the stretching rates, defining the background strain rates. Hence, a stiffening of the lithosphere and consequent mode switching from diffuse to localized, it is not unequivocally explained by either a change in more viscous lithological composition of lithosphere in between phases, or by varying temperature profile and/or background strain rates, from warm to cooler geotherms and/or increasing strain rates, respectively.

While it remains difficult to justify varying lithological compositions between rifting phases, we have proposed that mode switching is more realistically explained as the consequence of varying boundary conditions; in particular here we have addressed the varying stretching velocity.

Variations of stretching velocities during rifting are documented during the opening of the southern Atlantic ([Heine et al. 2013](#)), where the oceanic spreading rates provide constraints on the divergence along neighboring crustal domains, but are also a common feature of many rifts and rifted margins ([White, 1993, 1994](#); [White. N. & Bellingham P., 2002](#); [Bellingham P. & White. N., 2000](#)), where strain rates histories illustrate recurring stretching episodes of variable intensity.

In this work, we presented the case of a wide to narrow rift mode switch recorded in the geological evolution of the Sirte Basin. Here the change in boundary rifting forces is recorded in the subsidence history of Sirte Basin, occurring ~ 55 - 48 Ma as the abrupt change of recovered strain rates, of one order of magnitude, all along the N-S trending ~400 km long Ajdabyia Trough.

Lithospheric modelling here is implemented in a similar setup to the published work (e.g. [van Wijk and Cloetingh, 2002](#)), using the same initial rheological parameters, layering, temperature and no initial perturbations, and instead model the variation of boundary conditions, that is two-stage varying stretching velocity. These models show rifting mode switching with a rifting history similar to the Sirte Basin's.

When compared to previous modelling, our outcomes provide self-consistent and better explanation for the coexistence of the wide rift and the localised crustal thinning beneath the Ajdabyia Trough, supporting the idea that the transition in deformation mode is controlled by the variation of boundary conditions in time.



The implication of the work presented here are likely far reaching. In fact, the application of the uniform rifting model by [McKenzie \(1978\)](#) is limited to a single major subsidence phase. Here, we have shown that the Paleogene major rifting in the Sirte Basin, although providing useful insights in this phase ([van der Meer & Cloetingh 1993a, b](#)), cannot explain the larger structure of the basin, in fact, cannot explain the structure at all, and remains a purely 1D model. Similarly, models based on this approach (e.g. [Buck 1991](#), [Kusznier & Park, 1987](#); [van Wijk & Cloetingh, 2002](#); [England, 1993](#); [Chenin, P., & Beaumont, C. \(2013\)](#); [Gueydan et al., 2008](#) ) have reproduced fundamental features, such as the wide or narrow rift, however they cannot address many complexities found in the structures and the evolutions of the basins. Here, we have shown that a deeper understanding of the basin evolution and predictions on the overall structure can be achieved when the whole history is considered.

In the case presented here, modeling the Paleogene rifting as the result of a single rifting phase explains the narrow rifting and the subsidence during this phase. Instead, when a longer history is considered we can use a polyphase model to reproduce a similar structure, with wide-to-narrow strain distribution switch, and the longer subsidence history can be matched. In fact, the Cretaceous rifting phase in the Sirte Basin was protracted for ~30 Myrs, and resulted in minor subsidence, which is usually neglected in rifting modeling. Instead, we have showed that although minor subsidence is the consequence, the modification the lithosphere undergoes (i.e., geothermal gradients and deformation diffusion) constrains strongly the structure of the lithosphere at the inception of the following Paleogene major rifting. In other words, the previous rifting phase provides evidence of the initial conditions during the major rifting phase, which cannot be neglected, nor can be inferred unequivocally.

In conclusion, we have shown here that the lithospheric deformation history is of fundamental importance when modelling the rift basin evolution such as the Sirte Basin. Variations in tectonic boundary forces and resulting stretching rates, exert a dominant control on the deformation of lithospheric-scale rifted basin.

Tab. 5.1 Parameters and values used for the numerical modelling

Parameter	Abbreviation	Unit	Range
<b>Geometrical parameters</b>			
Upper Crust thickness	UC	km	15
Lower Crust thickness	LC	km	15
Lithospheric Mantle	LM	km	70
<b>Thermal parameters and variables</b>			
Thermal conductivity	k	$\text{Wm}^{-1} \text{K}^{-1}$	2.6
Thermal diffusivity	$\kappa$	$\text{m}^2 \text{s}^{-1}$	$10^{-6}$
Crust radioactive production	H	$\text{mW m}^{-3}$	0-1-2
Lithosphere-Asthenosphere Boundary	$T_{\text{LAB}}$	$^{\circ}\text{C}$	1300
Moho Temperature (Rifting onset)	$T_{\text{m}}$	$^{\circ}\text{C}$	400 - 850
Initial Moho Temperature Depth (Rifting onset)	----	Km	30
Thermal expansion	$\alpha$	$10^{-5} \text{K}^{-1}$	3
<b>Mechanical parameters and variables</b>			
<i>Byerlee law</i>			
Upper Crust density	$\rho_{\text{UC}}$	$\text{kg m}^{-3}$	2700
Lower Crust density	$\rho_{\text{LC}}$	$\text{kg m}^{-3}$	2900
Lithospheric Mantle density	$\rho_{\text{LM}}$	$\text{kg m}^{-3}$	3300
Cohesion	Co	MPa	60
Friction coefficient	$\mu$	Dimensionless	0.6
Initial strain rates	$\dot{\epsilon}_{\text{in}}$	$\text{s}^{-1}$	$10^{-18} - 10^{-12}$
Gravity Constant	$\vec{g}$	$\text{m s}^{-2}$	9.81
Extensional regime coefficient	---	Dimensionless	0.65
Deviatoric stress	$\tau$	MPa	Calculated
Lithostatic Pressure	P	MPa	Calculated
<i>Power law</i>			
	Abbreviation	Unit	Range
Universal Gas Constant	R	$\text{J(mol K)}^{-1}$	8.314
Viscosity	$\eta$	Pa s	Calculated
<b>Localization parameters and variables</b>			
Brittle thickness on YSE	$th_{\text{b}}$	km	Calculated
Localization index	I	Dimensionless	Calculated

Tab. 5.2

Rock name	Pre-exponent constant: A [MPa <sup>-n</sup> s <sup>-1</sup> ]	Exponent: n [Dimensionless]	Activation Energy [KJ mol <sup>-1</sup> ]	References
<u>Upper Crust</u> <b>Wet Quartzite</b>	A <sub>UC</sub> <b>1.1x10<sup>-4</sup></b>	n <sub>UC</sub> <b>4</b>	E <sub>UC</sub> <b>223</b>	Gleason and Tullis (1995)
<u>Lower Crust</u> <b>Columbia diabase (weak)</b>	A <sub>LC</sub> <b>190</b>	n <sub>LC</sub> <b>4.7</b>	E <sub>LC</sub> <b>485</b>	Mackwell et al. (1998)
<u>Lithospheric Mantle</u> <b>Dry Anita Bay dunite</b>	A <sub>LM</sub> <b>4.5</b>	n <sub>LM</sub> <b>3.6</b>	E <sub>LM</sub> <b>535</b>	Chopra and Paterson (1981)







## CHAPTER 6: CONCLUSIONS

### 1. Role of the lithospheric rifting history on continental extension

The surface expressions of the lithospheric stretching are characterised by strong differences showing variation of deformation style in time and space. The main differences can be synthesized as follows:

- Size of the basins and passive margins (e.g. very wide sedimentary basins (e.g. Basin and Range, Aegean Sea) and hyper-extended margins (Iberia–Newfoundland) or narrow rifts and short passive margins (e.g. Red Sea, North sea);
- Shift in time from wide to narrow rift mode (e.g. Sirte Basin);
- Symmetry (e.g. symmetric: Gulf of Suez, Gulf of Aden; asymmetric: East Africa Rift);
- Breakup (only crust with unroofing of the mantle in Iberia–Newfoundland or lithospheric breakup in Red Sea);
- Magma (e.g. volcanic and non-volcanic margins along the Atlantic);
- Subsidence patterns (e.g. mid Norwegian margin and Sirte Basin).

Therefore, the scientific question raised was: “How is the same geodynamic/physical process able to create so many different geological features? “

Trying to answer this question lead us to re-analyse the geological records and geophysical data available in the literature (i.e. [McKenzie, 1978](#); [Kusznier & Karner, 2007](#); [Abadi et al., 2008](#); [Reston, 2009, 2010](#); [Abdunaser & McCaffrey, 2015](#); [Allen & Armitage, 2012](#); [van der Meer & Cloetingh S., 1993a,b](#)) in order to find the common denominator of the majority of rifted basins and passive margins.

This appears to be the complex stretching history made of several rifting phases and often intermitted by cooling stages.

For example, the Mid-Norwegian margin subsidence curves indicate episodes of rifting with intervening tectonic quiescence periods, which clearly indicates a polyphase rifting, as well as a migration in the locus of the extension. In fact, subsidence ratio can vary greatly between stretching phases within the same basin. The subsidence can be very

low or high in the first phase, then may stop and/or restart with a similar, higher or lower ratio. In other cases, such as the Sirte Basin, the subsidence curve is characterized by abrupt changes in ratio between rifting phases.

Therefore the common characteristic of all many geological examples is the variation in space and time of deformation, so a variation of deformation history.

It is inferred that the differences in deformation history, in styles and symmetry, subsidence patterns and production of magma could be ascribed to the variation of magnitude in boundary conditions, thus to tectonic tensile forces. This hypothesis was previously formulated by [Capitanio et al., \(2009\)](#). Here, I have developed a conceptual model based on this hypothesis, tested it against general geological observations (narrow vs wide strain modes, symmetric vs asymmetric basins, variability of subsidence patterns and episodic occurrence of melting) and then applied it to the Sirte Basin, which evolution is characterised by the shift in time from wide to narrow mode.

## **2. Role of rifting history: assumptions to maintain the generality of the results**

The research project aimed to investigate the role of episodic stretching on the long-term evolution of continental rifts, by means of numerical modelling and to investigate the development of rifting patterns as a consequence of distinct phases of lithospheric extension under different stretching rates and intervening cooling. In order to have general insights on the rifting process, the effect of the variation of boundary conditions has been isolated, neglecting other processes such as sedimentation, melting and presence of pre-existing heterogeneities.

In this approach I neglect the effect of sediment loading and isostasy. This is a consequence of the aim to highlight the first-order role of stretching history on the rift configurations. These would affect the depth and the inner architecture of the basins (the basin style), yet would not impact the lithospheric rifting mode. However, in order to reconcile the results with the available body of work on basins, I do account for these by calculating the tectonic subsidence, i.e. net of sediment load, under the assumption of isostasy.

For the same reason I did not account for the melting in the numerical calculation but calculated the potential melting in post processing. This was done also because the aim of the project was to highlight the relative difference in melting production induced by



variation of the rifting history, and not to study specifically the change in mechanics of the lithosphere due to melting effect. However, I recognise that the melt feeds back into mechanics having effects of localization (e.g. most faults weaken by creating gouge, clay, and mylonite zones and are favoured by melting processes), and that acting the melting zone can act as conduits for diking in volcanic margins (e.g. Afar rift).

The numerical domain used here mimics a pristine lithosphere, where initial perturbations are absent. This opposes to common practice in lithosphere numerical modelling, where a single or a series of perturbation are introduced in the model. While introducing a perturbation helps localization and allows to avoid border effects (e.g. localization at near numerical domain sides), I have tested that it favours necking of the of the lithosphere and narrow rift mode for very low velocities. Consequently, a non-perturbed lithosphere was chosen to allow for a wide range of deformation modes, therefore ensuring the generality of the results. Nevertheless, the localization in numerical homogenous materials can be possible due to the numerical approximations, which introduce numerical heterogeneities ([Peters et al., 2015](#)).

The boundary conditions driving the lithospheric extension used in the modelling were represented by horizontal velocities applied at both domain sides. Only varying the horizontal velocities created the different rifting histories. I have used a rift-cooling-rift cycle at the end of which the horizontal strain was the same for all the simulations; this was done in order to compare the models. To ensure the generality (isolate the solely effect of the rifting history), the lithosphere was defined as thermal boundary layer, which was allowed to recover the original thickness (at net of tectonic subsidence) at the end of the cooling stage. Since, the thinning achieved in the first rifting phase is function of the stretching velocity used to extend the lithosphere, the cooling time needed to recover the original lithospheric thickness is shorter in cases of first slow rifting events and larger for cases of first fast rifting events. This created different initial conditions for the onset of the second rifting event compared to the initial ones, which are function of previous history. They are, therefore, the interplay of boundary conditions used in first rift event and the cooling generate inherited conditions for the subsequent rifting, this are represented by a similar lithospheric thickness of the initial one (minus tectonic subsidence) but with a different rheological layering (e.g. [Fig. 3.12](#), [Fig. 4.2](#)), a re-equilibrated temperature profile bringing a lower Moho temperature and distributed/

localised heterogeneities (e.g. [Fig. 4.3](#))

The modelling approach assumed for this thesis is different from the classical one in which the rifting is simulated through a single phase or monophase ([McKenzie, 1978](#)). In fact, the monophase approach requires strongly different initial conditions in the lithosphere to be able to reproduce the differences found between the rift basins. For example, wide and narrow rifts are reproduced using different:

- Initial crustal thickness (e.g. [Buck, 1991](#));
- Initial Moho temperature (e.g. [Gueydan et al. 2008](#));
- Initial weak/strong lower crust (e.g. [Huismans & Beaumont, 2007](#));
- Initial diffused or concentrated heterogeneities (e.g. [Staples et al 2015](#)).

Few attempts of modelling the rifting as a polyphase process are found in literature ([Van Wees et al., 1998](#); [Armitage et al. , 2010](#); [Huismans & Beaumont, 2007](#); [Tett & Sawyer, 1996](#); [Naliboff & Buiter, 2015](#)). All of them are constrained by statistical observations in particular geological areas. Only [Naliboff & Buiter \(2015\)](#) have attempted a more general approach towards the problem giving an important contribution towards the understanding of the reactivation and migration of the rifting. However, they have used a specific range of cooling times (30-40 Myr), an initial perturbations and a restricted number of extensional velocities (2, 1 and 0.5 cm/yr). Therefore, their study is focused on a limit number of rifting histories.

For all the reasons above, the approach used in this thesis work can be considered unusual and, as such, it needed to comply with the scientific method procedures. On the basis of the problem and the work hypothesis presented in Chapter 2, a 1D conceptual model of polyphase lithospheric stretching has been realised and validated in Chapter 3. Chapter 3 also provided the validation of the numerical model set up used to perform the polyphase rifting in the last two chapters. Chapter 4 and 5 illustrate respectively the general results of the physics of the polyphase process in 2D and its application to a geological case (Sirte Basin).

### 3. Significance of the study

This study was conducted in 2D, finding this model setup appropriate to test in first approximation the role of different rifting histories on the same pristine lithosphere, and the effects on the resulting lithospheric strain mode. Here, it has been found that rifting histories feedback into basin style, subsidence patterns and magma production. Therefore, the results indicate that the approach used here could help to explain several complexities such as basin asymmetry or anomalous subsidence present in many extensional areas. Nevertheless, I recognise that there are many other features' variations parallel to the rift axis that require a three dimensional approach to be explained. Such variations along-strike can be basin depocenter's migration (e.g. along mid-Norwegian Margin), or magmatic deposits occurrence (e.g. along passive margins of North and South Atlantic) or basin width (e.g. variations of the width perpendicular to the extension direction in North China Craton).

The models presented in this work illustrated that the rifting histories are primarily controlled by the variation of the conditions driving the stretching (spreading velocities for the present study). In particular, rifting histories result from the interplay of the initial (temperature, layering, rheological parameters), boundary conditions (tectonic divergent forces or spreading velocities) applied to the system and inherited conditions (i.e. heterogeneities at Moho), self-developed between rifting events (e.g. [Fig. 3.2](#), [Fig. 4.3](#)).

Most importantly, with this study it was possible to identify when it is important to consider the previous lithospheric rifting history in modelling the evolution of the sedimentary basins. In fact, the results of numerical modelling help illustrating that the observed features of rifts might be strongly dependent on its long-term evolution. Diverse rifting patterns develop as a consequence of distinct phases of lithospheric extension under different stretching rates and intervening cooling. Alternative fast and slow stretching phases, intervened by cooling, lead to similar initial conditions (e.g. same horizontal strain in this study), then basins develop different rifting modes, according to their full history. The results show that fast stretching phases lead to narrow rifts, which are, in fact, the only ones found to be less sensitive to the rifting history (e.g. Red Sea, Rhine Graben, North Sea) ([Fig. 4.7](#), [Fig. 4.10](#), end member [Fig. 4.2f](#), [Fig. 4.3d](#)). Almost any other basin (i.e. asymmetric and symmetric wide basins and basins on hyper-thinned crust) is strongly affected by the prior rifting episodes of single basins ([Fig. 4.7](#), [Fig. 4.10](#) end members [Fig. 4.2c,d](#), [Fig. 4.3a,b](#)). When slow rifting phases are repeated, wide

asymmetric rift are the result (e.g. West Antarctic Rift Basin). Instead, slowly-stretching wide rifts tend to become increasingly symmetric as the stretching rates during the second phase become increasingly faster, thus progressively localising along the inherited heterogeneities (Fig. 4.7, Fig. 4.10 end member Fig. 4.2d, Fig. 4.3b). Strong localisation occurs under slow stretching when the rift underwent previously fast phase, thus a strong localised thinning of the crust above a lithospheric mantle develops, much like hyper-thinned crustal basins (e.g. Iberia Margin) (Fig. 4.7, Fig. 4.10, end member Fig. 4.2e, Fig. 4.3c). Previous rifting, under a variety of conditions, consistently enhances localisation in subsequent rifting phases. This has a profound impact on the subsidence and melting histories of basins (Fig. 4.4 and Fig. 4.5, Fig 4.6). When compared to the subsidence recovered on a single-rifting basin, multi-event rift subsidence rates are affected in duration and amount, thus potentially impacting the recovered strain rates and interpretation of natural cases. Similarly melting volumes of single rift basins, might underestimate melting volumes by a factor  $\sim 10$  to  $\sim 30$  when compared to rifts with complex histories. Albeit simplified, the analysis conducted here provides an attempt to reduce the complexities of the diverse natural rift basins into a general understanding, which might be of support of future studies and interpretation of rift evolutions.

In summary, this approach used in this theses of modelling the lithospheric stretching as a polyphase series of rifting and cooling events, has given additional insight into the physics of this important geodynamic process.

The outcomes of this thesis are the following:

- It provides a new general analytical framework, able to support the interpretation of the differences found in continual rift basins and passive margins;
- It demonstrates that numerical modelling of stretching evolution supports the interpretation of more complex basin evolutions;
- It demonstrates the first order role played by changing in boundary conditions that results in the variation of deformation history;
- It provides a method for interpreting the deformation of the deeper portion of the lithosphere from basin characteristics.

In conclusion, the variations of tectonic boundary forces and the resulting stretching rates, exert a dominant control on the deformation of lithospheric-scale rifted basin. Consequently, it is important to consider the rifting history when modelling the lithospheric stretching and basin evolution as this allows reconciling rifting deformational modes with:

- Different basin style;
- Complex subsidence patterns;
- Type of breakup (crust or lithosphere), and
- Episodic occurrence of melting production.

#### **4. Future work**

In order to isolate the effect of the variation of boundary conditions and, therefore, of the rifting histories, it was necessary to make several assumptions not considering into numerical computation important processes that affect the mechanics of the lithosphere.

In the present work the effect of the strain-induced weakening has also not been addressed. I recognise that it is an important process for localising deformation (either in the frictional-plastic or viscous domain, or both – see section 4.2.3.2.5) and it is used in many models to replicate natural phenomena linked to a reduction of the cohesion (e.g. [Huisman & Beaumont, 2002, 2007](#)), or grain size transformation/reduction with accumulated strain (e.g. [Gueydan, et al., 2014](#)). The reason behind this choice is that strain-induced weakening increases considerably the number of parameters to explore, which is outside the aim of the simple and generic models such as those presented here.

For the same reason here sedimentation and melting are not included in the numerical model.

I have also considered homogenous layers and no pre-existing perturbations in the lithosphere, i.e. no weak/strong seeds or thermal anomalies are introduced ([Fernandez and Ranalli, 1997](#)). Despite being commonly used in numerical modelling ([Peters et al., 2015](#)), and references therein) these heterogeneities can constrain the range of lithospheric deformation, favouring the lithospheric necking and localised strain. Although we have performed relevant resolution tests, I am aware that strain localisation of numerical homogenous materials might be affected by the consequences of numerical approximations, introducing numerical heterogeneities ([Peters et al., 2015](#)). Although this

is out of the scope of this paper, the inferences on strain localisation vs. diffusion remains valid, as localisation simply occurs at a larger strain/strain rate, with same features (e.g. [Schmeling, 2010](#)). Hence, in this paper we refer to “diffuse” and “localised” deformation meaning the weakly and strongly localised deformation. The absence of initial perturbations in the model setup was adopted by [Crameri and Kaus \(2010\)](#), since they have considered that lithospheric localisation is regulated by the thickness of the plastic field.

Nevertheless, the effects of strain-induced weakening, melting, sedimentation and effect of pre-existing heterogeneities together with the variation of rifting history, will be studied in the upcoming work, with the goal to deliver the results in future publications.

The immediate step is to extend this approach to the 3D and use it to interpret the evolution of the Red Sea, where the effect of variation of boundary conditions (e.g. [Almalki et al., 2014](#)) will be studied together with plate rotations and influence of the Afar plume (e.g. [McClusky et al., 2010](#)).







## REFERENCES

- Abadi, A.M., van Wees, J.D., van Dijk, P.M., Cloetingh, S.A.P.L., 2008. Tectonics and subsidence evolution of the Sirt Basin, Libya. *Am. Ass. Petrol. Geol. Bulletin* 92, 993–1027.
- Abadi, A.M., 2002. Tectonics of the Sirt basin. Inferences from tectonic subsidence analysis, stress inversion and gravity modeling. PhD thesis, Vrije University, Amsterdam, the Netherlands, 187 pp.
- Abdunaser K.M. McCaffrey J.W. Tectonic history and structural development of the Zallah-Dur al Abd Sub-basin, western Sirt Basin, Libya. *Journal of Structural Geology* 73 (2015) 33e48
- Ade-Hall, J. M., P. H. Reynolds, P. Dagley, A. E. Musette, T. P. Hubbard, and E. Klitzsch, 1974, Geophysical studies of north Africa Cenozoic volcanic areas: I. Hrauj Assuad Libya: *Canadian Journal of Earth Science*, v. 11, p. 998– 1006.
- Ade-Hall, J. M., and P. H. Reynolds, 1975, Geophysical studies of north Africa Cenozoic volcanic areas: II. Jabal Soda, Libya: *Canadian Journal of Earth Science*, v. 12, p. 1257–1263.
- Ahlbrandt, T.S., 2001. The Sirte Basin province of Libya–Sirte-Zelton total petroleum system. *U.S. Geol. Surv. Bull.*, 29, 2202-F.
- Allen P.A. & Allen R.J. (2005). *Basin Analysis: Principles and Application*, 2nd Edition, 549 pages, Blackwell Publishing.
- Allen P.A. & Allen R.J. (2013). *Basin Analysis: Principles and Application to Petroleum Play Assessment*, 3rd Edition, 642 pages, Wiley-Blackwell.
- Allen PA, Armitage JJ, 2012, *Cratonic Basins, Tectonics of Sedimentary Basins: Recent Advances*, Pages: 602-620, ISBN: 9781405194655
- Allen1 P. A., Eriksson P. G., Alkmim F. F., Betts P. G., Catuneanu O., Mazumder R., Meng Q. & Young G. M. (2015) Classification of basins, with special reference to Proterozoic examples. R. & Eriksson, P. G. (eds) 2015. *Precambrian Basins of India: Stratigraphic and Tectonic Context*. Geological Society, London, *Memoirs*, 43, 5–28, <http://dx.doi.org/10.1144/M43.2>
- Ali, M.Y. & Watts, A.B. (2013) Subsidence history, crustal structure, and evolution of the Somaliland-Yemen conjugate margin. *J. Geophys. Res.*, 118, 1–12.
- Allken, V., Huismans, R. S., Fossen, H., & Thieulot, C. (2013). 3D numerical modelling of graben interaction and linkage: a case study of the Canyonlands grabens, Utah. *Basin Research*, 25(4), 436–449. doi:10.1111/bre.12010
- Allken, V., Huismans, R. S., & Thieulot, C. (2011). Three-dimensional numerical modeling of upper crustal extensional systems. *Journal of Geophysical Research*, 116(B10), B10409. doi:10.1029/2011JB008319

- Allken, V., Huismans, R. S., & Thieulot, C. (2012). Factors controlling the mode of rift interaction in brittle-ductile coupled systems: A 3D numerical study. *Geochemistry Geophysics Geosystems*, 13(5), Q05010. doi:10.1029/2012GC004077
- Almalki, K. a., Betts, P. G., & Ailleres, L. (2014). Episodic sea-floor spreading in the Southern Red Sea. *Tectonophysics*, 617, 140–149. doi:10.1016/j.tecto.2014.01.030
- Ambrose, G., 2000. The geology and hydrocarbon habitat of the Sarir Sandstone, SE Sirt Basin, Libya. *J. Pet. Geol.* 23, 165e191.
- Argus, D. F., & Hefin, M. B. (1995). Plate motion and crustal deformation estimated with geodetic data from the Global Positioning System,. *Geophys. Res. Lett.*, 22.
- Anketell, J.M., 1996, Structural history of the Sirt Basin and its relationship to the Sabratah Basin and Cyrenaican Platform, northern Libya, in M. J. Salem, M. T. Busrewil, A. A. Misallati, and M. A. Sola, eds., *The geology of the Sirt Basin*: Amsterdam, Elsevier, v. 3. p. 57–87.
- Armitage, J. J., & Allen, P. a. (2010). Cratonic basins and the long-term subsidence history of continental interiors. *Journal of the Geological Society*, 167(1), 61–70. doi:10.1144/0016-76492009-108
- Armitage, J. J., Collier, J. S., & Minshull, T. a. (2010). The importance of rift history for volcanic margin formation. *Nature*, 465(7300), 913–7. doi:10.1038/nature09063
- Artemieva, I. M. (2006). Global 1°×1° thermal model TC1 for the continental lithosphere: Implications for lithosphere secular evolution. *Tectonophysics*, 416(1-4), 245–277. doi:10.1016/j.tecto.2005.11.022
- Artemieva, I. M. (2009). The continental lithosphere: Reconciling thermal, seismic, and petrologic data. *Lithos*, 109(1-2), 23–46. doi:10.1016/j.lithos.2008.09.015
- Artemieva I. (2009) *The Lithosphere An Interdisciplinary Approach*. Cambridge University Press.794
- Artemieva, I. M., & Meissner, R. (2012). Crustal thickness controlled by plate tectonics: A review of crust–mantle interaction processes illustrated by European examples. *Tectonophysics*, 530-531, 18–49. doi:10.1016/j.tecto.2011.12.037
- Artemjev M.E., Artyushkov E.V. (1971): Structure and isostasy of the Baikal rift and the mechanism of rifting. *Journal of Geophysical Research*. 76:1197-1211.
- Artyushkov, E. V. (2007). Formation of the superdeep South Caspian basin: subsidence driven by phase change in continental crust. *Russ. Geol. Geophys.*, 48, 1002–1014.
- Aslanian, D., & Moulin, M. (2010). Comment on “A new scheme for the opening of the South Atlantic Ocean and the dissection of an Aptian salt basin” by Trond H. Torsvik, Sonia Rousse, Cinthia Labails and Mark A. Smethurst. *Geophysical Journal International*, 183(1), 20–28. doi:10.1111/j.1365-246X.2010.04727.x

- Aslanian, D., Moulin, M., & et al. (2009). Brazilian and African passive margins of the Central Segment of the South Atlantic Ocean: Kinematic constraints. *Tectonophysics*, 468((1-4)), 98–112.
- Axen, G.J. & Bartley, J.M. (1997) Field test of rolling hinges: existence, mechanical types, and implications for extensional tectonics. *J. geophys. Res.* 102, 20515–37.
- Baldwin, S., White, N., & Müller, R. D. (2006). CHAPTER 17 — Resolving multiple rift phases by strain-rate inversion in the Petrel Sub-basin , northwest Australia, Geological Society of Australia Special Publication 22, 239–257.
- Baker, B.H., Mohr, P.A. and Williams, L.A.J. (1972) Geology of the Eastern Rift System of Africa. Special Paper Geological Society of America, 136
- Bellingham P. & White N. (2000). A general inverse method for modelling extensional sedimentary basins. *Basin Research* (2000) 12, 219–226
- Bassi, G., Keen, C. E., & Potter, P. (1993). Contrasting styles of rifting: Models and examples from the Eastern Canadian Margin. *Tectonics*, 12(3), 639–655. doi:10.1029/93TC00197
- Bassi, G.. 1991. Factors controlling the style of continental rifting: insights from numerical modelling. *Earth planet. Sci. Lett.*, 105, 430-452.
- Bassi, G., (1995) Relative importance of strain rate and rheology for the mode of continental extension. *Geophys. J. Int.* (IYY) 122, 1Y5-210
- Behn, M. D., Lin, J., & Zuber, M. T. (2002). A continuum mechanics model for normal faulting using a strain-rate softening rheology: implications for thermal and rheological controls on continental and oceanic rifting. *Earth and Planetary Science Letters*, 202(3-4), 725–740. doi:10.1016/S0012-821X(02)00792-6
- Bell, R. E., Jackson, C. a.-L., Whipp, P. S., & Clements, B. (2014). Strain migration during multiphase extension: Observations from the northern North Sea. *Tectonics*, n/a–n/a. doi:10.1002/2014TC003551
- Bellingham, P., & White, N. (2000). A general inverse method for modelling extensional sedimentary basins. *Basin Research*, 12(3-4), 219–226. doi:10.1046/j.1365-2117.2000.00122.x
- Bercovici, D., 1996. Plate generation in a simple model of lithosphere–mantle flow with dynamic self-lubrication. *Earth Planet. Sci. Lett.* 144, 41–51.
- Bercovici, D., Ricard, Y., Schubert, G., (2001a). A two-phase model for compaction and damage: 1. General theory. *J. Geophys. Res.* 106, 8887–8906.
- Bercovici, D., Ricard, Y., Schubert, G., (2001b). A two-phase model for compaction and damage: 3. Applications to shear localization and plate boundary formation. *J. Geophys. Res.* 106, 8925–8939.
- Birt, C. S., Maguire, P. K. H., Khan, M. A., Thybo, H., Keller, G. R., & Patel, J. (1997). The influence of pre-existing structures on the evolution of the southern Kenya

- Rift Valley—evidence from seismic and gravity studies. *Tectonophysics*, 278(1-4), 211–242.
- Biju-Duval, B., J. Letouzey, and L. Montadert, 1977, Structure and evolution of the Mediterranean Sea basin, in *Initial Reports of the Deep Sea Drilling Project*: Washington, U.S. Government Printing Office, v. 42, p. 951–984.
- Bonatti, E., 1985. Punctiform initiation of seafloor spreading in the Red Sea during transition from a continental to an oceanic rift. *Nature* 316, 33–37.
- Bond, G.C., 1991, Disentangling Middle Paleozoic sea level and tectonic events in cratonic margins and cratonic basins of North America: *Journal of Geophysical Research*, v. 96, no. B4, p. 6619–6639, doi: 10.1029/90JB01432.
- Bond, G.C., and Kominz, M.A., 1984, Construction of tectonic subsidence curves for the early Paleozoic miogeocline southern Canadian Rocky Mountains: Implications for subsidence mechanisms, age of breakup, and crustal thinning: *Geological Society of America Bulletin*, v. 95, p. 155–173, doi: 10.1130/0016-7606(1984)95<155:COTSCF>2.0.CO;2.
- Bott, M.H.P., Kusznir, N.J., 1979. Stress distribution associated with compensated plateau uplift structures with application to the continental splitting mechanism. *Geophys. J. R. Astron. Soc.* 56, 451–459.
- Bos B and Spiers CJ (2002) Frictional-viscous flow in phyllosilicate-bearing fault rock: Microphysical model and implications for crustal strength profiles. *Journal of Geophysical Research* 107(B2): 2028 (doi:10.1029/ 2001JB000301). Bosworth, W. (1985). Geometry of propagating continental rifts. *Letter of Nature*, 316(15).
- Brace WF and Kohlstedt DL (1980) Limits on lithospheric stress imposed by laboratory experiments. *Journal of Geophysical Research* 85: 6248–6252.
- Braile, L.W., Hinze, W.J., Keller, G.R., Lidiak, E.G., and Sexton, J.L. (1986) Tectonic development of the New Madrid Rift Complex, Mississippi Embayment, North America. *Tectonophysics*, 131, 1–21.
- Braun J. & Beaumont C. (1987). Styles of continental rifting: results from dynamical models of lithospheric extension. In: Beaumont C. & Tankard A.J. (Eds) *Sedimentary Basins and Basin-forming Mechanisms*. Canadian Society of Petroleum Geologists, 241 – 258
- Braun J., Beaumont C. (1989): A physical explanation of the relation between flank uplifts and the breakup unconformity at rifted continental margins. *Geology*. 17: 760-764.
- Braun, J., Chery, J., Poliakov, A., Mainprice, D., Vauchez, A., Tommasi, A., Daignieres, M., 1999. A simple parameterization of strain localization in the ductile regime due to grain size reduction: a case study for olivine. *J. Geophys. Res.* 104, 25167–25181.
- Baird, W. D., R. M. Aburawi, and J. N. Bailey, 1996, Geohistory and petroleum in the central Sirt Basin, in M. J. Salem, M. T. Busrewil, A. A. Misallati, and M. A. Sola, eds., *The geology of the Sirt Basin*: Amsterdam, Elsevier, v. 3, p. 3–56.

- Brekke, H. (2000). The tectonic evolution of the Norwegian sea continental margin with emphasis on the Vøring and Møre Basins. Geological Society, London, Special Publications, 167, 327–378.
- Bruce K. (1976) Development of graben associated with the initial ruptures of the Atlantic ocean. *Tectonophysics* Volume 36, Issues 1–3, 24 November 1976, Pages 93–112
- Burke, K., and J. Dewey, 1974, Two plates in Africa during the Cretaceous?: *Nature*, v. 249, p. 313–316.
- Brun, J.-P. & Choukroune, P. 1983 Normal faulting, block tilting and decollement in a stretched crust. *Tectonics* 2, 345–356
- Brun, J. P. (1999). Narrow rifts versus wide rifts: inferences for the mechanics of rifting from laboratory experiments. *Philosophical Transactions of the Royal Society A: Mathematical, Physical and Engineering Sciences*, 357(1753).
- Brun, J.-P. (2002). Deformation of the continental lithosphere: Insights from brittle-ductile models. Geological Society, London, Special Publications, 200(1), 355–370. doi:10.1144/GSL.SP.2001.200.01.20
- Brune, S.; Popov, A. A.; Sobolev, S. V. (2012): Modeling suggests that oblique extension facilitates rifting and continental break-up. *Journal of Geophysical Research*, 117, B08402. doi:10.1029/2011JB008860.
- Brune, S.; Autin, J. (2013): The rift to break-up evolution of the Gulf of Aden: Insights from 3D numerical lithospheric-scale modelling. *Tectonophysics*, 607, 65–79. doi:10.1016/j.tecto.2013.06.029.
- Brune, S., Heine, C., Perez-Gussinye, M., Sobolev, S.V. (2014): Rift migration explains continental margin asymmetry and crustal hyper-extension. *Nature Communications*, 5, 4014. doi:10.1038/ncomms5014.
- Brune, S., Popov, A. a., & Sobolev, S. V. (2012). Modeling suggests that oblique extension facilitates rifting and continental break-up. *Journal of Geophysical Research*, 117(B8), B08402. doi:10.1029/2011JB008860
- Buck WR (1991) Modes of continental lithospheric extension. *Journal of Geophysical Research*, B, Solid Earth and Planets 96(12): 20161–20178.
- Buck WR (1993) Effect of lithospheric thickness on the formation of high-and low-angle normal faults. *Geology* 21: 933–936.
- Buck WR (2004) Consequences of the asthenospheric variability on continental rifting. In: Karner GD, Taylor B, Driscoll NW, and Kohlstedt DL (eds.) *Rheology and Deformation of the Lithosphere at Continental Margins*, pp. 1–31. New York: Columbia University Press.
- Buck WR, Martinez F, Steckler MS, and Cochran JR (1988) Thermal consequences of lithospheric extension: Pure and simple. *Tectonics* 7: 213–234
- Buck, W.R., Lavier, L.L. & Poliakov, A.N.B. (1999) How to make a rift wide. *Phil. Trans. Roy. Soc. Lond. A* 357, 671–93.

- Buck WR, Lavier LL, and Babeyko A (2003) A numerical model of lithospheric extension producing fault bounded basins and ranges. *International Geology Review* 45(8): 712–723. Buck WR, Lavier LL, and Poliakov AN (2005) Modes of faulting at mid-ocean ridges. *Nature* 434: 719–723.
- Buiter, S.J.H., A.Yu. Babeyko, S. Ellis, T. V. Gerya, B. J.P. Kaus, A. Kellner, G. Schreurs, Y. Yamada, 2006, *The Numerical Sandbox: Comparison of Model Results for a Shortening and an Extension Experiment, Analogue and Numerical Modelling of Crustal-Scale Processes*, Geological Society, London, Special Publication 253, 29-64 Buiter, S. J. H., Huisman, R. S., & Beaumont, C. (2008). Dissipation analysis as a guide to mode selection during crustal extension and implications for the styles of sedimentary basins. *Journal of Geophysical Research*, 113(B6), B06406. doi:10.1029/2007JB005272
- Burov, E., Jaupart, C., & Mareschal, J. C. (1998). Large-scale crustal heterogeneities and lithospheric strength in cratons. *Earth and Planetary Science Letters*, 164(1-2), 205–219. doi:10.1016/S0012-821X(98)00205-2
- Burov, E., & Poliakov, a. (2001). Erosion and rheology controls on synrift and postrift evolution: Verifying old and new ideas using a fully coupled numerical model. *Journal of Geophysical Research*, 106(B8), 16461. doi:10.1029/2001JB000433
- Burov, E. B., and A. B. Watts (2006), The long-term strength of continental lithosphere: "jelly-sandwich" or "creme-brulee"? *GSA Today*, 16, 4–10.
- Burov, E.B., (2007). Plate rheology and mechanics, Ed.: G. Schubert, *Treatise on Geophysics*, Volume 6 – Crust and Lithosphere Dynamics (Volume Edt. A.B. Watts), Elsevier, TOGP00102, ISBN:978-0-444-51928-3, p 99-152, 611 pp.
- Burov, E. (2011), Rheology and strength of the lithosphere, *Mar. Pet. Geol.*, 28 (8), 1402–1443.
- Byerlee JD (1978) Friction of rocks. *Pure and Applied Geophysics* 116: 615–626.
- Bryan, Scott Edward, Cook, Alex, Allen, Charlotte M., Siegel, Coralie, Purdy, David, Greentree, James, & Uysal, Tonguc (2012) Early-mid Cretaceous tectonic evolution of eastern Gondwana : from silicic LIP magmatism to continental rupture. *Episodes*, 35(1), pp. 142-152.
- Capitanio, F. a, Faccenna, C., Zlotnik, S., & Stegman, D. R. (2011). Subduction dynamics and the origin of Andean orogeny and the Bolivian orocline. *Nature*, 480(7375), 83–6. doi:10.1038/nature10596
- Capitanio, F. a. (2013). Lithospheric-age control on the migrations of oceanic convergent margins. *Tectonophysics*, 593, 193–200. doi:10.1016/j.tecto.2013.03.003
- Capitanio, F. a. (2014). The dynamics of extrusion tectonics: Insights from numerical modeling. *Tectonics*, n/a–n/a. doi:10.1002/2014TC003688
- Capitanio, F. A., Faccenna, C., & Funicello, R. (2009). Supplement to The opening of Sirte Basin: Result of slab avalanching? *Earth and Planetary Science Letters*, 285, 1–3.

- Capitanio, F. a., Faccenna, C., & Funiciello, R. (2009). The opening of Sirte basin: Result of slab avalanching? *Earth and Planetary Science Letters*, 285(1-2), 210–216. doi:10.1016/j.epsl.2009.06.019
- Capitanio, F. a., & Replumaz, A. (2013). Subduction and slab breakoff controls on Asian indentation tectonics and Himalayan western syntaxis formation. *Geochemistry, Geophysics, Geosystems*, 14(9), 3515–3531. doi:10.1002/ggge.20171
- Cavazza, W. M., F.M. Roure, W. Spakman, G. M. Stampfli, and P. A. Ziegler, 2004. *The transmed atlas*: Berlin, Springer, 141 p.
- Chen, L. (2014). Stretching factor estimation for the long-duration and multi-stage continental extensional tectonics: Application to the Baiyun Sag in the northern margin of the South China Sea. *Tectonophysics*, 611, 167–180. doi:10.1016/j.tecto.2013.11.026
- Chenin, P., & Beaumont, C. (2013). Influence of offset weak zones on the development of rift basins: Activation and abandonment during continental extension and breakup. *Journal of Geophysical Research: Solid Earth*, 118(4), 1698–1720. doi:10.1002/jgrb.50138
- Chopra PN and Paterson MS (1981) The experimental deformation of dunite. *Tectonophysics* 78: 453–473.
- Chopra PN and Paterson MS (1984) The role of water in the deformation of dunite. *Journal of Geophysical Research* 89: 7861–7876.
- Christensen, U. R. (1992). An Eulerian technique for thermomechanical modeling of lithospheric extension. *Journal of Geophysical Research: Solid Earth*, 97(B2), 2015–2036. doi:10.1029/91JB02642
- Chester FM (1995) A rheologic model for wet crust applied to strike-slip faults. *Journal of Geophysical Research* 100(B7): 13033–13044.
- Clift, P., & Lin, J. (2001). Preferential mantle lithospheric extension under the South China margin. *Marine and Petroleum Geology*, 18(8), 929–945. doi:10.1016/S0264-8172(01)00037-X
- Clifton, A.E., Schlische, R.W., Withjack, M.O., Ackermann, R.V., 2000. Influence of rift obliquity on fault-population systematics: results of experimental clay models. *Journal of Structural Geology* 22, 1491–1509.
- Cloetingh, S., van Wees, J. D., van der Beek, P. a., & Spadini, G. (1995). Role of pre-rift rheology in kinematics of extensional basin formation: constraints from thermomechanical models of Mediterranean and intracratonic basins. *Marine and Petroleum Geology*, 12(8), 793–807. doi:10.1016/0264-8172(95)98848-Y
- Cloetingh, S., E. Burov, and A. A. Poliakov, 1999, Lithosphere folding: Primary response to compression? (from central Asia to Paris Basin): *Tectonics*, v. 18, p. 1064–1083.

- Cloetingh, S., Ziegler, P., Beekman, F., Andriessen, P., Matenco, L., Bada, G., ... Sokoutis, D. (2005). Lithospheric memory, state of stress and rheology: neotectonic controls on Europe's intraplate continental topography. *Quaternary Science Reviews*, 24(3-4), 241–304. doi:10.1016/j.quascirev.2004.06.015
- Cloetingh, S., and J. D. Van Wees, 2005, Strength reversal in Europe's intraplate lithosphere: Transition from basin inversion to lithospheric folding: *Geology*, v. 33, no. 4, p. 285–288.
- Conant, L.C., Goudarzi, G.H., 1967. Stratigraphic and tectonic framework of Libya. *Bull. Am. Assoc. Pet. Geol.* 51, 719–730.
- Corti, G. (2003). Transition from continental break-up to punctiform seafloor spreading: How fast, symmetric and magmatic. *Geophysical Research Letters*, 30(12), 1604. doi:10.1029/2003GL017374
- Corti, G. (2012). Evolution and characteristics of continental rifting: Analog modeling-inspired view and comparison with examples from the East African Rift System. *Tectonophysics*, 522-523, 1–33. doi:10.1016/j.tecto.2011.06.010
- Corti, G., Bonini, M., Conticelli, S., Innocenti, F., Manetti, P., & Sokoutis, D. (2003). Analogue modelling of continental extension: a review focused on the relations between the patterns of deformation and the presence of magma. *Earth-Science Reviews*, 63(3-4), 169–247. doi:10.1016/S0012-8252(03)00035-7
- Corti, G., Iandelli, I., & Cerca, M. (2013). Experimental modeling of rifting at craton margins. *Geosphere* 2013;9;138-154 doi: 10.1130/GES00863.
- Corti, G., van Wijk, J., Cloetingh, S., & Morley, C. K. (2007). Tectonic inheritance and continental rift architecture: Numerical and analogue models of the East African Rift system. *Tectonics*, 26(6), n/a–n/a. doi:10.1029/2006TC002086
- Crameri, F., & Kaus, B. J. P. (2010). Parameters that control lithospheric-scale thermal localization on terrestrial planets. *Geophysical Research Letters*, 37(9), n/a–n/a. doi:10.1029/2010GL042921
- Crameri, F., Schmeling, H., Golabek, G. J., Duretz, T., Orendt, R., Buitert, S. J. H., ... Tackley, P. J. (2012). A comparison of numerical surface topography calculations in geodynamic modelling: an evaluation of the “sticky air” method. *Geophysical Journal International*, 189(1), 38–54. doi:10.1111/j.1365-246X.2012.05388.x
- Dadlèz R., Narkiewicz M., Stephenson R. A., Visser M. T. M. (1995): Tectonic evolution of the Mid-Polish Trough: modelling implications and significance for central European geology. *Tectonophysics*. 252: 179-195.
- Davies G. F. (1999) *Dynamic Earth. Plates, Plumes and Mantle Convection*. Cambridge university press. 458 p.
- Dewey, J.F., Burke, K., 1975. Hot-spots and continental break-up. *Geology* 2, 57–60.
- Direen, N. G., Borissova, I., Stagg, H. M. J., Colwell, J. B., & Symonds, P. a. (2007). Nature of the continent ocean transition zone along the southern Australian



- continental margin: a comparison of the Naturaliste Plateau, SW Australia, and the central Great Australian Bight sectors. Geological Society, London, Special Publications, 282(1), 239–263. doi:10.1144/SP282.12
- Direen, N. G., Stagg, H. M. J., Symonds, P. a., & Colwell, J. B. (2011). Dominant symmetry of a conjugate southern Australian and East Antarctic magma-poor rifted margin segment. *Geochemistry, Geophysics, Geosystems*, 12(2), n/a–n/a. doi:10.1029/2010GC003306
- Direen, N. G., Stagg, H. M. J., Symonds, P. a., & Norton, I. O. (2012). Variations in rift symmetry: cautionary examples from the Southern Rift System (Australia-Antarctica). Geological Society, London, Special Publications, 369(1), 453–475. doi:10.1144/SP369.4
- Dupré, S., Cloetingh, S., & Bertotti, G. (2011). Structure of the Gabon Margin from integrated seismic reflection and gravity data. *Tectonophysics*, 506(1-4), 31–45. doi:10.1016/j.tecto.2011.04.009
- Duncan, R. A., 1981, Hotspots in the southern oceans—An absolute frame of reference for motion of the Gondwana continents: *Tectonophysics*, v. 74, p. 29–42.
- Dyksterhuis, S., Rey, P., Muller, R. D., & Moresi, L. (2007). Effects of initial weakness on rift architecture. Geological Society, London, Special Publications, 282(1), 443–455. doi:10.1144/SP282.18
- Ebinger, C.J. et al. (1999) Extensional basin geometry and the elastic lithosphere. *Phil. Trans. Roy. Soc. Lond. A* 357,741–65.
- Ebinger, C.J. (2005) Continental break-up: the East African perspective. *Astro. Geophys.* 46, 216–21.
- Ellis, S.M.; Beaumont, C.; Pfiffner, O.A. (1999) Geodynamic models of crustal-scale episodic tectonic accretion and underplating in subduction zones. *Journal of Geophysical Research. Solid Earth*, 104(B7): 15169-15190
- Ellis, S., Little, T.A., Wallace, L.M., Hacker, B.R., Buiter, S.J.H., (2011). Feedback between rifting and diapirism can exhume ultrahigh-pressure rocks. *Earth and Planetary Science Letters* 311, 427 – 438
- Ellouz, N., Patriat, M., Gaulier, J.-M., Bouatmani, R., and Sabounji, S., (2003), From rifting to Alpine inversion: Mesozoic and Cenozoic subsidence history of some Moroccan basins: *Sedimentary Geology*, v. 156, p. 185–212, doi: 10.1016/S0037-0738(02)00288-9. Emery (1977) Mineral deposits of the deep ocean floor: *Marine Mining* v.1 p. 1-71
- England P., (1983). Constraints on extension of continental lithosphere, *Journal of Geophysical Research*. 88 1145-1152.
- England, P., & McKenzie, D. (1982). A thin viscous sheet model for continental deformation. *Geophysical Journal International*, 70(2), 295–321. doi:10.1111/j.1365-246X.1982.tb04969.x

- Espurt, N., Callot, J.-P., Roure, F., Totterdell, J. M., Struckmeyer, H. I. M., & Vially, R. (2012). Transition from symmetry to asymmetry during continental rifting: an example from the Bight Basin-Terre Adélie (Australian and Antarctic conjugate margins). *Terra Nova*, 24(3), 167–180. doi:10.1111/j.1365-3121.2011.01055.x
- Evans, B., & Goetze, C. (1979). The temperature variation of hardness of olivine and its implication for polycrystalline yield stress. *Journal of Geophysical Research: Solid Earth*, 84(B10), 5505–5524.
- Falvey, D.A., and Mutter, J.C., (1981). Regional plate tectonics and the evolution of Austria's passive continental margins: *Journal of Australian Geology and Geophysics*, v. 6, p. 1–29.
- Falvey, D.A. (1974) The development of continental margins I plate tectonic theory *Journal of Australien Petrohm Exploration Association*, 14, 95-106.
- Farrington, R. J., Stegman, D. R., Moresi, L. N., Sandiford, M., & May, D. a. (2010). Interactions of 3D mantle flow and continental lithosphere near passive margins. *Tectonophysics*, 483(1-2), 20–28. doi:10.1016/j.tecto.2009.10.008
- Farrington, R. J., Moresi, L.-N., & Capitanio, F. A. (2014). The role of viscoelasticity in subducting plates. *Geochemistry, Geophysics, Geosystems*, 15, 4291–4304.
- Franke D. (2013). Rifting, lithosphere breakup and volcanism: Comparison of magma-poor and volcanic rifted margins *Marine and Petroleum Geology* 43 (2013) 63e87
- Fernandez, M. & Ranalli G., (1997). The role of rheology in extensional basin formation modelling, *Tectonophysics* 282 129-145 282
- Favre, P., & Stamp, G. M. (1992). From rifting to passive margin : the examples of the Red Sea , Central Atlantic and Alpine Tethys, 215, 69–97.
- Fleitout, L. & Froidevaux, C. (1982) Tectonics and topography for a lithosphere containing density heterogeneities. *Tectonics* 1, 21–56.
- Forsyth, D.W. & Uyeda, S. (1975) On the relative importance of the driving forces of plate motion. *Geophys. J. Roy. astr. Soc.* 43, 163–200.
- Forsyth, D. W. (1992). Finite extension and low-angle normal faulting. *Geology*, 20(1), 27. doi:10.1130/0091-7613(1992)
- Fowler, C.M.R., and Nisbet, E.G., (1985), The subsidence of the Williston Basin: *Canadian Journal of Earth Sciences*, v. 22, no. 3, p. 408–415
- Franke, D. (2013). Rifting, lithosphere breakup and volcanism: Comparison of magma-poor and volcanic rifted margins. *Marine and Petroleum Geology*, 43, 63–87. doi:10.1016/j.marpetgeo.2012.11.003
- Friedmann, S.J. and Burbank, D.W. (1995) Rift basins and supradetachment basins: Intracontinental extensional end members. *Basin Research*, 7, 109-127.

- Gabrielsen, R. H. , Odinsen, T. & Grunnaleite, I. 1999: Structuring of the Northern Viking Graben and the Møre Basin; the influence of basement structural grain, and the particular role of the MøreTrøndelag Fault Complex. *Marine and Petroleum Geology* 16,443-465
- Galushkin, Y. I., El, A., & Gtlawi, M. El. (2014). Thermal Regime and Amplitude of Lithosphere Extension in the Sirte Basin , Libya : Numerical Estimates in the Plane Basin Modeling System, 50(1), 75–88. doi:10.1134/S1069351313060025
- Ghanoush H.B., Imber J. & McCaffrey K. (Cenozoic Subsidence and Lithospheric Stretching Deformation of the Ajdabiya Trough Area, NE Sirt Basin, Libya.April 7, 2014 AAPG Annual Convention and Exhibition, Houston, TX 2014)
- Gartrell, A.P., 1997, Evolution of rift basins and low-angle detachments in multilayer analog models: *Geology*, v. 25, p. 615–618.
- Gartrell, A. P. (2001). Crustal rheology and its effect on rift basin styles Crustal rheology and its effect on rift basin styles. doi:10.1130/0-8137-1193-2.221
- Genik, G.J., 1992. Regional framework and structural aspects of of rift basins in Niger, Chad and the Central African Republic (e.A.R.). In: Ziegler, P.A. (Ed.), *Geodynamics of Rifting*, vol. II. Case History Studies on Rifts: North and South America and Africa. *Tectonophysics*, vol. 213, pp. 169–185. Geoffroy, L. (2005). Volcanic passive margins, 337, 1395–1408. doi:10.1016/j.crte.2005.10.006
- Gerya T. (2009). *Introduction to Numerical Geodynamic Modelling*. Cambridge University Press. 335 p.
- Gerya, T. V. (2013). Three-dimensional thermomechanical modeling of oceanic spreading initiation and evolution. *Physics of the Earth and Planetary Interiors*, 214, 35–52. doi:10.1016/j.pepi.2012.10.007
- Gleason GC and Tullis J (1995) A flow law for dislocation creep of quartz aggregates determined with the molten salt cell. *Tectonophysics* 247: 1–23.
- Goudanzi G.H. (1980). Strutture – Libya. In: *The geology of Lybia* (ed. M.J.Salem e M.T.Busrewil) Academic Press, London, III, 879-892.
- Goudarzi, G.H., 1981. Structure — Libya. In: Salem, N.J., Busrewil, M.T. (Eds.), *Geology of Libya*. Al-Fateh Univ., Tripoli, pp. 879–892.
- Goetze C and Evans B (1979) Stress and temperature in bending lithosphere as constrained by experimental rock mechanics. *Geophysical Journal of the Royal Astronomical Society* 59: 463–478.
- Gras, R., 1996. Structural style of the southern margin of the Messlah High. In: Salem, M.J., El-Hawat, A.S., Sbeta, A.M. (Eds.), *The Geology of Sirt Basin*. Elsevier, Amsterdam, pp. 201–210, vol. III.
- Gras, R., Thusu, B., 1998. Trap architecture of the Early Cretaceous Sarir Sandstone in the eastern Sirt Basin, Libya. In: MacGregor, D.S., Moody, R.T.J., Clark-Lowes, D.D.

- (Eds.), *Petroleum Geology of North Africa*, vol. 132. Geological Society, Special Publication, pp. 317-334.
- Gueydan, F., Morency, C., & Brun, J.-P. (2008). Continental rifting as a function of lithosphere mantle strength. *Tectonophysics*, 460(1-4), 83–93. doi:10.1016/j.tecto.2008.08.012
- Gueydan, F., Précigout, J., & Montesi, L. G. (2014). Strain weakening enables continental plate tectonics. *Tectonophysics*, 631, 189-196
- Guiraud, R., Maurin, J.-C.H., 1992. Early cretaceous rifts of Western and Central Africa: an overview. *Tectonophysics* 213, 153–168.
- Guiraud, R., and Y. Bellion, 1995, Late Carboniferous to Recent geodynamic evolution of west Gondwanian cratonic Tethyan margins, in A. Nairn, J. Dercourt, and B. Verielynk, eds., *Basins and margins: The ocean. The Tethys Ocean*: New York, Plenum, v. 8, p. 101–124.
- Guiraud, R., Bosworth, W., 1997. Senonian basin inversion and rejuvenation of rifting in Africa and Arabia: synthesis and implications to plate-scale tectonics. *Tectonophysics* 282, 39–82.
- Guiraud, R., 1998. Mesozoic rifting and basin inversion along the northern African Tethyan margin: an overview. In: MacGregor, D.S., Moody, R.T.J., Clark-Lowes, D.D. (Eds.), *Petroleum Geology of North Africa*, vol. 132. Geological Society Special Publication, London, pp. 217–229.
- Guiraud, R., B. Issawi, and W. Bosworth, 2001, Phanerozoic history of Egypt and surrounding areas, in P. A. Ziegler, W. Cavazza, A. H. F. Robertson, and S. Crasquin-Soleau, eds., *Peri-Tethys memoir 6: Peri-Tethyan rift/wrench basins and passive margins: Mémoires Museum National d'Histoire Naturelle*, Paris 186, p. 469–509.
- Guiraud, R., Bosworth, W., Frizon de Lamotte, D., Thierry, J., (2005) *Journal of African Earth Sciences. Phanerozoic geological evolution of Northern and Central Africa. Journal of African Earth Sciences*, doi:10.1016/j.jafrearsci.2005.07.017.
- Gumati, Y. D., and W. H. Kanes, 1985, Early Tertiary subsidence and sedimentary facies, north Sirt Basin, Libya: *AAPG Bulletin*, v. 69, p. 39–52.
- Gumati, Y. D., and S. Schamel, 1988, Thermal maturation history of the Sirte Basin, Libya: *Journal of Petroleum Geology*, v. 11, p. 205–218.
- Gumati, Y.D., Nairn, A.E.M., 1991. Tectonic subsidence of the Sirte Basin, Libya. *J. Pet. Geol.* 14, 93–102.
- Gupta S, Cowie PA, Dawers NH, Underhill JR. A mechanism to explain rift-basin subsidence and stratigraphic patterns through fault-array evolution. *Geology*. 1998 Jul 1;26(7):595-8.

- Hallett, D., El Ghouli, A., 1996. Oil and gas potential of the deep trough areas in the Sirt Basin. In: Salem, M.J., El-Hawat, A.S., Sbata, A.M. (Eds.), *The Geology of Sirt Basin*, vol. II. Elsevier, Amsterdam, pp. 455e482.
- Handy, M. ., & Brun, J.-P. (2004). Seismicity, structure and strength of the continental lithosphere. *Earth and Planetary Science Letters*, 223(3-4), 427–441. doi:10.1016/j.epsl.2004.04.021
- Hanne, D., White, N., Butler, A., and Jones, S. (2004) Phanerozoic vertical motions of Hudson Bay. *Canadian Journal of Earth Science*, 41, 1181–1200.
- Harding, T., 1984. Graben hydrocarbon occurrences and structural style. *Bull. Am. Assoc. Pet. Geol.* 68, 333e362.
- Heine, C., Zoethout, J., & Müller, R. D. (2013). Kinematics of the South Atlantic rift. *Solid Earth*, 4(2), 215–253. doi:10.5194/se-4-215-2013
- Heine, C., Mullar, D., Steinberger, B., Trond, T., & Torsvikb, 1. (2008). Subsidence in intracontinental basins due to dynamic topography. *Physics of the Earth and Planetary Interiors*.
- Hirth, G., and D. Kohlstedt (2004), Rheology of the upper mantle and the mantle wedge: A view from the experimentalists, in *Inside the Subduction Factory*, Geophys. Monogr. Ser., vol. 138, edited by J. Eiler, pp. 83–105, AGU, Washington.
- Hopper, J.R. et al. (2004) Continental breakup and the onset of ultraslow seafloor spreading off Flemish Cap on the Newfoundland rifted margin. *Geology* 32, 93–6.
- Houseman, G., & England, P. (1986). A dynamical model of lithosphere extension and sedimentary basin formation. *Journal of Geophysical Research*, 91(B1), 719. doi:10.1029/JB091iB01p00719
- Huerta, A.D., and Harry, D.L., 2007, The transition from diffuse to focused extension: Modeled evolution of the West Antarctic Rift System: *Earth and Planetary Science Letters*, v. 255, p. 133–147, doi:10.1016/j.epsl .2006.12.011.
- Huismans, R. S., Podladchikov, Y. Y., & Cloetingh, S. A. P. L. (2001). Transition from passive to active rifting: Relative importance of asthenosphere doming and passive extension of the lithosphere, *Journal Of Geophysical Research*, Vol. 106, No. B6, Pages 11,271-11,291
- Huismans, R. S., & Beaumont, C. (2002). Asymmetric lithospheric extension: The role of frictional plastic strain softening inferred from numerical experiments *Asymmetric lithospheric extension : The role of frictional plastic strain softening inferred from numerical experiments*. doi:10.1130/0091-7613(2002)030<0211
- Huismans, R. S., & Beaumont, C. (2003) Symmetric and asymmetric lithospheric extension: Relative effects of frictional-plastic and viscous strain softening *Journal Of Geophysical Research*, Vol. 108, No. B10, 2496, doi:10.1029/2002JB002026, 2003

- Huismans, R. S. (2005). Effect of plastic-viscous layering and strain softening on mode selection during lithospheric extension. *Journal of Geophysical Research*, 110(B2), B02406. doi:10.1029/2004JB003114
- Huismans, R. S., & Beaumont, C. (2007). Roles of lithospheric strain softening and heterogeneity in determining the geometry of rifts and continental margins. *Geological Society, London, Special Publications*, 282(1), 111–138. doi:10.1144/SP282.6
- Huismans, R. S., & Beaumont, C. (2008). Complex rifted continental margins explained by dynamical models of depth-dependent lithospheric extension. *Geology*, 36(2), 163. doi:10.1130/G24231A.1
- Huismans, R., & Beaumont, C. (2011). Depth-dependent extension, two-stage breakup and cratonic underplating at rifted margins. *Nature*, 473(7345), 74–8. doi:10.1038/nature09988
- Huismans, R., & Beaumont, C. (2014). Rifted continental margins: The case for depth-dependent extension. *Earth and Planetary Science Letters* 407(2014)148–162
- Ismail-Zadeh, A. T., and Tackley, P. J., *Computational Methods for Geodynamics*, Cambridge University
- Janssen, M. E., R. A. Stephenson, and S. Cloetingh, 1995, Temporal and spatial correlation between change in plate motions and evolution of rifted basin in Africa: *Geological Society of America Bulletin*, v. 107, p. 1317–1332.
- Jerzykiewicz, T., Ghummed, M.A., Abugares, M.M., Tshakreen, S.O., 2002. Evolution of the Western Margin of the Sirt Basin of Libya in Late Cretaceous Time. Abstract, Extended Abstract and Talk at CSPG Convention in Calgary, Compact Disc and Abstract Volume, p. 179.
- Jin, D.H., Karato, S.I., Obata, M., 1998. Mechanisms of shear localization in the continental lithosphere: inference from deformation microstructures of peridotites from the Ivrea zone, northwestern Italy. *J. Struct. Geol.* 20, 195–209.
- Kameyama, M., Yuen, D.A., Fujimoto, H., 1997. The interaction of viscous heating with grain-size dependent rheology in the formation of localized slip zones. *Geophys. Res. Lett.* 24, 2523–2526.
- Karato S (1998) Effects of pressure on plastic deformation of polycrystalline solids: Some geological applications. *Materials Research Society Symposium Proceedings* 499: 3–14.
- Karato S-I, Paterson MS, and FitzGerald JD (1986) Rheology of synthetic olivine aggregates: Influence of the grain size and water. *Journal of Geophysical Research* 91: 8151–8176.
- Katz, R. F., Spiegelman, M., & Langmuir, C. H. (2003). A new parameterization of hydrous mantle melting. *Geochemistry, Geophysics, Geosystems*, 4(9), n/a–n/a. doi:10.1029/2002GC000433

- Kaus, B. J. P., Connolly, J. A. D., Podladchikov, Y. Y., & Schmalholz, S. M. (2005). Effect of mineral phase transitions on sedimentary basin subsidence and uplift. *Earth and Planetary Science Letters*, 223, 213–228.
- Kaus, B. J. P. (2010). Factors that control the angle of shear bands in geodynamic numerical models of brittle deformation. *Tectonophysics*, 484(1-4), 36–47. doi:10.1016/j.tecto.2009.08.042
- Kaus, B. J. P., and Y. Y. Podladchikov (2006), Initiation of localized shear zones in viscoelastoplastic rocks, *J. Geophys. Res.- Solid Earth*, 111(B4)
- Kaus, B. J. P., Steedman, C., & Becker, T. W. (2008). From passive continental margin to mountain belt: Insights from analytical and numerical models and application to Taiwan. *Physics of the Earth and Planetary Interiors*, 171(1-4), 235–251. doi:10.1016/j.pepi.2008.06.015
- Kearey P., Klepeis K.A., Vine F.J. (2010). *Global Tectonics* – 3rd ed. 463 Pages. John Wiley & Sons
- Keen, C. E. (1985). The dynamics of rifting: deformation of the lithosphere by active and passive driving forces. *Geophysical Journal International*, 80(1), 95–120. doi:10.1111/j.1365-246X.1985.tb05080.x
- Keen, C. E., P. Potter, and S. P. Srivastava (1994), Deep seismic reflection data across the conjugate margins of the Labrador Sea, *Can. J. Earth Sci.*, 31, 192–205, doi:10.1139/e94-016.
- Keen, C.E., (1987) Dynamical extension of the Lithosphere during rifting: Some numerical model results, in *Composition, Structure and Dynamics of the Lithosphere-Asthenosphere System* pp. 189-203, Edited by K.Fuchs and C. Froidevaux, Am. Geophys. Union, *Geodynamics Series* 16
- Keen, C.E., (1987) Some important consequences of lithospheric extension, in *Continental Extensional Tectonics* edited by M.P. Coward, J.F. Dewey, and P.L. Hancock, pp. 67-73, Geological Society Special Publication no. 28
- Keen, C.E. and D.L. Barrett (1981), Thinned and subsided continental crust on the rifted margin of eastern Canada: crustal structure, thermal evolution and subsidence history, *Geophys. J. R. astr. Soc.*, 65, 443-465
- Keen, C.E., R. Boutilier, B. de Voogd, B. Mudford, and M.E. Enachescu (1987), Crustal geometry and models of the evolution of the rift basins on the Grand Banks off Eastern Canada: Constraints from deep seismic data, in *Sedimentary Basins and Basin-Forming Mechanisms* edited by C. Beaumont and A.J. Tankard, Canadian Society of Petroleum Geologists Memoir 12
- Keen, C.E., Boutilier, R.R., 1995. Lithosphere-asthenosphere interactions below rifts. In: Banda, E., Talwani, M., Tornd, M. (Eds.), *Rifted Ocean-Continent Boundaries*. Kluwer, Dordrecht, pp. 247-263.
- Keen, C.E. and B. de Voogd, (1987) The Continent-Ocean boundary at the rifted margin off eastern Canada: New results from deep seismic reflection studies, *Tectonics*

- Keen, C. E., and R. R. Boutilier (2000), Interaction of rifting and hot horizontal plume sheets at volcanic margins, *J. Geophys. Res.*, 105, 13,375–13,387, doi:10.1029/2000JB900027.
- Khain, V.Yu., 1992. The role of rifting in the evolution of the Earth's crust. *Tectonophysics* 215, 1–7.
- Kirby SH, Durham W, and Stern L (1991) Mantle phase changes and deep-earthquake faulting in subducting lithosphere. *Science* 252: 216–225.
- Kirby SH and Kronenberg AK (1987) Rheology of the lithosphere: Selected topics. *Review of Geophysics* 25: 1219–1244 (correction 1680–1681).
- Klemperer, S.L. (1988) Crustal thinning and nature of extension in the northern North Sea from deep seismic reflection profiling. *Tectonics*, 7, 803–821.
- Klitzsch, E., 1971. The structural development of parts of north Africa since Cambrian time. In: Gray, C. (Ed.), *First Symposium on the Geology of Libya* Faculty of Science. University of Libya, Tripoli, pp. 253–262.
- Klepeis, K.A., King, D., De Paoli, M., Clarke, G.L. & Gehrels, G. (2007) Interaction of strong lower and weak middle crust during lithospheric extension in western New Zealand. *Tectonics* 26, TC4017.
- Klitzsch E. H. & C. H (1990). Squyres. Paleozoic and Mesozoic geological history of northeastern Africa based upon new interpretation of Nubian strata *AAPG Bulletin*, August, v. 74, p. 1203–1211
- Kohlstedt, D. L., Evans, B., & Mackwell, S. J. (1995). Strength of the lithosphere: Constraints imposed by laboratory experiments. *Journal of Geophysical Research*, 100(B9), 17,587–17,602.
- Kooi, H., Cloetingh, S. and Burrus, J. (1992) Lithospheric necking and regional isostasy at extensional basins; 1. Subsidence and gravity modeling with an application to the Gulf of Lions margin (SE France). *Journal of Geophysical Research*, 97, 17553–17571.
- Kooi, H. and Beaumont, C. (1994) Escarpment retreat on high elevation rifted continental margins: Insights derived from a surface-processes model that combines diffusion, reaction and advection. *Journal of Geophysical Research*, 99, 12191–12209.
- Kooi, H. and Beaumont, D. (1996) Large-scale geomorphology: Classical concepts reconciled and integrated with contemporary ideas via a surface processes model. *Journal of Geophysical Research*, 101, 3361–3386.
- Koopmann H., Brune S., Franke D., and Breuer S. (2014). Linking rift propagation barriers to excess magmatism at volcanic rifted margins. *Geology*, December 2014; v. 42; no. 12; p. 1071–1074; Data Repository item 2014368 doi:10.1130/G36085.1



- Koptev A., Calais E., Burov E., Leroy S. and Gerya T. (2015) Dual continental rift systems generated by plume–lithosphere interaction. *Nature Geoscience Letters* DOI: 10.1038/NGEO2401
- Koyi H. (1997) Analogue modelling: from a qualitative to a quantitative technique—a historical outline - *Journal of Petroleum Geology*, 1997 - Wiley Online Library
- Kusznir, N. (1982) Lithosphere response to externally and internally derived stresses: a viscoelastic stress guide with amplification. *Geophys. J. R. astr. SOC.* (1982) 70, 399-414
- Kusznir, N., & Karner, G. (1985). Dependence of flexural rigidity of the continental lithosphere on rheology and temperature. *Letters to Nature*, 316(11).
- Kusznir, N. J., & Park, R. G. (1987). Geological Society, London, Special Publications The extensional strength of the continental lithosphere: its dependence on geothermal gradient, and crustal composition and thickness Email alerting service Permission The extensional strength of the co. Geological Society, London, Special Publications, 28(1), 35–52. doi:10.1144/GSL.SP.1987.028.01.04
- Kusznir, N. J., & Karner, G. D. (2007). Geological Society, London, Special Publications Continental lithospheric thinning and breakup in response to upwelling divergent mantle flow: application to the Woodlark, Newfoundland and Iberia margins service Continental lithospheric thinning and b. Geological Society, London, Special Publications, 282(1), 389–419. doi:10.1144/SP282.16
- Lai W.M., Rubin D., Kremp E. (2009) Introduction to Continuum Mechanics, Fourth Edition 4th Edition by W Michael Lai (Author), David Rubin (Author), Erhard Krempf (Author) Publisher: Elsevier; 4 edition (September 3, 2009) 608 p.
- Landuyt, W., Bercovici, D., 2009. Formation and structure of lithospheric shear zones with damage. *Phys. Earth Planet. Int.* 175, 115–126.
- Lavier, L. L., Buck, W. R., & Poliakov, A. N. B. (1999). Self-consistent rolling-hinge model for the evolution of large-offset low-angle normal faults. *Geology*, 27(12), 1127. doi:10.1130/0091-7613(1999)027<1127:SCRHMF>2.3.CO;2
- Lavier, L. L., Buck, W. R., & Poliakov, A. N. B. (2000). Factors controlling normal fault offset in an ideal brittle layer. *Journal of Geophysical Research*, 105(B10), 23431. doi:10.1029/2000JB900108
- Lavier, L. L., & Manatschal, G. (2006). A mechanism to thin the continental lithosphere at magma-poor margins. *Nature*, 440(7082), 324–8. doi:10.1038/nature04608
- Laubscher, H., and D. Bernoulli, 1977, Mediterranean and Tethys, in A. E. M. Nairn, W. H. Kanes, and F. G. Stechl, eds., *The ocean basin and margins*: New York, Plenum, p. 1–69.
- Le Pichon, X., & Sibuet, J.-C. (1981). Passive margins: A model of formation. *Journal of Geophysical Research*, 86(B5), 3708. doi:10.1029/JB086iB05p03708

- Le Pichon, X., Sibuet, J.-C., & Frabcheteau, J. (1977). The fit of the continents around the north Atlantic ocean. *Tectonophysics*, 38, 169–209.
- Liao, J., Zhou, D., Zhao, Z., Zhang, Y., & Xu, Z. (2011). Numerical modeling of the anomalous post-rift subsidence in the Baiyun Sag, Pearl River Mouth Basin. *Science China Earth Sciences*, 54(8), 1156–1167. doi:10.1007/s11430-011-4184-3
- Liao, J., & Gerya, T. (2014). Influence of lithospheric mantle stratification on craton extension: Insight from two-dimensional thermo-mechanical modeling. *Tectonophysics*, 631, 50–64. doi:10.1016/j.tecto.2014.01.020
- Liao, J. and Gerya, T. (2014). From continental rifting to seafloor spreading: Insight from 3D thermo-mechanical modeling. *Gondwana Res.* Volume 28, Issue 4, December 2015, Pages 1329–1343
- Lindsay JF, 2002. Supersequences, superbasins, supercontinents – evidence from the Neoproterozoic– Early Palaeozoic basins of central Australia. *Basin Research* 14, 207–223
- Lister, G.S., Etheridge, M.A. & Simons, P.A. (1986) Detachment faulting and the evolution of passive continental margins. *Geology* 14, 246–50.
- Lister, G. S., & Davis, G. A. (1898). Lister, G.S., Davis, G.A., 1989. The origin of metamorphic core complexes and detachment faults formed during Tertiary continental extension in the northern USA Colorado River region. *Journal of Structural Geology*, 11, 65–94.
- Lowell, J.D. and Genik, GJ. (1972) Sea floor spreading and structural evolution of southern Red Sea. *Bulletin American Association of Petroleum Geologists*, 56, 247–259.
- Lowrie W. (2007). *Fundamentals Of Geophysics*. 2nd Edition. Cambridge University Press. 390 p.
- Lizarralde D., Axen G. J., Brown H. E, Fletcher J. M., Gonzalez-Fernandez A., Harding A. J., Holbrook W. S., Kent G. M, Paramo P., Sutherland F. & Umhoefer P. J. (2007). Variation in styles of rifting in the Gulf of California. *Nature Letters*. Vol 448|26 July 2007| doi:10.1038/nature06035
- Lu, G., Kaus, B. J. P., & Zhao, L. (2011). Thermal localization as a potential mechanism to rift cratons. *Physics of the Earth and Planetary Interiors*, 186(3-4), 125–137. doi:10.1016/j.pepi.2011.04.006
- Lyngsie, S. B., Thybo, H., & Lang, R. (2007). Rifting and lower crustal reflectivity: a case study of the intracratonic Dniepr-Donets rift zone, Ukraine. *Journal of Geophysical Research*, 112.
- Manatschal, G. (2004). New models for evolution of magma-poor rifted margins based on a review of data and concepts from West Iberia and the Alps. *International Journal of Earth Sciences*, 83, 432–466.

- Manatschal, G., & Bernoulli, D. (1999). Architecture and tectonic evolution of nonvolcanic margins: Present-day Galicia and ancient Adria. *Tectonics*, 18(6), 1099–1119. doi:10.1029/1999TC900041
- Manatschal, G., Lavier, L., & Chenin, P. (2015). The role of inheritance in structuring hyperextended rift systems: Some considerations based on observations and numerical modeling. *Gondwana Research*, 27(1), 140–164. doi:10.1016/j.gr.2014.08.006
- Marotta, A. M., A.M., Bayer, U., & Thybo, H. (2000). The legacy of the NE German Basin: reactivation by compressional buckling. *Terra Nova*, 12, 132–140.
- Mason, W. G., Moresi, L., Betts, P. G., & Miller, M. S. (2010). Three-dimensional numerical models of the influence of a buoyant oceanic plateau on subduction zones. *Tectonophysics*, 483(1-2), 71–79. doi:10.1016/j.tecto.2009.08.021
- Mackwell SJ, Zimmerman ME, and Kohlstedt DL (1998) Hightemperature deformation of dry diabase with applications to tectonics on Venus. *Journal of Geophysical Research* 103: 975–984.
- May, D. a., & Moresi, L. (2008). Preconditioned iterative methods for Stokes flow problems arising in computational geodynamics. *Physics of the Earth and Planetary Interiors*, 171(1-4), 33–47. doi:10.1016/j.pepi.2008.07.036
- McClusky, S., Reilinger, R., Ogubazghi, G., Amleson, A., Healeb, B., Vernant, P., ... Kogan, L. (2010). Kinematics of the southern Red Sea-Afar Triple Junction and implications for plate dynamics. *Geophysical Research Letters*, 37(5), n/a–n/a. doi:10.1029/2009GL041127
- McKenzie, D. P. (1967). Sea-floor spreading, *J. Geophys. Res.* 72, 6261– 6273.
- Mckenzie, D. (1978). Some remarks on the development of sedimentary basins. *Earth and Planetary Science Letters*, 40(1), 25–32. doi:10.1016/0012-821X(78)90071-7
- McKenzie, D., Bickle, M.J., 1988. The volume and composition of melts generated by extension of the lithosphere. *J. Petrol.* 29, 625– 679.
- Michon, L., & Merle, O. (2003). Mode of lithospheric extension: Conceptual models from analogue modeling. *Tectonics*, 22(4), n/a–n/a. doi:10.1029/2002TC001435
- Molnar, P., & Jones, C. H. (2004). A test of laboratory based rheological parameters of olivine from an analysis of late Cenozoic convective removal of mantle lithosphere beneath the Sierra Nevada, California, USA. *Geophysical Journal International*, 156(3), 555–564. doi:10.1111/j.1365-246X.2004.02138.x
- Montadert, L., Roberts, D.G., de Charpal, O. and Guennoc, F. (1979) Rifting and subsidence of the northern continental margin of the Bay of Biscay. In Montadert, L., Roberts, D.G., et al., *Init. Repts. DSDP*, 48: Washington (U.S. Govt. Printing Office), 1025-1060.

- Montési, L.G.J. & Zuber, M.T. (2002) A unified description of localization for application to large-scale tectonics. *J. geophys. Res.* 107, 2045, doi:10.1029/2001JB000465.
- Moore T.C., Klitgord K.D., Golmstok A.Ya., Weber E. (1997) Sedimentation and subsidence patterns in the central and north basins of Lake Baikal from seismic stratigraphy *Geological Society of America Bulletin*, 109, pp. 746–766
- Moresi, L. (n.d.). Mantle-scale geodynamics.
- Moresi, L., Dufour, F., & Mühlhaus, H.-B. (2003). A Lagrangian integration point finite element method for large deformation modeling of viscoelastic geomaterials. *Journal of Computational Physics*, 184(2), 476–497. doi:10.1016/S0021-9991(02)00031-1
- Moresi, L., Quenette, S., Lemiale, V., Mériaux, C., Appelbe, B., & Mühlhaus, H.-B. (2007). Computational approaches to studying non-linear dynamics of the crust and mantle. *Physics of the Earth and Planetary Interiors*, 163(1-4), 69–82. doi:10.1016/j.pepi.2007.06.009
- Morgan, W. J., 1980, Hotspot tracks and the opening of the Atlantic and Indian Oceans, in C. Emiliani, ed., *The sea: Wiley*, New York, v. 7, p. 443–467.
- Morgan, W. J., 1983, Hotspot tracks and the early rifting of the Atlantic: *Tectonophysics*, v. 94, p. 123–139.
- Moulin, M., Aslanian, D., & Al., E. (2005). Geological constraints on the evolution of the Angolan margin based on reflection and refraction seismic data (ZaïAngo project). *Geophysical Journal International*, 162, 793–810.
- Nagel, T. J., & Buck, W. R. (2004). Symmetric alternative to asymmetric rifting models. *Geology*, 32(11), 937. doi:10.1130/G20785.1
- Nagel, T. J., & Buck, W. R. (2007). Control of rheological stratification on rifting geometry: a symmetric model resolving the upper plate paradox. *International Journal of Earth Sciences*, 96(6), 1047–1057. doi:10.1007/s00531-007-0195-x
- Naliboff, J. and S.J.H. Buiter, 2015, Rift reactivation and migration during multiphase extension, *Earth and Planetary Science Letters*, 421, 58,-67, doi: 10.1016/j.epsl.2015.03.050
- Newman, R., & White, N. (1997). Rheology of the continental lithosphere inferred from sedimentary basins. *Letter of Nature*, 385(13), 621–624.
- Newman, R., White, N., Buck, W. R., Gallagher, K., Watts, A. B., Mckenzie, D., Geli L., White, R. S. (1999). The Dynamics of Extensional Sedimentary Basins : Constraints from Subsidence Inversion [ and Discussion ] Source : *Philosophical Transactions : Mathematical , Physical and Engineering Sciences* , Vol . 357 , No . 1753 , Response of the Earth ' s Lithospher, 357.

- Olsen, K.H., Morgan, P., 1995. Introduction: progress in understanding continental rifts. In: Olsen, K.H. (Ed.), *Continental Rifts: Evolution, Structure, Tectonics. Developments in Geotectonics*, vol. 25, pp.
- Pascal, C., Wijk, J. W. Van, Cloetingh, S. A. P. L., & Davies, G. R. (2002). Effect of lithosphere thickness heterogeneities in controlling rift localization : Numerical modeling of the Oslo Graben. *Geophysical Research Letters* Volume 29, Issue 9 May 2002 Pages 69-1–69-4 Patton, T. L. (n.d.). *Tectonic Evolution and Structural Setting of the Suez Rift*.
- Pawellek, T., 2007. *A Field Guidebook to the Geology of Sirt Basin, Libya*. Gutenberg Press, Malta, pp. 1–102. RWE fieldtrip guidebooks. Tripoli.
- Perez-Gussinye, M. (2012). Geological Society , London , Special Publications A tectonic model for hyperextension at magma-poor rifted margins : an example from the West Iberia – Newfoundland conjugate margins service Subscribe A tectonic model for hyperextension at magma-poor rift. Geological Society, London, Special Publications, 369(1), 403–427. doi:10.1144/SP369.19
- Pérez-Gussinyé M., Morgan, J., Reston, T., & Ranero, C. (2006). The rift to drift transition at non-volcanic margins: Insights from numerical modelling. *Earth and Planetary Science Letters*, 244(1-2), 458–473. doi:10.1016/j.epsl.2006.01.059
- Peron-Pinvidic, G., & Manatschal, G. (2010). From microcontinents to extensional allochthons: Witnesses of how continents rift and break apart. *Petroleum Geoscience.*, 16(3), 207–15.
- Peron-Pinvidic, G., Manatschal, G., & Osmundsen, P. T. (2013). Structural comparison of archetypal Atlantic rifted margins: A review of observations and concepts. *Marine and Petroleum Geology*, 43, 21–47. doi:10.1016/j.marpetgeo.2013.02.002
- Péron-Pinvidic, G., Manatschal, G., Minshull, T. A., & Sawyer, D. . (2007). Tectonics Commentary evolution of the deep Iberia–Newfoundland margins: evidence for a complex breakup history. *Tectonics*, TC2011.
- Petit, C. & Ebinger, C. (2000) Flexure and mechanical behavior of cratonic lithosphere: gravity models of the East African and Baikal rifts. *J. geophys. Res.* 105, 19,151–62.
- Petersen, K. D., Armitage, J. J., Nielsen, S. B., & Thybo, H. (2015). Mantle temperature as a control on the time scale of thermal evolution of extensional basins. *Earth and Planetary Science Letters*, 429, 61–70.
- Petrini, K., & Connolly, J.A.D., Podlachikov, Y. (2001). A coupled petrological-tectonic model for sedimentary basin evolution: the influence of metamorphic reactions on basin subsidence. *Geochem. Geophys. Geosyst.*, 6.
- Philippon M., Thieulot C., van Wijk J., Sokoutis D., Willingshofer E. & Sierd Cloetingh (2013) Influence of the heterogeneities within the lithosphere on the deformation pattern of continental rift systems. EGU meeting, Vienna, April 2013

- Pollack, H. N. and Chapman, D. S. (1977). On the regional variation of heat flow, geotherms and the thickness of the lithosphere. *Tectonophysics*, 38, 279–296.
- Porth, R. (2000). A strain-rate-dependent force model of lithospheric strength. *Geophysical Journal International*, 141(3), 647–660. doi:10.1046/j.1365-246x.2000.00115.x
- Ranally G and Murphy D (1987) Geological stratification of the lithosphere. *Tectonophysics* 132: 281–295.
- Ranalli, G. (1995) *Rheology of the Earth*, 2nd edn Chapman & Hall, London.
- Reemst P (1995) Tectonic modeling of rifted continental margins; Basin evolution and tectono-magmatic development of the Norwegian and NW Australian margin. PhD thesis, Vrije Universiteit, Amsterdam, 163p.
- Reemst, P., & Cloetingh, S. (2000). Polyphase rift evolution of the Vøring margin (mid-Norway): Constraints from forward tectonostratigraphic modelling. *Tectonics*, Volume 19, Issue 2, April 2000, Pages 225–240
- Regenauer-Lieb, K., Yuen, D.A., 2004. Positive feedback of interacting ductile faults from coupling of equation of state, rheology and thermal-mechanics. *Phys. Earth Planet. Int.* 142, 113–135.
- Regenauer-Lieb, K., & Yuen, D. a. (2006). Quartz Rheology and Short-time-scale Crustal Instabilities. *Pure and Applied Geophysics*, 163(9), 1915–1932. doi:10.1007/s00024-006-0104-4
- Regenauer-Lieb, K., Rosenbaum, G. and Weinberg, R.F., 2008. Strain localisation and weakening of the lithosphere during extension. *Tectonophysics*, 458: 96-104.
- Rosenbaum, G., Weinberg, R.F. and Regenauer-Lieb, K., 2008. The geodynamics of lithospheric extension. *Tectonophysics*, 458: 1-8.
- Rosenbaum, G., Regenauer-Lieb, K., and Weinberg, R.F. (2010) Interaction between mantle and crustal detachments: A nonlinear system controlling lithospheric extension. *Journal Of Geophysical Research*, Vol. 115, B11412, doi:10.1029/2009JB006696
- Reilinger, R., & McClusky, S. (2011). Nubia-Arabia-Eurasia plate motions and the dynamics of Mediterranean and Middle East tectonics. *Geophysical Journal International*, 186(3), 971–979. doi:10.1111/j.1365-246X.2011.05133.x
- Reston, T. J. (2009). The extension discrepancy and syn-rift subsidence deficit at rifted margins. *Petroleum Geoscience*, 15(3), 217–237. doi:10.1144/1354-079309-845
- Reston, T. J. (2010). The opening of the central segment of the South Atlantic: symmetry and the extension discrepancy. *Petroleum Geoscience*, 16(3), 199–206. doi:10.1144/1354-079309-907

- Rey, P. F., Teyssier, C., & Whitney, D. L. (2009). The role of partial melting and extensional strain rates in the development of metamorphic core complexes. *Tectonophysics*, 477(3-4), 135–144. doi:10.1016/j.tecto.2009.03.010
- Reemst, P., & Cloetingh, S. (2000). Polyphase rift evolution of the V&#248;ring margin (mid-Norway): Constraints from forward tectonostratigraphic modeling, 19(2), 225–240.
- Roohi, M., 1996, Geological history and hydrocarbon migration pattern of the As Zaahra-Al Hufrah platform, in M. J. Salem, M. T. Busrewil, A. A. Misallati, and M. A. Sola, eds., *The geology of the Sirt Basin*: Amsterdam, Elsevier, v. 1, p. 195–232.
- Rosenbaum, G., Regenauer-Lieb, K., & Weinberg, R. F. (2010). Interaction between mantle and crustal detachments: A nonlinear system controlling lithospheric extension. *Journal of Geophysical Research*, 115(B11), B11412. doi:10.1029/2009JB006696
- Rosenbaum, G., Weinberg, R. F., & Regenauer-Lieb, K. (2008). The geodynamics of lithospheric extension. *Tectonophysics*, 458(1-4), 1–8. doi:10.1016/j.tecto.2008.07.016
- Royden, L., Keen, C.E., 1980. Rifting process and thermal evolution of the continental margin of eastern Canada determined from subsidence curves. *Earth Planet. Sci. Lett.* 51, 343– 361.
- Royden, L., Sclater, J.G., Herzen, R.P., 1980. Continental margin subsidence and heat flow; important parameters in formation of petroleum hydrocarbons. *Am. Assoc. Pet. Geol. Bull.* 62, 173– 187.
- Rusk, D.C., 2001, Libya. Petroleum potential of the underexplored basin centers-A twenty-first-century challenge: in M.W. Downey, J.C. Threet, and W.A. Morgan (eds), *Petroleum provinces of the twenty-first century: AAPG Memoir 74*, p. 429–452.
- Saheel, A.S., Samsudin, A.R.B., and Hamzah, U.B. (2010) Regional geological and tectonic structures of the Sirt Basin from potential field data, *Amer. J. Sci. Ind. Res.*, vol. 1, no. 3, pp. 448–462.
- Sandiford, M., Hansen D.L., McLaren, S.N., 2006, Lower crustal rheological expression in inverted basins, in *Analogue and Numerical Modelling of Crustal Scale Processes* (eds Buiter, S. & Schreurs, G.). Geological Society Special Publication, 253, 271–283.
- Sawyer, D. S. (1985a) Brittle Failure in the Upper Mantle During Extension of Continental Lithosphere *Journal Of Geophysical Research*, Vol. 90, No. B4, Pages 3021–302
- Schäfer, K., Kraft, K.H., Hausler, H., Erdman, J., 1980. In situ stresses and paleostresses in Libya. In: Salem, N.J., Busrewil, M.T. (Eds.), *Geology of Libya*, Al-Fateh Univ, Tripoli, 1981, pp. 907–922.

- Schubert, G., Turcotte, D.L., 1972. One-dimensional model of shallow-mantle convection. *J. Geophys. Res.* 77, 945–951.
- Selley, R.C. (1972) Diagnosis of marine and non-marine environments from the cambro-ordovician sandstones of Jordan. *Journal Geological Society London*, 128, 135–150.
- Selley, R.C., ed., 1997, *African basins*: Amsterdam, Elsevier, 394 p.
- Selley, R.C. (1997) The basins of northwest africa: structural evolution, in Selley, R.C. (Ed.) *African Basins: Sedimentary Basins of the World*, Elsevier, Amsterdam, 17–26.
- Şengör, A. M. C., & Natal'in, B. A. (2001). Rifts of the world. *Geological Society of America, Special Paper*, 352.
- Şengör, A.M.C., Burke, K., 1978. Relative timing of rifting and volcanism on Earth and its tectonic implications. *Geophys. Res. Lett.* 5, 419– 421.
- Sharples, W., L.-N. Moresi, M. A. Jadamec, and J. Revote (2015), Styles of rifting and fault spacing in numerical models of crustal extension, *J. Geophys. Res. Solid Earth*, 120, 4379–4404, doi:10.1002/2014JB011813
- Schroeter, T. (1996) Tectonic and sedimentary development of the central Zallah trough (west Sirt Basin, Libya), in M. J. Salem, M. T. Busrewil, A. A. Misallati, and M. A. Sola, eds., *The geology of the Sirt Basin*: Amsterdam, Elsevier, v. 3, p. 123–135.
- Schmeling, H. (2010). Dynamic models of continental rifting with melt generation. *Tectonophysics*, 480(1), 33-47.
- Shemenda Alexander I. (1994) *Subduction : insights from physical modeling* Dordrecht ; Boston : Kluwer Academic Publishers. 215 p
- Sibson, R. (1980), Transient discontinuities in ductile shear zones, *J. Struct.Geol.*, 2, 165–171. Sibson, R. H. (1982), Fault zone models, heat flow, and the depth distribution of earthquakes in the continent
- Sibson, R. H. (1982), Fault zone models, heat flow, and the depth distribution of earthquakes in the continental crust of the United States, *Bull. Seismol. Soc. Am.*, 72 (1), 151–163
- Sibson R.H., (1983): Continental fault structure and the shallow earthquake source, *Journal of Geologic Society of London*. 140: 741–767.
- Skuce, G. A., 1996, Forward modeling of compaction above normal faults: An example from the Sirt Basin, Libya, in P. G. Buchanan and P. A. Nieuwland, eds., *Modern development in structural interpretation, validation and modeling*: Geological Society Special Publication 99, p. 135–136.
- Solomatov, V. S., and L. N. Moresi (1996), Stagnant lid convection on Venus, *J. Geophys. Res.*, 101(E2), 4737–4753.



- Spohn, T., & Schubert, G. (1982). Convective thinning of the lithosphere: A mechanism for the initiation of continental rifting. *Journal of Geophysical Research*, 87(B6), 4669. doi:10.1029/JB087iB06p04669
- Spohn, T., Schubert, G., 1983. Convective thinning of the lithosphere: a mechanism for rifting and Mid-Plate volcanism on Earth, Venus and Mars. *Tectonophysics* 94, 67– 90.
- Stampfli, G. M., Borel, G. D., Marchant, R. & Mosar, J. 2002. Western Alps geological constraints on western Tethyan reconstructions. In: Rosenbaum, G. and Lister, G. S. 2002. Reconstruction of the evolution of the Alpine-Himalayan Orogen. *Journal of the Virtual Explorer*, 7, 75 - 104.
- Steckler, M. ., & Watts, A. . (1978). Subsidence of the atlantic-type continental margin off new york. *Earth and Planetary Science Letters*, 41, 1–16.
- Stegman, D. R., Farrington, R., Capitanio, F. a., & Schellart, W. P. (2010). A regime diagram for subduction styles from 3-D numerical models of free subduction. *Tectonophysics*, 483(1-2), 29–45. doi:10.1016/j.tecto.2009.08.041
- Stuwe K. (2012) *Geodynamics of the Lithosphere: An Introduction*. Springer-Verlag Berlin and Heidelberg GmbH & Co. KG. 462 p. 9783540417262
- Sutra, E., Manatschal, G., Mohn, G., & Unternehr, P. (2013). Quantification and restoration of extensional deformation along the Western Iberia and Newfoundland rifted margins. *Geochemistry, Geophysics, Geosystems*, 14(8), 2575–2597. doi:10.1002/ggge.20135
- Tawadros, E.E., 2001. *Geology of Egypt and Libya*. A.A. Balkema, Rotterdam, 468p.
- Thusu, B., 1996. Implication of the discovery of reworked and in situ late Palaeozoic and Triassic palynomorphs on the evolution of Sirt Basin, Libya. In: Salem, M.J., Mouzoughi, Hammuda, O.S. (Eds.), *The Geology of Sirt Basin*, vol. I. Elsevier, Amsterdam, pp. 455–474.
- Ter Voorde M and Cloetingh S (1996) Numerical modelling of extension in faulted crust: effects of localized and regional deformation on basin stratigraphy. *Geological Society, London, Special Publications* 99: 283–296.
- Tett, D. L., & Sawyer, D. S. (1996). 40 . Dynamic models of multiphase continental rifting and their implications for the newfoundland and iberia conjugate margins 1 description of the newfoundland-iberia conjugate margins. In Whitmarsh, R.B., Sawyer, D.S., Klaus, A., and Masson, D.G. (Eds.), 1996 *Proceedings of the Ocean Drilling Program, Scientific Results*, Vol. 149
- Tron, V., & Brun, J.-P. (1991). Experiments on oblique rifting in brittle-ductile systems. *Tectonophysics*, 188(1-2), 71–84. doi:10.1016/0040-1951(91)90315-J
- Turcotte, D. L. and Schubert, G. (1982). *Geodynamics: Applications of Continuum Physics to Geological Problems*, New York: J.Wiley.
- Turcotte, and Schubert (2002) *Geodynamics*. 2nd Edition. Cambridge University Press. 636 p.

- Turcotte, and Schubert (2014) *Geodynamics*. 3rd Edition. Cambridge University Press. 636 p.
- Unternehr, P., Peron-Pinvidic, G., Manatschal, G., & Sutra, E. (2010). Hyper-extended crust in the South Atlantic: in search of a model. *Petroleum Geoscience*, 16(3), 207–215. doi:10.1144/1354-079309-904
- Van Houten, F. B., 1983, Sirt Basin, north-central Libya, Cretaceous rifting over a fixed mantle hotspot?: *Geology*, v. 11, p. 115–118.
- Van der Meer, F., and S. Cloetingh, 1993a, Late Cretaceous and Tertiary subsidence history of the Sirt Basin (Libya), an example of the use of backstripping analysis: *ITC (International Institute for Geo-information Science and Earth Observation) Journal*, v. 93, no. 1, p. 68–76.
- Van der Meer, F., Cloetingh, S., 1993b. Intraplate stresses and the subsidence history of the Sirte Basin (Libya). *Tectonophysics* 226, 37–58.
- Van der Meer, F., Cloetingh, S., 1996. Intraplate stresses and the subsidence history of the Sirt Basin. In: Salem, M.J., Busrewil, M.T., Misallati, A.A., Sola, M.J. (Eds.), *The Geology of the Sirt Basin, III*. Elsevier, Amsterdam, pp. 211–230.
- Van Wees, J. D., & Stephenson, R. a. (1995). Quantitative modelling of basin and rheological evolution of the Iberian Basin (Central Spain): implications for lithospheric dynamics of intraplate extension and inversion. *Tectonophysics*, 252(1-4), 163–178. doi:10.1016/0040-1951(95)00101-8
- Van Wees, J. D., A. Arche, C. G. Bejldorff, J. Lopez- Gomez, and S. A. P. L. Cloetingh (1998). Temporal and spatial variations in tectonic subsidence in the Iberian Basin (eastern Spain): Inferences from automated modelling of high-resolution stratigraphy (Permian-Mesozoic), *Tectonophysics* , 300 ,285– 310.
- Van Wees J. –D., Stephenson R. A., Ziegler P. A., Bayer U., McCann T., Dadlèz R., Gaupp R., Narkiewicz M., Bitzer F., Scheck-Wenderoth M. (2000): On the origin of the Southern Permian Basin, Central Europe. *Marine and Petroleum Geology*. 17: 43-59.
- Van Wijk, J.W., R.S. Huismans, M. Ter Voorde and S.A.P.L. (2001). Cloetingh, Melt generation at volcanic continental margins: no need for a mantle plume? *Geophysical Research Letters*, 28, 3995-3998.
- Van Wijk, J.W. and S.A.P.L. (2002) Cloetingh, Basin migration caused by slow lithospheric extension, *Earth and Planetary Science Letters* 198, 275-288.
- Van Wijk, J. W. (2005). Role of weak zone orientation in continental lithosphere extension. *Geophysical Research Letters*, 32(2), L02303. doi:10.1029/2004GL022192

- Van Wijk, J. W., Lawrence, J. F., & Driscoll, N. W. (2008). Formation of the Transantarctic Mountains related to extension of the West Antarctic Rift system. *Tectonophysics*, 458(1-4), 117–126. doi:10.1016/j.tecto.2008.03.009
- Watts A. B. (2001) *Isostasy and Flexure of the Lithosphere*. Cambridge University press. 480 p.
- Watts A. B. & Burov E. (2003) Lithospheric strength and its relationship to the elastic and seismogenic layer thickness. *Earth and Planetary Science Letters* 213 (2003) 113–131
- Weinberg, R. F., Regenauer-Lieb, K., & Rosenbaum, G. (2007). Mantle detachment faults and the breakup of cold continental lithosphere. *Geology*, 35(11), 1035. doi:10.1130/G23918A.1
- Weissel, J.K. & Karner, G. (1989) Flexural uplift of rift flanks due to tectonic denudation of the lithosphere during extension. *J. geophys. Res.* 94, 13,919–50.
- Wernicke, B. (1981) Low angle normal faults in the Basin and Range Province – nappe tectonics in an extending orogen. *Nature* 291, 645–8.
- Wernicke, B. (1985) Uniform-sense simple shear of the continental lithosphere. *Can. J. Earth. Sci.* 22, 108–25.
- Westaway, R., 1996. Active tectonic deformation in the Sirt Basin and its surroundings. In: Salem, M.J., Busrewil, M.T., Misallati, A.A., Sola, M.J. (Eds.), *First Symposium on the Sedimentary Basins of Libya, Geology of the Sirt Basin*, vol. 3. Elsevier, Amsterdam, pp. 89–100.
- White N., (1993) Recovery of strain rate variation from inversion of subsidence data, *Nature* 366, 449-452.
- White, N. (1994). An inverse method for determining lithospheric strain rate variation on geological timescales 122, 351–371. *Earth and Planetary Science Letters* 122 (1994) 351-371
- White, N. & Bellingham P. (2002). A two-dimensional inverse model for extensional sedimentary basins 1. Theory. *Journal of Geophysical Research*, 107(B10), 2259. doi:10.1029/2001JB000173
- White, R.S. & D.P. McKenzie (1989) *Volcanism at Rifts* (Scientific American, July 1989, 62-71)
- Whitmarsh R. B. , Manatschal G. & Minshull T. A. (2001) Evolution of magma-poor continental margins from rifting to seafloor spreading. *Nature* |Vol 413 | 13
- Wijns, C., Weinberg, R., Gessner, K., & Moresi, L. (2005). Mode of crustal extension determined by rheological layering. *Earth and Planetary Science Letters*, 236(1-2), 120–134. doi:10.1016/j.epsl.2005.05.030
- Willet SD (1999) Orogeny and orography: The effects of erosion on the structure of mountain belts. *Journal of Geophysical Research* 104: 28957–28981.

- Wilks KR and Carter NL (1990) Rheology of some continental lower crustal rocks. *Tectonophysics* 182: 57–77.
- Wilson, M., 1989. *Igneous Petrogenesis, A Global Tectonic Approach*. Unwin Hyman, London. 466 pp.
- Wilson, M., and R. Guiraud, 1992, Magmatism and rifting in west and central Africa from Late Jurassic to Recent time: *Tectonophysics*, v. 213, p. 203–255.
- Withjack, M.O., Jamison, W.R., 1986. Deformation produced by oblique rifting. *Tectonophysics* 126, 99– 124.
- Wolin E, Stein S, Pazzaglia F, Meltzer A, Kafka A, Berti C. Mineral, Virginia, earthquake illustrates seismicity of a passive–aggressive margin. *Geophysical Research Letters*. 2012 Jan 1;39(2).
- Xie, X., Müller, R. D., Li, S., Gong, Z., & Steinberger, B. (2006). Origin of anomalous subsidence along the Northern South China Sea margin and its relationship to dynamic topography. *Marine and Petroleum Geology*, 23(7), 745–765. doi:10.1016/j.marpetgeo.2006.03.004
- Xie, X.Y., 2007, Sedimentary record of Mesozoic intracontinental deformation in the south Ordos Basin, China [Ph.D. thesis]: University of Wyoming, 280 p.
- Xie, X., & Heller, P. (2009). Plate tectonics and basin subsidence history. *Geological Society of America Bulletin* 1. doi:10.1130/B26398.1
- Zalan, P.V., Wolff, S., Astolfi, M.A.M., Santos Viera, I., Conceicao, J.C.J., Appi, V.T., Neto, E.V.S., Cerqueira, J.R., and Marques, A., (1990), *The Parana Basin, Brazil: American Association of Petroleum Geologists Memoir*, v. 51, p. 681–708.
- Zehnder M., C., C. Mutter, J., & Buhl, P. (1990). Deep Seismic and geochemical constraints on the nature of rift-induced magmatism during breakup of the North Atlantic. *Tectonophysics*, 173(1-4), 545–565. doi:10.1016/0040-1951(90)90245-4
- Zelt, C. A., Sain, K., Naumenko, J. V., & Sawyer, D. S. (2003). Assessment of crustal velocity models using seismic refraction and reflection tomography. *Geophysical Journal International*, 153, 609 – 626.
- Ziegler, P. A., 1988, Evolution of the Arctic-North Atlantic and the western Tethys: *AAPG Memoir* 43, 198 p.
- Ziegler, P. a. (1992). Geodynamics of rifting and implications for hydrocarbon habitat. *Tectonophysics*, 215(1-2), 221–253. doi:10.1016/0040-1951(92)90083-I
- Ziegler, P.A., (1995). Cenozoic rift system of western and Central Europe: an overview. *Geologie e Mijnbouw* 73, 99– 127
- Ziegler, P.A., 1996a. Hydrocarbon habitat in rifted basins. In: Roure, N., Ellouz, N., Shein, V.S., Skvortsov, I. (Eds.), *Geodynamic Evolution of Sedimentary Basins*. Technip, Paris, pp. 85–94.

- Ziegler, P. A., J. D. Van Wees, and S. Cloetingh, 1998, Mechanical control on collision-related compressional intraplate deformation: *Tectonophysics*, v. 300, p. 103–129.
- Ziegler, P., Cloetingh, S., 2003. Dynamic processes controlling evolution of rifted basins. *Earth Sci. Rev*
- Ziegler, P. a., & Cloetingh, S. (2004). Dynamic processes controlling evolution of rifted basins. *Earth-Science Reviews*, 64(1-2), 1–50. doi:10.1016/S0012-8252(03)00041-2
- Zoback MD, Apel R, Baumgartner J, Brudy M, et al. (1993) Upper-crustal strength inferred from stress measurements to 6 km depth in the KTB borehole. *Nature* 365: 633–635.





